Charge and spin control of electron and holes in silicon quantum dot arrays

Agostino Apra

THÈSE

Pour obtenir le grade de

DOCTEUR DE L'UNIVERSITÉ GRENOBLE ALPES

École doctorale : PHYS - Physique
Spécialité : Nanophysique
Unité de recherche : PHotonique, ELectronique et Ingéniérie QuantiqueS

Contrôle de la charge et du spin des électrons et des trous dans les arrays de points quantiques en silicium

Charge and spin control of electron and holes in silicon quantum dot arrays

Présentée par :

Agostino APRA

Direction de thèse :

Silvano DE FRANCESCHI — Directeur de thèse
Ingénieur HDR, CEA Centre de Grenoble

Rapporteurs :

FLORIS ZWANENBURG
Professeur, Universiteit Twente

ENRICO PRATI
Professeur associé, Università degli Studi di Milano

Thèse soutenue publiquement le **17 janvier 2023**, devant le jury composé de :

FLORIS ZWANENBURG Professeur, Universiteit Twente	Rapporteur
ENRICO PRATI Professeur associé, Università degli Studi di Milano	Rapporteur
JESPER NYGARD Professeur, Københavns Universitet	Président
ANASUA CHATTERJEE Professeur assistant, Københavns Universitet	Examinatrice
CLEMENS WINKELMANN Maître de conférences HDR, GRENOBLE INP	Examinateur
JULIA MEYER Professeur des Universités, UNIVERSITE GRENOBLE ALPES	Examinatrice

CHARGE AND SPIN CONTROL OF ELECTRONS AND HOLES IN SILICON QUANTUM DOT ARRAYS

Fatti non foste a viver come bruti,
ma per aver virtute e canoscenza.

You were not born to live like brutes,
but to pursue virtue and knowledge.

Dante Alighieri

Dio mi ha dato un cervello,
se non lo usassi gli mancherei di rispetto.

God gave me a brain,
if I didn't use it I would disrespect him.

Michele Salvemini

CONTENTS

Abstract v

Résumé vii

1 Introduction 1
1.1 From classical to quantum computing . . . 1
1.2 Quantum computing with spins in semiconductor quantum dots . . . 4
1.3 Thesis overview . . . 5

2 Quantum computation with spins in quantum dots 11
2.1 Semiconductor quantum dots . . . 11
2.1.1 A single electron transistor . . . 11
2.2 Quantum dot spectroscopy . . . 14
2.3 Coulomb peaks lineshapes for different transport regimes . . . 17
2.3.1 Linear transport . . . 17
2.3.2 Non linear transport . . . 18
2.3.3 Theory overview . . . 19
2.4 Dispersive readout for spin qubit . . . 20
2.5 Quantum capacitance . . . 22
2.6 Double quantum dot energy diagram . . . 23
2.6.1 Charge qubit . . . 23
2.6.2 Spin qubit . . . 25
2.7 Spin readout . . . 27
2.7.1 Energy-selective tunneling readout . . . 27
2.7.2 Pauli spin blockade readout . . . 28
2.8 Spin-orbit coupling . . . 30
2.9 Spin manipulation . . . 32
2.10 Active interferometry measurement of a quantum dot . . . 34

3 Methods and materials 43
3.1 Experimental setup . . . 43
3.2 Sample preparation . . . 46
3.3 Noise filtering . . . 46
3.3.1 DC noise . . . 47
3.3.2 KiKass filters: PCB Layout . . . 47
3.3.3 Thermal noise . . . 50
3.4 Effective electronic temperature with DC filters . . . 50
3.5 Device fabrication . . . 52

4 QD characterization from room temperature to 4K 57
4.1 A systematic characterization of quantum dot devices . . . 57
4.2 Room temperature characterization and comparison with low temperature properties at high bias . . . 58
4.3 Coulomb-diamond analysis methods . . . 60
4.4 Coulomb peak analysis at zero bias . . . 61

4.5 Diamond reconstruction method . . . 62
4.6 Line cut across the Coulomb valley . . . 66
4.7 Summary of the 3 methods . . . 67
4.8 Summary of the measurement procedure . . . 69
4.8.1 Final remarks . . . 69
4.9 Characterization and Lambert-W Function based modeling of FDSOI five-gate qubit MOS devices down to cryogenic temperatures . . . 70
4.9.1 Saturation of the subthreshold swing . . . 70
4.9.2 Lambert W-function based modeling . . . 72
4.9.3 Evaluation of the mobility . . . 73

5 Electron spin readout in bilinear arrays of quantum dots 81
5.1 The device . . . 81
5.1.1 Dispersive readout in bilinear quantum dot arrays arrays . . . 83
5.2 Evaluate tunnel coupling with gate-based reflectometry . . . 83
5.3 RF charge-sensing vs dispersive readout measurement for large interdot tunnel coupling . . . 87
5.4 Magnetospectroscopy of the double quantum dot . . . 87
5.4.1 Comparison of the two fits . . . 89
5.5 Spin dependent tunneling . . . 91
5.5.1 Evaluation of tunnel rates at $B = 0$ T . . . 91
5.5.2 Spin dependent tunneling: magnetic field dependence . . . 93
5.6 Fast, high-fidelity charge-sensing of spin dependent tunneling . . . 95
5.7 Electric dipole spin resonance (EDSR) . . . 97
5.7.1 Detuning dependence of EDSR . . . 101
5.8 Double arrays of quantum dots: how to scale up? . . . 102

6 Hole spin control and manipulation in linear arrays of quantum dots 113
6.1 Device tuning for double charge-sensing with reservoir-based reflectometry . . . 114
6.2 Probing double dot dynamics simultaneously with double charge-sensing . . . 120
6.3 Measuring tunnel rates . . . 125
6.4 Energy-selective readout of a hole spin . . . 128
6.5 Energy-selective readout of a hole qubit . . . 131
6.5.1 Temperature dependence of T_1 . . . 135
6.6 Gate reflectometry dispersive readout and coherent control of a hole spin qubit in silicon . . . 136
6.6.1 Magnetospectroscopy of the hole DQD . . . 138
6.6.2 EDSR and readout optimization . . . 140
6.6.3 Coherent manipulation of hole spin qubit . . . 143
6.6.4 Scaling gate reflectometry dispersive readout . . . 146

7 Conclusion 155

Acknowledgements 163

List of Publications 165

ABSTRACT

This PhD thesis deals with the experimental investigation of charge and spin dynamics in silicon-based quantum dot arrays, confining either electrons or holes.
The work presented was carried out in collaboration with the CEA-LETI, where the samples were fabricated on 300-mm SOI (Silicon-On-Insulator) substrates using an industrial-level CMOS platform. With this technology, quantum dots are confined inside silicon nanowires etched in the SOI. The compatibility of these quantum devices with microelectronics production lines can eventually play a key role in the development of a large-scale quantum computing platform based on semiconductor quantum bits (qubits).
In this prospect, the development of efficient and scalable qubit readout and manipulation schemes is a crucial step. To this aim, I have focused on the development of solutions that can simplify the control and readout circuitry.
Ideally, one would like to manipulate the spin of an electron, or of a hole, via a simple modulation of the gate voltage (in the range of tens of GHz), and to read the spin state via a radiofrequency reflectometry technique (typically in the range of several hundred MHz or even above), which can be implemented by connecting a gate, or an ohmic contact, to an LC resonator. Such an idea has motivated several experiments carried out within the framework of this thesis.

A first experiment was carried out on an n-type array with 2×3 quantum dots. It compares two readout schemes based on gate reflectometry. The first one, based on a dispersive readout mechanism, requires no additional control gates, facilitating the scale-up to large qubit arrays. The second one, based on charge-sensing readout, requires additional readout components, and hence additional control gates. On the other hand, this second scheme is less sensitive to the tunnel coupling between neighbouring quantum dots. As shown in this thesis, it also allows for fast charge detection, a necessary condition for single-shot qubit readout.
Regarding spin manipulation, in this thesis I was able to measure signatures of electron spin resonance induced by an electric-field modulation. This observation confirmed the existence of a spin-orbit coupling mechanism for electrons, already reported in an earlier experiment carried out before the beginning of my thesis. However, the spin-orbit interaction turned out to be too weak to enable the observation of Rabi oscillations.

Holes in silicon have an intrinsically stronger spin-orbit coupling than electrons. Therefore, holes are better suited for electrically-driven spin manipulation. In this thesis, I present an experimental study on a p-type device with six gates, demonstrating independent and simultaneous single-shot readout of the charge states of two quantum dots defined by the two central gates. The readout is carried out by means of rf reflectometry through two large hole quantum dots positioned at the ends of the silicon channel and acting as charge sensors.
In a following experiment, an extension of the same readout technique was applied to a four-gate p-type device in which we have been able to demonstrate the coherent electrical control of a qubit based on a single hole and to achieve a coherence time close to 100 microseconds, well beyond the state-of-the-art.

In order to minimize the number of control and readout gates, we studied and demonstrated the functionality of an elementary building block consisting of a double quantum dot defined in a p-type device with two gates. The first dot hosted a hole spin qubit and the second one was used for the readout of that qubit via dispersive reflectometry. The readout scheme used did not require any coupling to a Fermi reservoir, thereby offering an extremely compact and potentially scalable solution.

Throughout this thesis, I implemented spin-to-charge conversion based on energy-selective readout (a method commonly known as "Elzerman readout") or Pauli spin blockade in a triplet-singlet transition between two adjacent quantum dots. The first method requires a sufficiently low electronic temperature, well below the energy gap between the two spin states. The second one can be applied in a wider range of temperatures, or at lower magnetic fields, which allows for longer spin relaxation times.

In conclusion, this thesis work has largely focused on the exploration of different possible solutions for the readout of spin qubits in silicon nanowire SOI devices containing linear or bilinear arrays of quantum dots. In particular, my interest has focused on the development of solutions compatible with future large-scale integration.

RÉSUMÉ

Cette thèse de doctorat traite de l'étude expérimentale de la dynamique de charge et de spin dans des réseaux quantiques à base de silicium, confinant des électrons ou des trous.
Ces travaux ont été effectués en collaboration avec le CEA-LETI où les échantillons sont réalisés en utilisant une plateforme de fabrication de niveau industriel à partir de substrats SOI (Silicon-On-Insulator) de 300 mm. Dans la technologie employée, les boîtes quantiques sont confinées à l'intérieur de nanofils de Silicium gravés dans le SOI. La compatibilité de ces dispositifs quantiques avec les lignes de production de la microélectronique pourrait jouer un rôle clé dans le développement d'une plate-forme de calcul quantique à grande échelle basée sur des bit quantiques (qubits) semi-conducteurs.
Dans cette perspective, le développement de schémas de lecture et de manipulation efficaces et compatibles avec le passage à l'échelle est une étape cruciale. À cette fin, je me suis concentré sur des solutions qui cherchent de simplifier la circuiterie de contrôle et lecture.
Idéalement, on voudrait manipuler le spin d'un électron, ou d'un trou, par une simple modulation de la tension d'une grille dans la gamme de la dizaine de GHz, et de lire l'état de spin par une technique de réflectométrie à la radiofréquence (typiquement plusieurs centaines de MHz ou même au-dessus), qui peut être réalisé en connectant une grille, ou un contacte Ohmic, à un résonateur LC. Une telle idée a a motivé plusieurs expériences effectuées dans le cadre de ce travail de thèse.

Une première expérience a été réalisée avec un réseau de 2×3 boîtes quantiques de type n. Elle compare deux schémas de lecture basés sur la réflectométrie de grille. Le premier, basé sur un mécanisme de lecture dispersive, ne requiert aucune grille de contrôle additionnel, facilitant ainsi la mise à l'échelle de grands réseaux de qubit. Le deuxième, basé sur une lecture à détection de charge, nécessite des composants de lecture supplémentaires, ce qui comporte des grilles de contrôle additionnels. En revanche, ce deuxième schéma est moins sensible aux niveaux de couplage entre boîtes quantiques voisines. Comme montré dans cette thèse, il permet aussi la détection rapide de la charge, une condition nécessaire pour la lecture en mode « single-shot » des qubits.
Concernant la manipulation de spin, dans cette thèse j'ai pu mesurer des signatures de la résonance de spin d'électrons induites par une modulation de champs électrique. Cette observation a confirmé l'existence d'un mécanisme de couplage spin-orbite pour les électrons, déjà rapporté dans une expérience antérieure effectuée avant le début de ma thèse. Cependant, cette interaction spin-orbit s'est révélé trop faible pour pour permettre l'observation des oscillations de Rabi.

Les trous dans le Silicium possèdent un couplage spin-orbit intrinsèquement beaucoup plus fort que celui des électrons. Par conséquent, les trous sont mieux adaptés à une manipulation de spin par des champs électriques. Dans cette thèse je présente une étude d'un dispositif à six grilles de type p, démontrant une lecture single-shot indépendante et simultanée des états de charge de deux boîtes quantiques définies par les deux grilles centrales. La lecture est effectuée par réflectométrie à travers deux grosses boîtes de trous positionnées aux deux extrémités du canal de Silicium et agissant comme détecteurs

de charge. Dans une expérience successive, une extension de la même technique de lecture est appliquée à un dispositif de type p à quatre grilles dans lequel nous avons pu démontrer le contrôle électrique cohérent d'un qubit basé sur un trou unique et des temps de cohérence proches de la centaine de microsecondes, largement au-delà de l'état de l'art.

Dans le bût de minimiser le nombre de grilles de contrôle et lecture, nous avons étudié et démontré la possibilité de réaliser une brique élémentaire constituée par une double boîte quantique définie dans un dispositif de type p avec deux grilles. La première boîte joue le rôle du qubit de spin et la deuxième sert à la lecture du qubit par réflectométrie dispersive. Le schéma de lecture utilisé ne nécessite aucun couplage avec des réservoirs de Fermi, offrant ainsi une solution compacte et potentiellement compatible avec un passage à l'échelle.

Tout au long de cette thèse, j'ai implémenté la conversion spin-to-charge basée soit sur un filtrage en énergie (selon la méthode communément connue comme "lecture Elzerman") soit sur le blocage de Pauli dans une transition triplet-singlet entre deux boîtes quantiques adjacentes. La première méthode exige une température électronique suffisamment basse, bien inférieur à l'écart d'énergie entre les deux états de spin. La deuxième méthode est applicable dans une plus large gamme de températures, ou à des champs magnétiques plus faibles, ce qui permet d'avoir des temps de relaxation de spin plus longs.

En conclusion, ce travail de thèse a été largement focalisé sur l'exploration de différentes solutions possibles pour la lecture de qubit de spin dans des dispositifs SOI à nanofil de Silicium contenant un réseau linéaire ou bilinéaire de boîtes quantiques. En particulier, je me suis intéressé à la problématique de rendre ces solutions compatibles avec une future intégration à large échelle.

1

INTRODUCTION

The fact that materials are made of atoms is the fundamental limitation and it's not that far away...We're pushing up against some fairly fundamental limits so one of these days we're going to have to stop making things smaller."

G. Moore

Nature isn't classical, dammit, and if you want to make a simulation of nature, you'd better make it quantum mechanical, and by golly it's a wonderful problem, because it doesn't look so easy.

R.P. Feynman

When people ask me "what do you do for living?" I usually answer that "I play with single electrons in electronic devices, similar to the ones that are embedded in your phone. Fundamentally the idea is to use a similar technology for quantum computing application". Then when I start talking about spins my interlocutor usually starts to be lost.
Already being able to isolate and move single electrons, while observing their displacement in real time, it is already very exciting. However this is only the starting point for achieving more ambitious goals.
In this introduction I'll briefly review why silicon has been the dominant semiconductor platform till nowadays and how spins in semiconductors can be used to build a processor based on the law of quantum mechanics.

1.1. FROM CLASSICAL TO QUANTUM COMPUTING

In the second half of last century silicon has been the key element for the development of modern microelectronic industry. Silicon is the second most present element on earth (after oxygen), and the eighth in the universe by mass. This wide availability, combined with low manufacturing costs has made it the perfect candidate for large scale production of electronic based devices.
Nevertheless, it must be said that the first transistor, that was based on a bipolar junction, has been realized in germanium. In the very early years of the semiconductor industry germanium was the dominant semiconductor material for transistors, rather than silicon, due to higher mobility properties. In fact, without any treatment, the mobility of silicon is limited because electrons can be easily trapped at the silicon surface.

1

In the late 50s Mohammed M.Atalla, an engineer from Bell labs, discovered a technique to clean the Si surface, paving the way to modern semiconductor industry.
He understood that the formation of a thermally grown silicon dioxide (SiO_2) layer greatly reduces the electronic concentration at the surface. This led him also to the invention of the first MOSFET (Metal Oxide Semiconductor Field Effect Transitor).
It has been estimated that since then $\simeq 10^{22}$ MOSFETs have been produced, drastically changing our daily lives.
The MOSFET was the first generation of transistor that could be miniaturized and mass produced.
In 1965 Gordon Moore, one of the co-founders of Intel anticipated that the number of components per integrated circuit would increase exponentially with time. More precisely, he argued that it would double every year[1]. The first commercial microprocessor using MOS technology was released by Intel in 1971 (Intel 4004) and the transistor size was around 10 μm. In 1975 Moore revised his forecast to doubling every two years [2].
This empirical trend, known as the Moore's law, has been followed until early 2000s and it has been slowing down in the last two decades. The last generation of IPhone make use of the processor Apple A14 Bionic, which is the first commercially available product to be manufactured on a 5 nm process node[1] (in Taiwan), with MOS 2000 times smaller than just 50 years ago.
We are close to approach some fundamental limits in the shrinking of these nano devices. In a 2007 interview, Moore himself admitted that *"...the fact that materials are made of atoms is the fundamental limitation and it's not that far away...We're pushing up against some fairly fundamental limits so one of these days we're going to have to stop making things smaller."*
Quantum tunnelling effects through the gate oxide layer are already an issue on 7 and 5 nm process node transistors and are becoming increasingly difficult to manage using existing semiconductor processes. Moreover, as transistors become smaller, problems with heat dissipation and power consumption might be a dramatic limitation.

While we are getting closer and closer to the end of the Moore's law, we are currently in the middle of what is called the second quantum revolution [3].
The first quantum revolution originates from a deep understanding of quantum mechanics and its implication in condensed matter physics helped us to understand chemical interactions, to develop the concept of electronic bands in solid-state systems, to understand electrical conduction, light emission and absorption etc. All electronic and optoelectronic devices rely on this knowledge. They are omnipresent in our daily life.
This second quantum revolution is based on an interdisciplinary collaboration between fundamental research and industrial development. In the past years more and more companies, such as IBM, Intel, Microsoft, Amazon, AliBaba and many others are investing on quantum information technology. New professional figures as quantum engineers, are simultaneously emerging.

Even though nowadays we are able to simulate quite complex problems on a simple laptop, there are some kinds of problems whose complexity would be far beyond the reach of even the most powerful supercomputer. That's the case, for example of the factorization of a large integer number M. With a classical algorithm the computational

[1] Historically, the process node name referred to geometrical features such as the gate length. Most recently, due to various marketing and discrepancies among foundries, the number itself has lost the exact meaning it once held. Recent technology nodes refers purely to a specific generation of chips made in a particular technology, without any correspondence with the transistor geometry.

time grows exponentially with M. The difficulty of this problem is at the core of widely used algorithms in cryptography (RSA [4]). By using the Shor algorithm [5] on a quantum computer, instead the factorization time would grow only polynomially with M.
A quantum bit (or qubit) embeds a 2-level system whose state can be set in a quantum superposition $|\Psi\rangle = \frac{\alpha|0\rangle+\beta|1\rangle}{\sqrt{\alpha^2+\beta^2}}$, where $|0\rangle$ and $|1\rangle$ are the basis state of the qubit (e.g. the spin states of an electron).
In fact, while the classical information is encoded on a binary state 0 or 1, the quantum information is encoded on the wavefunction of a quantum state. When considering the wavefunction of a multi-qubit system, that's essentially a statistical distribution of all the possible measurement outcomes, we know from the quantum mechanics principles that all the possible states co-exist until they collapse into a defined state when measuring. A classical computer is instead always in a well defined state.
The advantage of quantum computation originates from the intrinsic nature of a multi-qubit wavefunction that allows many computations to be carried out simultaneously, instead than trying all of them one by one.
Such a different computation paradigm would help in a wide variety of fields as for example in machine learning [6][7], optimization problems[8], materials science, quantum chemistry [9][10] and simulation of quantum systems [11] [12][13].

It must be said that having a large number of high fidelity qubits is a very hard scientific and technological challenge. To preserve its coherence a qubit needs to be sufficiently isolated from the surrounding environment. That's the case of ion traps, where a coherence time of more than one hour has been achieved [14].
At the same time, to run a quantum computation the qubits should also interact with each other and therefore they should also couple with their surrounding environment, which leads to decoherence on the qubit wavefunction.
We should accept to work with noisy and imperfect qubits. Therefore, running practical quantum computations requires to be able to deal with errors. This is not a dramatic limitation if we consider that also classical computers make use of error correction algorithms.
The quantum error correction would be realized by distributing the logical information over a certain number of physical qubits. This qubit overhead allows to detect and correct errors.
One of the less demanding quantum error correction techniques is the so-called surface code [15]. The physical qubit overhead for each logical qubit would depend strongly on the error rate. For example, to achieve a sufficient logic error rate to successfully execute the Shor's algorithm, it has been estimated that with a qubit error rate of 0.05%, approximately 3600 physical qubits would be required for each logical qubit.
Nowadays we are still far from having millions of qubits to run fault-tolerant quantum computation. Nevertheless in the last 20 years several advances have been realized in the field and now we are entering in the so called era of Noisy Intermediate Scale Quantum (NISQ) [16]. A NISQ processor is defined as a system that is too noisy to achieve the thresholds and scaling necessary for fault-tolerant quantum computation but that is sufficiently isolated from the environment and controllable that it has the potential to achieve a "quantum advantage" over a classical computer.
Nowadays, using the most powerful supercomputer we are able to simulate systems of roughly 50 qubits [17]. Google has recently claimed to have achieved quantum supremacy [18] (or quantum advantage), using a circuit with 53 superconducting qubits. The algorithm they run had the task of sampling the output of a pseudo-random quantum circuit.

Even though this supremacy has been debated[19], what is sure is that their technology is quite impressive and they might be able to perform some more useful tasks in the near term.
Also another recent claim of quantum supremacy has been made by the group of Jianwei Pan, who is also the lead scientist of Chinese quantum space program (QUESS:Quantum Experiments at Space Scale)[20].
Their experiment consists in sampling the output probability of a 50-photon interferometer [13], problem also known as Boson sampling [21]. They state that the sampling rate they achieved is faster than the simulation of a supercomputer by a factor of $\simeq 10^{14}$. This is, in my opinion, a perfect example of quantum simulation, more than quantum computation though.
What is sure is that the field of quantum computing is making remarkable progress, generating great excitement in the scientific community.

1.2. QUANTUM COMPUTING WITH SPINS IN SEMICONDUCTOR QUANTUM DOTS

The idea of using the spin degree of freedom of electrons in semiconductor quantum dots dates back to 1997 with the proposal of Daniel Loss and David DiVincenzo [22].
When dealing with electron (or hole) spins we are dealing with a two-level quantum system and we can therefore use the spin as the basis to encode an elementary bit of quantum information, i.e. a so-called qubit.

The first pioneering works with the spin of electrons in quantum dots [23][24][25] have been realized in GaAS-AlGaAs heterostructures. However, the interaction with the nuclear spins through the hyperfine coupling induces a rapid dephasing of the electron spin (tens of ns), imposing a severe limitation on qubit scale-up.
This problem can be avoided by choosing a host material with zero nuclear spin.
The problem of the coupling with nuclear spin can be partially solved by working with group-IV semiconductors, as for example carbon, silicon and germanium, whose isotopes are for the most part nuclear spin free.
Actually silicon is widely available in nature in its natural form, composed of three different isotopes with the following composition: ^{28}Si (92.2%), ^{29}Si (4.7%), and ^{30}Si (3.1%). Hyperfine interaction is still playing a role in natural silicon due to the presence of ^{29}Si. This isotope can be removed thanks to a procedure where first the isotopes are separated in the form SiF_4 (silicon tetrafluoride), then they are converted into SiH_4 (silane), obtaining ingots of polycrystalline silicon-28,-29, and-30. Finally these ingots are used for growing monocrystals of purified ^{28}Si [26].
The realization of ^{28}Si devices led to the development of electron spin qubits with much longer spin dephasing ($T_2^* = 120\ \mu$s) an coherence times (T_2^{CPMG} =22 ms) [27]). To date, the best silicon qubits have surpassed the threshold required for quantum error correction, with single-qubit fidelities above 99.9%[28] and two-qubit gate fidelities of 99.5% [29].
Recently, several advances have also been made in the implementation of two-qubit gates in silicon. Two spins belonging to two separate quantum dot can be entangled relying on their exchange interaction. This allows to realize controlled logical operations as for example a CNOT gate. The first experimental realization of a two-qubit gate in silicon has been reported in 2015 [30] and few other demonstrations have been reported more recently [31][32][33][34][35][29][36].

Another approach consists in encoding the qubit in the nuclear spins of implanted dopants. This idea dates back to 1998 [37], when Bruce Kane proposed the realization of spin qubits encoded in the nuclear spin of phosphorous dopants properly implanted in a silicon MOS device. Nuclear spins with coherence times up to 30 seconds [38] have been demonstrated using this approach.
Remarkably, not only the nuclear spin, but also the electron spin of the dopant can be used to store the quantum information. Two-qubit logic gates between electrons stored in dopants were demonstrated in Refs. [39][40].

Recently also SiGe/Ge/SiGe planar heterostructures are emerging as a promising alternative system [41]. In particular, the group of Delft managed, in only a couple of years, to demonstrate single[42], two[43],four [44] qubit in Ge and six-qubit processor in Si [45]. This rapid development has been possible thanks to the unique properties of holes confined in such a material, such as low effective masses, high mobility and low charge disorder. The small holes effective masses lead to large orbital level spacings in quantum dots, allowing to relax lithographic fabrication requirements. In this way relatively large quantum dots (diameter of $\simeq$ 100 nm) can be defined and tuned to contain only a single hole[42],
Moreover holes (both in Si and in Ge) offer the possibility of realizing electrically-driven spin resonance thanks to their intrinsically strong spin-orbit coupling [46][47]. This avoids the use of additional hardware such as micromagnets [28][48] or a microwave antenna [49][27], as it is usually the case for electron spin qubits in silicon.

In this thesis I focus on silicon based quantum dots, confining either electrons or holes. There is an increasing worldwide effort on silicon-based qubits. Indeed, besides long spin coherence, silicon offers the advantage of relying on a very well estabilished technology. The hope is that, once the elementary building blocks for a scalable architecture are developed, industrial grade fabrication will facilitate large-scale integration.
Some first demonstrations have already been realized on industry-standard (300 mm) Si and Si-on-insulator (SOI) wafers using CMOS fabrication process[46][50][51][52][47].

1.3. THESIS OVERVIEW

In this thesis I studied MOSFET based on SOI technology fabricated at CEA-LETI, with both electrons and holes. The manuscript is structured as following:

- In Chap. 2 I introduce the basic properties of semiconductor quantum dots. Particular attention is devoted to to understand the response obtained when performing the readout with RF reflectometry.
  In this chapter I also discuss the two main techniques to realize spin-to-charge conversion and I explain how to manipulate the spin state through an electric or magnetic field.

- In Chap. 3 I explain the principles behind the construction of the experimental setup, focusing on the noise filtering. In particular, I describe in detail a compact platform to filter the noise on the DC lines. The chapter ends discussing the process flow leading to the construction of our quantum devices.

- In Chap. 4 I discuss the device characterization based on their transport properties (i.e. by reading current). In particular, I investigate how to speed up the low-temperature characterization in the perspective of an electrical screening on the

full wafer scale.
In the second part of the chapter I analyze a p-type device with five gates in series, focusing on the dependence of the transistor parameters from the position of the gate relative to the reservoir. It has been found that the further away is the gate from the reservoir, the better is the mobility extracted from the transconductance characteristic. This, together with the experimental data of Chap. 6, let us think that qubits next to a doped contact region have a higher level of disorder which can impact their performances.

- In Chap. 5 I investigate charge and spin properties in a 3×2 bilinear array of electron quantum dots, using both gate reflectometry and RF charge-sensing simultaneously, when possible. I study in particular a regime where the interdot tunneling is spin dependent, due to Pauli spin blockade (PSB). I report some experimental signatures of electric-dipole spin resonance, demonstrating the presence of a weak spin-orbit coupling of electrons in silicon.

- In Chap. 6 I present 3 different experiments in arrays of hole quantum dots. In the first experiment I dicuss the use of two charge-sensors to simultaneously probe the dynamics of each dot.
In the second experiment I discuss the demonstration of a spin-qubit, read with an RF charge-sensor via energy-selective readout.
The last experiment consists in the realization of a compact qubit layout where readout is performed by means of gate-coupled RF reflectometry. In this case the spin-to-charge conversion is realized through PSB.

- Chap. 7 concludes the thesis, summarizing the main results and offering an outlook on future research directions and perspectives for the scalability of qubit arrays.

.

BIBLIOGRAPHY

[1] G. E. Moore. "Cramming more components onto integrated circuits, Reprinted from Electronics, volume 38, number 8, April 19, 1965, pp.114 ff." In: *IEEE Solid-State Circuits Society Newsletter* 11.3 (2006), pp. 33–35. DOI: 10.1109/N-SSC.2006.4785860.

[2] G. E. Moore. "Progress in digital integrated electronics [Technical literaiture, Copyright 1975 IEEE. Reprinted, with permission. Technical Digest. International Electron Devices Meeting, IEEE, 1975, pp. 11-13.]" In: *IEEE Solid-State Circuits Society Newsletter* 11.3 (2006), pp. 36–37. DOI: 10.1109/N-SSC.2006.4804410.

[3] Ivan H. Deutsch. "Harnessing the Power of the Second Quantum Revolution". In: *PRX Quantum* 1 (2 Nov. 2020), p. 020101. DOI: 10.1103/PRXQuantum.1.020101. URL: https://link.aps.org/doi/10.1103/PRXQuantum.1.020101.

[4] R. L. Rivest, A. Shamir, and L. Adleman. "A Method for Obtaining Digital Signatures and Public-Key Cryptosystems". In: *Commun. ACM* 21.2 (Feb. 1978), pp. 120–126. ISSN: 0001-0782. DOI: 10.1145/359340.359342. URL: https://doi.org/10.1145/359340.359342.

[5] Peter W. Shor. "Polynomial-Time Algorithms for Prime Factorization and Discrete Logarithms on a Quantum Computer". In: *SIAM J. on Computing* (1997), pp. 1484–1509.

[6] Sergey Bravyi, David Gosset, and Robert König. "Quantum advantage with shallow circuits". In: *Science* 362.6412 (2018), pp. 308–311. ISSN: 0036-8075. DOI: 10.1126/science.aar3106. eprint: https://science.sciencemag.org/content/362/6412/308.full.pdf. URL: https://science.sciencemag.org/content/362/6412/308.

[7] Jacob Biamonte et al. "Quantum machine learning". In: *Nature* 549.7671 (Sept. 2017), pp. 195–202. ISSN: 1476-4687. DOI: 10.1038/nature23474. URL: https://doi.org/10.1038/nature23474.

[8] Florian Neukart et al. "Traffic Flow Optimization Using a Quantum Annealer". In: *Frontiers in ICT* 4 (2017), p. 29. ISSN: 2297-198X. DOI: 10.3389/fict.2017.00029. URL: https://www.frontiersin.org/article/10.3389/fict.2017.00029.

[9] Alán Aspuru-Guzik et al. "Simulated Quantum Computation of Molecular Energies". In: *Science* 309.5741 (2005), pp. 1704–1707. ISSN: 0036-8075. DOI: 10.1126/science.1113479. eprint: https://science.sciencemag.org/content/309/5741/1704.full.pdf. URL: https://science.sciencemag.org/content/309/5741/1704.

[10] Cornelius Hempel et al. "Quantum Chemistry Calculations on a Trapped-Ion Quantum Simulator". In: *Phys. Rev. X* 8 (3 July 2018), p. 031022. DOI: 10.1103/PhysRevX.8.031022. URL: https://link.aps.org/doi/10.1103/PhysRevX.8.031022.

[11] Richard P Feynman. "Simulating physics with computers". In: *International journal of theoretical physics* 21.6/7 (1982), pp. 467–488.

[12] R. Blatt and C. F. Roos. “Quantum simulations with trapped ions”. In: *Nature Physics* 8.4 (Apr. 2012), pp. 277–284. ISSN: 1745-2481. DOI: 10.1038/nphys2252. URL: https://doi.org/10.1038/nphys2252.

[13] Han-Sen Zhong et al. “Quantum computational advantage using photons”. In: *Science* 370.6523 (2020), pp. 1460–1463. ISSN: 0036-8075. DOI: 10.1126/science.abe8770. eprint: https://science.sciencemag.org/content/370/6523/1460.full.pdf. URL: https://science.sciencemag.org/content/370/6523/1460.

[14] Pengfei Wang et al. “Single ion qubit with estimated coherence time exceeding one hour”. In: *Nature Communications* 12.1 (Jan. 2021), p. 233. ISSN: 2041-1723. DOI: 10.1038/s41467-020-20330-w. URL: https://doi.org/10.1038/s41467-020-20330-w.

[15] Austin G. Fowler et al. “Surface codes: Towards practical large-scale quantum computation”. In: *Phys. Rev. A* 86 (3 Sept. 2012), p. 032324. DOI: 10.1103/PhysRevA.86.032324. URL: https://link.aps.org/doi/10.1103/PhysRevA.86.032324.

[16] John Preskill. “Quantum Computing in the NISQ era and beyond”. In: *Quantum* 2 (Aug. 2018), p. 79. ISSN: 2521-327X. DOI: 10.22331/q-2018-08-06-79. URL: https://doi.org/10.22331/q-2018-08-06-79.

[17] Hans De Raedt et al. “Massively parallel quantum computer simulator, eleven years later”. In: *Computer Physics Communications* 237 (2019), pp. 47–61. ISSN: 0010-4655. DOI: https://doi.org/10.1016/j.cpc.2018.11.005. URL: http://www.sciencedirect.com/science/article/pii/S0010465518303977.

[18] Frank Arute et al. “Quantum supremacy using a programmable superconducting processor”. In: *Nature* 574.7779 (Oct. 2019), pp. 505–510. ISSN: 1476-4687. DOI: 10.1038/s41586-019-1666-5. URL: https://doi.org/10.1038/s41586-019-1666-5.

[19] Yiqing Zhou, E. Miles Stoudenmire, and Xavier Waintal. “What Limits the Simulation of Quantum Computers?” In: *Phys. Rev. X* 10 (4 Nov. 2020), p. 041038. DOI: 10.1103/PhysRevX.10.041038. URL: https://link.aps.org/doi/10.1103/PhysRevX.10.041038.

[20] Yu-Hao Deng et al. “Quantum Interference between Light Sources Separated by 150 Million Kilometers”. In: *Phys. Rev. Lett.* 123 (8 Aug. 2019), p. 080401. DOI: 10.1103/PhysRevLett.123.080401. URL: https://link.aps.org/doi/10.1103/PhysRevLett.123.080401.

[21] Scott Aaronson and Alex Arkhipov. *The Computational Complexity of Linear Optics*. 2010. arXiv: 1011.3245 [quant-ph].

[22] Daniel Loss and David P. DiVincenzo. “Quantum computation with quantum dots”. In: *Phys. Rev. A* 57 (1 Jan. 1998), pp. 120–126. DOI: 10.1103/PhysRevA.57.120. URL: https://link.aps.org/doi/10.1103/PhysRevA.57.120.

[23] J. M. Elzerman et al. “Single-shot read-out of an individual electron spin in a quantum dot”. In: *Nature* 430.6998 (July 2004), pp. 431–435. ISSN: 1476-4687. DOI: 10.1038/nature02693. URL: https://doi.org/10.1038/nature02693.

[24] Jason R Petta et al. “Coherent manipulation of coupled electron spins in semiconductor quantum dots”. In: *Science* 309.5744 (2005), pp. 2180–2184.

[25] F. H. L. Koppens et al. “Driven coherent oscillations of a single electron spin in a quantum dot”. In: *Nature* 442.7104 (Aug. 2006), pp. 766–771. ISSN: 1476-4687. DOI: 10.1038/nature05065. URL: https://doi.org/10.1038/nature05065.

[26] A. V. Gusev and A. D. Bulanov. "High-purity silicon isotopes 28Si, 29Si, and 30Si". In: *Inorganic Materials* 44.13 (Nov. 2008), p. 1395. ISSN: 1608-3172. DOI: 10.1134/S0020168508130013. URL: https://doi.org/10.1134/S0020168508130013.

[27] M. Veldhorst et al. "An addressable quantum dot qubit with fault-tolerant control-fidelity". In: *Nature Nanotechnology* 9.12 (Dec. 2014), pp. 981–985. ISSN: 1748-3395. DOI: 10.1038/nnano.2014.216. URL: https://doi.org/10.1038/nnano.2014.216.

[28] Jun Yoneda et al. "A quantum-dot spin qubit with coherence limited by charge noise and fidelity higher than 99.9%". In: *Nature Nanotech.* 13.2 (2018), pp. 102–106.

[29] Akito Noiri et al. "Fast universal quantum gate above the fault-tolerance threshold in silicon". In: *Nature* 601.7893 (Jan. 2022), pp. 338–342. ISSN: 1476-4687. DOI: 10.1038/s41586-021-04182-y. URL: https://doi.org/10.1038/s41586-021-04182-y.

[30] M. Veldhorst et al. "A two-qubit logic gate in silicon". In: *Nature* 526.7573 (Oct. 2015), pp. 410–414. ISSN: 1476-4687. DOI: 10.1038/nature15263. URL: https://doi.org/10.1038/nature15263.

[31] David M Zajac et al. "Resonantly driven CNOT gate for electron spins". In: *Science* 359.6374 (2018), pp. 439–442.

[32] TF Watson et al. "A programmable two-qubit quantum processor in silicon". In: *Nature* 555.7698 (2018), pp. 633–637.

[33] W. Huang et al. "Fidelity benchmarks for two-qubit gates in silicon". In: *Nature* 569.7757 (May 2019), pp. 532–536. ISSN: 1476-4687. DOI: 10.1038/s41586-019-1197-0. URL: https://doi.org/10.1038/s41586-019-1197-0.

[34] L. Petit et al. "Universal quantum logic in hot silicon qubits". In: *Nature* 580.7803 (Apr. 2020), pp. 355–359. ISSN: 1476-4687. DOI: 10.1038/s41586-020-2170-7. URL: https://doi.org/10.1038/s41586-020-2170-7.

[35] Adam R. Mills et al. "Two-qubit silicon quantum processor with operation fidelity exceeding 99%". In: *Science Advances* 8.14 (2022), eabn5130. DOI: 10.1126/sciadv.abn5130. eprint: https://www.science.org/doi/pdf/10.1126/sciadv.abn5130. URL: https://www.science.org/doi/abs/10.1126/sciadv.abn5130.

[36] Xiao Xue et al. "Quantum logic with spin qubits crossing the surface code threshold". In: *Nature* 601.7893 (Jan. 2022), pp. 343–347. ISSN: 1476-4687. DOI: 10.1038/s41586-021-04273-w. URL: https://doi.org/10.1038/s41586-021-04273-w.

[37] B. E. Kane. "A silicon-based nuclear spin quantum computer". In: *Nature* 393.6681 (May 1998), pp. 133–137. ISSN: 1476-4687. DOI: 10.1038/30156. URL: https://doi.org/10.1038/30156.

[38] Juha T Muhonen et al. "Storing quantum information for 30 seconds in a nanoelectronic device". In: *Nature Nanotech.* 9.12 (2014), pp. 986–991.

[39] Y. He et al. "A two-qubit gate between phosphorus donor electrons in silicon". In: *Nature* 571.7765 (July 2019), pp. 371–375. ISSN: 1476-4687. DOI: 10.1038/s41586-019-1381-2. URL: https://doi.org/10.1038/s41586-019-1381-2.

[40] Mateusz T. Madzik et al. “Conditional quantum operation of two exchange-coupled single-donor spin qubits in a MOS-compatible silicon device”. In: *Nature Communications* 12.1 (Jan. 2021), p. 181. ISSN: 2041-1723. DOI: 10.1038/s41467-020-20424-5. URL: https://doi.org/10.1038/s41467-020-20424-5.

[41] Giordano Scappucci et al. “The germanium quantum information route”. In: *Nature Reviews Materials* (Dec. 2020). ISSN: 2058-8437. DOI: 10.1038/s41578-020-00262-z. URL: https://doi.org/10.1038/s41578-020-00262-z.

[42] N. W. Hendrickx et al. “A single-hole spin qubit”. In: *Nature Communications* 11.1 (July 2020), p. 3478. ISSN: 2041-1723. DOI: 10.1038/s41467-020-17211-7. URL: https://doi.org/10.1038/s41467-020-17211-7.

[43] N. W. Hendrickx et al. “Fast two-qubit logic with holes in germanium”. In: *Nature* 577.7791 (Jan. 2020), pp. 487–491. ISSN: 1476-4687. DOI: 10.1038/s41586-019-1919-3. URL: https://doi.org/10.1038/s41586-019-1919-3.

[44] Nico W. Hendrickx et al. “A four-qubit germanium quantum processor”. In: *Nature* 591.7851 (Mar. 2021), pp. 580–585. ISSN: 1476-4687. DOI: 10.1038/s41586-021-03332-6. URL: https://doi.org/10.1038/s41586-021-03332-6.

[45] Stephan G. J. Philips et al. “Universal control of a six-qubit quantum processor in silicon”. In: *Nature* 609.7929 (Sept. 2022), pp. 919–924. ISSN: 1476-4687. DOI: 10.1038/s41586-022-05117-x. URL: https://doi.org/10.1038/s41586-022-05117-x.

[46] R Maurand et al. “A CMOS silicon spin qubit”. In: *Nature Comm.* 7 (2016), p. 13575.

[47] N. Piot et al. “A single hole spin with enhanced coherence in natural silicon”. In: *Nature Nanotechnology* 17.10 (Oct. 2022), pp. 1072–1077. ISSN: 1748-3395. DOI: 10.1038/s41565-022-01196-z. URL: https://doi.org/10.1038/s41565-022-01196-z.

[48] Erika Kawakami et al. “Electrical control of a long-lived spin qubit in a Si/SiGe quantum dot”. In: *Nature Nanotech.* 9.9 (2014), pp. 666–670.

[49] Jarryd J. Pla et al. “A single-atom electron spin qubit in silicon”. In: *Nature* 489.7417 (Sept. 2012), pp. 541–545. ISSN: 1476-4687. DOI: 10.1038/nature11449. URL: https://doi.org/10.1038/nature11449.

[50] A. Crippa et al. “Gate-reflectometry dispersive readout and coherent control of a spin qubit in silicon”. In: *Nature Communications* 10.1 (July 2019), p. 2776. ISSN: 2041-1723. DOI: 10.1038/s41467-019-10848-z. URL: https://doi.org/10.1038/s41467-019-10848-z.

[51] R. Li et al. “A flexible 300 mm integrated Si MOS platform for electron- and hole-spin qubits exploration”. In: *2020 IEEE International Electron Devices Meeting (IEDM)*. 2020, pp. 38.3.1–38.3.4. DOI: 10.1109/IEDM13553.2020.9371956.

[52] A. M. J. Zwerver et al. “Qubits made by advanced semiconductor manufacturing”. In: *Nature Electronics* 5.3 (Mar. 2022), pp. 184–190. ISSN: 2520-1131. DOI: 10.1038/s41928-022-00727-9. URL: https://doi.org/10.1038/s41928-022-00727-9.

2

QUANTUM COMPUTATION WITH SPINS IN QUANTUM DOTS

Any fool can know. The point is to understand

Albert Einstein

This chapter introduces the theoretical framework necessary for the discussion of the experimental results presented in this thesis. Here I consider the basic aspects of quantum dots in semiconductors [1][2][3], and their use as spin qubits. In particular, I discuss how such spin qubits can be initialiazed, manipulated and measured, through either transport or dispersive measurements.

2.1. SEMICONDUCTOR QUANTUM DOTS

A semiconductor quantum dot (QD) is a small charge island, where electrons or holes can be isolated thanks to an interplay between the electrostatic field applied and the interfaces between materials.
The size of the quantum dot, usually between 10 and 100 nm, determines its level spacing. The physical distance between the quantum dots, their size and energetic structure determines the mutual interaction between nearby quantum dots.

2.1.1. A SINGLE ELECTRON TRANSISTOR

Here we start considering a single quantum dot in a MOSFET-like device. In such a platform it is possible to control the displacement of a single electron and it is commonly referred to as single electron transistor (SET).
The SET can be modelled as a charge island underneath the gate, capacitively coupled with the reservoirs and the gate itself. If sufficiently small, this charge island, made of electrons (or holes) in a potential well, can behave as an artificial atom, or quantum dot.
Our quantum dot devices are fabricated on 300 mm silicon-on insulator (SOI) wafers, using a transistor technology close to what is commoly referred to as fully-depleted SOI (FDSOI)[4].
Electrons are confined at the Si-SiO_2 interface, in an analogue manner to classical transistors. The spacers instead are deliberately longer than in conventional transistors. In this way the potential applied mainly acts underneath the gate. This, together with the

increased access resistances, allows local charge confinement, as can be understood from the schematic of the potential landscape of the device of Fig. 2.1 b).
When going down to low temperature , i.e. below a few Kelvin, the thermal energy $k_B T$ is smaller than the energy level spacing in the quantum dot. As a result we can distinguish quantized energy levels and, consequently, observe single-electron tunneling.

The Si channel is undoped and hence no carriers are present at zero gate voltage. We need a positive (negative) potential to accumulate electrons (holes) below the gate.
In other semiconductor platforms, as highly doped materials or III-V semiconductors, in the conduction channel there is a 2-D electron gas and, conversely, a negative (positive) potential is needed to deplete locally the channel from electrons (holes), leaving a small charge island.

In the simplest physical picture, the SET can be described with a classical capacitive model, as depicted in Fig. 2.1, where C_s is the capacitance between the source and the dot, C_g is the one between the dot and the gate and C_d is the one between the dot and the drain.

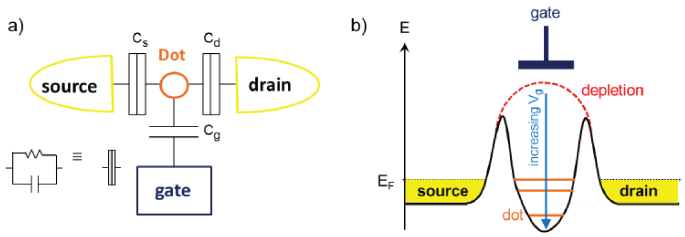

Figure 2.1: a) Schematic of the circuit in a three-terminal single electron transistor. b) Potential landscape of the device. The access barriers confine electrons, thus defining the charge island between the Fermi seas of source and drain.

In order to add one electron to the quantum dot we should provide enough energy to overtake the electrostatic repulsion of the dot. The amount of energy that must be spent in order to increase by one the charge population in the capacitor defines the charging energy E_c:

$$E_c = \frac{e^2}{C_{tot}} \tag{2.1}$$

where $C_{tot} = C_s + C_d + C_g = |e|\frac{C_g}{\alpha}$.
Since the dot is also capacitively coupled to source and drain the potential applied on it is only a fraction of the one applied on the gate. The conversion factor between the gate voltage applied and the effective electrochemical potential applied on the dot is the so-called lever-arm parameter $\alpha = |e|C_g/C_{tot}$.
We can assume to have a planar dot with area A, and see the dot and the gate as the two plates of a capacitor. The gate capacitance therefore is given by $C_g = \epsilon_0 \epsilon_r \frac{A}{d}$ and the charging energy can be rewritten as a function of the gate capacitance $E_c = e\frac{\alpha}{C_g}$.
The dot area can then be estimated as:

$$A = \frac{e\alpha}{Ec}\frac{d}{\epsilon_0 \epsilon_r} \tag{2.2}$$

where ϵ_0 is the vacuum permittivity, $d = 6$ nm is the thickness of the gate oxide (SiO_2) of our devices, with dielectric constant $\epsilon_r \simeq 3.9$.

The amount of charges confined in the quantum dot can be considered fixed assuming that the tunnel resistance with source and drain R are thick enough to have negligible quantum fluctuations of the energy on the measurement timescale ($R > h/e^2$), condition easily satisfied with large spacers. Moreover thermal fluctuations should be much lower than E_C, condition usually satisfied at few Kelvin.

The single electron functionality has already been achieved also at room temperature [5][6]. Anyways, for a reliable room temperature operation of a silicon SET, its charging energy E_c should be at least $4k_BT \simeq 100$ meV and consequently, the dot diameter should be of few nm (see eq. 2.2).
When sweeping the gate voltage under a drain-source bias, at low temparature we can observe quantized transport, as shown in Fig. 2.2 c). This can be understood considering that when an energy level of the dot falls inside the bias window, transport between source and drain is allowed (Fig. 2.2 b). Otherwise transport is blocked, and this is commonly defined as the Coulomb blockade regime (Fig. 2.2 a)). The first experimental observations of Coulomb blockade dates back to 1989 in silicon nanowires [7] and GaAS heterostructures [8].

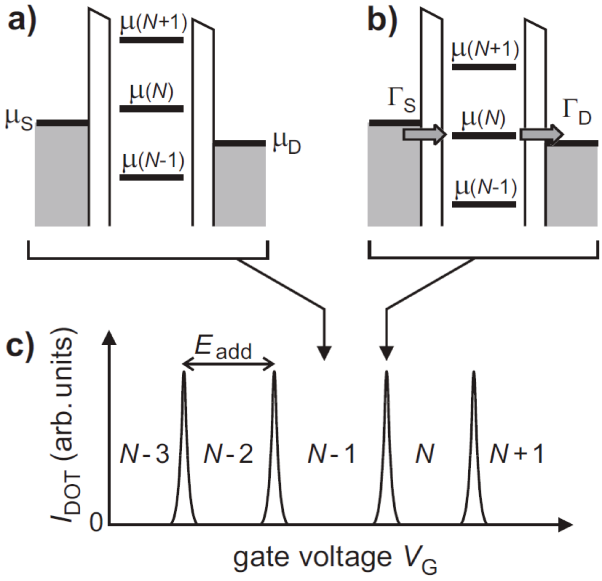

Figure 2.2: a) Coulomb blockade, there is no energy level within the bias window and current is blocked.
b) Resonant tunneling condition. c) Expected current I (in arbitrary units) as a function of gate voltage V_G, assuming that only one energy level contributes to transport and that the tunneling rates with the reservoirs are constant. Image from Ref. [1].

In Fig. 2.2 c) all peaks show the same intensity of current. This corresponds to assume that:

- for each peak only one energy level (or a costant number of energy levels, as it is the case for a metallic SET) contributes to the conduction.
- the couplings with the reservoirs Γ_S, Γ_D are constant.

Experimentally the first assumption may hold only at very low bias and very low temperature, in fact the orbital level spacing is usually in a range between 100 μeV and few meV. The second one instead would hold only for a dot with size and position independent from electron number and shape of the confining potential, which is almost never the case in realistic experiments. The coupling with the reservoir is in fact intrinsically dependent on the size of the dot, or more precisely on the size of its wave function, that increases with increasing electron number.

As we will see in the following section the spacing between the peaks is not constant in the quantum regime, where the energy necessary to add one electron, i.e. the addition energy E_{add}, is the sum of charging energy E_c and the orbital level spacing Δ_N.
MOreover, the peaks width is broadened both by temperature and tunneling with the reservoir.

A measurement of the spacing between two peaks in gate voltage ΔV_G (that's the easiest parameter to measure) and a measurement of the addition energy E_{add} gives the gate-lever arm parameter α. Conversely, a measurement of α and ΔV_G, gives the addition energy E_{add}.
For each couple of Coulomb peaks then:

$$\alpha \Delta V_G = E_{add} \tag{2.3}$$

2.2. QUANTUM DOT SPECTROSCOPY

So far the discussion has been entirely classical. However, we have to take in account that the quantum dot obeys quantum mechanics laws and it can be modeled as a particle confined in a potential well. Therefore its energy levels are quantized.
For small quantum dots in fact the discreteness of the energy levels of the electrons becomes pronounced, like those in atoms and molecules, so one can talk about "artificial atoms and molecules".
The simplest model which combines both the Coulomb blockade effect and the energy spectrum of a quantum dot is the constant-interaction model ([3], [9]). The key assumptions in this model are:

- the quantized levels can be calculated regardless of the number of electrons in the dot.
- The Coulomb interactions among the electrons in the dot and between electrons in the dot and the environment can be parameterized in terms of a constant capacitance C_{tot}.

This model provides an analytic expression of the chemical potential $\mu(N)$ for a certain electronic configuration:

$$\mu_N = E_N + \frac{(N - N_0 - 1/2)e^2}{C_{tot}} - e\frac{C_g}{C_{tot}} V_G$$

In this definition the integer N is the number of electrons for a certain gate voltage V_G and N_0 is the number of electrons at $V_G = 0$.

The single-particle state E_N for the $N-th$ electron depends on the characteristics of the confinement potential.
The main result of this model is the definition of the addition energy:

$$\mu(N) - \mu(N-1) = E_c + \Delta_N = E_{add}$$

with $\Delta_N = E_N - E_{N-1}$.
By considering the quantum dot as a particle in a 2D box with surface A its level spacing can be calculated as [6]:

$$\Delta_N^{2D} = \frac{2\pi\hbar^2}{g_{spin} g_{valley} m^* A} \tag{2.4}$$

where $g_{spin(valley)}$ take into account the double degeneracy of spin (valley) state of each level and m^* is the effective mass of the electrons. In silicon the conduction band edges are spheroids oriented along the equivalent [100] directions in the Brillouin zone, with mass parameters $m_L = 0.92 m_e$ and $m_T = 0.19 m_e$ [10], giving an average effective mass of $m^* = (m_L m_T^2)^{\frac{1}{3}} = 0.32 m_e$.
By considering a 3D dot instead the level spacing is expected to decrease with increasing filling N[3]:

$$\Delta_N^{3D} = \left(\frac{1}{3\pi^2 N}\right)^{1/3} \frac{2\pi^2\hbar^2}{g_{spin} g_{valley} m^* A} \tag{2.5}$$

Realistic quantum dots in semiconductor are not perfect 2D structure and, even though they are mainly squeezed in the channel plane a dependence of the level spacing from the electron filling N is still expected.
Being proportional to the inverse of the dot area, the orbital level spacing is significant for small dots. For example given $A = 20 \times 20$ nm^2 we expect $\Delta_N \simeq 1$ meV.
For high filling the dot also increases in size, and the orbital level spacing usually becomes negligible compared to E_c. In such a regime the dot behaves following the classical picture, where $E_{add} \simeq E_c$. This is commonly referred to as the metallic regime for a quantum dot.
A measurement of the addition energy as a function of gate voltage in a Si QD is shown in Fig. 2.3. The extra addition energy needed to add the fifth and thirteenth electron can be attributed to complete filling of the first and second orbital shells.
The orbital structure of the dot can be understood considering that in silicon there is a double valley degeneracy such that the first orbital (s-type) can be filled twice with 2 electrons of opposite spin and therefore we need 4 electrons to fill the first orbital shell. Similarly, the second orbital shell has a double degeneracy that, combined with twofold spin degeneracy and twofold valley degeneracy, is such that we need 8 electrons to fill the second shell [11].

The most intuitive way to measure the addition energy E_{add} is to measure the current as a function of gate voltage V_G and bias voltage V_{ds}.
A measurement of the addition energy in V_{ds} indeed can be directly converted in eV and, together with the peak spacing ΔV_G it also provides the α-factor (using formula 2.3).
Due to the shapes they acquire (see Fig. 2.4), the blockaded regions in the two-axis stability diagram (V_G vs V_{ds}) are called Coulomb diamonds.
A scheme of the QD energy diagram corresponding to different points on the edges of a Coulomb diamond is presented in Fig. 2.4. For clarity in the figure the electrochemical potentials μ_d is fixed and only μ_s is moved by eV_{ds}, following the application of a bias voltage.

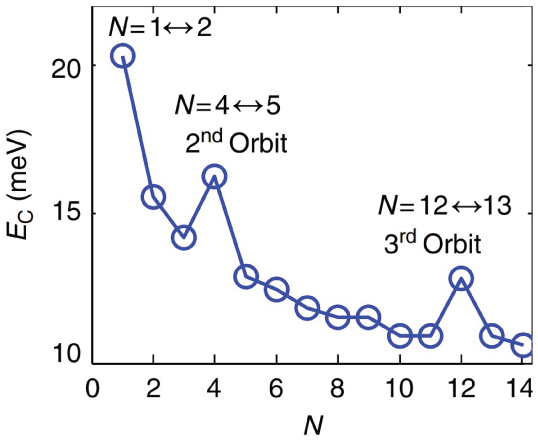

Figure 2.3: Addition energy as a function of the electron number N in a silicon device. The two valleys are nearly degenerate and therefore the orbital and valleys degeneracy are multiplied together. From Ref. [11]

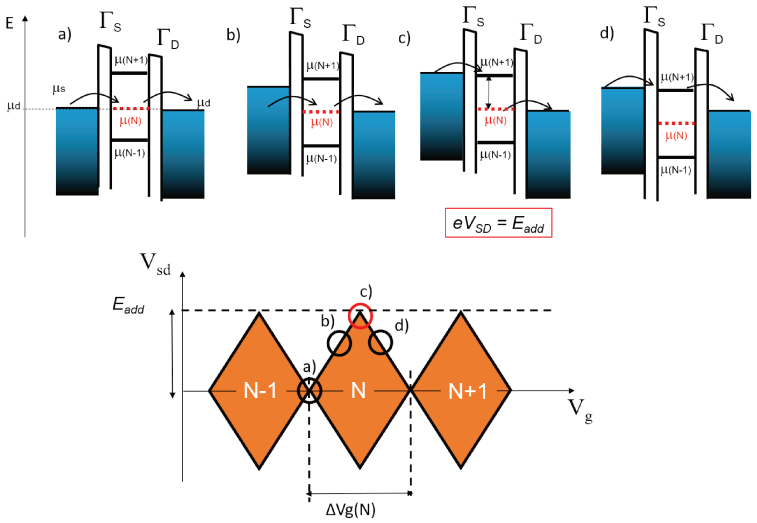

Figure 2.4: a) At zero bias the conduction is allowed only when $\mu_s = \mu(N) = \mu_d$; b) Along the left edge of the diamond the electrochemical potential of the dot is aligned with the drain $\mu_d = \mu(N)$; c) On the diamond tip the bias matches the addition energy $\mu_s - \mu_d = \mu(N+1) - \mu(N)$; d) Along the right edge of the diamond the electrochemical potential of the $N+1$-th electron in the dot is aligned with the source $\mu_s = \mu(N+1)$.

From figure 2.4 b), d) it can be understood that the edges of the diamonds correspond to the physical situation where the energy level of the dot is aligned with the Fermi energy of one of the reservoirs.
The tip of the diamond is the point where the bias eV_{ds} matches E_{add} (Fig. 2.4 c).
From the positive (m_+) and negative (m_-) slopes of the diamonds and E_{add} we can therefore estimate separately the capacitive couplings of the dot with the two reservoirs C_d, C_s,

and the gate capacitance C_g.

$$\begin{aligned} C_s &= \frac{|e|}{E_{add}} \frac{m_-(1-m_+)}{m_- - m_+} \\ C_d &= -\frac{|e|}{E_{add}} \frac{m_+}{m_- - m_+} \\ C_g &= \frac{|e|}{E_{add}} \frac{m_+ m_-}{m_- - m_+} \end{aligned} \tag{2.6}$$

2.3. COULOMB PEAKS LINESHAPES FOR DIFFERENT TRANSPORT REGIMES

The current level of the Coulomb peaks is also dependent on the tunneling rates Γ_s, Γ_d with the reservoirs. Since the dot size increases by filling in more electrons, also the overlap of its wavefunction with the two reservoirs increases and therefore the tunnel couplings. For a system with i electrons we can define unique parameters for each electronic configuration, as for instance $\Gamma_s^{(i)}, \Gamma_d^{(i)}$.
Another effect of increasing the size of the dot is to increase the capacitive coupling between the the dot and the reservoirs, leading to an increase in the total capacitance $C_{tot}^{(i)}$. Even $C_g^{(i)}$ is proportional to the dot area, that increases with i, but it does not increase much as compared to $C_{tot}^{(i)}$, therefore $\alpha^{(i)} = C_g^{(i)}/C_{tot}^{(i)}$ is expected to decrease with increasing electron filling i.

2.3.1. LINEAR TRANSPORT

The theory beyond the different conductance regimes for a QD is discussed in detail in Refs. [9][3][12]. Here we consider the linear resonant regime, where only one energy level at a time may enter in the bias window ($V_{ds} < \Delta_N$). Depending on the energy scales given by temperature ($k_B T$) and tunneling ($h\Gamma$) we can analyze different transport regimes. We'll consider what happens by going down in temperature.

At high temperature the discrete nature of the electron charge cannot be appreciated, meaning that when $k_B T \gg E_c, \Delta_N$, the SET behaves as a classical field-effect transistor. In this regime the conductance does not depend on the number of electrons, and is given by the Ohm's law for the conductances across the barriers with source and drain contacts. The current increases linearly till reaching a saturation regime (above threshold voltage). At high temperature the conductance is just the Ohmic sum of the two barrier conductances.

$$G_\infty = (1/G_s + 1/G_d)^{-1} \propto (1/\Gamma_s + 1/\Gamma_d)^{-1} \tag{2.7}$$

Going to cryogenic temperature $k_B T \ll E_{add}$.
When the coupling with the reservoir is sufficiently low, i.e when $h\Gamma \ll k_B T$, we are in the weak coupling regime. This is usually already the case at 4.2K (^4He temperature), where $k_B T/h \simeq 80$ GHz. Depending on the energy level spacing of the QD Δ_N and temperature, with bias $eV_{sd} \ll \Delta_N$ we can distinguish between two main conductance regime:

- $h\Gamma, \Delta_N \ll k_B T$, $eV_{sd} \ll \Delta_N$. *Classical coulomb blockade or metallic regime.*

$$G = G_{max} cosh^{-2}\left(\frac{\alpha_g^{(i)}(V_g^{(i)} - V_G)}{2.5 k_B T}\right) \tag{2.8}$$

Where $V_g^{(i)}$ is the value of the gate voltage on resonance. The peaks full width at half maximum (FWHM) is linear with $k_B T$ and it is FWHM$\simeq 4.375 k_B T$.
The peak height is independent of temperature in this regime, and equal to half the high temperature value $G_{max} = G_\infty/2$. This is because, due to Coulomb blockade, a new electron can hop onto the dot only if another electron has tunneled out and therefore the tunnel probability is halved.

- $h\Gamma \ll k_B T \ll \Delta_N$, $eV_{sd} \ll \Delta_N$. *Quantum Coulomb blockade regime, or single-level transport regime.*

$$G = G_{max}^{(i)} cosh^{-2}\left(\frac{\alpha_g^{(i)}(V_g^{(i)} - V_G)}{2k_B T}\right) \tag{2.9}$$

Here the FWHM is still linear with respect to T (FWHM$\simeq 3.5 k_B T$).
If we consider that only a single level in the dot participates in the conduction, then the peak amplitude is given by $G_{max}^{(i)} = \frac{e^2}{4k_B T}(1/\Gamma_s^{(i)} + 1/\Gamma_d^{(i)})^{-1}$ [9].
Differently from the classical regime the peak maximum G_{max} is inversely proportional to temperature. This temperature dependence allows to distinguish a quantum peak from a classical peak.

An important assumption for the above description of tunneling in both the quantum and classical Coulomb blockade regimes is that the barrier conductances are small: $G_{s,d} \ll e^2/h$. The charge is well defined under this condition and quantum fluctuations in the charge number can be neglected. This statement is equivalent to the requirement that only first order tunneling has to be taken into account.

When the tunneling with the reservoirs is dominant compared to thermal effects ($k_B T \ll h\Gamma$), and considering only first order tunneling ($eV_{sd} \ll h\Gamma \ll \Delta_N$) we are in the coherent or strong coupling regime. In this regime the maximum conductance of each peak can be expressed as [13]:

$$G = \frac{e^2}{\hbar}\left(\frac{1}{\Gamma_s^{(i)}} + \frac{1}{\Gamma_d^{(i)}}\right)^{-1} \tag{2.10}$$

The on-resonance peak height is equal to the quantum of conductance $e^2/\hbar$, multiplied by a factor that depends on the symmetry of the tunnel rates $\Gamma_s^{(i)}$ and $\Gamma_d^{(i)}$.

2.3.2. NON LINEAR TRANSPORT

Experimentally we often find that, when applying source-drain bias, the current inside a Coulomb diamond is not null due to an interplay between multiple energy levels contributing to the conduction and thermal excitations.
Finite temperature effects for a double junction system are studied in detail in Ref. [14], as well as the distinction between "inelastic" (different electrons participate to multiple tunneling) and "elastic" (the same electron tunnels through a virtual state) co-tunneling. The two physical situations are schematized in Fig. 2.5.
At very low bias voltage ($eV_{ds} < \Delta_N$) only elastic co-tunneling is allowed by energy conservation [15]. For higher bias ($eV_{ds} > \Delta_N$) inelastic co-tunneling is usually the dominant process, and the extra energy required is provided by the bias voltage.

When $k_B T, eV_{ds} < E_c$, the expression of the inelastic co-tunneling current is given in [14][16]:

$$I(V_{ds}) = \frac{h}{6e^2}\sigma_s\sigma_d\left(\frac{1}{E_s}+\frac{1}{E_d}\right)^2\left((k_B T)^2+\left(\frac{eV_{ds}}{2\pi}\right)^2\right)V_{ds} \tag{2.11}$$

where σ_s, σ_d are the conductances through the reservoirs barrier. The current results from stochastic single electrons tunneling across the barriers between the dot and the two reservoirs.
If n_s and n_d electrons have crossed the two barriers then E_s, E_d are the change in charging energy for the single electron transitions, respectively $(n_s, n_d) \rightarrow (n_s+1, n_d)$ and $(n_s, n_d) \rightarrow (n_s, n_d+1)$ (see Fig. 2.5 b),c)).
The equation 2.11 is valid if $k_B T < E_s, E_d$.
Inside the Coulomb blockade region the current is $\propto V_{ds}^3$.
When the bias voltage overtakes the addition energy, i.e. $V_{ds} > V_{off} = E_{add}/e$ the current starts to be linear with V_{ds}:

$$I \propto G_\infty(V_{ds} - V_{off})$$

meaning that it is determined by the series tunnel conductance of the two reservoirs G_∞. Therefore the threshold value V_{off}, where the currents starts to be linear with V_{ds}, provides the addition energy.
When the source-drain bias applied $eV_{ds} \gg \Delta_N$ we can neglect elastic tunneling effects. That's the case of the analysis in Sec. 4.6 where eq.2.11 is applied to extract the addition energy.

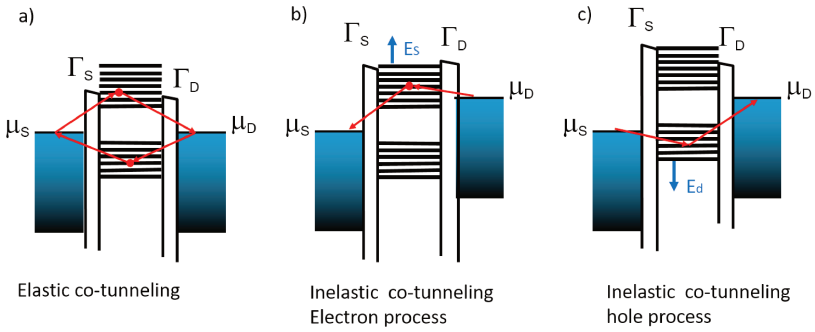

Figure 2.5: a) Elastic cotunneling: even if the system is in Coulomb blockade electrons can tunnel through the potential barrier with the reservoirs if $k_B T \simeq \Delta_N$. b),c) inelastic co-tunneling process for electrons and holes.

2.3.3. THEORY OVERVIEW

As usually happens in physics, when dealing with reality there are further aspects that should be added to the theoretical model.
For our quantum dot devices we list some of the deviations that should be taken in account:

- Real quantum dot devices do not have perfect parabolic potentials. They usually contain potential fluctuations due to impurities in the substrate.

- The shape of the gate is not always symmetric in the plane of the active channel and this can impact quantum dot properties[17], in particular for what concern spin dependent tunneling.
- The quantum dot thickness in the z-direction is not zero but typically 5-10 nm [3].
- By increasing V_G we not only lift the confinement potential, but we also vary its shape.
- In the experiments often the bias applied is not symmetric, but it is applied to only one of the the reservoirs, while the other one is kept grounded.
  The system can be schematized as a voltage divider (with $R_1 = R_2$ the resistances between dot and the two reservoirs) and therefore the effective gate voltage applied (if $R_1 = R_2$) is $V_g^{eff} = V_G + V_{ds}/2$. This effect can be corrected by subtracting the bias $V_{ds}/2$ to the gate voltage.

Nevertheless, the constant interaction model and other more advanced theories give the same qualitative picture. The experiments described will clearly confirm the common aspects of the different theories.

2.4. DISPERSIVE READOUT FOR SPIN QUBIT

In the perspective of a large-scale, semiconductor-based, quantum processor it will probably be necessary to read the state of quantum dots far away from the reservoirs, and to reduce as much as possible the hardware required for the qubit readout.
Whereas transport measurements are not appropriate for a local readout of many dots, radio-frequency reflectometry (RFR) [18] is a suitable candidate to overcome these problems. It essentially consists in monitoring small variation of capacitance in the device, mainly due to resonant transitions between quantum dots or between a dot and a reservoir.
The technique can be understood starting from a simple transmission line. By sending an oscillating signal with amplitude V_{in} on the gate, because of the impedance mismatch between our cables ($Z_0 = 50\ \Omega$) and the nanodevices we use (typically $Z \simeq 100\ k\Omega$), a portion of the signal is reflected, with amplitude V_r given by:

$$V_r = \frac{Z - Z_0}{Z + Z_0} V_{in} \tag{2.12}$$

The incoming and outgoing waves can be separated through a directional coupler and then it's possible to measure only the signal reflected by the electrode where the rf excitations are applied (see Fig. 2.6 a)).
The large impedance mismatch ($Z \gg Z_0$) results in a poor sensitivity to small variation of Z. The matching condition ($Z = Z_0$) instead is where the greatest sensitivity occurs.
One way to achieve this matching condition is to plug an inductance on one of the electrodes (on a gate or a reservoir). The parasitic capacitance C_p is provided by the coupling of the electrode with the surrounding environment. It is mainly affected by the wire bonding and the sample holder geometry and materials.
The electrostatic coupling between the electrodes (gate or reservoir) in the load also gives a small capacitive contribution called geometrical capacitance C_G, typically of the order of tens of aF, that can be included in C_p (they are summed in parallel). The impact of a double dot device on the reflectometry signal will be clarified in Sec. 2.5.
We can treat the load impedance as a purely resistive contribution R_L for the moment.

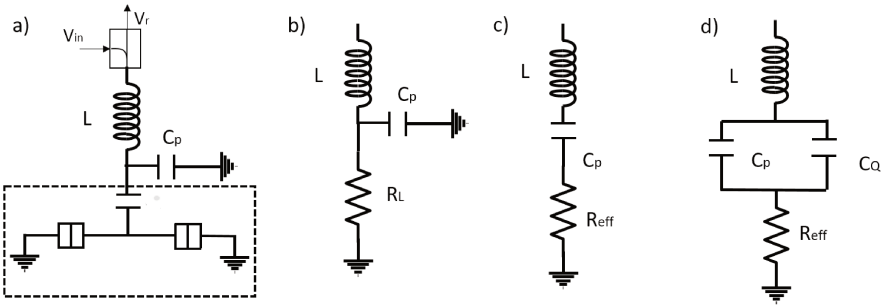

Figure 2.6: a) Scheme of the readout circuit. The dashed line highlights the device. b) Simplified scheme where the device capacitance C_G is included in C_p. c) Near the resonant frequency $\omega = 1/\sqrt{LC_p}$ the circuit can be approximated as a RLC series, with $R_{eff} = \frac{L}{C_p R_L}$. d) If there are charge transitions in the load we have to consider the contribution of an additional quantum capacitance C_Q, that shifts the resonant frequency to $\omega_0 = 1/\sqrt{L(C_p + C_Q)}$.

As sketched in the circuit diagram of Fig. 2.6 b), this circuit can be schematized as an RLC circuit, where L is the value of the inductance plugged on the electrode.
The total impedance of this circuit can be written as:

$$Z = j\omega L + \frac{1}{j\omega C_p + \frac{1}{R_L}}$$

In practical cases $\omega C_p R_L \gg 1$ (typical orders of magnitude $\omega \simeq 100$ MHz, $C_p \simeq 100$ fF and $R_L \simeq 100\ k\Omega$ respectively), and in close proximity to the resonant frequency the overall impedance can be approximated as the one of an RLC series circuit (Fig. 2.6 c):

$$Z = R_{eff} + j\omega L + \frac{1}{j\omega C_p}$$

with $R_{eff} = L/(C_p R_L)$ typically of the order of few tens of Ω. This overall impedance is minimized when $\omega = 1/\sqrt{LC_p}$ and consequently the signal reflected off the resonator too. The matching can still be improved, indeed on resonance the residual impedance is

$$Z = \frac{L}{R_L C_p}$$

One could think to add a resistance to compensate the residual mismatch, but that would dissipate the energy delivered to the device.
A better option is to plug a further matching capacitor C_M in parallel with the RLC circuit that, if chosen properly improves the matching. Indeed, after applying such a capacitor in parallel the effective impedance of the matched circuit becomes

$$Z = \left(j\omega C_M + \frac{1}{j\omega L + R_{eff} + \frac{1}{j\omega C_p}} \right)^{-1}$$

The matching condition in this case is reached when:

$$Z = \frac{\sqrt{LC_p}}{C_M} = Z_0 \tag{2.13}$$

With practical values of an inductor of $L \simeq 300$ nH and a parasitic capacitance of $C_p \simeq 0.5$ pF we would need $C_M \simeq 10$ pF to achieve the desired 50 Ω matching.

2.5. QUANTUM CAPACITANCE

So far the load of the circuit has been considered as a purely resistive object. When dealing with quantum dot devices we should consider an additional capacitive contribution, associated with charge tunneling in the device. This additional parametric capacitance C_{par} is in parallel with the geometrical capacitance C_G given by the electrostatic coupling between the electrodes, which we have previously included in the parasitic capacitance C_p (see Fig. 2.6 d)).
Therefore the total capacitance reads:

$$C_{tot} = C_G + C_{par}$$

In this way, when there are tunneling resonances in our device, the resonator frequency is slightly shifted. This is enough to appreciate differences in amplitude and phase (or I and Q) of the reflected signal.

We consider a tunnel-coupled double quantum dot (DQD) where the two dots QDi i = 1,2 are connected to an rf gate electrode via gate capacitances C_{Gi} and to grounded charge reservoirs via C_{Di} (Fig. 2.7).
The expression of the device capacitance C_{tot} can be obtained simply by differentiating the total charge in the DQD as a function of gate voltage [19].
We first expand the total gate charge in the DQD as a function of the gate coupling factors, $\alpha_i = C_{Gi}/(C_{Di} + C_{Gi} + C_m)$ and the average electron occupation probability $\langle n_i \rangle$ in QDi, .
We further assume the weak DQD coupling limit, i.e. $C_m \ll C_{Di} + C_{Gi}$. The total charge in the DQD reads:

$$Q_1 + Q_2 = \sum_i \alpha_i (C_{Di} V_G + e\langle n_i \rangle). \tag{2.14}$$

where V_G is the gate voltage applied.

The total capacitance can be obtained by differentiating eq. 2.14 with respect to V_G:

$$C_{tot} = \frac{d(Q_1 + Q_2)}{dV_G} = C_G + \sum_i e\alpha_i \frac{d\langle n_i \rangle}{dV_G} \tag{2.15}$$

We obtain, as expected, a gate voltage independent term, i.e. the geometrical capacitance: $C_G = \alpha_1 C_{D1} + \alpha_2 C_{D2}$ and a gate voltage dependent term, i.e. the parametric capacitance $C_{par}(V_G)$.
If we consider the gate current

$$I_G = \frac{d(Q1 + Q2)}{dt} = C_{tot} \frac{dV_G}{dt} \tag{2.16}$$

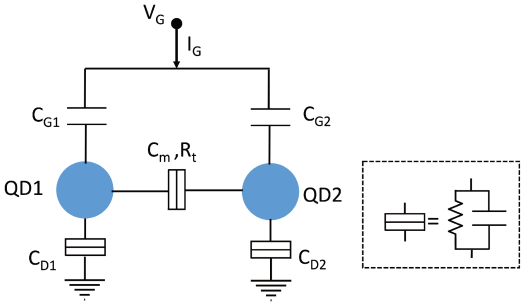

Figure 2.7: DC equivalent circuit of a DQD. The tunnel barriers, indicated by rectangles, consist of a capacitor in parallel with a resistor.

we note that for interdot charge transitions $\frac{d\langle n_2\rangle}{dt} = -\frac{d\langle n_1\rangle}{dt}$ [18]. Moreover we can rewrite $\alpha' = (\alpha_2 - \alpha_1)$ and therefore I_G can be expressed as:

$$I_G = C_G \frac{dV_G}{dt} + e\alpha' \frac{d\langle n_2\rangle}{dt} \tag{2.17}$$

At this point, if we apply a sinusoidal modulation on the gate voltage, at the resonant frequency f_r of the tank circuit, it will induce an oscillatory variation of the DQD energy difference $\epsilon = \mu_1 - \mu_2 = e\alpha'(V_G - V_G^0)$, where V_G^0 is the gate voltage offset at which the difference is zero.
For a small oscillating gate voltage applied (with respect to the energy difference ΔE between the ground and excited DQD state) we can write $\frac{dV_G}{d\epsilon} = \frac{1}{(e\alpha')}$ and the gate current can be expressed as:

$$I_G = \left(C_G + (e\alpha')^2 \frac{d\langle n_2\rangle}{d\epsilon}\right) \frac{dV_G}{dt} \tag{2.18}$$

where the second term in the parentheses defines the parametric capacitance:

$$C_{par} = (e\alpha')^2 \frac{d\langle n_2\rangle}{d\epsilon} \tag{2.19}$$

The problem is now reduced to understanding how the population $\langle n_2\rangle$ of the dot QD2 varies with the energy detuning ϵ. In order to do this it is necessary to introduce a physical model for the DQD.

2.6. DOUBLE QUANTUM DOT ENERGY DIAGRAM

2.6.1. CHARGE QUBIT

We start considering a DQD with only one electron. This provides a two level system, where the two possible charge states $|n_1, n_2\rangle$ are $|1,0\rangle$ and $|0,1\rangle$.

We can write the Hamiltonian representing this system considering two states with energy difference ϵ and with an overlap between the wavefunctions that we can describe as an off-diagonal tunnel coupling energy t:

$$H = \begin{pmatrix} -\epsilon/2 & t \\ t & +\epsilon/2 \end{pmatrix} \tag{2.20}$$

and the corresponding eigenenergies are:

$$E_{e,g} = \pm\frac{1}{2}\sqrt{\epsilon^2 + (2t)^2} \tag{2.21}$$

2

An analogue calculation can be done, for example, considering a hydrogen molecule, where the coupling between two atomic orbitals give raise to bonding (ground state) and antibonding state (excited state, where the two atoms are separated).

Let's now consider the time-averaged excess electron in the dot 2, as the sum of the average number of electrons in ground and excited state, each one with its own probability:

$$\langle n_2 \rangle = \langle n_2 \rangle_g P_g + \langle n_2 \rangle_e P_e \tag{2.22}$$

where the average excess of charges in each state is[19]:

$$\langle n_2 \rangle_{e,g} = \frac{1}{2}\left(1 + 2\frac{\partial E_{e,g}}{\partial \epsilon}\right) = \frac{1}{2}\left(1 \pm \frac{\epsilon}{\sqrt{\epsilon^2 + (2t)^2}}\right) \tag{2.23}$$

We can define the energy difference between ground and excited state $\Delta E = \sqrt{\epsilon^2 + (2t)^2}$, the probability difference $\Delta P = P_g - P_e$, and substitute the average excess of charges in each dot 2.22 in 2.19, finding the expression of the parametric capacitance for a charge qubit:

$$C_{par} = \frac{(e\alpha')^2}{2(2t)}\left(\underbrace{\frac{(2t)^3}{\Delta E^3}\Delta P}_{C_Q} + \underbrace{\frac{(2t)\epsilon}{\Delta E}\frac{\partial \Delta P}{\partial \epsilon}}_{C_T}\right) \tag{2.24}$$

The first term is the so-called quantum capacitance, related to the curvature of the energy band of each state with energy E_i [20][21], or in other terms

$$C_Q \propto \sum_i P_i \frac{\partial^2 E_i}{\partial \epsilon^2} \tag{2.25}$$

is the sum of the curvature of each i state, weighted by its occupation probability P_i. This is the term usually relevant at equilibrium and when the states posses a dispersion over energy.
The occupation probabilities follow the Boltzmann distribution where the occupation probability of each state is:

$$P_i = \frac{e^{-E_i/k_B T}}{Z} \tag{2.26}$$

Where $Z = \sum_i e^{-E_i/k_B T}$ is the canonical partition function, necessary to renormalize the probabilities.
The second term of eq. 2.24, called tunneling capacitance, is relevant when non adiabatic processes, such as resonant excitations, occur at a rate comparable with the reflectometry probing frequency.
In the general case the tunneling capacitance [22] can be expressed as:

$$C_T \propto \sum_i \langle n_2 \rangle_i \frac{\partial P_i}{\partial \epsilon} \tag{2.27}$$

Using the Boltzmann distribution of eq. 2.26 ($\beta = \frac{1}{k_B T}$) we can calculate the analytical expression of the charge distribution. Considering two singlets states with energies $E_{e,g} = \pm\frac{\Delta E}{2}$:

$$\Delta P_S(\epsilon) = P_g - P_e = \frac{e^{\frac{\Delta E(\epsilon)}{2}\beta} - e^{\frac{-\Delta E(\epsilon)}{2}\beta}}{Z} = tanh\left(\frac{\Delta E(\epsilon)}{2k_B T}\right) \tag{2.28}$$

2.6.2. SPIN QUBIT

The physical picture of spin states in a DQD changes completely when they share two or, more generally, an even number of charges.
Two charges in the same dot indeed can only form a spin singlet S(0,2) (total spin number $S = 0$), due to the Pauli exclusion principle. When the charges are in two separate dots instead we have to consider four possible spin states, i.e the antysimmetric singlet $|S(1,1,)\rangle$ and three symmetric triplets $|T(1,1)\rangle$.
We therefore find five energy states:

$$\begin{cases} |S(1,1)\rangle = \frac{|\uparrow,\downarrow\rangle - |\downarrow,\uparrow\rangle}{\sqrt{2}} \\ |T_0(1,1)\rangle = \frac{|\uparrow,\downarrow\rangle + |\downarrow,\uparrow\rangle}{\sqrt{2}} \\ |T_+(1,1)\rangle = |\uparrow,\uparrow\rangle \\ |T_-(1,1,)\rangle = |\downarrow,\downarrow\rangle \\ |S(0,2)\rangle = |0,\downarrow\uparrow\rangle \end{cases} \tag{2.29}$$

For simplicity here we neglect the presence of any valley state (present only for electrons) and of the excited triplet $|T(0,2)\rangle$, assuming that they are lying up in energy compared to the other five states.

In absence of magnetic field, interdot tunnel coupling, and assuming the same g-factor for the two dots, all the $|1,1\rangle$ spin states are degenerate. The tunnel coupling energy t and the g-factor difference defines the splitting between $|S(1,1)\rangle$ and $|T_0(1,1)\rangle$. The degeneracy between the triplet states instead is broken when a magnetic field is applied. If we consider a system made of electrons in silicon, we can do the following assumptions:

- The g-factor is the same for both the QDs.
- The spin-orbit coupling, that couples triplet and singlet states t_{SO}, is negligible.
- We neglect nuclear field anisotropy. As a consequence, in the limit of same g-factor, the effective magnetic field seen by the two dots is the same.

Under the assumptions above the states $|S(1,1)\rangle$ and $|T_0(1,1)\rangle$ are still degenerate for high detuning ϵ, also in presence of a magnetic field. For $\epsilon = 0$ instead their splitting is given by the tunnel coupling energy t. We use this simplified picture to describe the physics of the electron device described in Chap. 5.

Now we consider what happens when the Zeeman splitting of the spins in the two dots is different.
In III-V heterostructures the difference in Zeeman energy ΔE_Z between the two QDs is given by an anisotropic nuclear magnetic field [23].

In silicon-based electron quantum dots the nuclear field is weak, or not existent in the ideal case of isotopically purified ^{28}Si. Two QDs having the same g-factor, see the same magnetic field and therefore, in order to distinguish them, the magnetic field anisotropy is usually introduced artificially with a local micromagnet [24][25][26].

2

When dealing with holes the splitting between $S(1,1)$ and $T_0(1,1)$ is provided by the difference of g factor between the two dots [27][28].
We then consider the general Hamiltonian for a holes DQD with two charges.
With holes we also have to take in account that the strong spin-orbit couples singlet and triplet states [27], through the term t_{SO}. In the energy diagram of Fig. 2.8 this coupling is translated into a further anti-crossing between energy states.
The 5x5 Hamiltonian of the system can be written in both the singlet-triplet basis of eq. 2.29 or in the single spin basis. We choose to write it here in the singlet-triplet basis $\{S(0,2), S(1,1), T_+(1,1), T_0(1,1), T_-(1,1)\}$:

$$H = \begin{pmatrix} +\frac{\epsilon}{2} & t & t_{SO} & 0 & t_{SO} \\ t & -\frac{\epsilon}{2} & 0 & \frac{1}{2}\Delta g \mu_B B & 0 \\ t_{SO} & 0 & -\frac{\epsilon}{2} + \frac{1}{2}\sum g \mu_B B & 0 & 0 \\ 0 & \frac{1}{2}\Delta g \mu_B B & 0 & -\frac{\epsilon}{2} & 0 \\ t_{SO} & 0 & 0 & 0 & -\frac{\epsilon}{2} - \frac{1}{2}\sum g \mu_B B \end{pmatrix} \tag{2.30}$$

where $\sum g = g_1 + g_2$ and $\Delta g = g_1 - g_2$.
We can use such Hamiltonian to simulate the energy levels of the system as shown in Fig. 2.8.

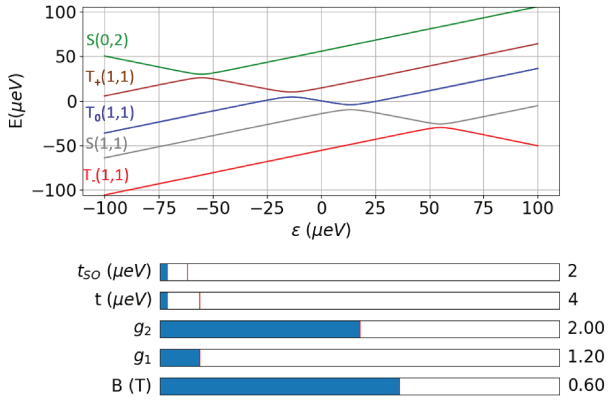

Figure 2.8: Energy diagram simulation of a DQD for an even-odd charge configuration. The interactive sliders for the t_{SO}, t, g_1, g_2 and B parameters allow for real time update of the energy levels diagram. The python code for this simulation can be found in [29]. The difference in g-factor is responsible of the curvature of the T_0 state near the anticrossing with the singlet states.

Remarkably, when there is a difference in the two dot g-factors also the T_0 state acquires a curvature. It comes from the electric dipole due to the coupling with $S(1,1)$ via the off-diagonal terms $\frac{1}{2}\Delta g \mu_B B$, which eventually implies a second-order coupling with $S(0,2)$.

This additional curvature of the T_0 is the key for the readout of the qubit described in Sec. 6.6 and it is particularly evident in Fig. 6.22.
Moreover, according to the energy diagram of Fig. 2.8 it is possible that also the states T_-, T_+ acquire a curvature due to their interaction with other states through the spin-orbit coupling term t_{SO}.
In this case the full dispersive response should be calculated using the formula of the quantum capacitance 2.25.

When doing charge-sensing instead the only important thing is the difference of occupation probabilities between the two charge states:

$$\Delta P = P_{11} - P_{02} = P_g + P_{T-} + P_{T+} + P_{T_0} - P_e \tag{2.31}$$

where each occupation probability is weighted over a five states partition function Z.

2.7. SPIN READOUT

The two spin states of a particle in a QD don't show any appreciable difference in their capacitive response. At the same time measuring the magnetic moment of a single particle (either electron or hole) is a very hard task, simply because it is very small. In free space the electron magnetic moment is of the order of $10^{-23} J/T$. Usually a cyclotron is necessary to measure such a magnetic moment [30]. A direct spin readout is still out of reach in semiconductor QDs platforms.
What we can do is read charges through either transport, charge-sensing measurement or gate reflectometry. We therefore need an efficient way to make transport spin-dependent, i.e. to realize spin-to-charge conversion.

We'll discuss two techniques for spin readout, both used across this thesis. The first technique, described in the following section, relies on a single QD coupled with a reservoir and requires a charge sensor to reveal a single tunneling event that allows to discriminate if the spin loaded was $|\uparrow\rangle$ or $|\downarrow\rangle$.
However, relying on N reservoirs for the measurement of N quantum dot would hardly be a scalable solution.
In the perspective of scaling-up to complex architectures, a more suitable readout approach is the one based on Pauli spin blockade (PSB), simply because it relies on two QDs instead than a dot and a reservoir. With this approach one QD is used as the readout qubit and the other one as an ancillary qubit, halving the number of dots available for the computation. As we will see across this thesis the PSB regime can be detected with both gate-based dispersive readout and charge-sensing.
Another advantage of PSB readout is that it is more suitable to work at higher temperature, as demonstrated by the fact that the few demonstrations of "hot" spin qubits ($T \simeq 1$ K) in silicon relied on this technique [31][32]. The negative impact of temperature on measurements based on energy-selective readout will be discussed in Sec. 6.5.1.

2.7.1. ENERGY-SELECTIVE TUNNELING READOUT

This technique, also named Elzerman readout [33], makes use of a single QD coupled with a Fermi sea. It requires an odd number of charges in the dot, in order to be able to load a spin $|\uparrow\rangle$ or $|\downarrow\rangle$ with equal probability.
Under a magnetic field the spin states are split by the Zeeman energy $E_Z = g\mu_B B$, where g is the Landé factor and μ_B the bohr magneton. If the Zeeman splitting exceeds the thermal energy ($Ez \gg k_B T$) it is possible to tune the energy of the dot such that the $|\uparrow\rangle$

and $|\downarrow\rangle$ spin states lie respectively above and below the Fermi energy of the reservoir.
A three-step pulsing sequence is necessary in order to empty the dot, load a random spin and measure it:

- *Empty stage*: The electrochemical potential of the dot is above the Fermi level and we remove its spin.
- *Load stage*: The electrochemical potential of both the spin states is below the Fermi level of the reservoir and we can load a random spin. This stage should last less than the spin relaxation time T_1.
- *Read stage*: Only the excited spin state should be above the reservoir Fermi energy. If the tunneling is faster than T_1, the favourable relaxation path is to first tunnel into the reservoir and successively tunnel back into the dot as a spin down. If the spin was initially in its ground state instead nothing happens.

A charge sensor is necessary to realize spin-to-charge conversion in the measurement stage.
A scheme of the measurement procedure is shown in Fig. 2.9. This scheme is taken from Ref. [33], where the experiment has been realized on a GaAs/AlGaAs heterostructure, where g is negative and therefore the $|\uparrow\rangle$ spin state is the ground state.

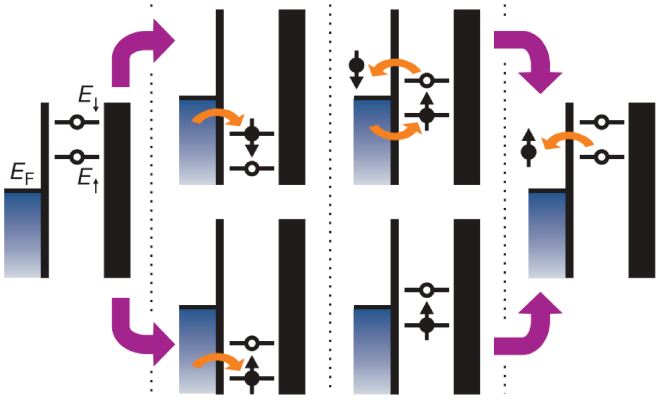

Figure 2.9: Schematic energy diagrams during the measurement cycle. From left to right the QD is emptied, then a random spin is loaded and then measured. This cycle is repeated many times in order to obtain a statistics on the initial population of the dot. Black vertical lines indicate the tunnel barriers and the shaded blue boxes indicate the Fermi sea of the reservoir. From ref. [33].

This measurement scheme also allows to measure the spin relaxation time T_1 by varying the duration of the load stage and measuring the spin population as a function of the time spent in the loading stage. We'll use this spin readout technique in Chap. 6.

2.7.2. PAULI SPIN BLOCKADE READOUT

This technique fundamentally relies on the Pauli exclusion principle [34], stating that two particles occupying the same orbital level must have anti-parallel spin. Differently from the previous readout mechanism a DQD is necessary to demonstrate this technique. The DQD should be prepared in an (odd, odd) or ("1,1")-like charge configuration. Then, by

changing the gate voltages, the charge ground state can be moved to an (even-even) or ("0,2")-like configuration. If the spins of the charges in the separate dots have the same orientation interdot tunneling is forbidden by the Pauli principle.
Starting from the first demonstration in 2002 [35] in GaAs, this technique has been widely used in many different semiconductor QD platforms [36][37][38][39][40].
Most of the demonstrations of this technique relied on measuring a spin dependent current through two dots in series, that is suppressed when the spins within the DQD are parallels.
Without a charge sensor the first charge transitions are not always visible through transport measurement, because of low tunnel coupling with the reservoir, and it is therefore not always possible to know a priori when we are dealing with a $("1,1") \leftrightarrow ("0,2")$ transition.
Historically the common way to identify PSB is by measuring the so-called bias triangles. Fundamentally, when applying bias, transport is allowed not only when the energy levels of two dots are aligned with the Fermi energy of the reservoirs (elastic tunneling), but also when there is an energy mismatch between the initial and final state (inelastic tunneling). Therefore, when applying source drain bias, some conduction areas with a triangular shape are formed, the edges of these triangles correspond to the situation where the energy level of one of the two dots is aligned with the reservoir, the tip corresponds to the case where the energy difference between the dots is equal to the bias. Hence when one of the two dot energy level is brought out of the bias window transport is no more allowed.
Experimentally many different features can be observed in these triangles, depending on the energetic structure of the dots (presence of excited states), spin-mixing mechanisms and the different coupling of the two dots with the reservoir. More details about the theory [41] of bias triangles and a collection of experimental measurements can be found in Refs. [1][2].
In Fig. 2.10 we consider a $("1,1") \leftrightarrow ("0,2")$ transition in the case where the tunneling with the two reservoirs is symmetric and when the bias applied is higher than the orbital splitting. In the left diagram a positive bias is applied on the source and electrons flow from the right (drain) to the left (source) reservoir through the dots. Since the right dot ground state is in an antysimmetric $S(0,2)$ spin state, transport to the $(1,1)$ state is always allowed.
Conversely in the diagram on the right the bias applied is negative and the electrons flow is from source to drain and hence the transition involved is from $("1,1") \rightarrow ("0,2")$. In this case when the spins in the two dots are parallel transport is forbidden by Pauli blockade. A spin-flip is necessary to allow transport in this case and, depending on how fast is this spin-flip mechanism, in realistic cases it is possible to observe either a decrease or a full suppression of the current at the base of the triangles.
Here the bias applied is higher than the orbital splitting between the $S(0,2)$ and $T(0,2)$. When the upper excited state falls below the ("1,1") energy level the spin can occupy a different orbital in the right dot and no more spin selection rules are involved. This explains why it can be observed a revival of the current in the blockaded triangles.

During this thesis I have almost always worked with dots isolated from the reservoirs. Without having access to transport measurement we found that PSB can also be detected by measuring a magnetic field dependent interdot tunneling time, as it will be explained in Sec. 5.5.2.
In Sec. 6.6 it will also be demonstrated that, instead of relying on transport or charge-sensing measurement, it is also possible to detect dispersively the spin-dependent trans-

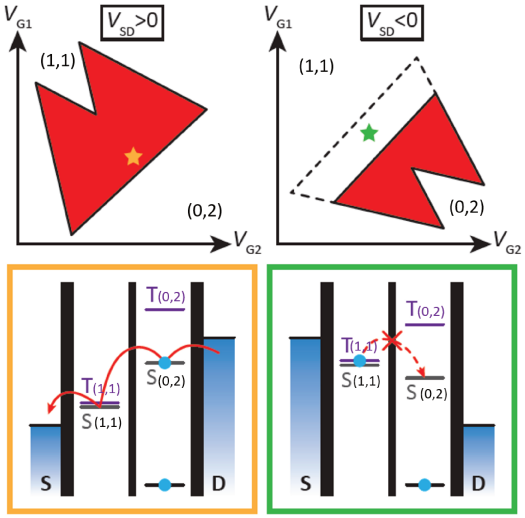

Figure 2.10: Theoretical source drain current as a function of gate voltages V_{G1} and V_{G2} in the cases of positive (left) and negative (right) bias, corresponding respectively to a ("0,2") → ("1,1") transition and to a ("1,1") → ("0,2"). The red color indicates the regions where transport is allowed. The dashed lines in the right diagram represent the limits of the bias triangles in the absence of PSB. The bottom energy diagrams (corresponding to the points indicated by a star in the upper diagrams) show the transport mechanism at the bases of triangles, explaining the current suppression when $V_{SD} < 0$.

port through the DQD, offering a potentially scalable solution for spin readout in larger qubit arrays.

2.8. SPIN-ORBIT COUPLING

The spin-orbit coupling (SOC) is a relativistic effect that couples the orbital motion of the electron to its spin.
Fundamentally an electron moving in an electric field experiences in its reference frame an effective magnetic field that couples to its spin.
The spin-orbit hamiltonian can be derived directly from the Dirac equation in the non relativistic approximation [42]. For a particle moving in an electrostatic potential $\boldsymbol{V}$ it can be written as:

$$H_{SO} = -\frac{e\hbar}{4m_0^2c^2}\boldsymbol{\sigma}\cdot(\boldsymbol{p}\times\nabla_{\boldsymbol{r}}\boldsymbol{V}) \tag{2.32}$$

where m_0 is the particle effective mass, c the speed of light. The vectors here are indicated in bold: $\boldsymbol{\sigma} = (\sigma_x, \sigma_y, \sigma_z)$ is a vector of of spin 1/2 Pauli matrices and $\boldsymbol{p}$ is the canonical momentum operator.
Another way to see the Hamiltonian 2.32 is that a charge with a mass m_0 and moving with a velocity vector $\boldsymbol{v} = \boldsymbol{p}/m_0$ in an electric field $\boldsymbol{E} = (1/e)\nabla_r \boldsymbol{V}$, sees in its own reference frame an effective magnetic field $B_{SO} = \boldsymbol{p}\times\boldsymbol{E}/(m_0c^2)$.

In an atom this internal magnetic field acting on the spin depends on the orbital the electron occupies. Since both the momentum of a particle and the electric field get larger

when approaching the nucleus of an atom, the spin-orbit interaction is higher the closer we get to the atomic core. First orbitals exhibit therefore the strongest spin-orbit interaction and a similar logic leads to stronger spin-orbit interactions for heavier elements.

In crystals instead the local electric fields can be associated with asymmetric confining potentials that give rise to a spin-orbit interaction. This spin-orbit contribution associated with structural inversion asymmetry (SIA) is known as the Rashba SOC [43]. Only in an ideal symmetric quantum well with symmetric doping, this contributions would be zero.
In structures that exhibit bulk inversion asymmetry, such as in the zinc-blende structure of GaAs, the local electric fields lead to another contribution to the spin-orbit interaction, acting on the growth direction. This effect is known as the Dresselhaus contribution to the spin-orbit interaction [44].
Even though this contribution is null in centrosymmetric crystals such as Si and Ge, a local electric field due to interface inversion asymmetry [45][46] might still play a role. This contribution often is also called the Dresselhaus term because it has an analogue representation in the spin-orbit Hamiltonian 2.33.

In a 2D system, assuming that the confining field is along the growth direction z (corresponding to the main crystallographic axis [0,0,1]), the spin-orbit hamiltonian of eq. 2.32 can be rewritten as [1]:

$$H_{SO} = \alpha(p_x\sigma_y) + \beta(-p_x\sigma_x + p_y\sigma_y) \tag{2.33}$$

where α and β (m/s) quantifies respectively the magnitude of the Rashba and Dresselhaus terms of SOC.
Both terms are much smaller, by $\simeq 3$ orders of magnitude, in Si[47][48] than for example in GaAs[1]. The low SOC leads to much longer spin relaxation time T_1 in Si than in GaAs. On the other hand in Si this may represent an issue when trying to couple the electron spin with an external AC electric field. The SOC indeed allows the direct electrical spin manipulation, that in a silicon nanowire is much more efficient for holes than for electrons and usually a micromagnet is required to enable artificial SOC of electrons in silicon[49][50].

In QDs, the confinement is such that the momentum of a particle, on average, is zero in any direction, i.e. $\langle p_x\rangle = \langle p_y\rangle = 0$.
This leads to the result that for two spins on the same orbital:

$$\langle nl,\uparrow|H_{SO}|nl,\downarrow\rangle = \langle n,l|p_{x,y}|n,l\rangle\langle\uparrow|\sigma_{x,y}|\downarrow\rangle = 0 \tag{2.34}$$

where n and l label the principal and the orbital quantum number in the QD orbital.
Consequently, the spin-orbit Hamiltonian of eq. 2.33 does not couple different spins on the same orbital but couples only states with different orbitals and spin components [51]. This means that pure spin states are replaced by pseudo-spin states, that are admixtures of both orbital and spin states.
The hybridization between spin and orbital states allows an external electric field to couple to the pseudo-spin states of the same Kramers doublet through SOC.

The hybridization between spin and orbital states in a QD is strongly dependent on the energetic band structure of the crystal. The conduction band has an s-like character and, excluding valley states, it has only spin degeneracy and therefore no SOC is expected, since two electrons in the conduction band would lie on the same orbital. The SOC could

be enabled by the mixing between different orbitals or, in the case of electrons in silicon, orbital and valley states [52], [53]. As shown in Ref. [54] this mixing can be controlled by tuning the tunnel barrier between the QDs.

When dealing with holes confined in silicon or germanium nanowire, the SOC is intrinsically strong, due to the mixing between the heavy holes and light holes band.
Indeed, under strong confinement, the band structure is modified compared to the one of the bulk material, as shown in Ref. [55]. When considering the valence band it should be taken in account a further degeneracy in the total angular momentum due to its p-like character [42].
The orbital angular momentum l=1 and the spin angular momentum s=1/2 generate six states characterized by total angular momentum quantum numbers j and m_j:

$$|j, m_j\rangle = \left|\frac{3}{2}, \pm\frac{3}{2}\right\rangle, \left|\frac{3}{2}, \pm\frac{1}{2}\right\rangle, \left|\frac{1}{2}, \pm\frac{1}{2}\right\rangle$$

When considering spin-orbit interaction the energy of states with j=1/2 is lowered down. This is called the split-off band and it is usually negligible in bulk materials.
The other two bands with $j = 3/2$ follow a different parabolic dispersion relation and, since their curvature is related to the effective mass these represents the heavy holes (HH), with $m_j = \pm 3/2$, and light holes band (LH), with $m_j = \pm 1/2$.
The confinement in a nanowire lead to strong HH-LH mixing [55][56]. This mixing is the main reason why SOC is stronger for holes than for electrons confined in a nanowire. This intrinsic contribution to the SOC can be included as a Rashba-like term in eq. 2.33 and it is often referred to as direct Rashba SOC [56] because of this analogy.

2.9. SPIN MANIPULATION

Electron spin states can be manipulated by electron spin resonance (ESR). The transition between two spin states ($|\uparrow\rangle$ and $|\downarrow\rangle$) can be induced by applying an oscillating magnetic field which has an orthogonal component to the external magnetic field and whose energy is equal to the energy difference between two spin states. The splitting in energy between two spins is given by the Zeeman energy $E_Z = g\mu_B B_0$, which increases linearly with the external magnetic field. The Landé g-factor can instead be modified by varying the static magnetic field direction [57][46].

The oscillating magnetic field can be generated by an alternate current I_{ac} flowing through a stripline, acting as an antenna, as schematized in Fig. 2.11 a). The frequency of the AC current should match the Larmor frequency $f = \frac{E_Z}{h}$.
Fundamentally the AC magnetic field provides photons matching the Zeeman splitting and allowing coherent spin oscillations. This is the technique historically used in standard nuclear magnetic resonance, with the difference that here the spin belongs to an electron (or a hole) and not to the nuclei. Many recents experiments have exploited this technique [38][58] [59].
The intensity of B_{ac}, proportional to I_{ac}, determines instead the speed of the Rabi oscillations between $|\uparrow\rangle$ and $|\downarrow\rangle$ spin.

In the perspective of a scalable spin qubit architecture, the use of magnetic fields to control the spin is unpractical, because it is nearly impossible to localize the magnetic field in order to affect only one qubit and not its neighbors.
Another drawback of using a stripline as an antenna could be the heating induced by the

current flowing through it. However, this issue can be solved by using a superconducting antenna.

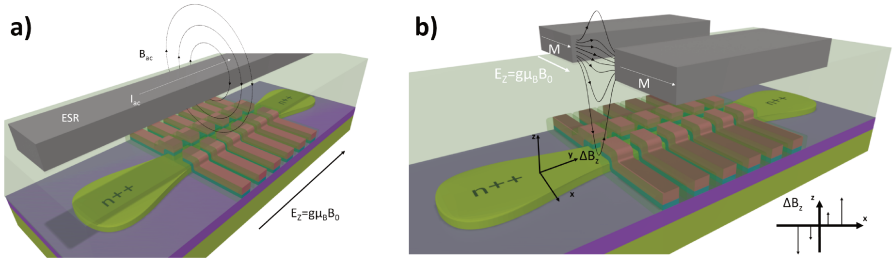

Figure 2.11: Two possible schemes for electron spin manipulation on a n-type double array of QDs, as the one of Chap. 5. In black are represented the field lines a) A metal stripline lies on top the dielectric covering the array. An AC current flowing through it provides the alternating magnetic field necessary for electron-spin resonance (ESR). A large static magnetic field B_0 parallel to the Si nanowire split spin degeneracy by the Zeeman energy $E_Z = g\mu_B B_0$. ESR occurs when the AC frequency equals $\frac{E_Z}{h}$. b) Alternative scheme for electron-spin manipulation. The ESR stripline in a) is replaced by properly oriented micromagnets with magnetization M. The micromagnets create a magnetic-field gradient along z, perpendicular to the static field B_0. As a result, a gate-voltage modulation laterally shaking the electron wave function in the QD provides the oscillatory magnetic field needed for electron-spin resonance. In other words, the micromagnets generate a synthetic SOC. Image from [60].

As explained in the previous section, the SOC allows the direct coupling between an electric field, that can be applied on the gate confining the QD, and the spin.
The spin manipulation through an electric field is usually denoted as electric dipole spin resonance (EDSR) and it is the technique used in the experiments described in Secs. 5.7, 6.5,6.6. EDSR has also the practical advantage that high frequency electric fields are often easier to apply and localize than magnetic fields,

The SOC mechanism is usually intrinsically strong for holes in a silicon nanowire. Conversely, when dealing with electrons in silicon, a synthetic SOC can be induced with a local micromagnet, as shown in Fig. 2.11 b). The mechanism of EDSR with a micromagnet was first presented in [50] for a 1D quantum dot.
The SOC is induced by the gradient in the local magnetic field of the micromagnet. As can be understood from eq. 2.32, the SOC can be induced also by a local gradient in the electrostatic field $\nabla \boldsymbol{V}$ that allows the electron spin to couple with electric fields.
Another way to see this synthetic SOC is that when we apply an oscillating gate voltage the electron wavefunction starts jiggling in a magnetic field gradient, experiencing an oscillating magnetic field that would couple directly to its spin.
In a similar manner the gradient in the local magnetic field can also be induced naturally by the inhomogeneity of the Overhauser field induced by the nuclei, as can be the case in GaAs [61].

In the perspective of scaling up the architecture of Fig. 2.11 b), we should also consider the independent control of each spin in multiple QDs (addressability), i.e. the Zeeman energy, and hence the Larmor frequency, of each electron (hole) should be different. In order to discriminate the Larmor frequencies, the g-factor of each electron (hole) or the local magnetic field felt by each electron should be different. The magnetic field gradient

produced by the micromagnet guarantee individual addressability, as well as enabling electrical spin control.
When dealing with holes the g-factor of each QD is intrinsically different, ensuring that each dot has a different Larmor frequency. The strong variability of holes g-factor is due to the fact that the HH-LH mixing mechanism has a strong dependence from the magnetic field direction [42][57].

2.10. ACTIVE INTERFEROMETRY MEASUREMENT OF A QUANTUM DOT

In this section I describe an experiment that highlight the core principles of gate-based reflectometry. Here we demonstrate that, through an interferometric technique, it is possible to read small capacitance variations in the device without an LC resonator.
Interferometry was initially introduced as an extreme-impedance measurement technique[62].
The impedance of the device under test (DUT) Z, that here is the gate impedance, in our case is usually between tens to few hundreds of $k\Omega$, much larger than the characteristic impedance of the cables $Z_0 = 50\ \Omega$ and therefore nearly all the signal is reflected off the device (see 2.12). It is therefore very hard to reach the sensitivity necessary to measure the small variation of the reflected signal $V_r + \delta V_r$ due to an additional quantum capacitance in the DUT, on top of a way bigger signal ($\delta V_r \ll V_r$).
With the interferometric technique we demonstrate here we show that, by cancelling out the reflected signal with another wave, it is instead possible to read small variation of such a signal on top of a small amplitude quasi-flat signal ($\delta V_r > V_r \simeq 0$)[63][64].

As explained in Sec. 2.4 the matching condition can be achieved with an LC resonator. A scalable version of this technique to readout many qubits demands a considerable engineering effort. The interferometry technique instead does not need any active component at the sample level and is tunable in-situ. Nevertheless in a many qubit system the electronics at the base temperature stage of the cryostat would be quite invasive, since we need two directional coupler for each readout line.
We demonstrate the use of this technique by sensing single charge transport through a QD in a silicon-on-insulator nanowire p-type transistor.
In the setup of Fig. 2.12 a), the RF signal is first split into two paths. The left path is sent through a manual phase shifter, a pass-band filter, 40 dB of attenuation, and finally to the coupled port of a directional coupler. The signal then, reflected off from the gate of the device, passes back through the directional coupler and then to a second directional coupler. This last coupler combines the reflected signal $S(t)$ with the cancellation signal from the right port of the power splitter $C(t)$. This second signal arrives at the coupler after passing through a variable attenuator, a pass-band filter, and 40 dB of fixed attenuation. The signals are first summed with a directional coupler and then amplified and measured with an IQ mixer.
We may say that such a system is the electrical equivalent of a Mach-Zender interferometer.
The setting of the interferometric measurement essentially consist of two or three steps:

1. Find a frequency ω_0 such that the the reflected signal $S(t,\omega) = A_S\Gamma(\omega)sin(\omega t + \omega t_0(\omega))$ and the cancellation wave $C(t,\omega) = A_C sin(\omega t)$ are dephased by π. The term $t_0(\omega)$ is the delay between the two signals $S(t,\omega)$ and $C(t,\omega)$. It is due to the difference between their paths and by the phase acquired after the reflection. For a frequency $\omega = \omega_0$ the maximum phase mismatch is reached when $\omega_0 t_0(\omega_0) =$

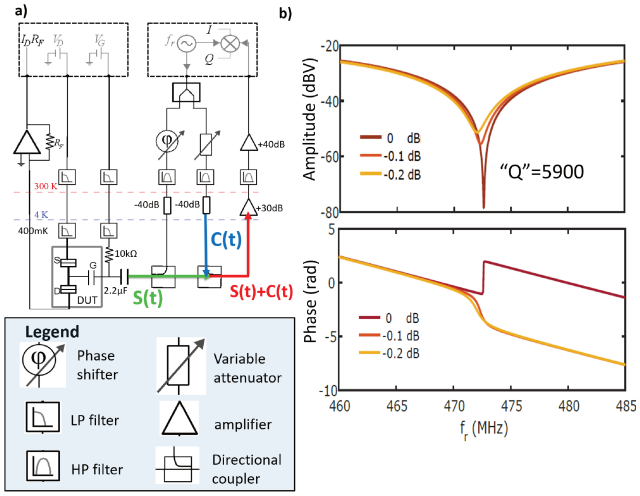

Figure 2.12: a) Schematic of the interferometry setup. b) Measurement of the amplitude and phase of the demodulated signal for optimal phase mismatch and different amplitudes of the cancellation signal.

$(2n+1)\pi$.

2. Match the amplitude of the two signals, i.e. $A_S\Gamma(\omega_0) = A_C$, by tuning the amplitude of the cancellation signal. At this point $S(t) + C(t) \simeq 0$.

3. Optionally the phase shifter can be used to readjust the phase of the reflected signal without changing the working frequency. In our case this was comfortable because the signal wasn't stable in time, because of very small fluctuations in the room temperature electronics.

Once the cancellation is optimized, the total signal $C(t) + S(t)$ is almost nullified.
At this point we are ready to measure the QD charge transitions that, as in the gate reflectometry, can be detected if the tunneling rate is of the same order as the probing frequency [65].
The big advantage of this technique over lumped element or distributed LC resonators is that the working frequency can be tuned at will, since we are not obliged to match any resonator frequency. In principle this could allow to detect dispersively charge transitions with tunnel rate of several GHz, while in the gate reflectometry case the sensitivity range is mainly determined by the ratio between the timescale of the probing tone and the charge dynamics to be probed.
Moreover the amplitude and phase characteristics resembles the ones of an LC resonator, as shown in Fig. 2.12 b). In analogy, we can define an effective Q-factor:

$$Q = \frac{f_0}{\Delta f}$$

where Δf is the FWHM of the amplitude signal. In the figure 2.12 b) it is shown a case where $Q \simeq 5900$. We manage to reach an effective Q-factor of$\simeq$ 40000. Unfortunately, even

though we observed that the magnitude of both phase and amplitude signal increases linearly with Q, increasing the value of this Q-factor does not improve significantly the signal-to-noise ratio (SNR) of the measurement.

In Fig. 2.13 it is shown a measurement of a Coulomb diamond in current, compared with the interferometric measurement. The three measurements are recorded simultaneously. The data presented are collected using an integration time of 100 ms per point. We can

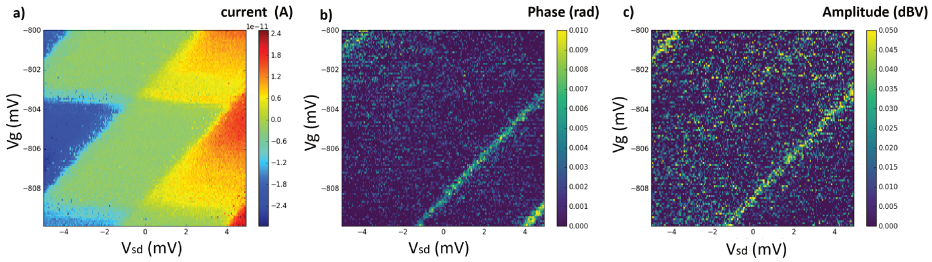

Figure 2.13: a) Measurement of Coulomb diamonds in current. The potential is applied on the source, as can be noticed by observing that the transitions with the source are nearly horizontal in V_g. b,c) Phase and amplitude of the interferometric signal. For these measurements $Q \simeq 10000$.

observe only the transition line of the QD with the source, indicating that the dot wave function (and hence the tunneling rates) is not symmetric.
There are two key limitations in the current setup. The first one is a poor signal-to-noise ratio (SNR), such that we have to use an integration time of 100 ms, slowing down significantly the measurement compared for example to RF gate reflectometry.
The second limitation is the significant drift over time in the RF signal. We currently attribute this drift to the lack of phase stable cables at room temperature and the poor stability of our phase shifter and variable attenuators. This issue could be solved by placing the variable attenuator and the phase shifter inside the cryostat, where temperature fluctuations are negligible, and controlling them electrically.

Lastly we propose to combine the technique described with RF reflectometry. This would mean to use a cancellation signal on top of the signal reflected off by an LC resonator. Amplifying the reflectometry signal might allow to increase its SNR and hence the readout fidelity. However, empirically we found that with this technique the SNR of the interferometry enhanced phase signal is around 2, which is not astonishing, but might still be beneficial in terms of qubit readout fidelity. Further research is required to assess the benefits of this technique when combined with RF reflectometry.

BIBLIOGRAPHY

[1] R. Hanson et al. “Spins in few-electron quantum dots”. In: *Rev. Mod. Phys.* 79 (4 Oct. 2007), pp. 1217–1265. DOI: 10.1103/RevModPhys.79.1217. URL: https://link.aps.org/doi/10.1103/RevModPhys.79.1217.

[2] W. G. van der Wiel et al. “Electron transport through double quantum dots”. In: *Rev. Mod. Phys.* 75 (1 Dec. 2002), pp. 1–22. DOI: 10.1103/RevModPhys.75.1. URL: https://link.aps.org/doi/10.1103/RevModPhys.75.1.

[3] L. P. Kouwenhoven et al. “Mesoscopic electron transport”. In: (1997), pp. 105–214.

[4] S. De Franceschi et al. “SOI technology for quantum information processing”. In: Dec. 2016, pp. 13.4.1–13.4.4. DOI: 10.1109/IEDM.2016.7838409.

[5] L. Zhuang, L. Guo, and S.Y. Chou. In: *Applied Physics Letters* 72.1205 (1998).

[6] T. Ando, A.B. Fowler, and F. Stern. In: *Reviews of Modern Physics* 54.41 (1982).

[7] J. H. F. Scott-Thomas et al. “Conductance Oscillations Periodic in the Density of a One-Dimensional Electron Gas”. In: *Phys. Rev. Lett.* 62 (5 Jan. 1989), pp. 583–586. DOI: 10.1103/PhysRevLett.62.583. URL: https://link.aps.org/doi/10.1103/PhysRevLett.62.583.

[8] U. Meirav et al. “One-dimensional electron gas in GaAs: Periodic conductance oscillations as a function of density”. In: *Phys. Rev. B* 40 (8 Sept. 1989), pp. 5871–5874. DOI: 10.1103/PhysRevB.40.5871. URL: https://link.aps.org/doi/10.1103/PhysRevB.40.5871.

[9] C. W. J. Beenakker. “Theory of Coulomb-blockade oscillations in the conductance of a quantum dot”. In: *Phys. Rev. B* 44.1646 (1991).

[10] Charles Kittel. *Introduction to Solid State Physics*. 8th ed. Wiley, 2004. ISBN: 9780471415268.

[11] C. H. Yang et al. “Spin-valley lifetimes in a silicon quantum dot with tunable valley splitting”. In: *Nature Communications* 4.1 (June 2013), p. 2069. ISSN: 2041-1723. DOI: 10.1038/ncomms3069. URL: https://doi.org/10.1038/ncomms3069.

[12] Floris A. Zwanenburg et al. “Silicon quantum electronics”. In: *Rev. Mod. Phys.* 85 (3 July 2013), pp. 961–1019. DOI: 10.1103/RevModPhys.85.961. URL: https://link.aps.org/doi/10.1103/RevModPhys.85.961.

[13] M. Buttiker. “Coherent and sequential tunneling in series barriers”. In: *IBM Journal of Research and Development* 32.1 (1988), pp. 63–75. DOI: 10.1147/rd.321.0063.

[14] D. V. Averin and Yu. V. Nazarov. “Virtual electron diffusion during quantum tunneling of the electric charge”. In: *Phys. Rev. Lett.* 65 (19 Nov. 1990), pp. 2446–2449. DOI: 10.1103/PhysRevLett.65.2446. URL: https://link.aps.org/doi/10.1103/PhysRevLett.65.2446.

[15] S. De Franceschi et al. “Electron Cotunneling in a Semiconductor Quantum Dot”. In: *Phys. Rev. Lett.* 86 (5 Jan. 2001), pp. 878–881. DOI: 10.1103/PhysRevLett.86.878. URL: https://link.aps.org/doi/10.1103/PhysRevLett.86.878.

[16] D.C. Glattli et al. “Co-tunneling of the charge through a 2-D electron island”. In: *Z. Phys. B - Condensed Matter 85, 375-380 (1991)* 85 (1991), pp. 375–380. URL: https://link.springer.com/content/pdf/10.1007/BF01307633.pdf.

[17] S. Amasha et al. “Electrical Control of Spin Relaxation in a Quantum Dot”. In: *Phys. Rev. Lett.* 100 (4 Jan. 2008), p. 046803. DOI: 10.1103/PhysRevLett.100.046803. URL: https://link.aps.org/doi/10.1103/PhysRevLett.100.046803.

[18] Florian Vigneau et al. *Probing quantum devices with radio-frequency reflectometry*. 2022. DOI: 10.48550/ARXIV.2202.10516. URL: https://arxiv.org/abs/2202.10516.

[19] Ryo Mizuta et al. “Quantum and tunneling capacitance in charge and spin qubits”. In: *Phys. Rev. B* 95.4 (2017), p. 045414.

[20] T. Duty et al. “Observation of Quantum Capacitance in the Cooper-Pair Transistor”. In: *Phys. Rev. Lett.* 95 (20 Nov. 2005), p. 206807. DOI: 10.1103/PhysRevLett.95.206807. URL: https://link.aps.org/doi/10.1103/PhysRevLett.95.206807.

[21] M. A. Sillanpää et al. “Direct Observation of Josephson Capacitance”. In: *Phys. Rev. Lett.* 95 (20 Nov. 2005), p. 206806. DOI: 10.1103/PhysRevLett.95.206806. URL: https://link.aps.org/doi/10.1103/PhysRevLett.95.206806.

[22] Theodor Lundberg et al. *Non-reciprocal Pauli Spin Blockade in a Silicon Double Quantum Dot*. 2021. arXiv: 2110.09842 [cond-mat.mes-hall].

[23] Jason R Petta et al. “Coherent manipulation of coupled electron spins in semiconductor quantum dots”. In: *Science* 309.5744 (2005), pp. 2180–2184.

[24] Jun Yoneda et al. “A quantum-dot spin qubit with coherence limited by charge noise and fidelity higher than 99.9%”. In: *Nature Nanotech.* 13.2 (2018), pp. 102–106.

[25] David M Zajac et al. “Resonantly driven CNOT gate for electron spins”. In: *Science* 359.6374 (2018), pp. 439–442.

[26] W. Huang et al. “Fidelity benchmarks for two-qubit gates in silicon”. In: *Nature* 569.7757 (May 2019), pp. 532–536. ISSN: 1476-4687. DOI: 10.1038/s41586-019-1197-0. URL: https://doi.org/10.1038/s41586-019-1197-0.

[27] Rami Ezzouch et al. “Dispersively Probed Microwave Spectroscopy of a Silicon Hole Double Quantum Dot”. In: *Phys. Rev. Applied* 16 (3 Sept. 2021), p. 034031. DOI: 10.1103/PhysRevApplied.16.034031. URL: https://link.aps.org/doi/10.1103/PhysRevApplied.16.034031.

[28] Daniel Jirovec et al. “A singlet-triplet hole spin qubit in planar Ge”. In: *Nature Materials* (June 2021). ISSN: 1476-4660. DOI: 10.1038/s41563-021-01022-2. URL: https://doi.org/10.1038/s41563-021-01022-2.

[29] Rami Ezzouch. “Gate reflectometry as readout and spectroscopy tool for silicon spin qubits”. Theses. Université Grenoble Alpes [2020-....], June 2021. URL: https://tel.archives-ouvertes.fr/tel-03337854.

[30] D. Hanneke, S. Fogwell, and G. Gabrielse. “New Measurement of the Electron Magnetic Moment and the Fine Structure Constant”. In: *Phys. Rev. Lett.* 100 (12 Mar. 2008), p. 120801. DOI: 10.1103/PhysRevLett.100.120801. URL: https://link.aps.org/doi/10.1103/PhysRevLett.100.120801.

[31] L. Petit et al. “Universal quantum logic in hot silicon qubits”. In: *Nature* 580.7803 (Apr. 2020), pp. 355–359. ISSN: 1476-4687. DOI: 10.1038/s41586-020-2170-7. URL: https://doi.org/10.1038/s41586-020-2170-7.

[32] C. H. Yang et al. “Operation of a silicon quantum processor unit cell above one kelvin”. In: *Nature* 580.7803 (Apr. 2020), pp. 350–354. ISSN: 1476-4687. DOI: 10.1038/s41586-020-2171-6. URL: https://doi.org/10.1038/s41586-020-2171-6.

[33] J. M. Elzerman et al. “Single-shot read-out of an individual electron spin in a quantum dot”. In: *Nature* 430.6998 (July 2004), pp. 431–435. ISSN: 1476-4687. DOI: 10.1038/nature02693. URL: https://doi.org/10.1038/nature02693.

[34] W. Pauli. “Über den Zusammenhang des Abschlusses der Elektronengruppen im Atom mit der Komplexstruktur der Spektren”. In: *Zeitschrift für Physik* 31.1 (Feb. 1925), pp. 765–783. ISSN: 0044-3328. DOI: 10.1007/BF02980631. URL: https://doi.org/10.1007/BF02980631.

[35] K. Ono et al. “Current Rectification by Pauli Exclusion in a Weakly Coupled Double Quantum Dot System”. In: *Science* 297.5585 (2002), pp. 1313–1317. ISSN: 0036-8075. DOI: 10.1126/science.1070958. eprint: https://science.sciencemag.org/content/297/5585/1313.full.pdf. URL: https://science.sciencemag.org/content/297/5585/1313.

[36] R Maurand et al. “A CMOS silicon spin qubit”. In: *Nature Comm.* 7 (2016), p. 13575.

[37] A. Crippa et al. “Gate-reflectometry dispersive readout and coherent control of a spin qubit in silicon”. In: *Nature Communications* 10.1 (July 2019), p. 2776. ISSN: 2041-1723. DOI: 10.1038/s41467-019-10848-z. URL: https://doi.org/10.1038/s41467-019-10848-z.

[38] F. H. L. Koppens et al. “Driven coherent oscillations of a single electron spin in a quantum dot”. In: *Nature* 442.7104 (Aug. 2006), pp. 766–771. ISSN: 1476-4687. DOI: 10.1038/nature05065. URL: https://doi.org/10.1038/nature05065.

[39] K. C. Nowack et al. “Coherent Control of a Single Electron Spin with Electric Fields”. In: *Science* 318.5855 (2007), pp. 1430–1433. ISSN: 0036-8075. DOI: 10.1126/science.1148092. eprint: https://science.sciencemag.org/content/318/5855/1430.full.pdf. URL: https://science.sciencemag.org/content/318/5855/1430.

[40] R. Brunner et al. “Two-Qubit Gate of Combined Single-Spin Rotation and Interdot Spin Exchange in a Double Quantum Dot”. In: *Phys. Rev. Lett.* 107 (14 Sept. 2011), p. 146801. DOI: 10.1103/PhysRevLett.107.146801. URL: https://link.aps.org/doi/10.1103/PhysRevLett.107.146801.

[41] F. Qassemi, W. A. Coish, and F. K. Wilhelm. “Stationary and Transient Leakage Current in the Pauli Spin Blockade”. In: *Phys. Rev. Lett.* 102 (17 Apr. 2009), p. 176806. DOI: 10.1103/PhysRevLett.102.176806. URL: https://link.aps.org/doi/10.1103/PhysRevLett.102.176806.

[42] Roland Winkler. *Spin-orbit coupling effects in two-dimensional electron and hole systems*. Springer tracts in modern physics. Berlin: Springer, 2003. DOI: 10.1007/b13586.

[43] E. Rashba. “Properties of semiconductors with an extremum loop. I. Cyclotron and combinational Resonance in a magnetic field perpendicular to the plane of the loop”. In: *Sov. Phys.-Solid State* 2 (1960), p. 1109. URL: https://ci.nii.ac.jp/naid/10018760249/en/.

[44] G. Dresselhaus. “Spin-Orbit Coupling Effects in Zinc Blende Structures”. In: *Phys. Rev.* 100 (2 Oct. 1955), pp. 580–586. DOI: 10.1103/PhysRev.100.580. URL: https://link.aps.org/doi/10.1103/PhysRev.100.580.

[45] L. E. Golub and E. L. Ivchenko. “Spin splitting in symmetrical SiGe quantum wells”. In: *Phys. Rev. B* 69 (11 Mar. 2004), p. 115333. DOI: 10.1103/PhysRevB.69.115333. URL: https://link.aps.org/doi/10.1103/PhysRevB.69.115333.

[46] Tuomo Tanttu et al. “Controlling Spin-Orbit Interactions in Silicon Quantum Dots Using Magnetic Field Direction”. In: *Phys. Rev. X* 9 (2 May 2019), p. 021028. DOI: 10.1103/PhysRevX.9.021028. URL: https://link.aps.org/doi/10.1103/PhysRevX.9.021028.

[47] Xiaojie Hao et al. “Electron spin resonance and spin–valley physics in a silicon double quantum dot”. In: *Nature Communications* 5.1 (May 2014), p. 3860. ISSN: 2041-1723. DOI: 10.1038/ncomms4860. URL: https://doi.org/10.1038/ncomms4860.

[48] C. H. Yang et al. “Spin-valley lifetimes in a silicon quantum dot with tunable valley splitting”. In: *Nature Communications* 4.1 (June 2013), p. 2069. ISSN: 2041-1723. DOI: 10.1038/ncomms3069. URL: https://doi.org/10.1038/ncomms3069.

[49] M Pioro-Ladriere et al. “Electrically driven single-electron spin resonance in a slanting Zeeman field”. In: *Nature Phys.* 4.10 (2008), pp. 776–779.

[50] Yasuhiro Tokura et al. “Coherent Single Electron Spin Control in a Slanting Zeeman Field”. In: *Phys. Rev. Lett.* 96 (4 Jan. 2006), p. 047202. DOI: 10.1103/PhysRevLett.96.047202. URL: https://link.aps.org/doi/10.1103/PhysRevLett.96.047202.

[51] Alexander V. Khaetskii and Yuli V. Nazarov. “Spin-flip transitions between Zeeman sublevels in semiconductor quantum dots”. In: *Phys. Rev. B* 64 (12 Sept. 2001), p. 125316. DOI: 10.1103/PhysRevB.64.125316. URL: https://link.aps.org/doi/10.1103/PhysRevB.64.125316.

[52] Andrea Corna et al. “Electrically driven electron spin resonance mediated by spin–valley–orbit coupling in a silicon quantum dot”. In: *npj Quant. Inform.* 4.1 (2018), p. 6.

[53] Léo Bourdet and Yann-Michel Niquet. “All-electrical manipulation of silicon spin qubits with tunable spin-valley mixing”. In: *Phys. Rev. B* 97 (15 Apr. 2018), p. 155433. DOI: 10.1103/PhysRevB.97.155433. URL: https://link.aps.org/doi/10.1103/PhysRevB.97.155433.

[54] Will Gilbert et al. “On-demand electrical control of spin qubits”. In: *Nature Nanotechnology* (Jan. 2023). ISSN: 1748-3395. DOI: 10.1038/s41565-022-01280-4. URL: https://doi.org/10.1038/s41565-022-01280-4.

[55] Giordano Scappucci et al. “The germanium quantum information route”. In: *Nature Reviews Materials* (Dec. 2020). ISSN: 2058-8437. DOI: 10.1038/s41578-020-00262-z. URL: https://doi.org/10.1038/s41578-020-00262-z.

[56] Christoph Kloeffel, Marko J. Ran či ć, and Daniel Loss. “Direct Rashba spin-orbit interaction in Si and Ge nanowires with different growth directions”. In: *Phys. Rev. B* 97 (23 June 2018), p. 235422. DOI: 10.1103/PhysRevB.97.235422. URL: https://link.aps.org/doi/10.1103/PhysRevB.97.235422.

[57] Alessandro Crippa et al. “Electrical spin driving by g-matrix modulation in spin-orbit qubits”. In: *Phys. Rev. Lett.* 120.13 (2018), p. 137702.

[58] Jarryd J. Pla et al. “A single-atom electron spin qubit in silicon”. In: *Nature* 489.7417 (Sept. 2012), pp. 541–545. ISSN: 1476-4687. DOI: 10.1038/nature11449. URL: https://doi.org/10.1038/nature11449.

[59] M. Veldhorst et al. “A two-qubit logic gate in silicon”. In: *Nature* 526.7573 (Oct. 2015), pp. 410–414. ISSN: 1476-4687. DOI: 10.1038/nature15263. URL: https://doi.org/10.1038/nature15263.

[60] A. Aprà et al. “Physical and technological challenges towards silicon-based quantum computing”. In: *2021 Silicon Nanoelectronics Workshop (SNW)*. 2021, pp. 1–2. DOI: 10.1109/SNW51795.2021.00003.

[61] E. A. Laird et al. “Hyperfine-Mediated Gate-Driven Electron Spin Resonance”. In: *Phys. Rev. Lett.* 99 (24 Dec. 2007), p. 246601. DOI: 10.1103/PhysRevLett.99.246601. URL: https://link.aps.org/doi/10.1103/PhysRevLett.99.246601.

[62] M. Randus and K. Hoffmann. “A simple method for extreme impedances measurement - experimental testing”. In: *2008 72nd ARFTG Microwave Measurement Symposium* (2008), pp. 40–44.

[63] Gerasimos Vlachogiannakis et al. “An I/Q-mixer-steering interferometric technique for high-sensitivity measurement of extreme impedances”. In: *2015 IEEE MTT-S International Microwave Symposium*. 2015, pp. 1–4. DOI: 10.1109/MWSYM.2015.7166830.

[64] Silviu-Sorin Tuca et al. “Interferometer Scanning Microwave Microscopy: Performance Evaluation”. In: *IEEE Transactions on Nanotechnology* 16.6 (2017), pp. 991–998. DOI: 10.1109/TNANO.2017.2725383.

[65] M. G. House et al. “Radio frequency measurements of tunnel couplings and singlet–triplet spin states in Si:P quantum dots”. In: *Nature Communications* 6.1 (Nov. 2015), p. 8848. ISSN: 2041-1723. DOI: 10.1038/ncomms9848. URL: https://doi.org/10.1038/ncomms9848.

3

METHODS AND MATERIALS

The journey of a thousand miles begins with one step.

Lao-Tze

In this chapter I describe the experimental setup used during my thesis. The electronic setup is partially at room temperature and partially inside a ^{3}He homemade dilution refrigerator.
Particular attention is devoted to the the compact design of a noise filtering platform for the DC lines and its impact on the electronic temperature.
In the end I explain the main steps and the motivations behind the fabrication process of the devices made by CEA-Leti.

3.1. EXPERIMENTAL SETUP

The experimental setup mainly consists of a home made ^{3}He dry refrigerator (shown in Fig. 3.1) and all the instrumentation necessary for electric and dispersive measurements.
A dry, or cryogen-free, dilution refrigerator relies on a pulse tube (PT) for the primary cooling of the cryostat, in place of liquid nitrogen or liquid ^4He used in a so-called wet cryostat.
The primary cooling of the cryostat allows to reach $\simeq$ 3.5 K. At such a temperature the ^{3}He can start to condense and circulating in a close loop, allowing further cooling till $\simeq$ 300 mK.
Inside the cryostat we wired 24 DC lines and 6 AC lines (2 for reflectometry in-out and 4 for pulsing).
A superconducting single-axis magnet is anchored at the second stage of the pulse tube (at $\simeq 3.5K$) and the sample holder is in a cavity inside such a magnet, but thermally connected with the lowest stage of the cryostat. The magnetic field is always in the vertical direction of Fig. 3.1 and to control the relative position between the sample and the field orientation the only degree of freedom is to physically tilt the sample.
Alternatively 3-axis magnets are available on the market.

A schematic of the setup at the different stages of the cryostat is shown in Fig. 3.2. Through the years such a setup has been improved continuously. Here the last version of the setup is shown, used for the double charge-sensing experiment described in Chap. 6.
We use an ultra high frequency lock-in (UHF-LI) from Zurich Instruments for both the

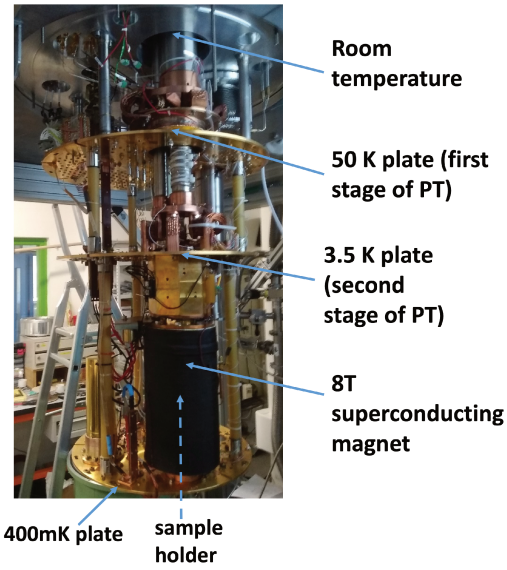

Figure 3.1: Picture of the homemade dry ^{3}He dilution fridge (named Tritonito). Each plate is at a different temperature and is thermally insulated from the others by thin wall stainless steel tubes or fiber glass tubes. The pulse tube (PT) used for the primary cooling of the cryostat is also separated in the first two thermally insulated temperature stages, allowing stronger cooling power in the second stage. Credits to Iulian Matei.

generation and the demodulation of the reflectometry tone. The printed circuit board (PCB), surrounded by a green dashed line in the setup scheme, is the one shown in Fig. 3.3 b), which allows frequency multiplexing for the reflectometry tone. This means that we are able to feed 4 resonators with a single RF tone carrying 4 different frequencies and then we can demodulate the reflected signals at 4 different frequencies with the UHF-LI. The SMP (Sub Miniature Push-on) connectors and the RF cabling indeed are quite invasive (see Fig. 3.3 b) and, while we cannot save any space for what concern the pulsing lines (4 in this case), it is crucial to save space at least on the readout lines.
The reflectometry tones are pass band filtered (PBF) at room temperature and attenuated at different stages of the fridge to suppress thermal noise, as explained in Sec. 3.3.3.
The reflectometry tones are then added with the DC signals using a bias-tee, i.e. a diplexer, mounted on a sample holder.
Such a bias-tee behaves as a low-pass filter from the DC side, where there is a resistor ($R = 300\ k\Omega$) and as a high-pass filter from the RF side, where there is a capacitor($C = 220$ pF). The cutoff frequency of the bias-tee can be calculated as $f_c = \frac{1}{2\pi RC}$. In general the value of the cutoff frequency at low temperature is higher than the one expected from the specs, because of the decreased value of the resistor at cryogenic temperatures.
The signal reflected by the device (RF out) is then separated from the incoming signals (RF in) using a directional coupler (Mini-circuits ZEDC-15-2B).
The signal is then amplified using a cryogenic amplifier from Low Noise Factory ($LNF - LNC0.2\_3A$), with a gain of $\simeq 32$ dB for a frequency range between 300 and 500 MHz. At this point the signal reflected by the resonator can be demodulated and analyzed using the UHFLI.

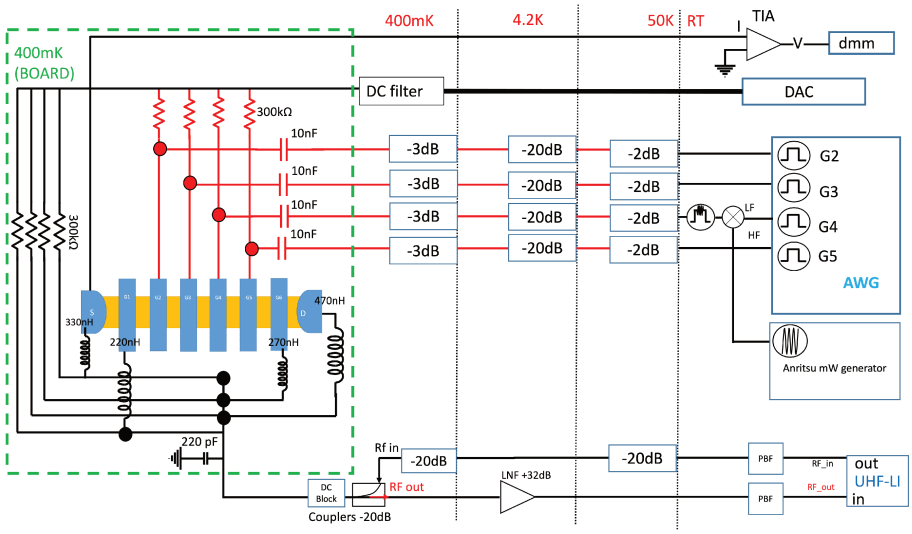

Figure 3.2: Schematic of the experimental setup from room temperature (right) to the sample (left). The electronics in the PCB is sourrounded by a green dashed line for clarity. RF lines used for pulsing are highlighted in red. All the DC lines are filtered and the AC lines attenuated. Each AC line is combined with a DC signal by a bias-tee.

An arbitrary waveform generator (AWG) is used to send pulses of different shapes and duration to the gates.
These pulses are crucial to move quickly between different charge states of the quantum dot and eventually we can sum them with a microwave signal (in the GHz range) to drive the spin of electrons or holes.
The pulses and microwave signals are combined using a diplexer (ZDSS-3G4G-S+), as shown for the G4 line.
The UHF-LI has an integrated AWG and this is practical because we can use the same UHF-LI also to trigger the microwave burst and, eventually, use the same trigger to turn on-off the reflectometry tone.
In an analogue manner to the RF tone also the pulses are attenuated and added with the DC voltages using bias-tees ($R = 300\ k\Omega$, $C = 10$ nF).

The DC voltages are generated at room temperature using a rack of low noise digital to analog converters (DAC) from iTest company (BE2142).
The DC lines are further low-pass filtered at the lowest stage of the cryostat using a series of low-pass filters, as it will be explained in detail in Sec. 3.3.2.
Finally current flowing through the device can be read from either source or drain. Such a current is amplified at room temperature, using a low noise transimpedance amplifier (TIA) with variable gain (Femto DLPCA-200), and converted into a voltage. The voltage signal can then be read using a digital multimeter (dmm) and reconverted into a current by knowing the gain of the amplifier, which is typically 10^8.
Eventually, the source/drain contact can be grounded if current measurement are no longer necessary.

3.2. SAMPLE PREPARATION

We receive our devices in a 300 mm wafer, composed of 298 dies with dimensions of $\simeq 13 \times 16 mm^2$, of which 48 are processed with electron beam lithography and are the ones of interest.
These dies are nominally identical and all the devices with one to four gates are tested in an automatic probe station (there are only 6 needles on our probe station).
From the room temperature characteristics we can guess which device is more suitable to be studied. Nevertheless, to have something more accurate than a guess, a low temperature screening would be necessary as for example using a cryogenic probe station (see Fig. 4.1).
We then cut the wafer in dices using a diamond pen. After doing a small cut, by applying a small pressure, the wafer breaks straight along the silicon crystalline axis.
After dicing we need to further cut the part where there is the sample of interest in order to fit it in the sample holder, where the space for the sample has an area of $5 \times 5 mm^2$.
The sample holder is a printed circuit board. In Fig. 3.3 a),b) we show the two PCB used respectively in the experiments described in Chap. 5 and in section 6.6 and the one used for the other experiments of chapter 6.

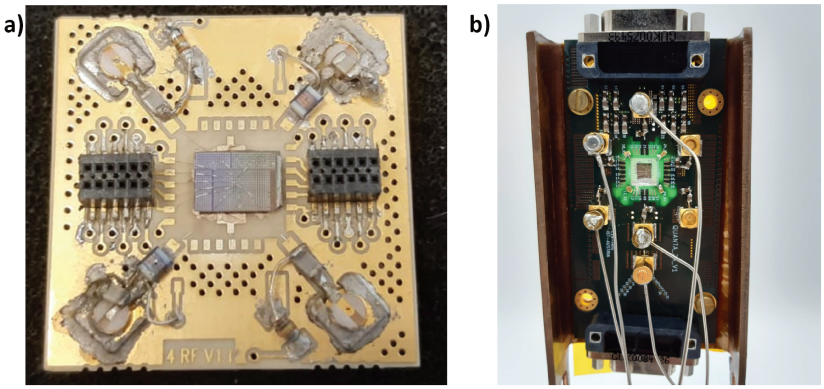

Figure 3.3: Two PCBs used respectively in the experiments of Chaps. 5, 6.6 and in 6. In a) there are two RF lines for reflectometry and two for pulsing (SMP connectors are in the four corners on the back of the PCB). In b) one reflectometry line (bottom connector) is split into four lines on the PCB, while the other four (out of six) RF lines are used for pulsing.

The main improvement of the new PCB is the possibility of multiplexing the rf lines, allowing 4 lines for reflectometry readout. The possibility of multiplexing the reflectometry lines without significant cross-talk is a fundamental step towards the scaling of this readout technique.

3.3. NOISE FILTERING

The most relevant noise sources are Flicker noise (often referred to as $1/f$ noise) and thermal noise.
The $1/f$ noise generally dominates at low frequencies and hence is the dominant noise source for DC voltages.
The thermal noise is instead dominant for AC voltages.

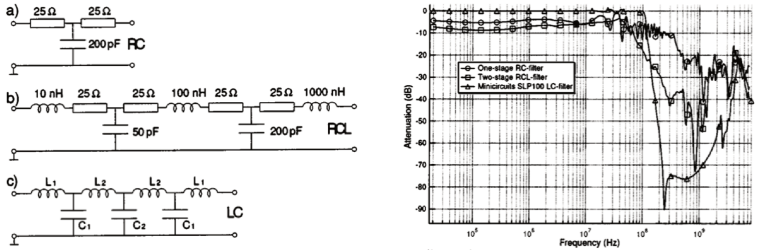

Figure 3.4: a) One-stage RC filter, b) two-stage RCL filter, and c) the Minicircuits 7 stage LC filter, also called π-filter. The attenuation as a function of frequency is measured at 4.2 K. From Ref. [1].

3

3.3.1. DC NOISE

Here it is described in detail a compact filter for 24 DC lines, placed in the coldest stage of the cryostat.
In principle the low frequency noise can be cut just by using low-pass filters stacked in series. However these filters re-open at high frequencies because of parasitic effects. An example of the typical behaviour of 3 different low-pass filters is shown in Fig. 3.4. Many strategies have been developed to cut high frequency noise, such as metal powder filters, relying on skin damping effect [2], thermo-coaxial filters[3], PCB based metal powder filters [4] and PCB filters based on lumped-elements.
The metal-powder filters rely on the fact that, because of skin damping effect, the resistance of the material increases with the signal frequency ($R \propto \sqrt{(\omega)}$) and the high frequency are therefore heavily attenuated.
We use lumped-element components mounted on a PCB. Stacking many low-pass filters together allows to attenuate the noise also in the re-opening window of the other filters.

The two main objectives that justify the development strategy of these cryogenic filters are the minimization of electrical noise and electronic temperature.
We realized two versions of the filters with dimensions a 86×63 mm^2 and 99×44mm^2. These dimensions could be further reduced, but a bigger space between the components helps to avoid ground loops and to reduce the heating due to the electrical signal passing through.

3.3.2. KIKASS FILTERS: PCB LAYOUT

Two differents PCBs have been designed in order to cover different frequencies range.
The idea is to stack the two PCBs together through a micro-D connector with male input and female output. However the two boards can also be used independently.
The only difference in the design of the two boards are the footprints for the soldering of different components.
The so-called KiKass RC board is designed to cut low frequencies, filtering a range between 100 kHz and 80 MHz. The KiKass RF board is instead designed to cut higher frequency noise.

The KiKass RC PCB makes use of a 7 stage pi-filter LFCN 80+ with a cutoff frequency of 80 MHz and 2 RC filter.
The RC filter mounted on the central part of the board are realized with C = 2.2 nF and R = 500 Ω, giving a cutoff frequency of f_c=144 kHz.
The last RC filters are instead realized with C=1 nF and R=1.2 kΩ, giving a cutoff frequency

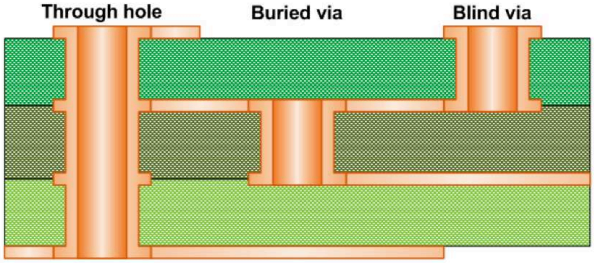

Figure 3.5: Schematics of a 4 copper layer PCB with different type of vias. We used blind vias for interconnection between components. The through hole vias are plated and are used to share a solid ground between different layers and to avoid thermal gradient between the different layers of the board.

of f_c=132 kHz. The re-opening of the filter due to parasitic effect is dominated by the capacitors. The choice of two close cutoff frequency values with different combination of the components values ensure that re-opening of one of the two filters for a certain frequency will be compensated by the attenuation of the other filter.
The KiKass RF PCB makes use of three 7 stages pi-filter with cutoff frequencies of respectively 80 MHz, 1.45 GHz, 5 GHz.
The components used have been previously tested at 4 K and they still offer performances close to their specs at room temperature. In the following tab we list the names of these components.

type of component	KiKass RC
π-filter (f_c = 80 MHz)	LFCN 80+
R (500 Ω)	RR05P499KDCT-ND
R (1.2 $k\Omega$)	RR05P1.2KDCT-ND
C (2.2 nF)	C1206C222J5GAC AUTO
C (1 nF)	C1206C102J5GAC AUTO

KiKass RF	π-filters (f_c)
LFCN 80+	80 MHz
LFCN 1450+	1.45 GHz
LFCN 5000+	5 GHz

These components are selected based on their small size, availability, and performance at extremely low temperatures.
We opted for a 4 copper layers design, as schematized in Fig. 3.5.
The space between different layers is filled with FR4, an electrical insulator.
The conducting layers are plated with electroless nickel, covered by a thin layer of gold, which protects the nickel from oxidation. This technique is widely used in PCBs manifacturing (Electroless nickel immersion gold, or ENIG).
The surface-mounted components are placed on the external layers. In particular, 12 DC lines are in the front layer (label F1-F12) and 12 are in the bottom one (label F13-F24). A top view of the two boards is shown in Fig. 3.6.
The connections between components belonging to the same line are realized through blind vias, i.e. vias that pass through an inner layer and go back to the outer one only for the connection with the next component (see Fig. 3.5). This provides a better thermalization of the electrons and shielding from electromagnetic interferences.
A good thermalization of the inner layers is also favoured by many through hole vias. Also these vias are plated with ENIG, favouring a better thermalization of the inner layers. The other aim of these vias is to provide a strong common ground for all the layers.
We decided to not use any solder mask (usually green layer on top of the PCB) on our boards. These masks are just an help for the manual soldering but prevent the ground

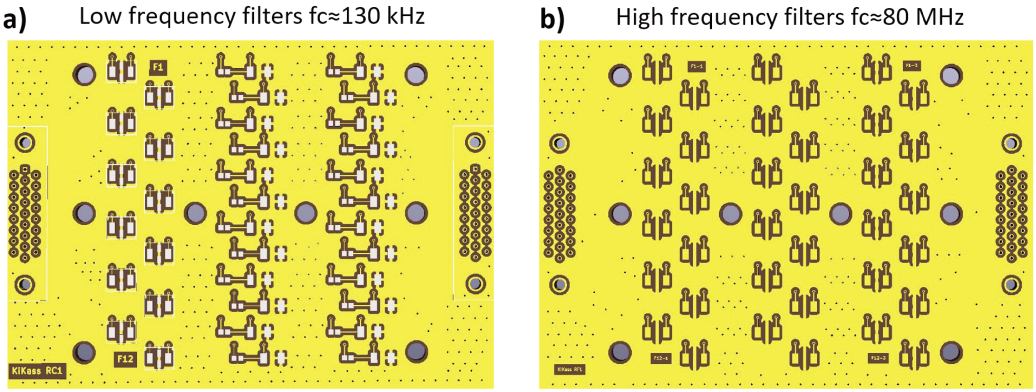

Figure 3.6: a) KiKass RC board, designed to filter low frequency noise; b) KiKass RF board, for high frequency noise. The connections between the components are in the inner layer of the board. The labels for the lines F1-1, F12-1 indicates the input side of the board. There are other 12 lines on the other side of the board.

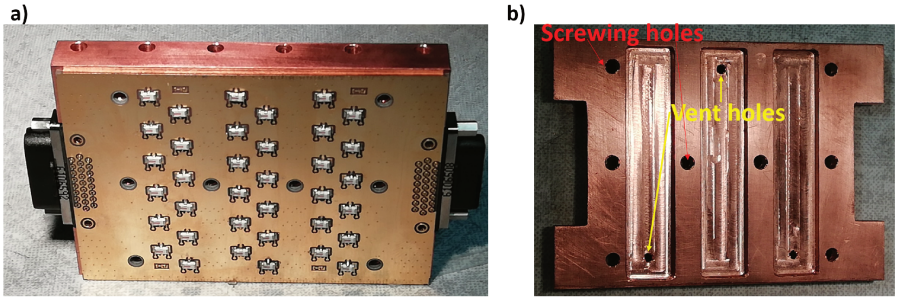

Figure 3.7: a) Bottom side of the board with the metal cage around. b) Inner side of the board cage. The big holes are for screwing the cage and the board together. A small vent hole in each groove allows vacuum to enter inside the cage, and is also helpful for the cooling of the board.

plane to be exposed and hence to thermalize.

Moreover a metal enclosure can be mounted on top of the PCB.
It is a Faraday cage and provides shielding from electromagnetic interferences.
Eventually it can be done with highly conductive gold-plated copper, providing a further aid for an efficient cooling of the PCB.
This cage can be directly screwed on the mounting holes of the board, providing a solid thermal contact (Fig. 3.7).
In the inner part of the cage three small grooves are necessary to reserve few mm of space, corresponding the components height. Also a small vent holes is present in each groove, in order to help vacuum to enter the and to cool the board. Some lateral holes allows to attach the board enclosure directly to the lowest temperature plate of the fridge, again to help the thermalization.

Finally it is also important to pay attention to the wiring of the lines carrying the DC signals to the filters. A useful trick to further reduce the DC voltage noise before the filters

is to use shielded twisted pair cables[5], i.e. two insulated loom of copper wires twisted together in a double spiral shape. One of the wire is used for transmitting the voltage and the other one as a ground reference. In this way some part of the noise signals is in the direction of data signals while the other parts are in the opposite directions. Thus the external waves cancel out due to the different twists. In this way a better immunity against noise is obtained.

3.3.3. THERMAL NOISE

At high temperature (more than 4K) the phonon temperature, is usually equal to the electronic temperature of the device under test.
When going down to low temperatures, around hundreds of mK, electrons and phonons are decoupled and the phonon temperature can be seen just as a lower bound for the electron temperature.
A proper cooling of the electron allows to reduce the thermal noise.
The thermal noise is essentially given by the blackbody radiation, that in one dimensional cables is known as Johnson–Nyquist noise.
The Planck's law provides the energy of a one-dimensional blackbody:

$$U(f,T) = \frac{hf}{e^{hf/k_B T} - 1} \tag{3.1}$$

Such an energy can be seen also as the noise power per unit of frequency (J=W/Hz), or power spectral density.
In the classical limit $hf \ll k_B T$ one recovers the original Johnson-Nyquist formula $U \simeq k_B T$.
In a coaxial cable connecting room temperature electronics to base temperature circuits, thermal photons propagate in both directions. To reduce the spectral density of thermal radiation a series of attenuators is installed at each stage of the cryostat.
Actually such a noise could be either filtered or attenuated. It has been shown that attenuators perform better than non attenuating filters regarding the performance of a superconducting qubit [6].

An attenuator effectively acts as a beam splitter. If for example we use an attenuator of $A_i = 20$ dB, i.e a factor 100 in power, the attenuator transmit $1/A_i$ of the incident signal and adds blackbody radiation on the rest of the signal $(1 - 1/A_i)$, with the energy given by the temperature at this stage $(U_i(T,f))$. Differently from the signal, the blackbody radiation propagates in both the directions.
The noise power density at a certain stage of the cryostat with attenuation i can therefore be expressed as

$$U_i = \frac{U_{i-1}}{A_i} + (1 - \frac{1}{A_i})U_i \tag{3.2}$$

where U_{i-1} is the noise power in the previous stage of the cryostat. The attenuation is expressed in terms of power ratio.
An important remark here is that for kHz frequency the approximation $U = k_B T$ holds well also for temperatures of few hundreds mK. When considering higher frequencies instead we should use the formula 3.1.

3.4. EFFECTIVE ELECTRONIC TEMPERATURE WITH DC FILTERS

We measured the electron temperature in a Bluefors dilution refrigerator, that can go down to 10 mK. We realized this measurement to evaluate the performances of the filters

described in the previous section.
In order to extract the electron temperature we consider a transition between a quantum dot and its nearby lead. The device we refer to here is the same p-type device used for the qubit described in Sec. 6.5.
The device has 4 gate ($G_{1,2,3,4}$) in series separated by 40 nm each. A big quantum dot is accumulated below gates G_3, G_4 in order to sense charge transition of the small dot accumulated below gate G_2. The sensor tuning procedure is explained in 6.1.
The transition is detected through an RF charge sensor on the reservoir, as it will be explained in Chap. 6. The transition used is shown in Fig. 3.8 a). The width of the transisition is given by the Fermi energy distribution of the holes in the lead[7][8][9].

$$f(\epsilon) = \frac{1}{1 + e^{-\frac{\epsilon}{k_B T}}} \tag{3.3}$$

The experimental data and their fits (black solid lines) for 3 different temperatures (using eq. 3.3) are shown in Fig. 3.8 b). In order to realize these fits we first have to measure the lever-arm parameter along the dot-lead direction ϵ. By assuming that at the highest temperature measured (650 mK) the electronic temperature is equal to the mixing chamber (MC) temperature, the lever-arm can be extracted by fitting the charge signal with the Fermi function 3.3. We can use the lever-arm found, i.e. $\alpha = 0.38 \pm 0.1 eV/V$, to fit the same curves at lower temperature.

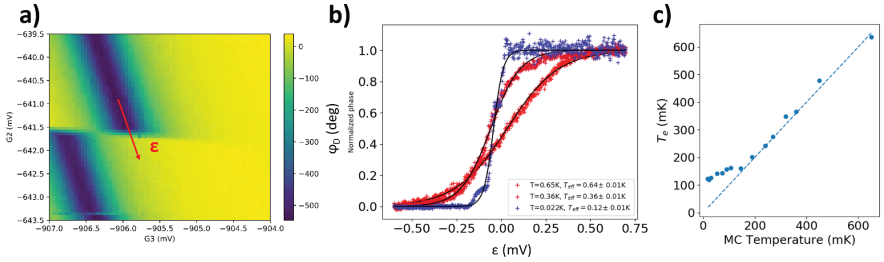

Figure 3.8: a) Charge sensor signal corresponding to a transition between a big quantum dot, accumulated below gate 3 and 4, and its lead. The signal is measured through an RF charge sensor on the drain and is sensitive to charge shift in the dot accumulated below gate G_2. The red arrow indicates the direction of the dot-lead axis ϵ. b) Normalized phase corresponding to the same transition at different temperatures. Black lines fit the data with a Fermi function. c) Electron temperature measured in correspondence of the mixing chamber (MC) temperature.

The values of the effective temperature extracted from the fit are plotted together with the temperature of the mixing chamber (Fig. 3.8 c)).
We can observe that below 150 mK the electronic temperature starts to be decoupled from the temperature of the phonons.
Many of the experiment described in this thesis are performed in a ^{3}He refrigerator, whose base temperature is between 350 and 450 mK. At the wiring and filtering level there is not a huge different between the setup of Fig. 3.2 and the one used for the experiment of Fig. 3.8. Therefore for many experiments, when not explicitly stated, we'll assume that the electronic temperature is the same as the fridge temperature.

3.5. DEVICE FABRICATION

In this section it is described the detailed process flow that leads to our quantum dot devices. It is worth to remark that the details reported here are specific for the device described in Chap. 5, and few steps of the fabrication might slightly change for other kind of devices. Nevertheless the main step of the process are always essentially the same.
Our quantum dot devices are fabricated on 300 mm silicon-on insulator (SOI) wafers, adapted from a commercial fully-depleted SOI (FDSOI) transistor technology [10]. A fully depleted SOI MOSFET has a very thin top silicon layer, in this way the channel is completely depleted from the majority carriers. Since the SOI layer is much smaller than the depletion width of the device its potential is tightly controlled by the gate. Starting

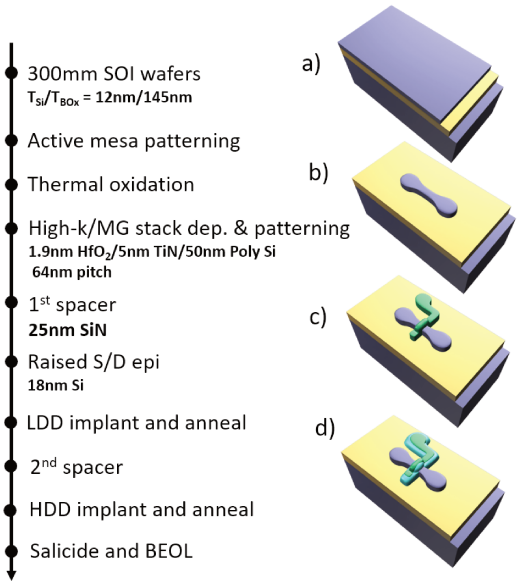

Figure 3.9: Left: Summary of the fabrication process. Right: Visual representation of the main step of the process flow from top to bottom: a) starting from silicon (blue) on top of SiO_2 yellow). b) The silicon layer is etched, leaving only the active silicon channel (mesa patterning). c) The metal gate (green) is created on top of the undoped Si channel. d) First spacers (light blue) are deposited, in order to protect Si channel from ion implantation.

with a blank SOI wafer (Fig. 3.9 a)) (12 nm Si / 145 nm SiO_2), the active mesa patterning is performed in order to define a thin, undoped nanowire via a combination of deep-ultra-violet (DUV) lithography and etching (Fig. 3.9 b)).
With the current mask set the channel width can be varied between 80 and 120 nm. However, these dimensions can be further reduced using a step of resist trimming prior to silicon etch.
Then, a 6 nm thick SiO_2 gate oxide is grown via thermal oxidation. Typically this process consumes roughly 3 nm of Si, and after the thickness of the silicon nanowire is around 10 nm.
To define the metal gate, a 5 nm thick layer of TiN followed by 50 nm of n-doped polysilicon is deposited (Fig. 3.9 c)).
Then, 25-nm thick Si_3N_4 spacers between gates and source/drain(S/D) regions are formed

(Fig. 3.9 d). The spacers are crucial to protect the undoped channel from the ion implantation.
In standard devices, spacers are relatively small (≃ 10 nm) so that the junctions lie at the edge of the gate or slightly overlap it (with a compromise to find to avoid "short-channel" effects). For our purposes, we make them much larger than usual to offset the position of the charge reservoirs and define tunnel barriers between dot and reservoirs [11]. Indeed wide spacers allows better gate-defined quantum dot confinement, since a thin and undoped SOI region separates the dot from the reservoirs.
Afterwards, raised S/D contacts are regrown to 18 nm to reduce access resistances.

Then, to obtain low access resistances, S/D are doped in two steps: first with lightly-doped drain (LDD) implant (using As at moderate doping conditions) and consecutive annealing to activate dopants, and then with highly-doped drain (HDD) implant (As and P at heavy doping conditions). In between LDD and HDD an additionnal spacer is deposited to offset them and create some kind of dopant concentration gradient from S/D to channel (in microelectronics, this limits hot carrier effects).
It is worth to remark here that p-type dopants (Boron in our case) usually diffuse more than n-type dopants, reducing the mobility close to the reservoir contacts, as it will be shown in Sec. 4.9.
The gate and lead contact surfaces are then metalized to form NiPtSi (salicidation). In this way the contacts are ready to be connected to the bonding pads on the external part of the wafer.
These interconnections to bonding pads, are made using a standard copper based back-end-of-line process (done by ST microelectronics). In this process the device is also encapsulated in a protective glass of SiO_2 and SiN.
The device in the end is buried 2-3 μm below the wafer surface.

Furthermore, this technology can be extended to realize multi-gate devices, with N gates in series or 2×N arrays with the gates on the opposite sides of the silicon channel [12][13][10][14]. The gate patterning can be done by etching the gates using electronic beam litography (EBL). For example a long gate of $L_g = 280$ nm can be cut in 4 gate of 40 nm, with 40 nm spacing in between each of them.
These linear an bilinear arrays of gates (or even 3-d structures in the future) may allow to develop quantum dot based quantum computing platforms of increasing complexity.

BIBLIOGRAPHY

[1] K. Bladh et al. “Comparison of cryogenic filters for use in single electronics experiments”. In: *Review of Scientific Instruments* 74.3 (2003), pp. 1323–1327. DOI: 10.1063/1.1540721. eprint: https://doi.org/10.1063/1.1540721. URL: https://doi.org/10.1063/1.1540721.

[2] John M. Martinis, Michel H. Devoret, and John Clarke. “Experimental tests for the quantum behavior of a macroscopic degree of freedom: The phase difference across a Josephson junction”. In: *Phys. Rev. B* 35 (10 Apr. 1987), pp. 4682–4698. DOI: 10.1103/PhysRevB.35.4682. URL: https://link.aps.org/doi/10.1103/PhysRevB.35.4682.

[3] A. B. Zorin. “The thermocoax cable as the microwave frequency filter for single electron circuits”. In: *Review of Scientific Instruments* 66.8 (1995), pp. 4296–4300. DOI: 10.1063/1.1145385. eprint: https://doi.org/10.1063/1.1145385. URL: https://doi.org/10.1063/1.1145385.

[4] Filipp Mueller et al. “Printed circuit board metal powder filters for low electron temperatures”. In: *Review of Scientific Instruments* 84.4 (2013), p. 044706. DOI: 10.1063/1.4802875. eprint: https://doi.org/10.1063/1.4802875. URL: https://doi.org/10.1063/1.4802875.

[5] Montana Instruments. *User Guides: wiring for cryostat*. URL: https://www.montanainstruments.com/library/files/Wiring-10-Things-to-Know.pdf.

[6] S. Krinner et al. “Engineering cryogenic setups for 100-qubit scale superconducting circuit systems”. In: *EPJ Quantum Technology* 6.1 (May 2019), p. 2. ISSN: 2196-0763. DOI: 10.1140/epjqt/s40507-019-0072-0. URL: https://doi.org/10.1140/epjqt/s40507-019-0072-0.

[7] D. Maradan et al. “GaAs Quantum Dot Thermometry Using Direct Transport and Charge Sensing”. In: *Journal of Low Temperature Physics* 175.5 (June 2014), pp. 784–798. ISSN: 1573-7357. DOI: 10.1007/s10909-014-1169-6. URL: https://doi.org/10.1007/s10909-014-1169-6.

[8] S. Gasparinetti et al. “Nongalvanic thermometry for ultracold two-dimensional electron domains”. In: *Applied Physics Letters* 100.25 (2012), p. 253502. DOI: 10.1063/1.4729388. eprint: https://doi.org/10.1063/1.4729388. URL: https://doi.org/10.1063/1.4729388.

[9] A. Mavalankar et al. “A non-invasive electron thermometer based on charge sensing of a quantum dot”. In: *Applied Physics Letters* 103.13 (2013), p. 133116. DOI: 10.1063/1.4823703. eprint: https://doi.org/10.1063/1.4823703. URL: https://doi.org/10.1063/1.4823703.

[10] S. De Franceschi et al. “SOI technology for quantum information processing”. In: Dec. 2016, pp. 13.4.1–13.4.4. DOI: 10.1109/IEDM.2016.7838409.

[11] M. Hofheinz et al. “Simple and controlled single electron transistor based on doping modulation in silicon nanowires”. In: *Applied Physics Letters* 89.14 (2006), p. 143504. DOI: 10.1063/1.2358812. eprint: https://doi.org/10.1063/1.2358812. URL: https://doi.org/10.1063/1.2358812.

[12] Fabio Ansaloni et al. “Single-electron operations in a foundry-fabricated array of quantum dots”. In: *Nature Communications* 11.1 (Dec. 2020), p. 6399. ISSN: 2041-1723. DOI: 10.1038/s41467-020-20280-3. URL: https://doi.org/10.1038/s41467-020-20280-3.

[13] Emmanuel Chanrion et al. “Charge Detection in an Array of CMOS Quantum Dots”. In: *Phys. Rev. Applied* 14 (2 Aug. 2020), p. 024066. DOI: 10.1103/PhysRevApplied.14.024066. URL: https://link.aps.org/doi/10.1103/PhysRevApplied.14.024066.

[14] A. Aprà et al. “Dispersive vs charge-sensing readout for linear quantum registers”. In: *2020 IEEE International Electron Devices Meeting (IEDM)*. 2020, pp. 38.4.1–38.4.4. DOI: 10.1109/IEDM13553.2020.9372090.

4

QD CHARACTERIZATION FROM ROOM TEMPERATURE TO 4K

The only true wisdom is in knowing you know nothing

Socrates

In this chapter I discuss the problem of a systematic characterization and benchmarking of qubit devices, focusing on some extraction methods for a fast and systematic evaluation of the QD properties. Furthermore I will present a study of the gate dependent mobility in a five-gate device, demonstrating that the more a gate is far away from source/drain contacts the better is its mobility. This justifies the experimental strategy of the following chapters of working with QDs as isolated as possible from the reservoirs.

4.1. A SYSTEMATIC CHARACTERIZATION OF QUANTUM DOT DEVICES

In the first part of this chapter I discuss the problem of performing QD measurements over a large number of samples using a fast and systematic approach.
The procedures we are going to describe can help acquiring statistical information on the QD electronic properties, as well as identifying just QDs having the lowest amount of charge traps, dopants or any other kind of defects.
I show also how to obtain information about the size and the energy-level spacing of a QD.
Systematic measurements of 300 mm wafers are a common routine in semiconductor industry, where automated probe station are available since a long time. Instead only recently the Finnish company Bluefors has developed an automated probe station for cryogenic measurements (Fig. 4.1) of a 300 mm wafer, reaching temperatures down to 2 K.
In fact, even though commercial cryogenic probe station were available even before, they weren't designed to measure 300 mm wafers.
The work described in the following has been part of my internship at CEA-LETI. Although the measurements of this chapter are performed in a liquid helium dewar, they serve as a test bench to guide the development of systematic procedures for wafer-scale characterization at low temperature in the Blufors probe station.

Figure 4.1: Cryogenic probe station designed for measurements of 300 mm wafers.

4.2. ROOM TEMPERATURE CHARACTERIZATION AND COMPARISON WITH LOW TEMPERATURE PROPERTIES AT HIGH BIAS

We first discuss the useful transistor parameters that are used by the microelectronics industry in order to quantify the device performance.
Normally industries target high mobility and large I_{ON}/I_{OFF} ratio.
This allows to operate at low gate voltage V_G, and therefore to decrease power consumption and to mitigate self-heating issues.
For quantum dot devices instead these problems are not relevant yet. We are interested in evaluating the reproducibility of the fabrication process, as well as defining the properties that defines a good QD.

We also want to compare the device properties at low temperature and at room temperature. As we will see in Sec. 4.9 the analysis of the mobility as a function of temperature allows to determine the concentration of neutral defects, which might eventually have a negative impact at the level of the spin qubit coherence time.

In the first part of this chapter we study single gate CMOS-like device, where, as explained in Sec. 3.5, the long spacer that separates the gate from the reservoirs allows local confinement of charges at low temperatures.
At room temperature the QD device behaves as a standard transistor, while at low temperature a similar behaviour is restored only when the bias applied is much bigger than the addition energy ($eV_{ds} \gg E_{add} \simeq 1-10$ meV). We then compare the $I(V_G)$ characteristics at low and room temperature by keeping fixed $V_{ds} = 50$ mV.

I first define the main parameters we want to measure:

- Threshold voltage V_{th}: it tell us the minimum V_G needed to create a conducting path between the source and drain terminals. It is worth to remark that there are many different extraction techniques for this value, e.g. using eq. 4.4 or 4.8. The definition of this parameter is not unique, and its value will be slightly different depending on the extraction method.

- Subthreshold swing SS, measured in mV/dec. A dec (decade) corresponds to a 10 times increase of the current I, and the SS is the required increase in V_G to increase

the current by a factor of 10.
In the subthreshold region, the drain current has an exponential dependence on gate voltage, reflecting a thermally activated carrier concentration [1]. The $I(V_G)$ relation can be expressed as $I \propto e^{\frac{eV_G}{nk_BT}}$ where e is the elementary charge, k_B is the Boltzmann's constant, V_G the gate voltage applied, and n is the subthreshold ideality factor. Then the expression of SS can be obtained by taking the derivative of V_G with respect to log I:

$$SS(T) = n\frac{dV_G}{dlog(I)} = n\left(\frac{k_BT}{e}\right)ln10 \tag{4.1}$$

At room temperature the ideal value of the SS (for n=1) is expected to be approximately 60 mV/dec.
However, given the complexity of the fabrication, a transistor is very likely to contain various kinds of defects resulting from interface traps, residual impurities, strain, charges in the oxide, surface roughness etc.
Despite the existence of different types of disorder, the interface traps density is the main parameter used to quantify the degradation of SS for FD-SOI transistors. The interface traps distributed on the Si/SiO_2 interface generate an additional parasitic capacitance C_{IT}, connected in series with the silicon oxide capacitance C_{OX}. Moreover, the depletion capacitance C_D [2], connected in series with C_{OX} should also be taken into account.
The ideality factor n quantifies the impact of these additional capacitances over the transport and can be expressed as [3]:

$$n = 1 + \frac{C_{IT} + C_D}{C_{OX}} \tag{4.2}$$

- I_{on} can be defined as the current at $V_G = V_{th} + 500$ mV.
- I_{off} can be defined as the current at $V_G = V_{th} - 500$ mV.
- The device resistance can be calculated in strong inversion ($V_G \gg V_{th}$) simply with the Ohm's law: $R = V_{ds}/I_{on}$.

Here V_{th} is evaluated by taking the tangent of the $I(V_G)$ curve where its slope is maximized, and then taking the intercept with the V_G axis as V_{th}, as shown by the dashed lines of Fig. 4.2.

For bias $V_{ds} \gg E_{add}$ our QD devices behave standard transistors and we can compare the same parameters at room temperature and at low temperature.
In Fig. 4.2 it is shown the comparison between the room temperature $I(V_G)$ curve and the one measured at 4 K (both with V_{ds} = 50 mV), for a device with channel width W=70 nm and gate length L_g= 50 nm.
From the two $I(V_G)$ curves we measured the threshold voltage V_{th}, which increases from 70 to 480 mV at 4.2 K. An increase of V_{th} at low temperature can be understood thinking that many charges are frozen in the impurities present in the channel and higher V_G is needed to open the conductive channel.
A model to calculate analytically V_{th}, taking in account both freezeout and field-assisted ionization in the Poisson-Boltzmann equation is presented in [4]. Electron scattering

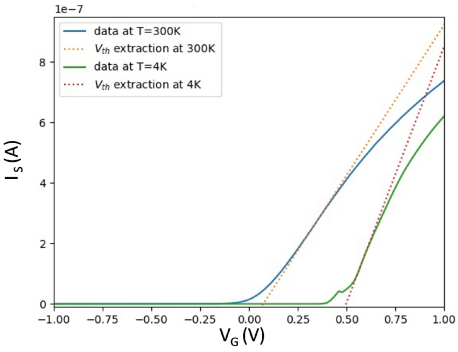

Figure 4.2: Comparison between the source current I_S measured at room temperature and in the helium bath. For both V_{ds} = 50 mV. The values of V_{th} are respectively 70 mV and 480 mV.

in the channel is reduced at low temperature, as a consequence the channel resistance decreases, varying from 108 kΩ at room temperature to 84 kΩ at 4.2 K.
For what concerns the subthreshold swing we measured a value of 173 mV/dec at room temperature, and 96 mV/dec at 4.2 K. As expected the $I(V_G)$ curve is steeper at low temperature [5], and hence the SS is lower. The main factor affecting this parameter is the temperature-dependent occupation of interface charge traps.

4.3. COULOMB-DIAMOND ANALYSIS METHODS

In the previous section we used a high bias $V_{ds} \gg E_{add}$. By studying the behaviour of the device at lower bias (V_{ds}łE$_{add}$), as explained in Sec. 2.2, we can measure the energy-level spacing of the dot, as well as its size and the gate lever-arm parameter α.
We could extract the addition energy and the gates and reservoir lever-arm through an analysis of Coulomb diamonds, using formulas 2.6. The main problem is that an accurate measurement of many Coulomb diamonds can be extremely time consuming.
The measurement of the Coulomb peak position in gate voltage $V_G^{(i)}$ is trivial and the problem is reduced to extract either $E_{add}^{(i)}$ or $\alpha^{(i)}$ for each electronic configuration.
I developed three analysis methods with the goal to reduce as much as possible the measurement time.

- **Coulomb peak analysis at zero bias**: This method is based on the assumption that the broadening of the Coulomb peaks is dominated by temperature ($k_B T \gg \hbar\Gamma$). It relies on fitting each Coulomb peak with eq. 2.8 or 2.9 to determine the filling-dependent lever-arm $\alpha^{(i)}$.
- **Diamond reconstruction method**: This method relies on finding the edges of the diamonds from a few $I(V_G)$ measurements at different source/drain bias voltages. A reconstruction of the diamond edges allows to measure directly the addition energy $E_{add}^{(i)}$ of each diamond, defined as the bias energy eV_{sd} such that the two edges intercept.
- **Line cut across the Coulomb valley** The diamond axis is defined by the minima of

the Coulomb oscillations (valley) at different bias. This method relies on finding the diamond axis from a few $I(V_G)$ measurements at finite source/drain bias voltage. A measurement of the current along a diamond axis, where transport is ruled by eq. 2.11, allows to determine $E_{add}^{(i)}$.

In the following I'll describe each method in detail, evaluating pro and cons of each of them.

4.4. COULOMB PEAK ANALYSIS AT ZERO BIAS

At 4.2K we are very likely in a regime where the tunnel coupling rates are negligible compared to temperature ($k_B T \gg \hbar\Gamma$). In this regime, the peak width is determined solely by temperature.
However we observed that the peak width in V_G increases with the number of electrons N in the QD. This is due to a V_G-dependent lever-arm.
Therefore by measuring the width of each peak we can obtain the lever-arm parameter $\alpha^{(i)}$, which is found to decrease with N.
In order to fit the peaks all together, we can rewrite one of the equations 2.8 or 2.9 as a sum of peaks, each one with its own amplitude $A^{(i)}$ and width $\sigma^{(i)} \propto \frac{\alpha^{(i)}}{\beta k_B T}$. We use the following fitting function:

$$\sum_{i=0}^{N} A^{(i)} cosh^{-2}\left(I(V_G) = \frac{\alpha^{(i)}(V_G^{(i)} - V_G)}{\beta k_B T}\right) \tag{4.3}$$

Where the parameter β takes the value 2.5 or 2 depending on whether the QD level spacing is smaller (classical limit of eq. 2.8) or larger (quantum limit of eq. 2.9) than $k_B T$, respectively.
With few considerations about the dot size and temperature, we can understand that we are always in the classical Coulomb blockade regime ($k_B T \gg \Delta_N$).

To appreciate the quantized level spacing of the dot its size must be such that its energy level spacing is bigger than the thermal broadening of the Fermi distribution of the reservoirs, i.e 3.5 $k_B T$. For a temperature of 4.2 K we have $3.5 k_B$T$\simeq$ 1.2 meV, and to appreciate the level spacing the corresponding dot diameter (using eq. 2.4) should be $\leq$ 20 nm, which is a realistic estimate when the dot is in the few-electron regime.
However, in these quantum dot devices we cannot observe the few-electron regime in transport. This is due to the fact that in the few-electron regime the tunnel rates through the barriers become too small, preventing measurable currents.
For the first observable transitions we can estimate the dot area from the spacing between adjacent peaks ΔV_G using eq. 2.2. We measured $\Delta V_G \simeq 10$ mV, which tells that the expected dot diameter is $\simeq$ 60 nm.
Assuming that the dot is a planar disc we can calculate the expected level spacing using eq. 2.4, which provides $\Delta_N \simeq 130$ μeV, smaller than the thermal energy.
In practice at a temperature of 4.2 K, considering the tunnel barrier and the size of the dot studied here, we are in the classical Coulomb blockade regime (eq. 2.8) for all the peaks observed and we can assume $\beta = 2.5$.

In order to fit N Coulomb peaks with eq. 4.3, in principle we need to fit 3N parameters, i.e. $(A^{(i)}, \alpha^{(i)}, V_G^{(i)})$ for $i = 1, ..., N$. The peak position $V_G^{(i)}$ can be easily measured as the maximum of each conductance peak and fed as input to the fitting function. Therefore

the fitting parameters are reduced to 2N.
The results obtained using this fitting function are plotted in Fig. 4.3.
Fig. 4.3 shows: a) linear conductance measured with applied voltage V_{ds} = 100 μeV, smaller than the thermal energy at 4 K; b) gate lever-arm α extracted from the fit of each peak as a function of gate voltage; c) addition energy calculated as $E_{add}^{(i)} = \alpha_i (V_G^{(i+1)} - V_G^{(i)})$.

This method in principle is the fastest one, since it requires only a single, high resolution measurement of the linear conductance as a function of gate voltage.
Moreover on other devices, with smaller dots and/or tunnel barriers, it would be possible to observe the few-electron regime, where eventually only one energy level contributes to transport. In this case the fitting model should take into account a transition between quantum ($\beta = 2$) and classical ($\beta = 2.5$) Coulomb blockade regime when increasing V_G.
Another drawback of this method is that the model may fail for very high electron filling, because when $h\Gamma \gg k_B T$ the weak coupling model fails.
A possible generalization of this method could be to use a self-adapting fit function, able to analyze each peak and to choose the model (weak coupling classical or quantum, or coherent regime) that minimizes the standard deviation of the fit.

4.5. DIAMOND RECONSTRUCTION METHOD

In this section I describe a technique to reconstruct the position of the edges of the Coulomb diamonds.
This method relies on extracting numerically the transconductance dI/dV_G. The position of a diamond edge can be defined as the one where dI/dV_G has a maximum or a minimum.
A measurement of the signal in current and its derivative for different source-drain bias voltages is shown in Fig. 4.4 a), b).
A Coulomb peak generically identifies a region where the charge oscillates between N and $N+1$, and it lies between two blockaded region with a fixed charge of N (on its left) and $N+1$ electrons (on its right).
The vertical dashed lines in Fig. 4.4 identify the edges of a single-electron transport region corresponding to the $N \rightarrow N+1$ charge transition at $V_{ds} = 2.5$ mV.
Hence the left flank of a Coulomb peak would correspond to the right edge of the N electrons blockaded region, whereas its right flank corresponds to the left edge of the $N+1$ electrons blockaded region. From Fig. 4.4 a) we can observe that for increasing bias the single-electron transport regions broaden following the diamond edges, and from the extrema in dI/dV_G we can reconstruct the V_G position of the diamond edges, as shown in Fig. 4.4 b).
A few line cuts at different V_{ds} can be sufficient to reconstruct the the diamond edges through a linear fit of the points found. The V_{ds} values corresponding to the intercepts of these lines provide the addition energies.

An example of diamond reconstruction is shown in Fig. 4.5, for another sample with $L_g = 310$ nm, $W = 80$ nm. The results obtained for the same sample of Fig. 4.4 will be shown in Sec. 4.8, where the 3 methods are compared.
Figure 4.5 shows a comparison between the diamonds reconstructed from line cuts and the corresponding full measurement of current vs (V_G, V_{ds}).
This method, differently from the previously described one, keeps on working when a few mV source-drain bias voltage is applied, regardless of the type of conduction regime and

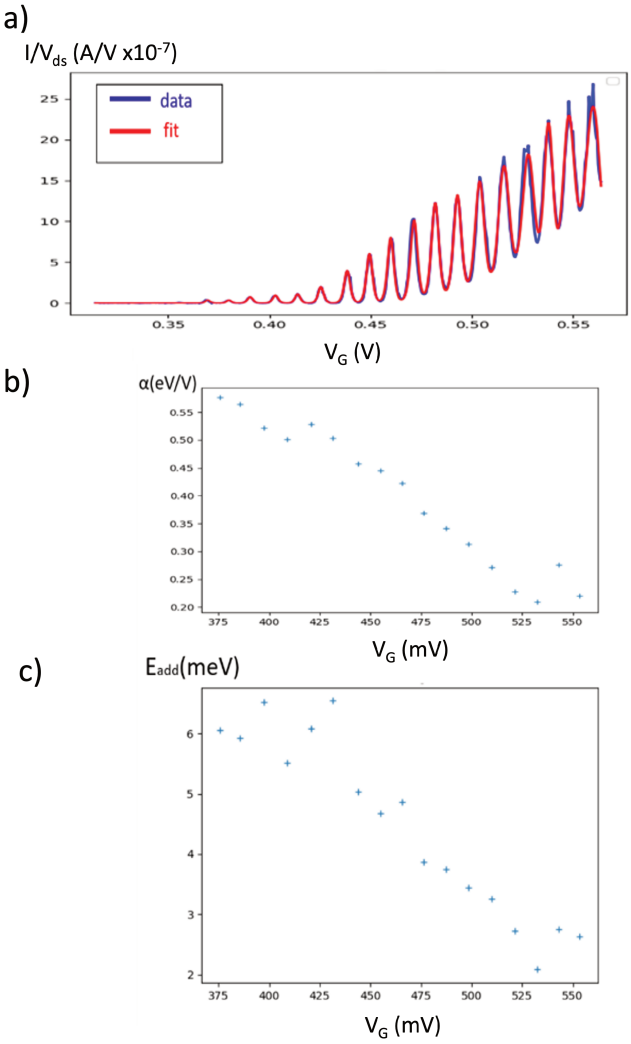

Figure 4.3: a) Linear conductance I/V_{ds} vs V_G. The experimental data are in blue, the fit in red. Here $V_{ds} = 100$ μeV, $\beta = 2.5$. b) Evolution of the gate lever-arm parameter α as a function of V_G. c) Addition energy as a function of gate voltage. The measurement of $\alpha^{(i)}$ allows to express the distance between two Coulomb peaks as an energy: $E_{add}^{(i)} = \alpha^{(i)}(V_G^{(i+1)} - V_G^{(i)})$.

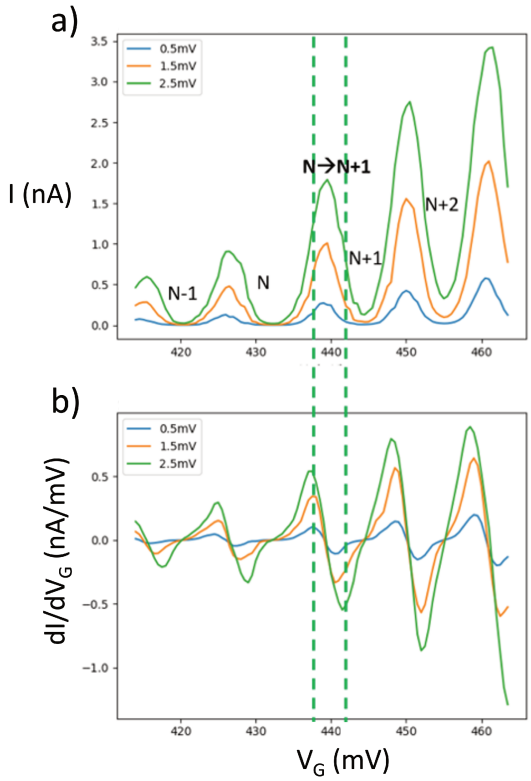

Figure 4.4: a) Measurement of current I as a function of gate votage, V_G for three different source-drain bias voltage (blue,orange,green), taken at V_{ds}=0.5, 1.5, 2.5 mV, respectively. b) Numerical derivative $\frac{dI}{dV_G}$ of the line cuts in a). The two vertical green dashed lines pinpoint the position of a maximum and a minimum in the $\frac{dI}{dV_G}$ trace at V_{ds} = 2.5 mV, identifying the V_G position of the diamond edge.

it is therefore more extensively applicable.
On the other hand, the code required for this data analysis is significantly more complex than the one employed in the previously described method, which involves a rather simple fit.

The differences in the slopes of the two diamond edges can be associated with an asymmetric capacitive coupling of the gate with the two reservoirs and/or to an asymmetric bias applied.
In the case studied here the bias is not symmetrically applied on the two contacts, but we bias on the drain and measure the current I_s on the source, and the I/V converter is connected to ground.
If we start with the dot electrochemical potential aligned with the source, after applying a bias ΔV_{ds} on the drain, the quantum dot electrochemical potential stays close to the source Fermi level, moving only slightly because of the drain-gate α_{G_D} and gate-source

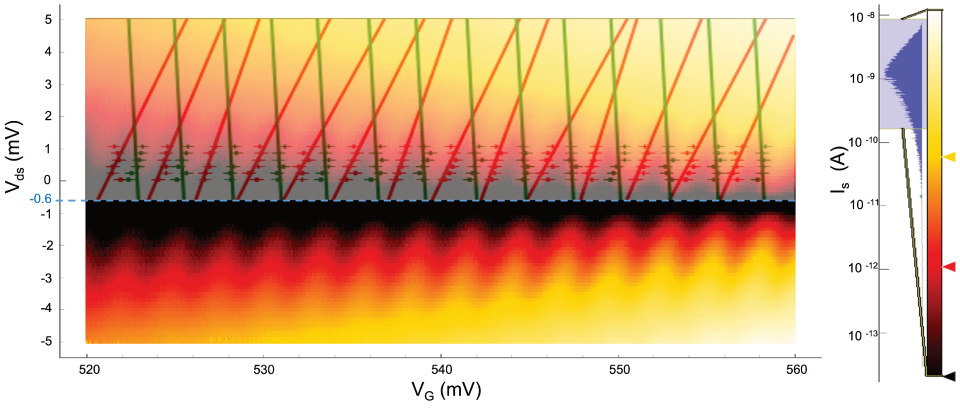

Figure 4.5: Reconstructed diamonds superimposed to a measurement. The current is plotted in a logarithmic color scale and it is saturated on purpose (black color for every current less than 0.2 nA) to help in visualizing the diamonds. For the reconstructed diamonds the bias axis is shifted by 0.6 mV, to compensate for the bias offset in the experimental measurement. Green points: measured edge positions for different bias voltages (maxima of dI/dV_G). Red points: measured edge position for different bias voltages (minima of dI/dV_G). Green and red lines: reconstructed edges.

cross coupling α_{G-S}, and a small gate voltage applied is sufficient to realign them. Conversely, starting with the dot electrochemical potential aligned with the drain, after applying ΔV_{ds}, to keep the dot aligned with the drain we should apply a gate voltage $e\Delta V_G = \alpha_{G-D}\Delta V_{ds}$, bigger than the previous case.
As a consequence the transition with the ohmic contact where the bias is not applied (source in this case) will be steeper in the $V_G - V_{ds}$ plane since, after a variation of the drain-source bias, a smaller gate voltage variation is sufficient to realign the electrochemical potential of the dot with the Fermi energy of the drain. Therefore we can relate the left edge (red lines in Fig. 4.5) of each diamond to a resonant dot-drain transition and the right one (green lines) to a resonant dot-source transition, as explained in the energy diagram of Fig. 2.4.
We note that the reconstruction works better for the less steep diamond edge (red one in Fig. 4.5). A symmetrical bias therefore would be beneficial when using this technique.

For each edge I impose two constraints in the reconstruction algorithm: on its slope and on its intercept with the V_G axis. The intercept with the $V_{ds} = 0$ axis must be in proximity (± 0.05 mV) of the peak position measured in the linear conductance regime (at $V_{ds} = 100$ μV), while the slope must be positive (negative) for the raising (lowering) edge of the diamond.

From the V_{ds} position of the intercepts of all consecutive pairs of diamond edges we can obtain the addition energies $E_{add}^{(i)}$ of each charge state i, together with the corresponding gate lever-arm: $\alpha^{(i)} = \frac{E_{add}}{\Delta V_G^{(i)}}$.

4.6. LINE CUT ACROSS THE COULOMB VALLEY

The first step of this method is to find the axis of each Coulomb diamond, namely the line connecting its two apexes. To do so we look for the V_G position of the conductance minimum at different bias. We make the reasonable assumption that the diamond axis lies close to the line connecting such minima (valley).
Here I define also V^*_{ds} as the projection of the diamond axis on the bias axis V_{ds}.
Based on the considerations about non linear transport made in Sec. 2.3.2, and more accurately in references [6][7][8], we can identify two main conductance regimes along the diamond axis:

1. $V_{ds} < E_{add}$ the current increases $\propto V^3_{ds}$.
2. $V_{ds} > E_{add}$ the current increases $\propto \Gamma_s \Gamma_d \, V_{ds}$.

We remark here that the assumptions above are based on an inelastic co-tunneling model, where $k_B T > \Delta_N$, and therefore multiple levels contributes to conductance and this explains why the current is not null inside the diamond.
If the coupling with the two reservoirs (and the biasing) had been symmetric, then the diamond axis would have been vertical as in Fig. 4.6 b). In this case only one measurement would have been sufficient to identify the V_G position of the diamond axis.
Some current vs V_G traces at different bias are shown in Fig. 4.6 c). We can observe that the position of the minima moves with bias, as schematized in Fig. 4.6 a). This is due to both the asymmetric coupling with the reservoirs and biasing.

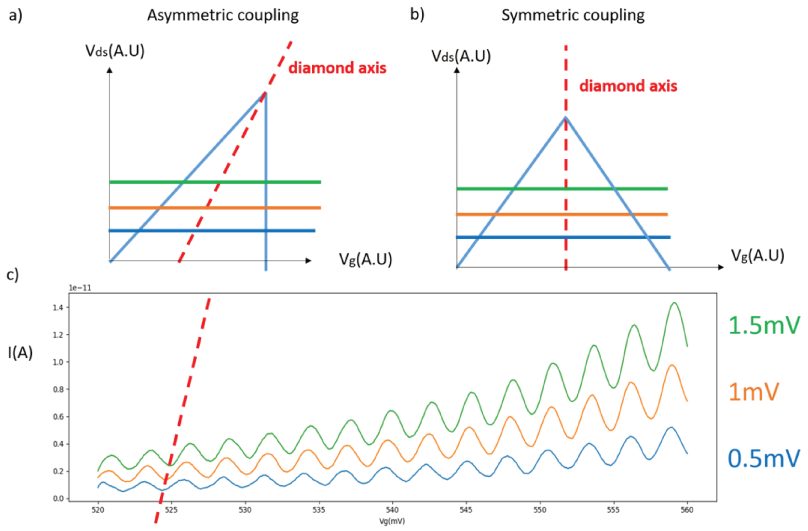

Figure 4.6: a) Asymmetric diamond, the diamond axis is defined by the V_G position of the minima of current. b) If coupling with reservoir and biasing had been symmetric, then the diamonds would be isosceles triangles, and their axis vertical. c) Current traces at different bias V_{ds} =0.5, 1, 1.5 mV for a device with L_g = 310 nm, W = 80 nm (same as Fig. 4.5). It can be observed that the position of minima and maxima moves with bias.

Looking at Fig. 4.7 we can observe that the $I(V^*_{ds})$ curve starts to increase linearly (in first

approximation) with V^*_{ds} after a certain threshold $V^*_{ds} > eE_{add}$, as it would happen across a resistor.

However, for high bias the current response is still slightly non linear and, depending on the nature of the coupling with the reservoirs, its slope might either increase ore decrease with V^*_{ds}. Therefore we cannot follow the same procedure used for the extraction of the threshold voltage, where the tangent is evaluated where the slope is maximized.
Instead the tangent should be taken in the region where the slope is constant (see green line of Fig. 4.7).
For the data shown we find $E_{add} = 2.5$ meV.
This method finds results comparable with the other two.

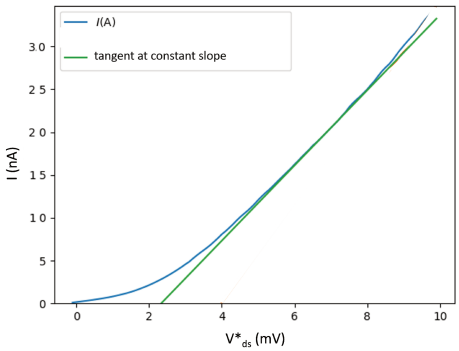

Figure 4.7: Blue: current signal along diamond axis. Green: tangent evaluated where the slope is constant, the intercept with the x-axis provides $E_{add} = 2.5$ meV.

4.7. SUMMARY OF THE 3 METHODS

Here we compare the results obtained on two similar samples, belonging to the same wafer, and with same channel width $W = 70$ nm and gate length $L_g = 50$ nm (Fig. 4.8 left) and $L_g = 60$ nm (Fig. 4.8 right).
In Fig. 4.8 we plot the values of the addition energies obtained with the three methods on these two devices.
I would like to make a few last observation about the characteristic measurement time, error sources and possible improvements for the three methods:

- *Fit of Coulomb peaks at zero bias*: this method relies on a single high resolution measurement and is the fastest one.
  Here we observed that the peaks were broadened by temperature ($k_B T \gg \hbar\Gamma$) and we were in the classical Coulomb blockade conduction regime ($k_B T \gg \Delta_N$). With different device geometries and/or temperatures, we may end up in a regime where the quantized level spacing becomes relevant ($k_B T \ll \Delta_N$) and we should use eq. 2.9 instead than 2.8. However, in both cases the linewidth of the Coulomb peak is determined by temperature.

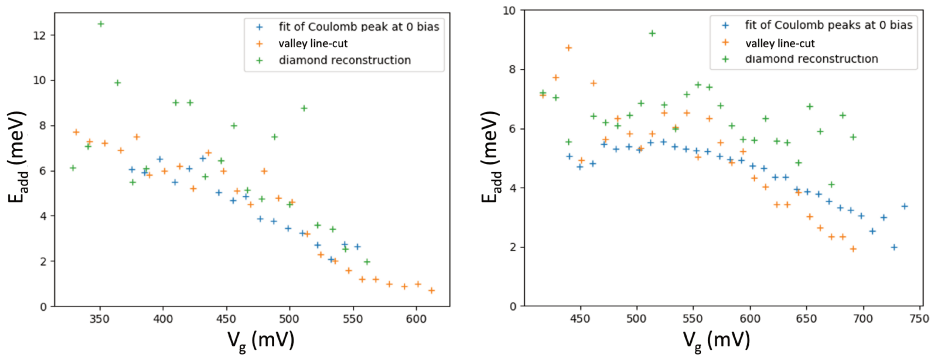

Figure 4.8: Values of the addition energies extracted with the three characterization techniques described in the main text and applied to two nominally identical samples. The V_G position of the points is respectively the position of the Coulomb peaks at ≃0 bias (blue crosses), at 2 mV (green crosses), and of the current minima (orange crosses).

With this method here we missed the first five Coulomb peaks that could instead be observed with higher source-drain bias.

- *Diamond reconstruction*: this method relies on 3-4 high resolution measurements at different source-drain bias voltages and it is therefore 3-4 times slower than the previous one.
  It is based on the only assumption that the current variation (i.e. the transconductance, dI/dV_G) is maximized at the edge of a Coulomb blockade region. This method is in principle the most versatile since, contrary to the previous one, it does not rely on the hypothesis of thermally broadened Coulomb blockade resonances. Despite this the results obtained with this method revealed a generally larger uncertainty as compared to the other methods.
  This can be understood considering that for a noisy signal the noise propagates dramatically in the derivative. Even though we smooth the experimental signal before extracting the numerical derivative, sometimes it is still possible to commit a small mistake in evaluating the edge position.
  We might expect to improve this method by measuring directly the transconductance dI/dV_G, for example by applying a small modulation on the gate voltage δV_G and then demodulating the signal with a low frequency lock-in.
  I tried also this last approach and I observed that the quality of the diamond reconstructed in this way was not remarkably better than the one obtained from the numerical derivative of the current signal.

- *Line cut across the Coulomb valley*: this technique is the slowest one, because it requires a measurement for each diamond. It would therefore be suitable only to study a small set of diamonds.
  Rather than extracting E_{add} from a linear extrapolation of the $I(V^*_{ds})$ characteristic in the high-voltage range, one could alternatively fit the low-voltage characteristic to the co-tunneling model of eq. 2.11.

Also a symmetric source-drain bias would be beneficial for this technique, as well as for the diamond reconstruction.

4.8. SUMMARY OF THE MEASUREMENT PROCEDURE

Here it is described the whole measurement protocol at high level, giving hints about how to possibly improve it.

1. In order to perform the peak analysis in a voltage range of interest we first need to know the position of the first detectable peak (FPP). An important remark is that the first peak we observe in current does not necessarily correspond to the first electron in our system. Usually a silicon quantum dot with only few electrons is still strongly decoupled from the reservoir and therefore, even if transport is energetically allowed, the current level is well below the detection limit. In order assess the number of electrons in the dot a charge sensor is necessary [9].
   However, implementing charge-sensing on large scale measurement over-complicate the problem and it is not the goal of this characterization.

   It is convenient to look for the first peak in current with high bias ($\simeq 5-10$ mV). For smaller bias indeed the current of the first observable peaks may be hidden in the noise. For example the first peak observed in the linear regime (Fig. 4.3 a)) is actually the 5-th transition that we are able to observe.
   Since we need to know only where to start the measurement, and not the precise peak position, this measurement can be performed quickly and with relatively low resolution (i.e 1 mV step in V_G).

2. The FPP can then be given as input parameter to decide the gate voltage range of interest for a fine resolution measurement near zero bias (linear regime).

3. The position of maxima and minima found near zero bias serve as input parameters for the measurement of E_{add}, via the "diamond reconstruction" and the "valley line cut" methods, respectively.
   In fact, the peak positions in current tell us where the diamond edges cross the V_G axis. Imposing these constraints significantly improves the linear fitting of the diamond edges. The positions of the current minima, on the other hand, provide the starting point of the valley line cuts.

Once we have measured the position of maxima and minima in the linear regime we can choose which method is more suitable for the analysis.
This choice is not trivial and, as discussed in the previous section, different methods may work better or worse, depending on voltage range of interest, temperature, material of the device and dot size.

4.8.1. FINAL REMARKS

In the first part of this chapter we discussed three techniques to characterize the properties of QDs. We tried to find a good trade-off between the precision of the measurements and their time consumption.

The diamond reconstruction method appears to suffer from a bigger error and the results are strongly dependent on the few bias voltages at which the $I(V_G)$ characteristics are taken. This technique may benefit from symmetric biasing, since I noticed that fitting uncertainty is significantly larger for steep diamond edges.

The "valley line cut method" instead seems to provide generally more reliable results, despite the fact that the extraction technique may be refined. Nevertheless it is the most time consuming, since it requires one line-trace measurement for each diamond.

Overall, fitting the Coulomb peaks in the linear regime (low bias) is the fastest method and provides reliable results. I would recommend this method for time-efficient massive characterizations. This method could be readily implemented on the 300-mm cryogenic probe station recently installed at Leti, which can perform wafer-scale characterizations down to 2 K. Going below 4 K might be counterproductive though, since we expect this model to work more accurately in the fully thermally broadened regime.

Finally, I would like to highlight that there is an ongoing research effort to combine machine learning approaches with measurements of semiconductor QDs [10][11][12] [13]. The increasing expertise and the publicly available machine learning based algorithm will surely be helpful in the near future for speeding up QD measurements, concerning both large scale and single device characterization.

4.9. CHARACTERIZATION AND LAMBERT-W FUNCTION BASED MODELING OF FDSOI FIVE-GATE QUBIT MOS DEVICES DOWN TO CRYOGENIC TEMPERATURES

In this section we characterize FD-SOI five-gate transistors down to 20 K[14][15].
In order to do so, we propose a model based on the Lambert $-W$ function. The validity of such a model is demonstrated down to low temperatures, fitting both the drain current and the Y-function and providing the dependence of subthreshold slope ideality factor, threshold voltage, low field mobility and access resistance with temperature.
Through this analysis we can highlight the different scattering contributions to the mobility and we conclude that the mobility of the central gate is the highest one, because it is the less affected from the scattering with the impurities that are incorporated during the doping process of the source and drain contacts.
The p-type five-gate device (5G) described here has been fabricated starting from CEA-LETI FD-SOI NanoWire (NW) process flow, as described in Sec. 3.5 and comes from the same wafer as the qubit device of Sec. 6.5.
The channel width is $W = 75$ nm, the gate length is $L_G = 40$ nm and the gate spacing is $S_H = 40$ nm.

4.9.1. SATURATION OF THE SUBTHRESHOLD SWING

Static measurements of the drain current were performed by sweeping the voltage on one gate (active gate), while keeping the other gates (external gates) at a fixed potential, namely $V_{G,ext} = -2$ V.

Fig. 4.9 a) shows the drain current $I_D(V_G)$ transfer characteristics for the five gates at room temperature (with the other gates at $V_{G,ext} = -2$ V). They have been measured in linear regime ($V_{sd} = 50$ mV). From these $I_D(V_G)$ curves it can be observed that each gate

exhibits a different threshold voltage V_{th} and a different low field mobility μ_0.

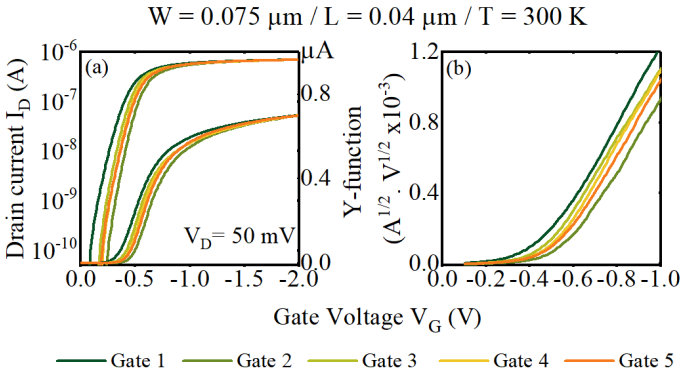

Figure 4.9: (a) $I_D(V_G)$ in linear and log scale and (b) $Y(V_G)$ for every gate (with the others set at $V_{G,ext} = -2$ V) for T = 300 K.

Furthermore, access resistances strongly affect the behavior of the device in the strong inversion regime. In the access resistance of a multi-gate device we should include both the contributions coming from source/drain resistances and from the external gate channels. Therefore the extraction was performed exploiting the Y-function method, which is known to eliminate series resistance effects[16][17].
The Y-function is defined as the ratio between the drain current I_D and the square root of the transconductance $g_m = \frac{dI_D}{dV_{G_i}}$:

$$Y(V_G) = \frac{I_D}{\sqrt{g_m}} = (V_G - V_{th})\sqrt{\frac{W}{L_{eff}} C_{OX} \mu_0 V_D} \tag{4.4}$$

where W is the device width, L_{eff} the effective gate length, C_{OX} is the gate oxide capacitance per unit area, μ_0 is the mobility of the active channel and V_D the bias applied.
The gate oxide capacitance per area is a known parameter and can be calculated as $C_{OX} = \frac{\epsilon_0 \epsilon_r}{d} = 5.75\ \frac{mF}{m^2}$, where $d = 6$ nm for is the thickness of the gate oxide, and $\epsilon_r \simeq 3.9$ is the relative permittivity of SiO_2.
By fitting each $I(V_G)$ trace to the Y-function it is possible to extract the corresponding mobility μ_0 and threshold voltage V_{th}.
Both $I_D(V_G)$ and $Y(V_G)$, are shown in Fig. 4.10, for temperatures ranging from 300 K to 20 K. These data refer to gate 4, but the same analysis has also been performed for the other gates.
We can observe a steeper subthreshold slope as temperature decreases, and hence a decreasing subthreshold swing . It can be noticed as well an increase (in absolute value) of both the threshold voltage and the drain current in strong inversion.

The subthreshold swing SS(T) (defined in eq. 4.2 and shown in Fig. 4.10 c)), follows the Boltzmann limit, i.e. it shows a linear behavior with temperature, down to T=70-80 K, before saturating to a value around 20 mV/dec[18]. The trend is roughly the same for each gate.

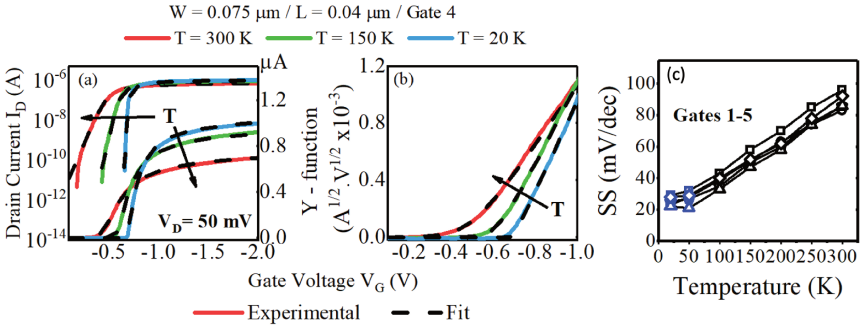

Figure 4.10: The gate voltage refers to gate 4, while setting the other gate voltages to -2 V. Experimental (fitting) traces are shown as solid (dashed) lines. (a) $I_D(V_G)$ in linear and log scale and (b) $Y(V_G)$ curves, for different temperatures. c) Subthreshold swing as a function of temperature for the 5 gates.

The saturation of the subthreshold swing at low temperature has been investigated in detail in Refs. [19] [3] [20]. Relying on numerical simulations, it was demonstrated that an exponential band tail in the conduction or valence band and the Fermi-Dirac statistics lead to saturation of the SS at deep cryogenic temperatures.
These exponential band tails in the conduction and valence band in MOSFET are likely related to potential-fluctuations-induced disorder [21], crystalline disorder, strain, residual impurities etc.
The saturation of the SS can be understood considering that the Fermi level approaches the valence (conduction) band when lowering the temperature [22]. When the Fermi level falls within the band tail the carriers are degenerate. In this case the Boltzmann statistics is not valid anymore, and the metallic degenerate statistics prevails.
Therefore eq. 4.2 doesn't hold at low temperature. An analytical expression of the SS in this regime is derived in [3].

4.9.2. LAMBERT W-FUNCTION BASED MODELING

The Lambert W-function, $LW(z)$, is defined by the equation:

$$z = LW(z)e^{LW(z)} \tag{4.5}$$

where z can be either a real or a complex number.
The LW function allows to model the channel inversion charge $Q_i(V_G)$ using as fitting parameters both the subthreshold ideality factor n and the threshold voltage V_{th} and, by turn, the drain current characteristic $I_D(V_G)$, for a given mobility μ_0 [23].
Here, we assume that the five gate device can be modeled as five independent gate-controlled resistances placed in series, whose values depend on V_G (active channel) and $V_{G,ext}$ (access channels).
The active channel resistance for each gate i is given by:

$$R_{Ch,i}(V_G, \mu_{0,i}, V_{th,i}, n_i) = \frac{1}{\frac{W}{L_G} Q_i(V_G, V_{th,i}, n_i)\mu_{0,i}} \tag{4.6}$$

The charge per unit area Q_i is modelled with the LW function:

$$Q_i(V_G, V_{th,i}, n_i) = n_i.C_{OX}\frac{k_B T}{q} LW\left(e^{\frac{V_G - V_{th,i}}{n_i \frac{kT}{q}}}\right) \tag{4.7}$$

where q is the electron charge.
The access resistance is computed as:

$$\begin{aligned} R_{Acc}(V_{G,ext}) = R_{ch,j}(V_{G,ext}, \mu_{0,j}, V_{th,j}, n_j) \\ +R_{ch,k}(V_{G,ext}, \mu_{0,k}, V_{th,k}, n_k) + R_{ch,l}(V_{G,ext}, \mu_{0,l}, V_{th,l}, n_l) \\ +R_{ch,m}(V_{G,ext}, \mu_{0,m}, V_{th,m}, n_m) + R_{Series} \end{aligned} \tag{4.8}$$

where $R_{ch,i}, R_{ch,j}, R_{ch,k}, R_{ch,l}$ are the channel resistances of gates i, j, k and l, and R_{Series} is an additional fitting parameter that takes into account the contribution of source and drain access resistances.
The parameter R_{series} determines the current in strong inversion and is therefore common for all the gates.
Each $I_D(V_G)$ is related to the sum of $R_{ch} + R_{Acc}$ through Ohm's law:

$$\frac{V_{ds}}{R_{ch} + R_{Acc}} = I_D(V_G) \tag{4.9}$$

This model successfully fits the drain current from subthreshold to strong inversion regime, as shown in Fig. 4.10, obtaining $\mu_{0,i}$, $V_{th,i}$, n and R_{acc} for each gate.

A standard method to extract the mobility $\mu_{0,i}$ and threshold voltage $V_{th,i}$ independently is from the Y-function (for each gate), while the ideality factor can also be estimated from the SS.
The access resistance R_{Acc} can also be derived using the first order attenuation factor $\theta_1 = \theta_{10} + R_{Acc}G_m$[16], where θ_{10} is the intrinsic mobility reduction factor and $G_m = \frac{W}{L}C_{OX}\mu_0$. θ_{10} has been neglected, since in such short channels access resistance effect prevails.
In Fig. 4.11 the parameters extracted using the formulas 4.8,4.6 (panels a)-d)) are compared with the ones extracted using standard methods (i.e. from Y-function, attenuation factor and subthreshold slope) in panels e)-h).
The values and trends extracted with the two methods are in good agreement.
We can observe that the threshold voltage decreases quasi linearly with temperature, independently on the gate.
The ideality factor n varies nearly as $1/T$ for T<80 K. This is a consequence of the saturation of the SS. Below 80 K the Boltzmann model is not valid anymore and the value of n is meaningless from a physical point of view. Anyhow it is still shown to validate the compactness of the W-function model.

4.9.3. EVALUATION OF THE MOBILITY

The low field mobility (inversely proportional to R_{ch}), shows different trends for each gate, revealing that the central device (gate 3) has a better mobility at low temperature. Such a mobility gets lower going to the gate closer to the reservoirs. This is a hint that the main scattering mechanism is with the defects located near source and drain. [24]. We can have a closer look at the mobility as a function of temperature exploiting the Mathiessen's

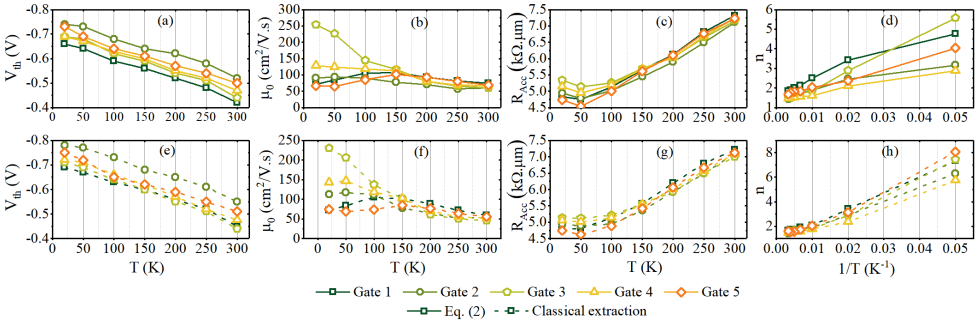

Figure 4.11: Parameters extracted for the every gate from room T down to 20 K using eq. 4.8 (a)-(d) and standard extraction methods (e)-(h), i.e. respectively Y-function in e)-f), attenuation factor in (g) and substhreshold slope in (h). In the plots c),g) the access resistance of each gate is multiplied with the channel width $W = 75nm$.

4

rule, which takes into account the temperature dependence of the different contributions to the mobility [25]:

$$\frac{1}{\mu_0} = \frac{T}{300\mu_{ph}} + \frac{300}{T\mu_C} + \frac{1}{\mu_{nd}} \tag{4.10}$$

where μ_{ph}, μ_C and μ_{nd} are the contribution coming respectively from phonon scattering, Coulomb repulsion and scattering with neutral defects.

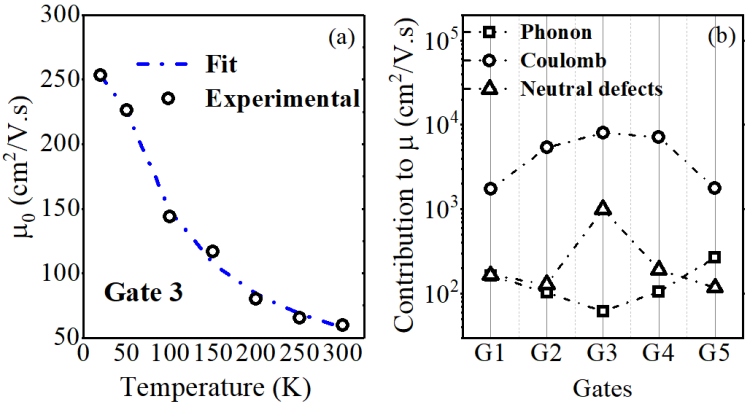

Figure 4.12: Experimental (circles) and simulated (dashed line) low field mobility of the central gate (Gate 3) as a function of temperature. (b) Contribution of different scattering mechanisms to the total mobility

Neutral defects are the limiting mechanism for gates closer to source and drain, whereas their impact is reduced on the central gate. Indeed, as shown in Fig. 4.12 a) the mobility of gate 3 increases as the temperature is lowered, consistent with a transport dominated by phonon scattering.
In Fig. 4.12 b) are reported three contributions to the mobility of each gate, extracted by fitting each gate mobility as a function of temperature. We highlight that the lower is the

contribution, the higher is the scattering rate.
Moreover the observation that the mobility gets better in the central gates, because fundamentally they are cleaner, justifies the experimental strategy used in the following chapters, i.e. to use the central gates to accumulate a double dot and the gate close to the reservoirs (or the reservoirs themselves) for RF charge-sensing.

We systematically observed a different, and generally more irregular, behaviour of the lateral gates compared to the central ones, both in p-type and n-type devices.
However the boron dopants used in p-type devices tend to diffuse more compared to n-type dopants (phosphorus in our case). In order to quantify the impact of n-type dopants compared to p-type ones an analysis analogous to the one described here would be required on a multi gate n-type device.

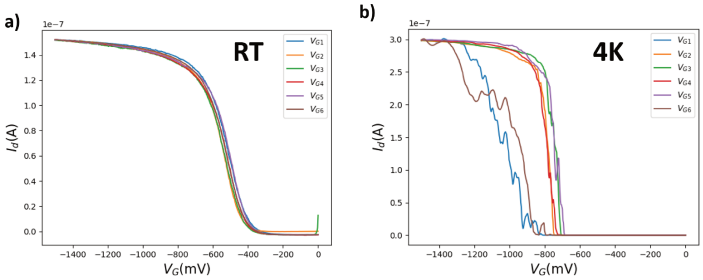

Figure 4.13: Current I_D as a function of V_G for each gate, measured on the six-gate device of Chap. 6 a) T=300 K and V_{ds}=5 mV b) T=4 K and V_{ds}=10 mV. The gate not swept are kept at $V_G = -1.5$ V.

Even when the gates are showing nearly the same behaviour at room temperature, when cooling down the lateral gates behave differently and often in an irregular way. As an example in Fig. 4.13 we show the $I_D(V_G)$ curves of a six-gate p-type device where it can be noticed the different behaviour of lateral gates G_1 and G_6 in blue and brown, respectively. We notice that the lateral gates are the ones finally controlling the conduction across the channel.The device of Fig. 4.13 is the one studied in Secs. 6.1-6.4.

The present analysis shows that the reservoir doping has a significant influence at low temperatures and it suggests that it may also have a negative impact at the level of qubit performance. Indeed, by accumulating a quantum dot far away from the reservoirs, together with a careful tuning of the magnetic field direction, it has been possible to reach record coherence times for holes in silicon [26].
Since in the perspective of realizing qubit we fundamentally don't care about having good transistor performances, finally it might be good to relax the level of doping implantation for the future devices and to study in a rigorous manner the correlation between qubit coherence times and level of doping implantation.

BIBLIOGRAPHY

[1] S.M. Sza and K.K. Ng. *Physics of semiconductor devices*. 3rd. Wiley, 2008.

[2] Mark Lundstrom. *Fundamentals of Nanotransistors*. Jan. 2022. URL: https://nanohub.org/resources/35865.

[3] Arnout Beckers, Farzan Jazaeri, and Christian Enz. "Theoretical Limit of Low Temperature Subthreshold Swing in Field-Effect Transistors". In: *IEEE Electron Device Letters* 41.2 (2020), pp. 276–279. DOI: 10.1109/LED.2019.2963379.

[4] A. Beckers, F. Jazaeri, and C. Enz. "Cryogenic MOSFET Threshold Voltage Model". In: *ESSDERC 2019 - 49th European Solid-State Device Research Conference (ESSDERC)*. 2019, pp. 94–97.

[5] A. Beckers, F. Jazaeri, and C. Enz. "Cryogenic MOS Transistor Model". In: *IEEE Transactions on Electron Devices* 65.9 (2018), pp. 3617–3625.

[6] D. V. Averin and Yu. V. Nazarov. "Virtual electron diffusion during quantum tunneling of the electric charge". In: *Phys. Rev. Lett.* 65 (19 Nov. 1990), pp. 2446–2449. DOI: 10.1103/PhysRevLett.65.2446. URL: https://link.aps.org/doi/10.1103/PhysRevLett.65.2446.

[7] D.C. Glattli. "Coulomb blockade and off-resonance tunneling in small electronic systems". In: *Physica B: Condensed Matter* 189.1 (1993), pp. 88–98. ISSN: 0921-4526. DOI: https://doi.org/10.1016/0921-4526(93)90149-Z. URL: http://www.sciencedirect.com/science/article/pii/092145269390149Z.

[8] L. P. Kouwenhoven et al. "Mesoscopic electron transport". In: (1997), pp. 105–214.

[9] A. Aprà et al. "Dispersive vs charge-sensing readout for linear quantum registers". In: *2020 IEEE International Electron Devices Meeting (IEDM)*. 2020, pp. 38.4.1–38.4.4. DOI: 10.1109/IEDM13553.2020.9372090.

[10] H. Moon et al. "Machine learning enables completely automatic tuning of a quantum device faster than human experts". In: *Nature Communications* 11.1 (Aug. 2020), p. 4161. ISSN: 2041-1723. DOI: 10.1038/s41467-020-17835-9. URL: https://doi.org/10.1038/s41467-020-17835-9.

[11] V. Nguyen et al. "Deep reinforcement learning for efficient measurement of quantum devices". In: *npj Quantum Information* 7.1 (June 2021), p. 100. ISSN: 2056-6387. DOI: 10.1038/s41534-021-00434-x. URL: https://doi.org/10.1038/s41534-021-00434-x.

[12] Justyna P. Zwolak et al. "Autotuning of Double-Dot Devices In Situ with Machine Learning". In: *Phys. Rev. Applied* 13 (3 Mar. 2020), p. 034075. DOI: 10.1103/PhysRevApplied.13.034075. URL: https://link.aps.org/doi/10.1103/PhysRevApplied.13.034075.

[13] N M van Esbroeck et al. "Quantum device fine-tuning using unsupervised embedding learning". In: *New Journal of Physics* 22.9 (Sept. 2020), p. 095003. DOI: 10.1088/1367-2630/abb64c. URL: https://doi.org/10.1088/1367-2630/abb64c.

[14] E. Catapano et al. “Characterization and Lambert – W Function based modeling of FDSOI five-gate qubit MOS devices down to cryogenic temperatures”. In: *2021 Joint International EUROSOI Workshop and International Conference on Ultimate Integration on Silicon (EuroSOI-ULIS)*. 2021, pp. 1–4. DOI: 10.1109/EuroSOI-ULIS53016.2021.9560671.

[15] E. Catapano et al. “Modeling and simulations of FDSOI five-gate qubit MOS devices down to deep cryogenic temperatures”. In: *Solid-State Electronics* 193 (2022), p. 108291. ISSN: 0038-1101. DOI: https://doi.org/10.1016/j.sse.2022.108291. URL: https://www.sciencedirect.com/science/article/pii/S0038110122000636.

[16] G. Ghibaudo. “New method for the extraction of MOSFET parameters”. In: *Electronics Letters* 24 (1988), pp. 543–545.

[17] Edoardo Catapano et al. “Statistical and Electrical Modeling of FDSOI Four-Gate Qubit MOS Devices at Room Temperature”. In: *IEEE Journal of the Electron Devices Society* 9 (2021), pp. 582–590. DOI: 10.1109/JEDS.2021.3082201.

[18] G. Ghibaudo et al. “On the modelling of temperature dependence of subthreshold swing in MOSFETs down to cryogenic temperature”. In: *Solid-State Electronics* 170 (2020), p. 107820. ISSN: 0038-1101. DOI: https://doi.org/10.1016/j.sse.2020.107820. URL: https://www.sciencedirect.com/science/article/pii/S0038110120300812.

[19] Heorhii Bohuslavskyi. “Cryogenic electronics and quantum dots on silicon-on-insulator for quantum computing”. Theses. Université Grenoble Alpes, Dec. 2018. URL: https://tel.archives-ouvertes.fr/tel-02183484.

[20] H. Bohuslavskyi et al. “Cryogenic Subthreshold Swing Saturation in FD-SOI MOSFETs Described With Band Broadening”. In: *IEEE Electron Device Letters* 40.5 (2019), pp. 784–787. DOI: 10.1109/LED.2019.2903111.

[21] Emil Arnold. “Disorder-induced carrier localization in silicon surface inversion layers”. In: *Applied Physics Letters* 25.12 (1974), pp. 705–707. DOI: 10.1063/1.1655369. eprint: https://doi.org/10.1063/1.1655369. URL: https://doi.org/10.1063/1.1655369.

[22] G Ghibaudo. “Transport in the inversion layer of a MOS transistor: use of Kubo-Greenwood formalism”. In: *Journal of Physics C: Solid State Physics* 19.5 (Feb. 1986), pp. 767–780. DOI: 10.1088/0022-3719/19/5/015. URL: https://doi.org/10.1088/0022-3719/19/5/015.

[23] T.A. Karatsori et al. “Full gate voltage range Lambert-function based methodology for FDSOI MOSFET parameter extraction”. In: *Solid-State Electronics* 111 (2015), pp. 123–128. ISSN: 0038-1101. DOI: https://doi.org/10.1016/j.sse.2015.06.002. URL: https://www.sciencedirect.com/science/article/pii/S003811011500177X.

[24] Minju Shin et al. “Low temperature characterization of mobility in 14 nm FD-SOI CMOS devices under interface coupling conditions”. English. In: *Solid-State Electronics* 108 (June 2015), pp. 30–35. ISSN: 0038-1101. DOI: 10.1016/j.sse.2014.12.013.

[25] M. Shin et al. “Low temperature characterization of mobility in 14 nm FD-SOI CMOS devices under interface coupling conditions”. In: *Solid-state Electronics* 108 (2015), pp. 30–35.

[26] N. Piot et al. “A single hole spin with enhanced coherence in natural silicon”. In: *Nature Nanotechnology* 17.10 (Oct. 2022), pp. 1072–1077. ISSN: 1748-3395. DOI: 10.1038/s41565-022-01196-z. URL: https://doi.org/10.1038/s41565-022-01196-z.

5

ELECTRON SPIN READOUT IN BILINEAR ARRAYS OF QUANTUM DOTS

The best that most of us can hope to achieve in physics is simply to misunderstand at a deeper level

Wolfgang Pauli

Among all solid-state platforms, silicon based spin qubits can rely on the reproducibility provided by current industrial fabrication standards. Many recent experiments benefited from the collaboration with industrial partners [1] [2]. Nearly the same fabrication technique of the device studied in this chapter has also been used in [3][4][5][6][7] (all these devices belong to the same wafer). We shared these devices coming from CEA-LETI in the context of the European project MOSQUITO.

We target a fast and scalable readout of qubit arrays. In this chapter two different readout approaches are compared, in order to probe both charge and spin state of coupled qubits. In Sec. 5.7 it is demonstrated that it is possible to manipulate electrically the electron spin. Unfortunately, the spin-orbit interaction turned out to be too weak to enable the observation of Rabi oscillations.
Finally it is proposed a scheme to extend the discussed charge-sensing readout into infinitely long bilinear arrays of quantum dots.

5.1. THE DEVICE

The device studied in this chapter has six gates partially overlapping a silicon-on-insulator nanowire (Fig. 5.1), three on the top side of the channel ($T_{1,2,3}$) and three on the bottom one ($B_{1,2,3}$). The finger gate structures are etched out of an initially defined single gate fully covering the nanowire. The gate lengths are $L_g = 40$ nm, the channel width $W = 90$ nm. Longitudinal and transversal spacings are $S_l = 40$ nm and $S_t = 50$ nm, respectively.

The initial idea of this experiment was to use gate reflectometry as in Refs. [8][9], in order to study each couple of QDs except $B_1 - B_2$. We noticed that the most regular, clean

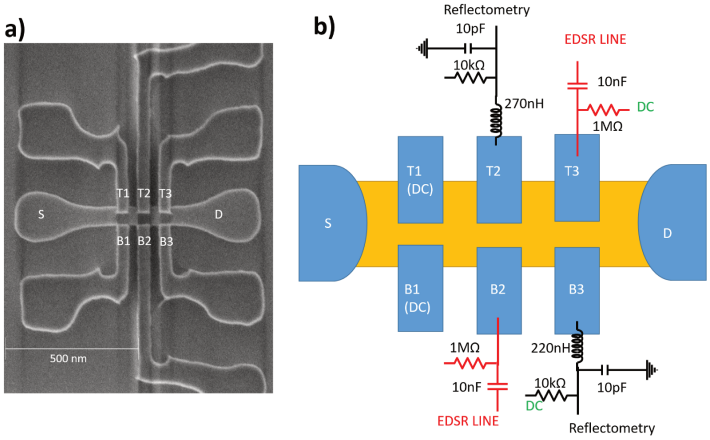

Figure 5.1: a) SEM (scanning electron micrograph) top view of a device nominally identical to the one measured. b) Schematic of the device with reflectometry setup on T_2 and B_3.The electrical lines on gates T_3 and B_2 are used to send fast microwaves (several GHz) and pulses for electron spin manipulation.

5

and isolated QDs were the ones below the two central gates. This is because, especially with a temperature of 350 – 450 mK, the diffusion of the ions deposited during the reservoir doping can easily affect the QDs close to them, that are therefore far to be ideal, as discussed in Sec. 4.9.3.
Moreover, previous studies on a 2x2 array (where each gate is close to a reservoir) showed that, for a transversal separation of the facing gates of $S_t = 40$ nm, the tunneling with the reservoirs tends to be still dominant compared to the interdot tunneling. On the other hand the strong tunnel coupling between lateral gates and reservoirs allows us to realize an RF charge sensor.
Most of the work described in this chapter has been presented in Ref. [10].

In order to be able to extract standard transitor parameters using measurements of current, as explained in Sec. 4.2, we need to open the conduction channel between source and drain. We can measure current by opening either all the top or all the bottom gates.

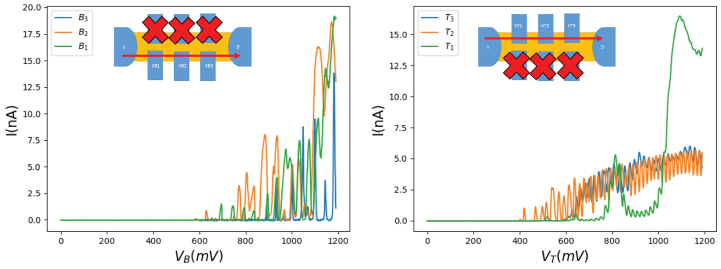

Figure 5.2: Quantized transport through the device for $V_{ds} = 5$ mV. In the left plot we keep the upper gates at V_T= 0 V and the bottom gate not swept at +1V. In the right plot we keep the lower part of the channel at V_B=0 V and the top gates not swept at +800 mV.

Nevertheless with sufficiently high gate voltage we could open a conduction channel also using 3 consecutive gates that are not on the same side of the channel as for example $B_1 - T_2 - B_3$. With V_{ds}<E_{add} we can observe quantized transport, that is a clear signature of quantum dot behaviour (see Fig. 5.2).
Moreover we start observing the first Coulomb peaks at lower voltages for the top gates, as we were expecting also from the lower threshold voltage measured at room temperature ($V_{th}^{T} \simeq$ -100 mV for the top gates and $V_{th}^{B} \simeq$+100 mV for the bottom ones). The different behaviour of top and bottom gates can be understood as a result of an asymmetric gate alignment, indeed the overlap with the Si nanowire is larger for the gates on the top side. This is evident also in the SEM image (Fig. 5.1 a)) of a device nominally identical to the one measured.
Another hint of this misalignment comes from the bigger charging energies of the dots in the bottom gates. From the first detectable Coulomb diamonds we measured $E_{add}^{B2} \simeq$13 meV and $E_{add}^{T2} \simeq$7 meV, as it would be expected for smaller dots, and hence smaller bottom gates.

5.1.1. DISPERSIVE READOUT IN BILINEAR QUANTUM DOT ARRAYS ARRAYS

To obtain the LC tank resonators for dispersive readout, we connect surface-mount inductors to gates T_2 and B_3 ($L_{T_2} = 270$ nH, $L_{B_3} = 220$ nH).
A schematic representation of the device layout with the two tank circuits, and their capacitive model is shown in Fig. 5.3.
The resonant frequencies of our resonators at 400 mK are $f_0(T_2) = 407.2$ MHz and $f_0(B_3) = 478.2$ MHz. Knowing these values we can extract the parasitic capacitances ($C_p = \frac{1}{L(2\pi f_0)^2}$), respectively $C_{T_2} = 0.57$ pF and $C_{B_3} = 0.50$ pF.
Moreover, as explained by eq. 2.13 we add a matching capacitor of $C_M = 10$ pF (value calculated with eq. 2.13) in parallel with the inductor, in order to improve the matching (Fig. 5.1 b)). For both the resonators we measured quality factors of $Q \simeq 100$.
Throughout this chapter, except in Sec. 5.2, we'll use the quantum dot configuration as shown in the schematic in Fig. 5.3 a), together with the reflectometry circuit b) and the capacitive models of the two detectors coupled with the QDs in c),d).

5.2. EVALUATE TUNNEL COUPLING WITH GATE-BASED REFLECTOMETRY

Here we evaluate the tunnel coupling of the central double dot with the nearby reservoirs using gate based reflectometry, with a technique similar to the one used in Ref. [11].

In this experiment the two central QDs, accumulated below gates B_2 and T_2, are in the few-electron regime (i.e. less than 10 charges in each dot). The top gates are polarized at $V_{T1,T3} = +1$ V, to keep the dot below T_2 well coupled with the reservoir. Conversely the bottom gates are polarized at $V_{B_1,B_3} = -300$ mV, such that the dot below B_2 is well isolated and can then be charged and discharged only through one of the top gates. A schematic configuration of the QDs is showed in Fig. 5.4 a).
We consider an interdot charge transition (ICT) where the interdot tunnel coupling is lower than the resonator frequency, as can be understood by the fact that we do not observe any dispersive signal corresponding to it (see Fig. 5.4 b,c). Meanwhile the tunnel coupling between the dot T_2 and the the reservoirs (controlled by the gates T_1, T_3) is fast enough to be resolved dispersively by the tank circuit on T_2 [12].

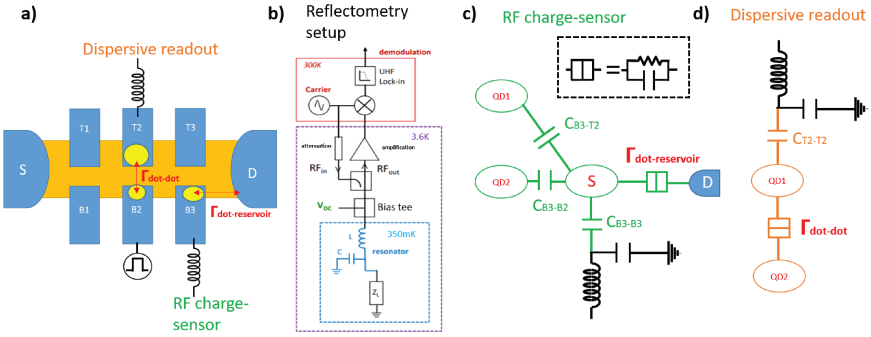

Figure 5.3: a) Sketch of the studied quantum dot configuration. The two central QDs, accumulated by T_2 and B_2, are simultaneously probed by means of two RF gate reflectometry setups based on dispersive readout via T_2, and charge-sensing readout via a dot defined by B_3 and tunnel coupled to the drain (D)) reservoir. Voltage pulses are applied to B_2 in order to induce charge transitions between central QDs. b) Reflectometry-setup. One gate (with a characteristic impedance Z_L depending on the charge configuration of the nearby QDs) is connected to an LC resonator made of a surface-mount inductor and parasitic capacitances. Following a directional coupler, the reflected rf signal is amplified using a semiconductor amplifier operating at 3.6 K. An ultra-high frequency digital lock-in demodulates the reflected signal at room temperature. c) Schematic of the charge-sensing readout scheme, measuring the charge occupation in dots QD_1 and QD_2, which are defined by gates T_2 and B_2; S is the sensor dot (below gate B_3). d) Schematic of dispersive readout scheme, which can probe the quantum capacitance associated with tunneling between QD_1 and QD_2.

We then want to evaluate how long does it take to add or remove one charge from B_2. We can access the charge dynamics of B_2 using the dispersive signal coming from the transition of the dot T_2 with one of the nearby dots, that are in strong accumulation and we can consider them as an extension of the reservoirs.
When we add one charge on B_2 the T_2-lead signal jumps because of an increased Coulomb repulsion from dot B_2. Conversely, if no charge jump has occurred, we can still observe the T_2-lead signal.

In Fig. 5.4 b), c) we plot the resonator phase signal $\phi(T_2)$ acquired while sending square wave pulses on gate B_2 with a total period of 20 ms and 20 μs, respectively. The duty cycle is 50% and the pulse amplitudes are $\pm$3.5 mV for both figures.
For slow pulses (i.e. 10 ms on each side of the pulse) we just observe a doubling of the signal, that corresponds to the time average of the phase of the resonator $\phi(T_2)$ acquired on the positive (red dashed line) and negative side of the pulse (white dashed line).
When the pulses are faster than the charging dynamics instead a prolongation of the T_2-lead signal can be observed (Fig. 5.4 c)), due to the fact that the charge in B_2 has no time to move elsewhere.

This measurement is useful to understand quickly the order of magnitude of the interdot tunnel rate.
For an accurate measurement we can trigger the acquisition on one of the two sides of the pulses and evaluate for how long the prolongation of the T_2-lead survives, that is equivalent to measure how long does it take to load or unload a charge in/out of dot B_2. We sit in the points indicated by the red and white arrows in Fig. 5.4 c). In particular, in

Figure 5.4: a) Electrostatic configuration of the experiment. We pulse on gate B_2 while reading the charge transition between the dot T_2 and its reservoirs through the tank circuit on T_2. b,c) Stability diagram of an interdot charge transition while pulsing. The phase signal obtained is an average of what is measured on the two sides of the pulse. The dashed lines indicate the signal acquired on the positive (red) and negative (white) sides of the pulses. Also the ICT (not visible) is highlighted with the same colors for clarity. A scheme of the pulse sequence (duty cycle 50%) can be found on the bottom right of the plots.
In b) it is shown for comparison that for slow pulses (10 ms on each side) we just observe a doubling of the signal. For fast pulses of 10 μs we can clearly see a prolongation of the T_2-lead transition, as indicated by a white and a red arrow. The arrows indicates the pulse direction and amplitude in correspondence of to the two prolongations observed.

the prolongation of the T_2-lead pointed at by the red arrow we pulse positively, meaning that we are adding one electron in B_2, thus measuring the loading time of the B_2 dot (Fig. 5.5, left). With the same argument on the other prolongation (pointed by the white arrow) we measure the dot unloading time (Fig. 5.5, right).
We can fit the phase signals in time with an exponential decay, obtaining $\tau_{in}^{B_2} = 0.4$ ms and $\tau_{out}^{B_2} = 0.8$ ms.

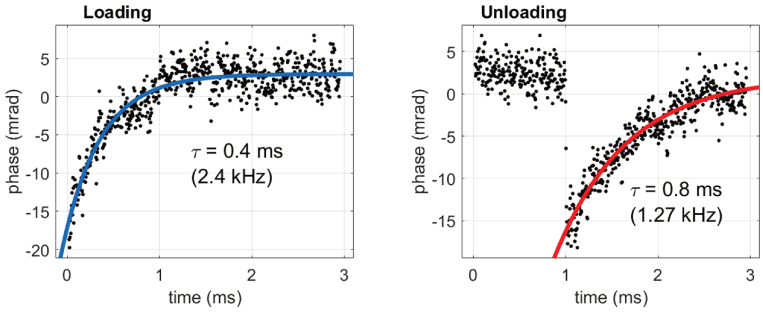

Figure 5.5: Measured tunnel rates. The loading time (left) is measured when sending positive pulses, i.e. on the lower dot lead of Fig. 5.4 b), as indicated by the red arrow. Analogously, the unloading time is measured when pulsing negatively, i.e. when removing an electron, as indicated by the white arrow on upper dot-lead of Fig. 5.4 b).

From this measurement we understand that we are able to isolate quite well the dot below B_2. At this point we could think to use the dot B_2 as the information quantum dot and the dot T_2 as an ancillary qubit, necessary for spin-to-charge conversion through Pauli spin blockade (PSB) as in Refs. [8][13].
In order to perform PSB readout we need to be able to read faster than the spin lifetime T_1, otherwise the spin state would relax before being able to measure it. The T_1 reported for electrons in silicon can range between hundreds of μs and few seconds [14][15][16][17][18]. The electronic temperature of around 400 mK has a negative impact on T_1, which is expected to be to be around tens of ms[14] in the best scenario, but it might as well be lower. In the present case the readout risks to be too slow, being limited to study spin transitions with T_1<0.8 ms.
Because of the large span of the possible values of T_1, having control over the interdot tunnel coupling is crucial for an efficient spin readout. Ideally we want to cut the access to the reservoirs, to enhance the qubit coherence, and to tune the interdot coupling with local gates, for a fast readout.
An additional gate layer to tune the tunnel couplings is realized routinely in academic clean-rooms, whereas in our process flow it is something ongoing [19] but it has not been implemented yet on the device discussed here.

In the following we'll see that the main degree of freedom we have to tune the interdot tunnel coupling is to vary the number of charges in the DQD. In particular, we'll study two ICTs: one transition at relatively high dot filling, where PSB can be observed with both gate-based dispersive readout and with the charge sensor (Secs. 5.3, 5.4); and another transition at lower dot filling where the interdot tunnel coupling is too low to study it with gate-based dispersive readout (Secs. 5.5, 5.6, 5.7).

5.3. RF CHARGE-SENSING VS DISPERSIVE READOUT MEASUREMENT FOR LARGE INTERDOT TUNNEL COUPLING

We now accumulate three QDs below gates T_2, B_2 and B_3 (see Fig. 5.3 a)). The other gates are negatively biased to ensure total charge depletion and isolation of the central dots. This configuration allows to implement and compare two alternative methods for charge and spin detection.
We use the quantum dot defined by B_3 to sense the charge state of the DQD defined by T_2 and B_2. To this aim, B_3 is tuned to have one level of the charge-sensing dot in resonance with the electron reservoir on the drain side. In this regime, any change in the charge occupation of the dots below T_2 and B_2 causes shifts in the resonant level and, correspondingly, capacitance variations that can be detected by rf gate reflectometry (Fig. 5.3 c)).
In order to keep the level of the sensor dot resonant with its lead while scanning gates T_2, and B_2 we have to consider that the potential applied on a gate also has an effect on the nearby gates, because of capacitive cross coupling, and we want to compensate for this effect.
More specifically we tune the gate voltage of the sensor dot depending on the electrostatic cross coupling ($\alpha_{B_2-B_3} = 0.22$, $\alpha_{T_2-B_3} = 0.15$) with the other two gates, thus keeping fixed the electrochemical potential of the sensor dot while sweeping the other gates.
The charge-sensing through a dot-reservoir transition is often called a single-electron box (SEB) [20][21].

An alternative readout scheme consists in directly measuring the reflected signal from an LC resonator connected to gate T_2 (Fig. 5.3 d)), as done in the previous section. Differently from the previous case, now the dot below T_2 is isolated from the reservoir, ensuring that the dominant process is interdot tunneling with the B_2 dot.
This approach is sensitive to charge tunneling resonances between the dots set by T_2 and B_2, provided the corresponding tunnel rates are at least comparable to the frequency of the reflectometry tone [12]. Indeed it is mainly sensitive to the quantum capacitance, which depends on the curvature of the energy states, and hence on the tunnel rates of the charge transitions between the two QDs, $\Gamma_{dot-dot}$.
The two readouts can be used simultaneously. Even though the basic principle is the same, we used them in a completely different way and the RF charge sensor signal, given by $\Gamma_{dot-lead}$ (fixed), allows to explore charge transitions where $\Gamma_{dot-dot}$ (dependent on dot filling) is way smaller than the RF probe frequency.
The stability diagrams in Fig. 5.6 a),b) clearly show the typical honeycomb pattern of a DQD, formed by the two QDs accumulated below the gates B_2 and T_2. In these plots the color scale is the phase signal recorded respectively with the RF charge sensor (Fig. 5.6 a)) and with direct gate-based reflectometry (Fig. 5.6 b)).
Moreover we can count charges of the quantum dot below T_2. The numbers in Fig. 5.6 a) refer to the charges in (B_2, T_2).
Since the capacitive coupling with the sensor is mainly determined by the filling of B_2 we decided to work with a fixed number of charges $N, N+1$ below B_2, such that we can fix our compensation parameters.

5.4. MAGNETOSPECTROSCOPY OF THE DOUBLE QUANTUM DOT

We first studied the interdot charge transition $(N+1,7) \rightarrow (N,8)$. In Fig. 5.7 it is shown the signal recorded simultaneously by the two sensors while we sweep magnetic field and gate voltages.

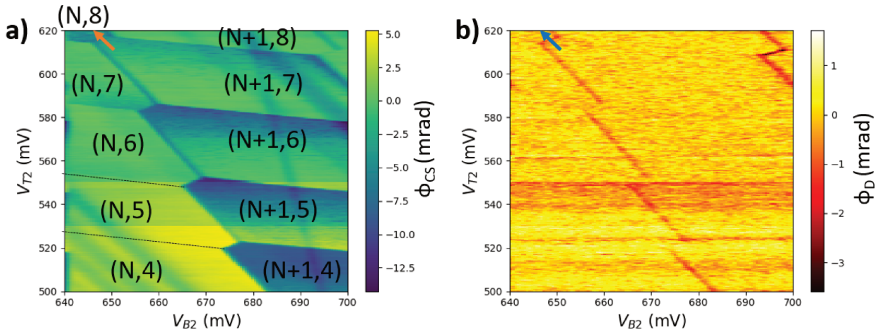

Figure 5.6: Stability diagrams of the central double quantum dot accumulated by gates B_2 and T_2. a) Phase response ϕ_{CS} of the charge-sensing readout setup. The two-dimensional plot was obtained by sticking together four consecutive measurements over adjacent T_2-voltage ranges. From one range to the other, the quantum dot sensor was re-tuned by changing the value of the voltage on B_3 in order to compensate the detector shift due to a change in the charge state of the dot below T_2. b) Simultaneous dispersive measurement by gate reflectometry on T_2. We notice that ϕ_D ridges with positive slopes, denoting interdot tunneling, are clearly visible only in the upper part of the plot, and quickly vanish for lower occupation numbers in the upper dot.

5

We observe that the gate reflectometry signal ϕ_D starts to vanish around $B = 0.5$ T. This behavior is a typical manifestation of a singlet/triplet PSB [22], which allows us to conclude that N (number of charges in B_2) is even. In fact, for $B > 0.5$ T the triplet state T_- becomes the ground state in the $(N+1,7)$ configuration, while the $(N,8)$ configuration holds a spin-singlet ground state $S(0,2)$-like (Fig. 5.7 c). As a consequence tunneling from $(N+1,7) \rightarrow (N,8)$ is forbidden by spin conservation leading to a vanishing quantum capacitance, and hence a vanishing dispersive signal ϕ_D.
We show here that also the charge sensor signal follows the displacement of the ground state, but without losing in intensity, since it is only proportional to the charge occupation of the dots, displaying a shift due to the B-evolution of the $T_-(1,1)$ ground state.

From this measurement we extracted the lever-arm parameter α along the detuning axis ϵ. The direction of ϵ is indicated by an arrow in the top left corner of the stability diagrams of Fig. 5.6.
We can calculate at which detuning ϵ^* the $T_-(1,1)$ crosses the singlet ground state S_g by solving the following system of equations

$$\begin{cases} T_-(1,1) = \epsilon/2 - g\mu_B B \\ S_g \qquad\quad = -\frac{(\epsilon^2+(2t)^2)^{1/2}}{2} \end{cases} \tag{5.1}$$

yielding :

$$\epsilon^* = g\mu_B B - \frac{t^2}{g\mu_B B} \tag{5.2}$$

We can now observe that both the signals of Fig. 5.7 start to move only for $B > 0.5$ T, i.e. when $g\mu_B B \simeq k_B T$ and $g\mu_B B \simeq t$.
For higher magnetic field ($g\mu_B B \gg t$) the displacement of the ground state $\Delta\epsilon$(V) moves linearly with B:

$$\alpha\Delta\epsilon(V) = g\mu_B \Delta B \tag{5.3}$$

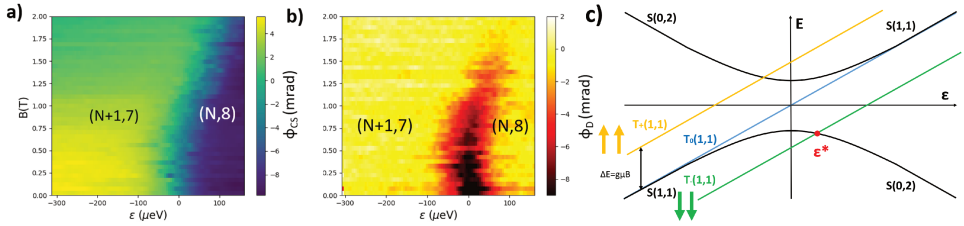

Figure 5.7: Magnetic-field B dependence of the (N+1,7)-(N,8) interdot charge transition, simultaneously measured with the two RF gate reflectometry setups. The ϕ_D moves toward the (N,8) charge domain and gradually vanishes. This signals a spin state evolving from a spin-0 singlet to spin-1 T_- triplet state with both spins counter aligned with B. This means that the multi-electron double-dot state effectively behaves as a two-particle state, which implies that N is an even number. Due to spin conservation, the T_- ground state cannot couple to the spin-0 ground state in the (N,8) configuration, which explains the vanishing of ϕ_D. The corresponding step in ϕ_{CS} (a) consistently moves to the same side but remains always clearly visible despite the vanishing tunnel coupling. c) Energy diagram of a singlet triplet DQD in presence of a magnetic field that split the spin states. In this diagram it is assumed that the two QDs have the same g-factor. The red point indicates the position of the crossing point ϵ^* between the singlet and the T-(1,1) state, i.e. the detuning point where the ground state changes.

5

From Fig. 5.7 we extract $\Delta\epsilon$(V) (in Volt) for a magnetic field variation ΔB, taken above 0.8 T to be sure to be in the linear regime of eq. 5.3.
Since we know approximately the Landè factor $g \simeq 2$ for electrons in silicon, we measure the lever-arm $\alpha = 0.28$ eV/V along the ϵ direction, that allows to write the horizontal axis of Fig. 5.7 as an energy.

5.4.1. COMPARISON OF THE TWO FITS

Here I explain how to fit the signal corresponding to the interdot transition $(N+1,7) \rightarrow (N,8)$ for $B = 0$ T. In particular, we evaluate the dependence of the two sensor signals on the energy detuning between the DQD. The detuning axis ϵ is indicated by an arrow in the top left corner of Fig. 5.6).
The main goal of these fits is to evaluate the tunnel coupling energy t, checking the consistency of the theoretical models with the two readout techniques used.
As explained in Sec. 2.5 the dispersive signal ϕ_D is mainly dependent on the curvature of the energy states, while the charge sensor signal depends only on the charge population. For $B = 0$ T singlet and triplets are degenerate but their population is still not negligible. Here we write the general fitting formulas, valid also in presence of magnetic field.
In absence of an external perturbation that might induce a further dynamics, we can neglect tunneling capacitance contributions and fit the dispersive signal using only the quantum capacitance of eq. 2.25.

It is important to know before the fit if the (1,1)-like state is at positive or negative detuning, in order to choose the proper signs for triplet energies. In our case, as can be understood from Fig. 5.7, the (1,1)-like charge state, i.e. (N+1,7), is at negative detuning. Therefore the triplets energies are $E_{T_\pm} = \epsilon/2 \pm g\mu_B B$. Even though the triplets here are not providing any quantum capacitance contribution, they still play a role in the overall charge distribution. The relative weight of each energy state is indeed normalized over

the partition function Z, that in this model is calculated over five energy states:

$$Z = \sum_i E_i = E_{S_g} + E_{S_e} + E_{T_0} + E_{T_-} + E_{T_+}$$

Substituting the energies of the singlet-triplet states and the Boltzmann occupation probabilities in eq. 2.25 we find:

$$\phi_D(T,t) = \phi_0 \frac{(2t)^2}{(\epsilon^2+(2t)^2)^{3/2}} \frac{e^{+\frac{(\epsilon^2+(2t)^2)^{1/2}}{2k_BT}} - e^{-\frac{(\epsilon^2+(2t)^2)^{1/2}}{2k_BT}}}{Z} \tag{5.4}$$

that fundamentally quantifies the contribution of the singlets curvatures, weighted with their thermal population, as a function of the detuning ϵ.

The charge sensor signal ϕ_D instead can be fitted simply with the occupation probability 2.31 multiplied by $\frac{\epsilon}{\sqrt{\epsilon^2+(2t)^2}}$ [23], term that takes in account a further broadening due to the tunnel coupling.

$$\phi_{CS}(T,t) = \phi_0 \frac{\epsilon}{\sqrt{\epsilon^2+(2t)^2}} \frac{e^{+\frac{(\epsilon^2+(2t)^2)^{1/2}}{2k_BT}} + e^{-\frac{\epsilon}{2k_BT}} + e^{-\frac{(\epsilon/2+g\mu_B B)}{k_BT}} + e^{-\frac{(\epsilon/2-g\mu_B B)}{k_BT}} - e^{-\frac{(\epsilon^2+(2t)^2)^{1/2}}{2k_BT}}}{Z} \tag{5.5}$$

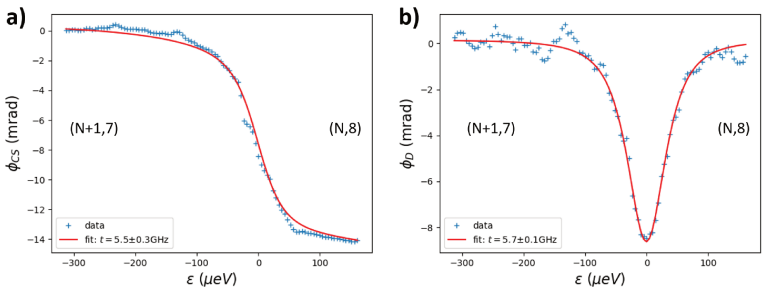

Figure 5.8: a),b) Simultaneous response of the two detectors for the charge transition $(N+1,7) \rightarrow (N,8)$. Red curves are fits to models [23][24], adapted for a singlet-triplet configuration, accounting for the interdot tunnel coupling and finite electronic temperature ($T_e \simeq 0.36$ K).

In this particular measurement the fridge temperature was 360 mK[1]. We use the lever-arm parameter $\alpha = 0.28$ eV/V, found from the displacement of the ground state in the magnetospectroscopy of Fig. 5.7, and we assume the fridge temperature as the effective electron temperature.
We find a tunnel coupling around $t/h \simeq 5.6$ GHz, consistent within the error bars of the two fits.

[1]This temperature was achieved only during this particular cool-down, the standard base temperature of this [3]He dry fridge is usually around 430 – 450 mK

Even though this transition is showing PSB, we didn't manage to resolve any dependence in the tunneling time from (N+1,7) to (N,8) with a magnetic field up to 2 T.
This means that, even if the transition is spin blocked, the spin-flip time (from $|\downarrow\rangle$ to $|\uparrow\rangle$) is below the temporal resolution of the charge detector, i.e. $\simeq 5\mu$s .
Another issue was that, without being able to pulse on gate T_2, we couldn't pass through an intermediate charge state for a proper initialization of the $|\uparrow\rangle$ state in one of the two dots, and hence we couldn't measure the spin relaxation time T_1.
Moreover we cannot read the qubit spin state as in Ref. [8]. Indeed, differently from holes (Fig. 6.22), the dispersive response of the magnetospectroscopy measurement of Fig. 5.7 b) does not reveal any curvature of the $T_0(1,1,)$ spin state that could be used for singlet/triplet readout in the "shallow" ("1,1") configuration. However, it would still be possible to detect dispersively the different curvature of these states close to the charge degeneracy point $\epsilon = 0$.
Because of the limitations described above we decided to move to a slower charge transition, that we cannot resolve with gate-based reflectometry but with a dynamics slower than the temporal resolution of the charge detector.

5.5. SPIN DEPENDENT TUNNELING

In this section we evaluate how the spin life-time evolves with magnetic field. Here we move to another ICT at lower filling, i.e. $(N,2)-(N+1,1)$ (stability diagram in Fig. 5.9 b).
We first move to this transition keeping the electrostatic configuration of Fig. 5.6, where the voltages of the other gates were: $V_{T1} = -0.3$ V, $V_{T3} = -0.3$ V, $V_{B1} = +0.5$ V, all below the accumulation threshold (see Fig. 5.2). We could notice, by monitoring the telegraphic noise on the interdot transition, that the interdot tunneling rate was on a Hz time scale, observable in real time by naked eye. Such a tunnel rate is probably slower than any spin life-time, and we decided to increase it.
Even though there were no barrier gate, it was possible to tweak the interdot coupling by decreasing nearby gates to $V_{B_1} = -0.4$ V and $V_{T_3} = -0.4$ V. The electrostatic repulsion of these gates pushes the two central dots closer together, increasing the tunnel coupling in the KHz range, i.e. by 3-4 orders of magnitude.
In order to study this transition we can rely only on the charge sensor. The dispersive signal from gate reflectometry indeed cannot be resolved because the tunnel rate is way lower than the frequency of the reflectometry tone. In particular, given a reflectometry tone at $\simeq 400$ MHz, we start to lose sensitivity for transitions with a tunnel rate lower than few MHz [12].

5.5.1. EVALUATION OF TUNNEL RATES AT $B = 0$ T

At $B = 0$ T the S(1,1) and the triplet states are degenerate for $|\epsilon| \gg 0$, i.e. at the charge equilibrium. We send a pulse symmetric with respect to $\epsilon = 0$ on gate B_2. The pulse sequence, amplitude (± 1 mV) and direction are indicated by green arrows in Fig. 5.9 a),b).

We highlight here that, in order to keep the energy level of the two dots at the same distance from the reservoirs levels, we should have pulsed along the detuning direction ϵ, i.e. perpendicularly to the interdot transition. Unfortunately the reflectometry lines are pass-band filtered by the LC resonator, and we cannot pulse directly on gate T_2.
Another option could have been to pulse on gate T_3, and hence on T_2 (T_3 is mainly capacitively coupled with gates T_2 and B_3), here the problem is that also the detector level would be affected this way, and we cannot send a counter-pulse to balance this effect

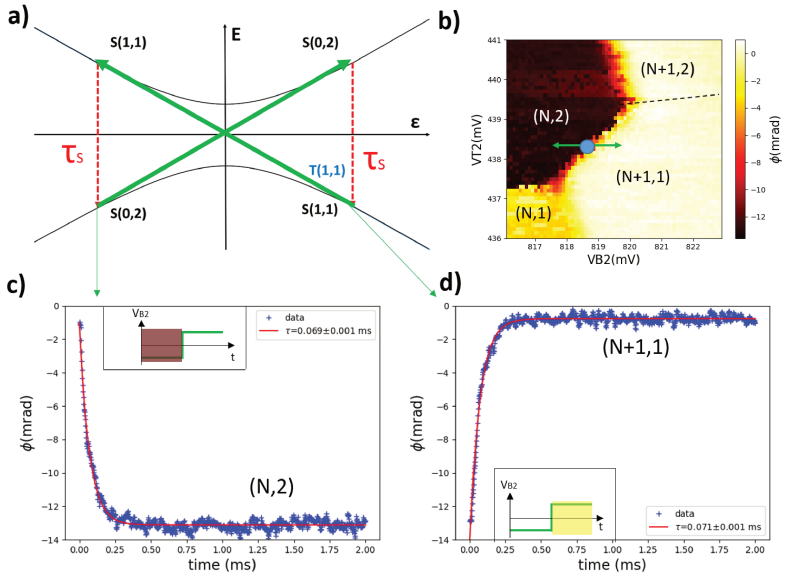

Figure 5.9: a) Energy level diagram at $B = 0$ T. b) Stability diagram of the interdot charge transition $(N+1,1) \rightarrow (N,2)$. c),d) Average charge distribution as a function of time. We send pulses on gate B_2, symmetrically to the interdot line. The pulse amplitude (± 250 μeV) and direction are indicated by the green double arrow in b). The acquisition is triggered respectively in $(N,2)$ and $(N+1,1)$. These measurements are averaged over 100 pulse sequences.

because also on B_3 there is an LC resonator for gate reflectometry.
A convenient alternative could have been to place the LC resonators on the reservoirs, such that we are able to pulse freely on each control gate, as it will be done in Sec. 6.2.

The charge sensor provides a 2-level signal that allows to directly correlate the phase value ϕ_{CS} with the population of the DQD. The time-domain traces can be fitted with a simple exponential decay $\phi = \phi_0 e^{-\frac{t}{\tau_S}}$, where the characteristic tunneling time τ_S is attributed to transitions from singlet to singlet, where no spin-flip is required.
We measured a charge transfer between the two dots on a time τ_S between 30 and 70 μs, for a detuning ϵ between 200 and 250 μeV. More importantly, by pulsing symmetrically with respect to $\epsilon = 0$, we observed the same tunneling time for both the charge transitions ($B = 0$ T), as shown in Fig. 5.9 c),d).

From the stability diagram of Fig. 5.9 b) we can also note that the dot-lead transition of the QD mainly controlled by V_{T2} is nearly horizontal. The fact that it is very slightly affected by changes in the gate voltage V_{B2} indicates that the QD is well localized below gate T_2. Conversely, the dot-lead transition of the other QD is affected by changes in both gate voltages, indicating that the other QD is located in the region between the gates T_2 and B_2.

5.5.2. SPIN DEPENDENT TUNNELING: MAGNETIC FIELD DEPENDENCE

Subsequently the magnetic field is raised, and we perform the exact same experiment as in Fig. 5.9. The field is applied perpendicularly to the plane of the Si nanowire.
The symmetry of the system is broken when we activate a magnetic field, due to PSB. In particular, we observed that tunneling time towards the (0,2)-like charge states increases with B due to PSB, while the one towards the (1,1)-like states does not depend on B.

In order to identify the PSB region we set $B = 1.8$ T and send pulses along V_{B_2}, with a total period of 14 ms and 50 % duty cycle. The acquisition is triggered on the negative side of the pulse, i.e. in $(N,2)$, for the first 450 μs, in order to identify where the tunneling is slow. This can be visualized as a trapezoidal light yellow region, corresponding to the charge state $(N+1,1)$, entering in the $(N,2)$ region. The metastable PSB region is shown in Fig. 5.10 a),b) for two different pulse amplitudes of ±0.5 mV and ±1 mV, respectively.
It can be observed that the tunneling is faster close to the triple points. The typical blockade triangle is indeed restricted to a narrow trapezoidal area, bounded by state cotunnelling via the reservoir (close to the triple points), as in Refs. [25][26].

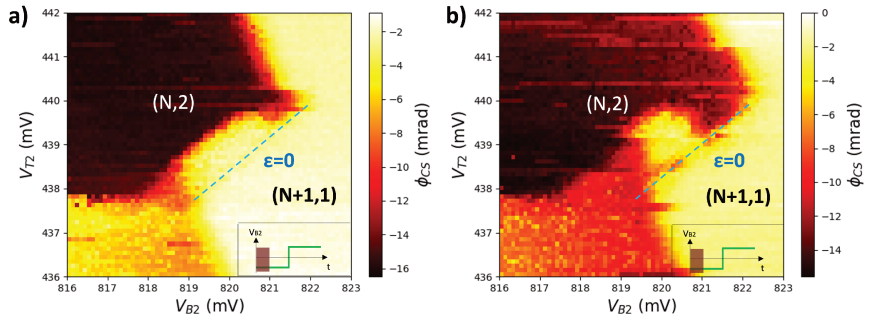

Figure 5.10: Metastable PSB region for two pulse amplitudes. The magnetic field, perpendicular to the Si channel, is set at $B = 1.8$ T. The size of the PSB region is effectively limited by the size of the pulse. A schematic of the pulse, with the time of acquisition highlighted in brown, can be found in the bottom right corner of the figures. a) Pulse amplitude $A_{B2} = \pm 0.5$ mV, and acquisition triggered for 450 μs right after pulsing in (N,2); b) Pulse amplitude $A_{B2} = \pm 1$mV, and acquisition triggered for 450 μs as in a).

It is important to consider that with a temperature of $T_e = 450$ mK, especially at low field, in (N+1,1) the system is initialized in a thermal mixture of singlet and triplet states.
In Fig. 5.11 we show the calculated occupation probabilities as a function of the magnetic field, using a simple Boltzmann distribution (see eq. 2.26).
We can do this calculation in the basis of the Zeeman Hamiltonian, which eigenstates are $\{|\downarrow,\downarrow\rangle, |\downarrow,\uparrow\rangle, |\uparrow,\downarrow\rangle, |\uparrow,\uparrow\rangle\}$ or, for coherence with the notation used, $\{T_-(1,1,), |\downarrow,\uparrow\rangle, |\uparrow,\downarrow\rangle, T_+(1,1,)\}$.
This simple calculation is valid if we neglect the nuclear field coming from the residual ^{29}Si isotopes [27][28], that induces a further splitting between $|\uparrow,\downarrow\rangle$ and $|\downarrow,\uparrow\rangle$.
By neglecting also the small difference in the g-factors of the two QDs, we can safely assume that the $|\downarrow,\uparrow\rangle$ and $|\downarrow,\uparrow\rangle$ states are degenerate in energy and they can be considered as the same state, with double weight.
Since we know the characteristic tunneling time τ_S, we can think to fit the charge occupa-

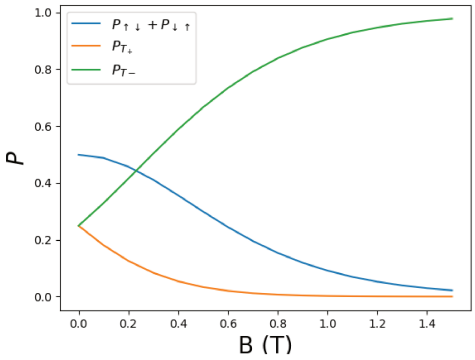

Figure 5.11: Calculated occupation probabilities using Boltzmann distribution for $T_e = 450$ mK.

tion as a function of time (at finite magnetic field) using the following formula:

$$\phi(t) = C(P_{T_-}e^{-t/\tau_{T_-}} + (P_{\uparrow\downarrow}+P_{\downarrow\uparrow})e^{-t/\tau_S} + P_{T_+}e^{-t/\tau_{T_+}}) + \phi_0 \tag{5.6}$$

that takes in account the contribution of each i state, with tunneling time τ_i, weighted with its occupation probability P_i.

The contribution of the T_+ state starts to be negligible already for $B > 0.3$ T (see Fig. 5.11) and we'll consider it always negligible in this analysis. Since we know τ_S we can fit the time-domain curves using only the population P_{T_-} and the $T_-(1,1) - S(0,2)$ tunneling time τ_{T_-} as free parameters.
An example of this double exponential fit is shown in Fig. 5.12 b), where we extract $\tau_{T_-} \simeq 1.5$ ms for $B = 1.5$ T.

In Fig. 5.12 c) we plot the tunneling time τ_{T_-}, extracted by fitting the charge sensor phase signal at each magnetic field using eq. 5.6. In panel d) we plot the corresponding (measured and calculated) occupation probabilities P_{T_-}.
We observed a tunneling time τ_{T_-} that increases with magnetic field, as in Ref. [29].

The decay from $|\downarrow,\downarrow\rangle$ to the singlet (0,2) can be seeen as two-step process. An excitation from $|\downarrow,\downarrow\rangle$ to either $|\uparrow,\downarrow\rangle$ or $|\downarrow,\uparrow\rangle$, followed by a spin-conserving relaxation to S(0,2). At relatively large magnetic fields (i.e. above $\simeq 1$ T) the first process is the slowest one, dominating the overall dynamics of the (1,1)→(0,2) transition. Figure 5.12 c) shows the experimental magnetic-field dependence of τ_{T_-}, and a fit to

$$\tau_{T_-}(B) = \frac{1}{\Gamma_0 e^{(-g\mu_B B/k_B T)}} \tag{5.7}$$

with the rate Γ_0 as fitting parameter. We find $\Gamma_0 = 54$ KHz.
The fitting formula can be understood considering that, as stated by the detailed balance condition [30], we expect the ratio between the excitation and relaxation tunnel rates to be proportional to the ratio of the populations of the excited and ground state at equilibrium:

$$\frac{\Gamma_{exc}}{\Gamma_{rel}} = \frac{P_{\downarrow\uparrow}+P_{\uparrow\downarrow}}{P_{\downarrow\downarrow}} = 2e^{-g\mu_B B/k_B T} \tag{5.8}$$

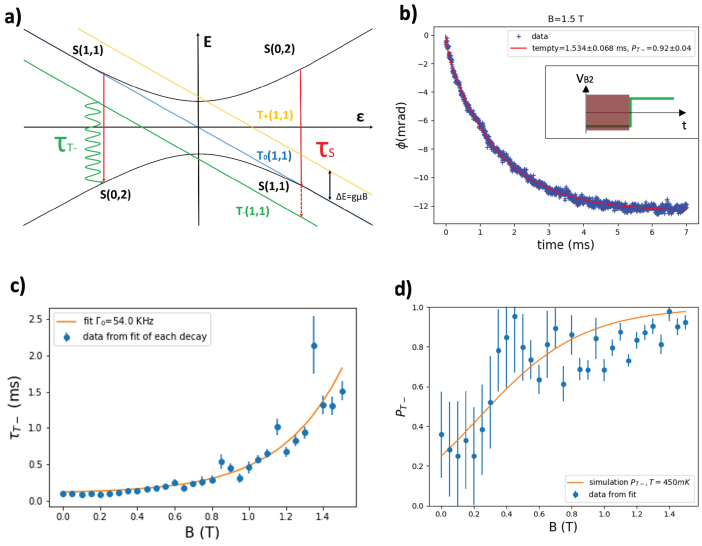

Figure 5.12: a) Energy level diagram of a DQD with magnetic field. The two-spin states T_+, T_- are separated in energy due to Zeeman splitting. At sufficiently large B, the ground state in the (N+1,1) configuration becomes a spin triplet T_- . As a result, charge relaxation from $(N+1,1)$ to $(N,2)$ is suppressed by PSB. b) The blue trace provides the averaged dynamics of charge relaxation at $B = 1.5$ T, giving a tunneling time of τ_{T_-}=1.5 ms, much longer than the one measured for the opposite pulsing direction, from $(N+1,1)$ to $(N,2)$, which remains essentially independent of B. c) Measured B dependence of the tunneling time τ_{T_-} from $(N+1,1)$ to $(N,2)$, as extracted from fitting the time-domain curves as in b) for different values of B. The orange curve fits the B field dependence of τ_{T_-} using formula 5.7 d) Measured B dependence of the population P_{T_-} in $(N+1,1)$ to $(N,2)$, extracted by fitting the time-domain curves at different values of B. The orange curve is the expected population of the $T_-(1,1)$ state, shown in Fig. 5.11.

and that $\tau_{T_-} = 1/\Gamma_{exc}$.

Assuming that Γ_0 ($2\Gamma_{rel}$) is independent of B is therefore an approximation. More generally, $\Gamma_{rel} = T_1^{-1}$ is expected to be a polynomial function of B with exponents depending on the nature of the dominant phonon/photon assisted relaxation process [31][14]. Our data do not allow us to capture this power-law dependence.

5.6. FAST, HIGH-FIDELITY CHARGE-SENSING OF SPIN DEPENDENT TUNNELING

Here we benchmark the charge readout fidelity of our sensor. The time-domain curves shown till here, as for example in Fig. 5.9 c),d) and in Fig. 5.12 b), are averaged over 1000 time-domain traces taken with 5 μs integration time per data point. s
An example of one of such traces (for B=1.5 T) is shown in Fig. 5.13. Charge tunneling events are clearly revealed as abrupt changes in ϕ_{CS}, demonstrating fast single-shot detection.
In order to estimate the fidelity, we have measured the phase of the sensor after a delay time of 6 ms in each charge region (acquisition points indicated by vertical dashed lines in Fig. 5.13), which largely exceeds τ_{T_-} (and hence τ_S) ensuring that tunneling has occurred every time before measuring.

For clearliness we also highlight that the charge signal right after pulsing in (N,2) is lower than the one observed in (N+1,1) just because of the capacitive coupling between gate B_2 (where we apply pulses) and the detector, and no other charge state is involved.

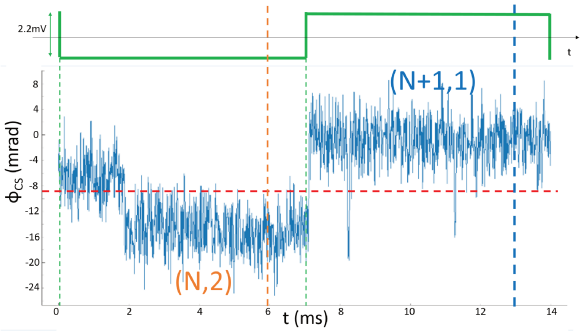

Figure 5.13: Single-shot trace and corresponding sketch of the voltage pulse on B_2. The pulse period is 14 ms. The sensor quantum dot is tuned in order to maximize the phase jump resulting from the $(N,2) \rightarrow (N+1,1)$ charge transition. Here $B = 1.5$ T and the spin-blockaded reversed transition $(N+1,1) \rightarrow (N,2)$ occurs on a 2-ms time scale. The two vertical dashed lines indicate the acquisition times (with 5μs integration) for the histogram of Fig. 5.14. The red dashed line represents the single-shot readout threshold for the two charge states, that we estimate as the intercept between the two Gaussian distributions of Fig. 5.14.

The histogram of the phase measured over 1000 events in each charge region is shown in Fig. 5.14. We obtained two distinct distributions that correspond to the charge states $(N,2)$ and $(N+1,1)$, which give an average charge readout fidelity of F=97% for an integration time of 5 μs. The overall fidelity is calculated as in Refs. [32][33]:

$$F = 1 - \frac{N^{wrong}_{(N,2)}}{N^{tot}_{(N,2)}} - \frac{N^{wrong}_{(N+1,1)}}{N^{tot}_{(N+1,1)}} \tag{5.9}$$

where the ratio N^{wrong}/N^{tot} is the probability of having an error in identifying a certain charge state. The error is detected when a point, expected to be in a certain charge region is above (or below) the readout threshold, which is identified by the overlap of the two Gaussian distributions of Fig. 5.14 (at $\phi \simeq -9$ mrad) .

The main source of noise comes from the thermal noise of the low noise amplifier placed at the 4K stage of the cryostat.
As we will see in the next chapter with our setup the best way to improve the SNR is simply to increase the signal of the resonator.
Our fidelity is also limited by thermal excitations. These excitations are clearly visible in the single-shot trace, in particular from $(N+1,1)$ to $(N,2)$.
In order to obtain such a signal we tune our detector on the dot-lead transition with the highest signal-to-noise ratio (SNR≃150 for an integration time of 10 ms).
Compared for example to Ref. [4], where a similar readout technique and device are used, the gate-based charge readout time can be reduced by more than one order of magnitude.
Moreover we highlight that, by doubling the integration time, we could reach a charge readout fidelity above 99%.

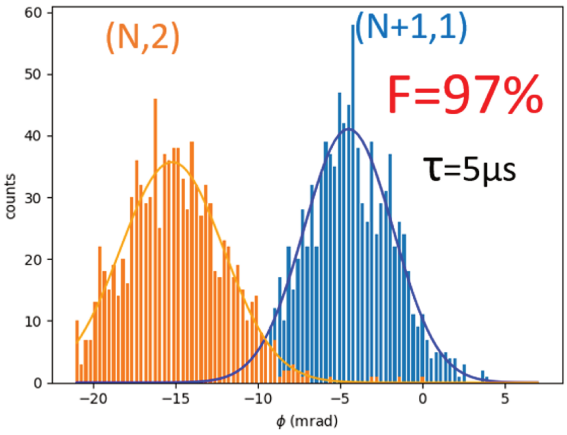

Figure 5.14: Charge readout fidelity and histogram of the phase values measured at the two charge configurations, $(N,2)$ and $(N+1,1)$. To acquire this data set, we applied a square-wave voltage pulse to B_2 as indicated in Fig. 5.9 b), with the same long period as in Fig. 5.13 (14 ms). To ensure full charge relaxation, phase values were recorded 6 ms after each voltage step region (orange and blue vertical dashed lines in Fig. 5.13), with an integration time of τ =5 μs. We estimate a corresponding charge readout fidelity of F=97 %.

One last remark about this measurement is that, even if we are measuring a charge transition ruled by PSB, our capacity to temporally resolve a spin, i.e. the spin readout fidelity, is limited by the average interdot tunneling time τ_S. Indeed, after the spin-flip, it is still necessary to wait a certain τ_S for the interdot tunneling event.
In other words we have an average uncertainty of $\tau_S \simeq 70$ μs between the spin-flip and the tunneling event that allows spin-to-charge conversion.
With a tunneling time τ_S shorter than the integration time instead we could have assumed that charge and spin readout fidelity were the same, as for example in Ref. [34], where the interdot tunneling can be tuned at will.

5.7. ELECTRIC DIPOLE SPIN RESONANCE (EDSR)

A powerful way of manipulating spins in semiconductors is electric dipole induced spin resonance (EDSR), which uses a high-frequency electric-field to induce coherent spin rotation.
Here we experimentally investigate EDSR applied to electrons in silicon. The electrical manipulation relies on the spin-orbit coupling (SOC), which in silicon is way weaker for electrons than for holes.
Because of the generally small intrinsic SOC of electrons in silicon QDs, the direct electrical driving is typically weak, and hence most of the demonstrations of EDSR rely on a synthetic SOC induced through a micromagnet[35][36][37][38]. However, the SOC can become significant if the electron is allowed to move between orbital configurations within the quantum dot [39].
So far (to my knowledge) only two demonstrations of EDSR rely on the intrinsic SOC of electrons in silicon. In the case of Ref. [40] the SOC is enhanced by the hybridization between spin and valley states, while in the case of Ref. [41] it is enhanced by the hybridization between states with different orbital configurations.
The experiment shown here provides further evidence of EDSR revealing a relatively weak

SOC in our system.
Also in this case the SOC is probably enhanced by the hybridization with an excited state (valley or orbital), but further investigation would be required to clarify its exact origin.

We apply pulses to gate B_2, with amplitude $A_{B_2} = \pm 1$ mV, a total period of 2 ms and a 50% duty cycle. The gate voltages and pulses are calibrated such that the DQD charge state oscillates between the (N+1,1) and the metastable (N,2) state, i.e. in the middle of the PSB region of Fig. 5.10 b). The amplitude of the pulses is calibrated such that the ϵ-dependent tunneling time is $\tau_S = 70$ μs, as measured in Fig. 5.9.
For simplicity from now on we'll refer to these states as (1,1) and (0,2).
Superimposed to the pulse we also send a continuous microwave(μw) excitation, whose frequency should match the Zeeman splitting $E_Z = g\mu_B B$.
We acquire the average phase signal during this two level pulse sequence.

In the range of magnetic field of Fig. 5.15, between 0.4 and 0.7 T, when no spin is driven the characteristic time of the $(1,1) \rightarrow (0,2)$ transition is $\tau_{T_-} \simeq 200$ μs, while the reverse $(0,2) \rightarrow (1,1)$ transition occurs in $\tau_S \simeq 70$ μs.
When we don't excite any spin therefore we expect an average population unbalanced to the (1,1) state (higher phase), in particular we expect to be on average in (1,1) for 1.13 ms and in (0,2) for 0.87 ms.
The resonant μw excitation acts predominantly on the spin confined in the dot closer to B_2, which should in fact be located between in the region between B_2 and T_2 as discussed in Sec. 5.5.1. As discussed below, we only observe one clear EDSR, and we thus ascribe it to the dot closer to gate B_2. The other QD (under T_2) lies further away from modulated B_2 gate, which may explain the absence of the corresponding EDSR signal.
When the DQD is in the (1,1) state the system oscillates between the $T_-(1,1)$ and the Zeeman eigenstate $|\downarrow,\uparrow\rangle$, much faster than the interdot tunneling time τ_S. When we pulse in the (0,2) charge region the DQD state keeps on oscillating between $T_-(1,1)$ and $|\downarrow,\uparrow\rangle$, until the interdot tunneling event, which occurs within the characteristic tunneling time $\tau_S = 70$ μs.
The average tunneling time of the (1,1)-(0,2) transition therefore gets reduced under resonant driving. As a result, we expect a negative signal corresponding to an increased (0,2) population. In line with the previous consideration the magnitude of the phase signal observed under resonant driving is of the order of 5−10% of the overall phase signal.

In Fig. 5.15 a),b) we plot the average charge sensor signal during the pulse sequence, as a function of the excitation frequency and magnetic field (for two different powers of the microwave excitation and two different magnetic field ranges).
In Fig. 5.16 we plot again the EDSR signal of Fig. 5.15 b). This image actually corresponds to the original acquisition (after subtracting the background and renormalizing the color scale).
Indeed these measurement are extremely time consuming, and we tried to reduce their duration by scanning in a range close to the expected one. The expected Landé g-factor for electrons decoupled from the environment is $g = 2$, that means we expect to match the Zeeman splitting energy around a Larmor frequency of

$$f_0 = \frac{2\mu_B B}{h} \tag{5.10}$$

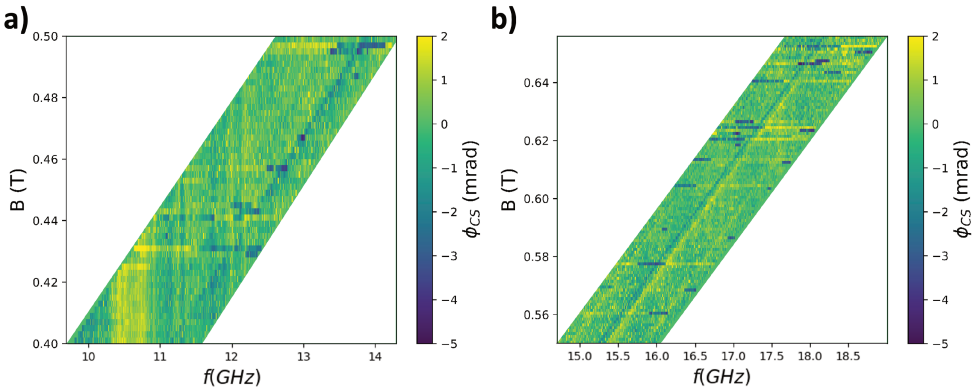

Figure 5.15: Frequency of microwaves excitation vs magnetic field. a) μw power=-65 dBm,b) μw power=-45 dBm. Plots acquired continuously while pulsing between $(N+1,1)$ and $(N,2)$ and sending μw excitation for all the duration of the pulse sequence. The background is subtracted to highlight the EDSR line.

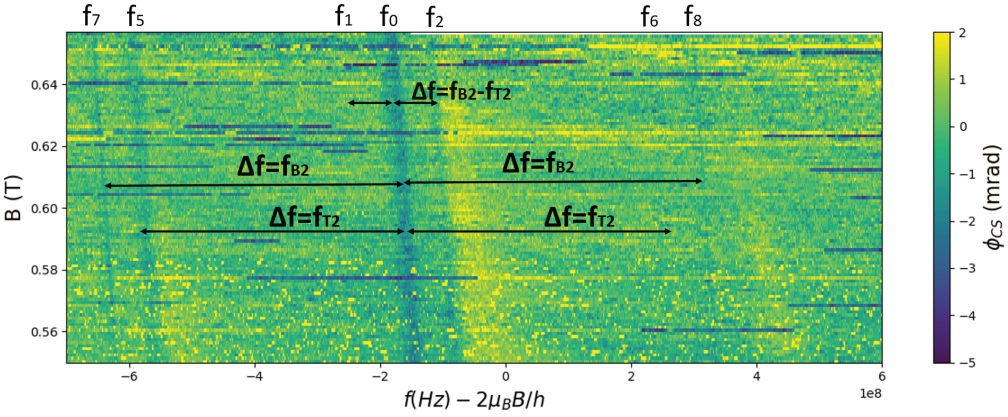

Figure 5.16: Frequency of microwaves excitation vs magnetic field, same range as Fig. 5.15 b). The frequency range (x axis) is centered at the expected Larmor frequency (g=2) for each magnetic field. The black double arrows indicate the expected and observed sidebands, due to the mixing between the excitation frequency and the reflectometry tones f_{T_2}=407.2 MHz and f_{B_2}=478.2 MHz .

The horizontal axis of Fig. 5.16 is centered at the expected Larmor frequency for each magnetic field. If $g = 2$ we would expect a vertical line centered around this axis.
We observe that the main signal is at a slightly smaller frequency than the expected one and it is not vertical, as one would expect for $g = 2$.
From the Larmor frequency $f_L(B) = (g\mu_B B)/h$ we can easily extract the g-factor.
For a magnetic field of $B = 0.55$ T we find a Larmor frequency of $f_L = 15.251 \pm 0.001$ GHz, which provides the electron g-factor $g = 1.981 \pm 0.001$.
We can extract the g-factor also from the slope of the EDSR line in the B vs f plane. We observe a shift in the Larmor frequency of $\Delta f = 31 \pm 2$ MHz for $\Delta B = 107$ mT, finding again the g-factor $g = 1.979 \pm 0.002$ GHz, consistent with the one extracted from the Larmor frequency.
The value obtained is close to the ones of Ref. [42], where it is also used a silicon on insulator platform, and a g-factor between 1.92 and 1.96 has been reported for a single dot, depending on the magnetic field direction.

In Fig. 5.16 we can observe four other lines appearing at frequencies different from the one of the main EDSR line at f_0. These lines are originated from processes of wave mixing between the EDSR signal and the two reflectometry tones at frequencies $f_{T_2} = 407.2$ MHz and $f_{B_2} = 478.2$ MHz.
It is well known that a frequency mixer can be built just by injecting the local oscillator signal (LO) and the intermediate frequency signal (IF) in the gate of a field effect transistor in saturation regime, which has an exponential (non linear) electrical response. However, we cannot explain the observed sidebands in these terms, because there is no current flowing through the device.
An overview of the possible mechanisms leading to nonlinear mixing in QDs can be found in Refs. [36] [43]. The origin of the nonlinearity can be attributed to: a position dependent magnetic field gradient, an anharmonic confining potential or a driving magnetic field not perpendicular to the static magnetic field [44]. According to Ref. [45] the nonlinear mixing is also expected for strongly interacting dots near the (1,1)-(0,2) charge transition. However, we are not sure that in our case the weak coupling between the dots is strong enough to enable the nonlinear mixing between the EDSR signal and the reflectometry tones.
Although the microscopic origin of the nonlinearity is not fully clear, in analogy with nonlinear optical elements [46], we can look at this process as generated by an effective nonlinear susceptibility ($\chi^{(i)}$) .

The energy and momentum conservation conditions give raise to signals at frequencies:

$$f_1 = f_0 + f_{B2} - f_{T2}$$
$$f_2 = f_0 - f_{B2} + f_{T2}$$
$$f_3 = f_0 + f_{B2} + f_{T2}$$
$$f_4 = f_0 - f_{B2} - f_{T2}$$

This four wave mixing (due an effective third order nonlinearity $\chi^{(3)}$), or 3-photon process, is at the origin of the sideband at $\Delta f = +70$ MHz= $f_{B2} - f_{T2}$ from the main EDSR line. We would expect also a line at $\Delta f = -70$ MHz from the main EDSR line but in this case the nonlinear coupling between the signals is too weak.
The sidebands at $f_{3,4}$ are outside the observed frequency range.
We are dealing also with three wave mixing (due an effective second order nonlinearity

$\chi^{(2)}$), or two-photon processes, where energy and momentum conservation gives four sidebands at frequencies:

$$f_{5,6} = f_0 \pm f_{T_2}$$
$$f_{7,8} = f_0 \pm f_{B_2}$$

5.7.1. DETUNING DEPENDENCE OF EDSR

We did the same experiment as in Fig. 5.15, shining microwaves continuously while pulsing between the two charge states (N,2) and (N+1,1). The magnetic field is fixed at $B = 0.4$ T and we scan the gate voltage V_{B_2}, while sweeping frequency (see Fig. 5.17).
We observe that the Larmor frequency $f_L = 11.085$ GHz is detuning independent, coherently with a system where the tunnel coupling energy between the dots is small. Indeed, in

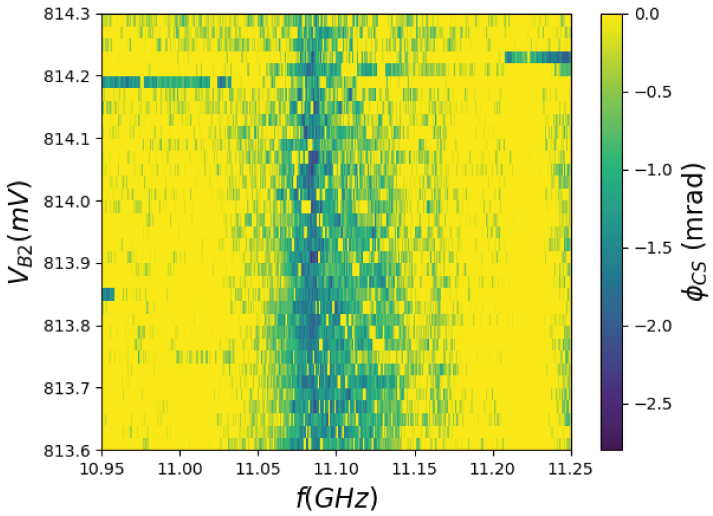

Figure 5.17: Dependence of EDSR signal from gate voltage V_{B_2}. Here $B = 0.4$ T. The background has been subtracted, to enhance the signal visibility. The pulse amplitude is kept constant while sweeping V_{B_2}, meaning that both initialization and readout point are shifted during the measurement.

the limit of very small interdot coupling $t \ll g\mu_B B$ and $t \ll \epsilon$, also the exchange coupling between the dot vanishes. In terms of the energy diagram (as the one of Fig. 5.12 a)) this means to draw the bonding and antibonding states with a crossing (the anticrossing size is determined by the tunnel coupling energy).
In this case the energy distance between $T_-(1,1)$ and $|\downarrow,\uparrow\rangle$ is constant and equal to $g\mu_B B$, regardless of the energy detuning ϵ and therefore we expect the Larmor frequency to be independent by ϵ.
Also the average thermal population of $T_-(1,1)$ and $|\downarrow,\uparrow\rangle$ at equilibrium stays constant when varying the gate voltage V_{B_2}.
In the measurement both the initialization and readout points are shifted when varying V_{B_2} and this results in small variation of intensity in the EDSR signal (partially washed out by the background subtraction). This can be understood considering that the tunnel rates (both τ_S and τ_{T-}) depends on the energy detuning ϵ (controlled by V_{B_2}) between two QDs.

This means that also the average charge population during the the 2 ms pulse sequence, which is not same as the average population at equilibrium, is detuning dependent.

This plot is a further confirmation that the two QDs are almost completely uncoupled and we are driving a single-spin transition in the quantum dot below gate B_2, whose frequency does not depend on the energy detuning between the two QDs.

5.8. DOUBLE ARRAYS OF QUANTUM DOTS: HOW TO SCALE UP?

In the final section of this chapter we propose a scheme for scaling up the charge-sensing readout [10] on a bilinear array design as the one studied through this chapter. Finally I briefly discuss and compare different designs of qubit arrays[1][47].

In the experiments described throughout this chapter we used the transition between a quantum dot and its nearby reservoir to sense the DQD system nearby. What is actually required for this sensing technique to work properly is just a transition (that can be sensed with dispersive readout) of an object that is capacitively coupled with the DQD system under study. Moreover, to keep the DQD well isolated, it should not be tunnel coupled with the sensor.

Our proposal is based on the idea that a charge reservoir is not strictly necessary to perform RF charge-sensing and also a transition between two QDs could be exploited. When using dispersive readout the SNR of an interdot transition could be optimized by tuning the interdot tunneling rate such that the reflectometry response is maximized [12], and by optimizing the resonator matching.
A visual representation of the scheme proposed is shown in Fig. 5.18. The architecture proposed is a double array of split gates, where one array (in red) contains the information qubits and the other one (in violet) is used for the readout via RF charge-sensing. The elementary cell of such an architecture (surrounded by the black dashed line) is made of three information qubits ($Q_{N-1,N,N+1}$), one ancillary qubit (AQ) initialized in a spin $|\downarrow\rangle$ state and two QDs (S_1 and S_2) for RF charge-sensing.

The spin-to-charge conversion is based on PSB readout and, after fixing the spin state of the AQ in the $|\downarrow\rangle$ state, tunneling would be allowed only if the spin in Q_N is in the $|\uparrow\rangle$ state. If tunneling is allowed the charge sensor would sense the increased number of charges in the AQ.

Finally the readout of the spins in Q_{N-1} and Q_{N+1} can be performed through swap operation with Q_N and then sequentially reading their spin through PSB.
The elementary cell described can then be replicated infinitely along the array.
One fundamental remark is that for such a scheme to work properly it is crucial to have local control over the tunnel coupling, as it could be done for example by adding a second layer of gates positioned in between each nearby gate. Indeed, in order to perform fast two-qubit logic operations, it is required to have a fast tunnel coupling between each qubit in the upper array. A fast tunneling between Q_N and AQ instead would allow a fast readout. At the same time we want the sensor to be sensitive only to the state of AQ and therefore we should suppress the tunnel coupling between qubits $Q_{N,N-1,..}$ and sensing dots.

In an alternative scheme it would also be possible to connect a common reservoir to the sensing array and apply the RF charge-sensing readout on transitions between single dots

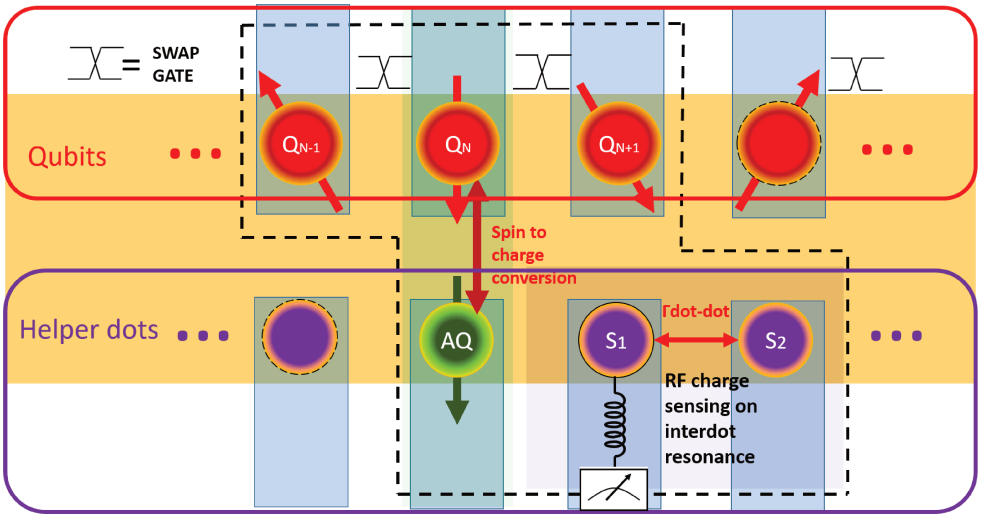

Figure 5.18: Proposal of scalable linear qubit register based on FDSOI nanowire technology. Qubit readout is performed using a parallel array of helper dots. Each repeatable elementary cell consists of three spin qubits and three helper dots, one used as ancilla qubit (AQ) and the other two (S_1 and S_2) as charge-sensing double dot, which is tuned to an interdot resonance. Readout of qubit Q_N is performed by enforcing electron spin-dependent tunneling from Q_N to AQ. Readout of Q_{N-1} (Q_{N+1}) is performed by the same process following a swap operation to exchange Q_{N-1} (Q_{N+1}) and Q_N. Q_{N+1}, Q_N, and Q_{N+1} can then be consecutively measured with a small set of swap and spin-measurement operations.

and the common reservoir. This approach would be similar to what has been proposed in Ref. [47] (Fig. 5.19 b)), relying on undoped Si/SiGe heterostructures. In this case each dot in the sensing array is connected to two reservoirs, allowing local charge-sensing of the qubit array, using either transport or dispersive readout.

We now consider another interesting bilinear array, recently presented by Intel [1]. In this case case the two arrays of QDs are on two separate, closely spaced, and capacitively coupled nanowires (Fig. 5.19 a)). The readout is performed by monitoring how the current flowing in the sensing array is affected by spin dependent transitions in the qubit array. Whereas using two separate nanowires might be an advantage compared to our scheme, because it inhibits tunneling events between the two arrays, on the other hand the spin-to-charge conversion is performed using energy-selective readout with the nearby reservoir and this would hardly be scalable, since it does not allow to read multiple electrons simultaneously and does not allow to probe the state of QDs that are far away from the reservoir.
Also in this case these problems could be solved by using RF charge-sensing on an interdot transition in the sensing array, instead than measuring current on a dot-lead transition.

The electrostatic coupling between the sensors and the QDs, and consequently the sensor sensitivity, can be enhanced by the presence of floating gates connecting the two nanowires (Fig. 5.19 c)), as it has been shown in Ref. [6]. This platform is very similar to the one of [1], except for the presence of floating gates, and again we could think to monitor spin dependent tunneling between QDs in the qubit array by doing charge-sensing on an interdot transition in the sensing array.

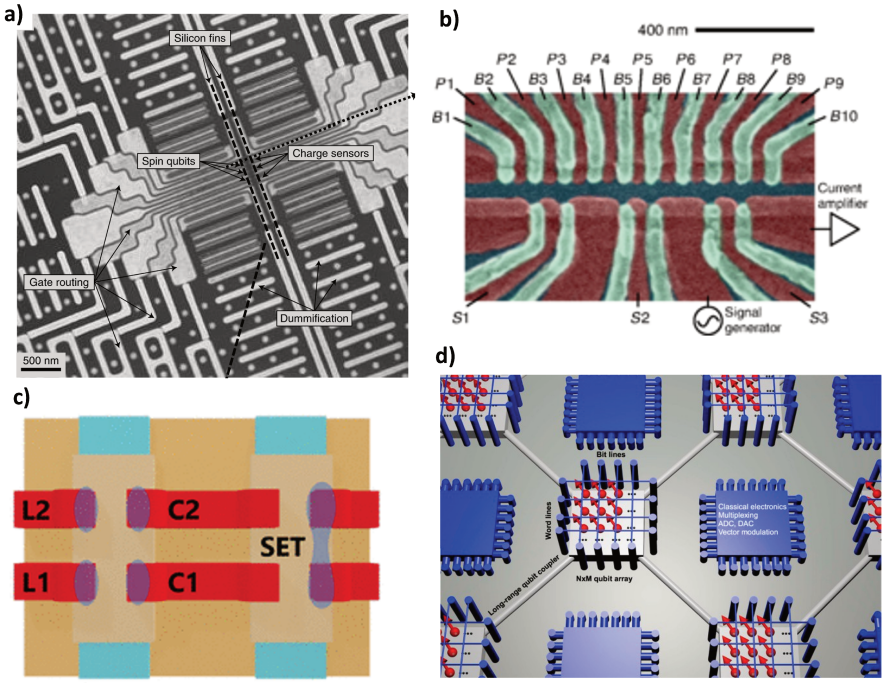

Figure 5.19: a) High-angle annular dark-field scanning transmission electron microscopy image (HAADF-STEM) of a SiMOS device with a double array of QDs recently presented by Intel [1]. b) False-color SEM image of a linear array of nine QDs [47], controlled by plunger gates P(1-9) and barrier gates B(1-10) and read by QD-based charge sensors S1, S2 and S3. c) Schematic layout of the device of Ref. [6]. Two nanowires are connected by floating gates C1 and C2, that increase the capacitive coupling between QDs belonging to different nanowires, increasing the sensitivity of the sensing array. d) Schematic layout of the architecture proposed in Ref. [48]. One elementary cell of N×M QDs encodes the logical qubit. Long-range spin-spin coupling can be achieved via a superconducting resonator [49].

It is worth to mention here that also the gate-based dispersive readout can be suitable for a scalable qubit readout, and this will be discussed more in detail in Sec. 6.6.4.

We discussed mainly the problem of a scalable readout, and a double array of gates combined with dispersive readout seems to be a good solution. However, it is important to consider that the main limitation of working with qubit arrays is that the interactions are limited to the nearest-neighbour. It has been proposed that quantum error correction could be realized in linear arrays [50]. The proposal is based on the nine qubit code introduced by Shor [51]. A single logical qubit can be realized with a minimum of 14 QDs (encoding 13 qubits) in a linear arrangement. This encoding scheme requires two qubit gates between qubits that cannot all be local in a linear arrangement and the nonlocal interactions must be mediated by SWAP gates.
It is clear that realizing multiple logical qubit on the same array would require a very high number of SWAP operation that might eventually degrade the qubit performances.
Also in the so-called surface code it takes a minimum of thirteen physical qubits to implement a single logical qubit [52], but a 2-D geometry would significantly reduce the number of SWAP gates necessary. However, linear and bilinear arrays might be suitable

for some proof of principle calculations.
In the perspective of scaling up to platform with hundreds of qubits it will be necessary to entangle qubits that are relatively far away from each other. An interesting proposal [48] envisions to separate each logical qubit into an elementary cell within which error correction can be realized (Fig. 5.19 d)). The coupling between spins belonging to different elementary cell can be mediated by microwave photons in a superconducting cavity, as recently demonstrated in Ref. [49] where are entangled spins of electrons that are separated by more than 4 mm.

Another important problem is the simultaneous manipulation of many qubits . Conventional manipulation techniques of electrons usually rely on an ESR stripline for magnetic manipulation, or on a micromagnet that enables a synthetic SOC and hence electrical manipulation. Both these techniques are quite invasive and imposes severe constraints in terms of scalability.
The easiest approach in terms of hardware is to drive the electron spin electrically, relying on its intrinsic SOC. As it has been shown in Sec. 5.7, electrons in silicon possess a SOC that can allow electrical manipulation, but often this effect is too small to allow coherent driving. In a recent paper it has been demonstrated that the naturally weak SOC in silicon can be enhanced by controlling the energy quantization of electrons in the nanostructure [41], enhancing the orbital motion. Another degree of freedom to control the SOC is the direction of the magnetic field applied [42]. This engineering of the SOC depends heavily on the energetic structure of a DQD, that can be tuned with a barrier gate to maximize the hybridization between orbital or valley states, and consequently the SOC. The results of Ref. [41] paves the way for the electrical manipulation of electrons in silicon on large scale.

There are many different architectures investigated all around the world like linear and bilinear arrays, but also 2-D [53] and 3-D structures [54].
Investigating all these platforms requires a significant scientific and technological effort in terms of design, setup, and material optimization.
Undoubtedly building large-scale quantum systems present gigantic challenges. However, the pace at which the field is growing and the strong effort of both academies and large tech companies leaves room for optimism.

BIBLIOGRAPHY

[1] A. M. J. Zwerver et al. “Qubits made by advanced semiconductor manufacturing”. In: *Nature Electronics* 5.3 (Mar. 2022), pp. 184–190. ISSN: 2520-1131. DOI: 10.1038/s41928-022-00727-9. URL: https://doi.org/10.1038/s41928-022-00727-9.

[2] R. Li et al. “A flexible 300 mm integrated Si MOS platform for electron- and hole-spin qubits exploration”. In: *2020 IEEE International Electron Devices Meeting (IEDM)*. 2020, pp. 38.3.1–38.3.4. DOI: 10.1109/IEDM13553.2020.9371956.

[3] Fabio Ansaloni et al. “Single-electron operations in a foundry-fabricated array of quantum dots”. In: *Nature Communications* 11.1 (Dec. 2020), p. 6399. ISSN: 2041-1723. DOI: 10.1038/s41467-020-20280-3. URL: https://doi.org/10.1038/s41467-020-20280-3.

[4] Emmanuel Chanrion et al. “Charge Detection in an Array of CMOS Quantum Dots”. In: *Phys. Rev. Applied* 14 (2 Aug. 2020), p. 024066. DOI: 10.1103/PhysRevApplied.14.024066. URL: https://link.aps.org/doi/10.1103/PhysRevApplied.14.024066.

[5] Theodor Lundberg et al. “Spin Quintet in a Silicon Double Quantum Dot: Spin Blockade and Relaxation”. In: *Phys. Rev. X* 10 (4 Oct. 2020), p. 041010. DOI: 10.1103/PhysRevX.10.041010. URL: https://link.aps.org/doi/10.1103/PhysRevX.10.041010.

[6] Will Gilbert et al. “Single-Electron Operation of a Silicon-CMOS 2 × 2 Quantum Dot Array with Integrated Charge Sensing”. In: *Nano Letters* 20.11 (Nov. 2020), pp. 7882–7888. ISSN: 1530-6984. DOI: 10.1021/acs.nanolett.0c02397. URL: https://doi.org/10.1021/acs.nanolett.0c02397.

[7] Jingyu Duan et al. “Remote Capacitive Sensing in Two-Dimensional Quantum-Dot Arrays”. In: *Nano Letters* 20.10 (Oct. 2020).

[8] A. Crippa et al. “Gate-reflectometry dispersive readout and coherent control of a spin qubit in silicon”. In: *Nature Communications* 10.1 (July 2019), p. 2776. ISSN: 2041-1723. DOI: 10.1038/s41467-019-10848-z. URL: https://doi.org/10.1038/s41467-019-10848-z.

[9] Rami Ezzouch et al. “Dispersively Probed Microwave Spectroscopy of a Silicon Hole Double Quantum Dot”. In: *Phys. Rev. Applied* 16 (3 Sept. 2021), p. 034031. DOI: 10.1103/PhysRevApplied.16.034031. URL: https://link.aps.org/doi/10.1103/PhysRevApplied.16.034031.

[10] A. Aprà et al. “Dispersive vs charge-sensing readout for linear quantum registers”. In: *2020 IEEE International Electron Devices Meeting (IEDM)*. 2020, pp. 38.4.1–38.4.4. DOI: 10.1109/IEDM13553.2020.9372090.

[11] Hans Huebl et al. “Electron tunnel rates in a donor-silicon single electron transistor hybrid”. In: *Phys. Rev. B* 81 (23 June 2010), p. 235318. DOI: 10.1103/PhysRevB.81.235318. URL: https://link.aps.org/doi/10.1103/PhysRevB.81.235318.

[12] M. G. House et al. “Radio frequency measurements of tunnel couplings and singlet–triplet spin states in Si:P quantum dots”. In: *Nature Communications* 6.1 (Nov. 2015), p. 8848. ISSN: 2041-1723. DOI: 10.1038/ncomms9848. URL: https://doi.org/10.1038/ncomms9848.

[13] R Maurand et al. “A CMOS silicon spin qubit”. In: *Nature Comm.* 7 (2016), p. 13575.

[14] L. Petit et al. “Spin Lifetime and Charge Noise in Hot Silicon Quantum Dot Qubits”. In: *Phys. Rev. Lett.* 121 (7 Aug. 2018), p. 076801. DOI: 10.1103/PhysRevLett.121.076801. URL: https://link.aps.org/doi/10.1103/PhysRevLett.121.076801.

[15] J van der Heijden et al. “Spin-orbit dynamics of single acceptor atoms in silicon”. In: *Science Adv.* 4.12 (2018), eaat9199.

[16] M. Xiao, M. G. House, and H. W. Jiang. “Measurement of the Spin Relaxation Time of Single Electrons in a Silicon Metal-Oxide-Semiconductor-Based Quantum Dot”. In: *Phys. Rev. Lett.* 104 (9 Mar. 2010), p. 096801. DOI: 10.1103/PhysRevLett.104.096801. URL: https://link.aps.org/doi/10.1103/PhysRevLett.104.096801.

[17] C. H. Yang et al. “Spin-valley lifetimes in a silicon quantum dot with tunable valley splitting”. In: *Nature Communications* 4.1 (June 2013), p. 2069. ISSN: 2041-1723. DOI: 10.1038/ncomms3069. URL: https://doi.org/10.1038/ncomms3069.

[18] C. B. Simmons et al. “Tunable Spin Loading and T_1 of a Silicon Spin Qubit Measured by Single-Shot Readout”. In: *Phys. Rev. Lett.* 106 (15 Apr. 2011), p. 156804. DOI: 10.1103/PhysRevLett.106.156804. URL: https://link.aps.org/doi/10.1103/PhysRevLett.106.156804.

[19] T. Bédécarrats et al. “A new FDSOI spin qubit platform with 40nm effective control pitch”. In: *2021 IEEE International Electron Devices Meeting (IEDM)*. 2021, pp. 1–4. DOI: 10.1109/IEDM19574.2021.9720497.

[20] Florian Vigneau et al. *Probing quantum devices with radio-frequency reflectometry*. 2022. DOI: 10.48550/ARXIV.2202.10516. URL: https://arxiv.org/abs/2202.10516.

[21] Virginia N. Ciriano-Tejel et al. “Spin Readout of a CMOS Quantum Dot by Gate Reflectometry and Spin-Dependent Tunneling”. In: *PRX Quantum* 2 (1 Mar. 2021), p. 010353. DOI: 10.1103/PRXQuantum.2.010353. URL: https://link.aps.org/doi/10.1103/PRXQuantum.2.010353.

[22] MD Schroer et al. “Radio frequency charge parity meter”. In: *Phys. Rev. Lett.* 109.16 (2012), p. 166804.

[23] L. DiCarlo et al. “Differential Charge Sensing and Charge Delocalization in a Tunable Double Quantum Dot”. In: *Phys. Rev. Lett.* 92 (22 June 2004), p. 226801. DOI: 10.1103/PhysRevLett.92.226801. URL: https://link.aps.org/doi/10.1103/PhysRevLett.92.226801.

[24] Ryo Mizuta et al. “Quantum and tunneling capacitance in charge and spin qubits”. In: *Phys. Rev. B* 95.4 (2017), p. 045414.

[25] B. M. Maune et al. “Coherent singlet-triplet oscillations in a silicon-based double quantum dot”. In: *Nature* 481.7381 (Jan. 2012), pp. 344–347. ISSN: 1476-4687. DOI: 10.1038/nature10707. URL: https://doi.org/10.1038/nature10707.

[26] M. A. Fogarty et al. “Integrated silicon qubit platform with single-spin addressability, exchange control and single-shot singlet-triplet readout”. In: *Nature Communications* 9.1 (Oct. 2018), p. 4370. ISSN: 2041-1723. DOI: 10.1038/s41467-018-06039-x. URL: https://doi.org/10.1038/s41467-018-06039-x.

[27] Klaus Schulten and Peter G. Wolynes. “Semiclassical description of electron spin motion in radicals including the effect of electron hopping”. In: *The Journal of Chemical Physics* 68.7 (1978), pp. 3292–3297. DOI: 10.1063/1.436135. eprint: https://doi.org/10.1063/1.436135. URL: https://doi.org/10.1063/1.436135.

[28] Jason R Petta et al. “Coherent manipulation of coupled electron spins in semiconductor quantum dots”. In: *Science* 309.5744 (2005), pp. 2180–2184.

[29] M. A. Broome et al. “High-Fidelity Single-Shot Singlet-Triplet Readout of Precision-Placed Donors in Silicon”. In: *Phys. Rev. Lett.* 119 (4 July 2017), p. 046802. DOI: 10.1103/PhysRevLett.119.046802. URL: https://link.aps.org/doi/10.1103/PhysRevLett.119.046802.

[30] Jörg Lehmann and Daniel Loss. “Cotunneling current through quantum dots with phonon-assisted spin-flip processes”. In: *Phys. Rev. B* 73 (4 Jan. 2006), p. 045328. DOI: 10.1103/PhysRevB.73.045328. URL: https://link.aps.org/doi/10.1103/PhysRevB.73.045328.

[31] Charles Tahan and Robert Joynt. “Relaxation of excited spin, orbital, and valley qubit states in ideal silicon quantum dots”. In: *Phys. Rev. B* 89 (7 Feb. 2014), p. 075302. DOI: 10.1103/PhysRevB.89.075302. URL: https://link.aps.org/doi/10.1103/PhysRevB.89.075302.

[32] C. Barthel et al. “Fast sensing of double-dot charge arrangement and spin state with a radio-frequency sensor quantum dot”. In: *Phys. Rev. B* 81 (16 Apr. 2010), p. 161308. DOI: 10.1103/PhysRevB.81.161308. URL: https://link.aps.org/doi/10.1103/PhysRevB.81.161308.

[33] C. Barthel et al. “Rapid Single-Shot Measurement of a Singlet-Triplet Qubit”. In: *Phys. Rev. Lett.* 103 (16 Oct. 2009), p. 160503. DOI: 10.1103/PhysRevLett.103.160503. URL: https://link.aps.org/doi/10.1103/PhysRevLett.103.160503.

[34] N. W. Hendrickx et al. “A single-hole spin qubit”. In: *Nature Communications* 11.1 (July 2020), p. 3478. ISSN: 2041-1723. DOI: 10.1038/s41467-020-17211-7. URL: https://doi.org/10.1038/s41467-020-17211-7.

[35] Yasuhiro Tokura et al. “Coherent Single Electron Spin Control in a Slanting Zeeman Field”. In: *Phys. Rev. Lett.* 96 (4 Jan. 2006), p. 047202. DOI: 10.1103/PhysRevLett.96.047202. URL: https://link.aps.org/doi/10.1103/PhysRevLett.96.047202.

[36] Erika Kawakami et al. “Electrical control of a long-lived spin qubit in a Si/SiGe quantum dot”. In: *Nature Nanotech.* 9.9 (2014), pp. 666–670.

[37] M Pioro-Ladriere et al. “Electrically driven single-electron spin resonance in a slanting Zeeman field”. In: *Nature Phys.* 4.10 (2008), pp. 776–779.

[38] X. Croot et al. “Flopping-mode electric dipole spin resonance”. In: *Phys. Rev. Research* 2 (1 Jan. 2020), p. 012006. DOI: 10.1103/PhysRevResearch.2.012006. URL: https://link.aps.org/doi/10.1103/PhysRevResearch.2.012006.

[39] Ross C. C. Leon et al. “Bell-state tomography in a silicon many-electron artificial molecule”. In: *Nature Communications* 12.1 (May 2021), p. 3228.

[40] Andrea Corna et al. “Electrically driven electron spin resonance mediated by spin–valley–orbit coupling in a silicon quantum dot”. In: *npj Quant. Inform.* 4.1 (2018), p. 6.

[41] Will Gilbert et al. “On-demand electrical control of spin qubits”. In: *Nature Nanotechnology* (Jan. 2023). ISSN: 1748-3395. DOI: 10.1038/s41565-022-01280-4. URL: https://doi.org/10.1038/s41565-022-01280-4.

[42] Tuomo Tanttu et al. “Controlling Spin-Orbit Interactions in Silicon Quantum Dots Using Magnetic Field Direction”. In: *Phys. Rev. X* 9 (2 May 2019), p. 021028. DOI: 10.1103/PhysRevX.9.021028. URL: https://link.aps.org/doi/10.1103/PhysRevX.9.021028.

[43] P Scarlino et al. “Second-harmonic coherent driving of a spin qubit in a Si/SiGe quantum dot”. In: *Phys. Rev. Lett.* 115.10 (2015), p. 106802.

[44] I. Gromov and A. Schweiger. “Multiphoton Resonances in Pulse EPR”. In: *Journal of Magnetic Resonance* 146.1 (Sept. 2000), pp. 110–121. DOI: 10.1006/jmre.2000.2143.

[45] Emmanuel I. Rashba. “Mechanism of half-frequency electric dipole spin resonance in double quantum dots: Effect of nonlinear charge dynamics inside the singlet manifold”. In: *Phys. Rev. B* 84 (24 Dec. 2011), p. 241305. DOI: 10.1103/PhysRevB.84.241305. URL: https://link.aps.org/doi/10.1103/PhysRevB.84.241305.

[46] Govind Agrawal. “Chapter 2 - Pulse Propagation in Fibers”. In: *Nonlinear Fiber Optics (Fifth Edition)*. Ed. by Govind Agrawal. Fifth Edition. Optics and Photonics. Boston: Academic Press, 2013, pp. 27–56. DOI: https://doi.org/10.1016/B978-0-12-397023-7.00002-4. URL: https://www.sciencedirect.com/science/article/pii/B9780123970237000024.

[47] D. M. Zajac et al. “Scalable Gate Architecture for a One-Dimensional Array of Semiconductor Spin Qubits”. In: *Phys. Rev. Applied* 6 (5 Nov. 2016), p. 054013. DOI: 10.1103/PhysRevApplied.6.054013. URL: https://link.aps.org/doi/10.1103/PhysRevApplied.6.054013.

[48] LMK Vandersypen et al. “Interfacing spin qubits in quantum dots and donorshot, dense, and coherent”. In: *npj Quant. Inform.* 3.1 (2017), p. 34.

[49] F. Borjans et al. “Resonant microwave-mediated interactions between distant electron spins”. In: *Nature* 577.7789 (Jan. 2020), pp. 195–198. ISSN: 1476-4687. DOI: 10.1038/s41586-019-1867-y. URL: https://doi.org/10.1038/s41586-019-1867-y.

[50] Cody Jones et al. “Logical Qubit in a Linear Array of Semiconductor Quantum Dots”. In: *Phys. Rev. X* 8.2 (2018), p. 021058.

[51] Peter W. Shor. “Scheme for reducing decoherence in quantum computer memory”. In: *Phys. Rev. A* 52 (4 Oct. 1995), R2493–R2496. DOI: 10.1103/PhysRevA.52.R2493. URL: https://link.aps.org/doi/10.1103/PhysRevA.52.R2493.

[52] Austin G. Fowler et al. “Surface codes: Towards practical large-scale quantum computation”. In: *Phys. Rev. A* 86 (3 Sept. 2012), p. 032324. DOI: 10.1103/PhysRevA.86.032324. URL: https://link.aps.org/doi/10.1103/PhysRevA.86.032324.

[53] Pierre-André Mortemousque et al. “Enhanced Spin Coherence while Displacing Electron in a Two-Dimensional Array of Quantum Dots”. In: *PRX Quantum* 2 (3 Aug. 2021), p. 030331. DOI: 10.1103/PRXQuantum.2.030331. URL: https://link.aps.org/doi/10.1103/PRXQuantum.2.030331.

[54] Louis Houtin et al. *Quantum device with spin qubits*. URL: https://patents.google.com/patent/US10607993B2/en.

6

HOLE SPIN CONTROL AND MANIPULATION IN LINEAR ARRAYS OF QUANTUM DOTS

Physics is like sex: sure, it may give some practical results, but that's not why we do it.

Richard P. Feynman

In the previous chapter I discussed the electrical control of the electron spin (Sec. 5.7) in arrays of quantum dots. As previously discussed in Sec. 2.9 the main drawback of working with the spins of electrons in silicon is the weak spin-orbit coupling. This implies that an additional hardware is usually required to allow qubit manipulation, as an ESR line or a micromagnet, imposing constraints for scalability. Although the spin-valley coupling [1][2] or the mixing between orbital states [3] can enhance the SOC of the electrons, this usually requires additional gates for the tuning of the interdot coupling, not available in the devices studied.
Holes in silicon offers two main advantages compared to electrons: the intrinsically stronger SOC due to HH-LH mixing, that enables electrical spin manipulation; and the strong g-factor variability, which can enable the dispersive readout of a spin qubit.

The chapter starts describing the readout technique that allows remote charge-sensing of QDs that are more than one gate away from the reservoir. In a first experiment, presented in Sec. 6.2, we study the dynamics of a DQD transition in a 6-gate array. The two central dots are probed individually through an RF charge sensor on each reservoirs.
In Sec. 6.3 it is explained in detail how to measure the tunnel rates between the dot and the sensor.
The knowledge, and possibly the control, of the tunnel rates allows to calibrate the spin measurements of section 6.4, where the spin-to-charge conversion is realized through energy-selective readout. By realizing the same readout simultaneously on each dot it would be possible to study the effect of spin-spin interaction, i.e. the exchange coupling J, crucial for the implementation of a two qubit logic gate.
Unfortunately this experiment was limited by a small T_1, due to the relatively high temperature ($T \simeq 450$ mK) and, as a consequence, also to the high magnetic field required.
By decreasing temperature and using an analogue readout technique on a similar 4-gate

device (Sec. 6.5) it has instead been possible to demonstrate a hole spin qubit.
Finally, the high susceptibility of the hole g-factor to the surrounding environment is such that a DQD will be very likely to have a significant g-factor difference Δg. We will see in Sec. 6.6 that, as a consequence, this enables the readout of the spin state of a single qubit in a DQD through gate reflectometry. This dispersive qubit readout scheme requires no coupling to a Fermi reservoir, thereby offering a compact and potentially scalable solution, whose operation may be extended above 1 K.

6.1. DEVICE TUNING FOR DOUBLE CHARGE-SENSING WITH RESERVOIR-BASED REFLECTOMETRY

The goal of this experiment is to study the DQD in the center of the array (below gates G_3 and G_4) using two RF charge sensors, that exploit a charge transition between a QD in $G_{1,6}$ and one of the two reservoirs.
The tunnel coupling between the QDs and their reservoirs can be tuned by using the gates G_2, G_5 as barrier gates. We'll describe step by step how to reach the desired configuration.

A scheme of the device layout with the four inductances defining the four tank LC circuits for reflectometry readout is shown in Fig. 6.1. From now on we'll refer to each quantum dot, accumulated below gate G_i, as QD_i.
By scanning the reflected signal as a function of frequency we observe, both in phase and amplitude, the four resonances corresponding to each LC resonator. As will be discussed in Sec. 6.5, these resonances are more pronounced by lowering the temperature and they start to be visible already below 100 K.

We have two kinds of resonant circuits, one connected to gates G_1 and G_6, which we'll refer to as gate reflectometry lines, and one connected to the Ohmic contacts S and D (reservoir reflectometry lines).
We observed that the shape of the resonances on the gate reflectometry lines are not significantly affected when the device is in the strong inversion regime (at most they are shifted in phase), while the ones on the reservoirs are. The amplitudes of the reservoir reflectometry are affected because the channel resistance is increased in strong inversion.
A comparison between the resonances when the device is in strong inversion, i.e. with all the gates at -2V (orange lines), and when the channel is empty (blue lines) is shown in Fig. 6.1 b), c). We observed a gate voltage dependent behaviour of the reservoir reflectometry also in other similar devices.
Even if the additional resistance is the same for source and drain, the residual impedance on resonance $Z = L/(RC_p)$ can be above or below $Z_0 = 50\ \Omega$, and the matching with the 50 Ω lines can either improve or get worse (as in our case).

The active channel of the device studied here has width $W = 75$ nm, the gate length is $L_g = 40$ nm and the gate spacing is $S_H = 40$ nm.
From the frequency of the resonances we can extract the parasitic capacitances of the four resonators: $C_p^D = 0.61$ pF ,$C_p^S = 0.55$ pF, $C_p^{G6} = 0.55$ pF, $C_p^{G1} = 0.56$ pF. Since the parasitic capacitance is mainly influenced by the geometry of the board and the length of the bonding wire, we find very similar values of C_p for the four lines.

For the implementation of the charge sensor we start by accumulating a single quantum dot below the two lateral gates G_1 and G_2 as shown in Fig. 6.2. The other gates are kept at 0 V.

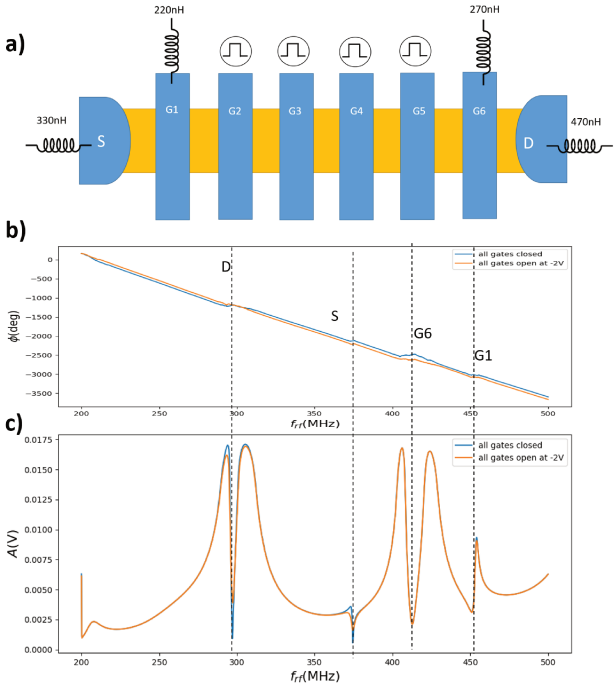

Figure 6.1: a) Scheme of the device layout. On the central gates we can send fast pulses and microwave excitations together with DC gate voltages. A charge transition between the dots in the lateral gates and the nearby reservir can be use for RF charge sensing. b,c) Plot of the reflected signal, in phase and amplitude, as a function of frequency. Four resonances, related to the four tank circuits connected to D,S, G6, G1 are clearly visible, and are indicated by dashed black lines. The blue and orange lines represent, respectively, the signal when the channel is empty and in strong inversion.

For low gate voltages we can observe the typical honeycomb pattern of a DQD (not shown), but we increase the gate voltages until the two dots fully merge. The single-dot regime can be identified when the dot-lead transition is at -45 degree in the plot V_{G1} vs V_{G2}.
After that, we prepare the same configuration on the other side of the device.

It is worth mentioning here that we can observe the same dot-lead transitions with both the gate and the reservoir reflectometry. Although we didn't study quantitatively their differences, we observed that the SNR is significantly better on the reservoir reflectometries. We calibrated the reflectometry frequencies to maximise the phase signal of the reservoir reflectometry and, to save time, we stop acquiring the gate reflectometry signals from now on.

Before trying this configuration, with a single big dot below two gates, we wanted to monitor the charges of QD_3 by using a charge detector between QD_1 and its reservoir, while keeping QD_2 empty. We noticed that an empty gate have a screening effect and therefore we are obliged to accumulate some charges below them and this is why it is necessary to use a big single-dot below two gates as a charge sensor.

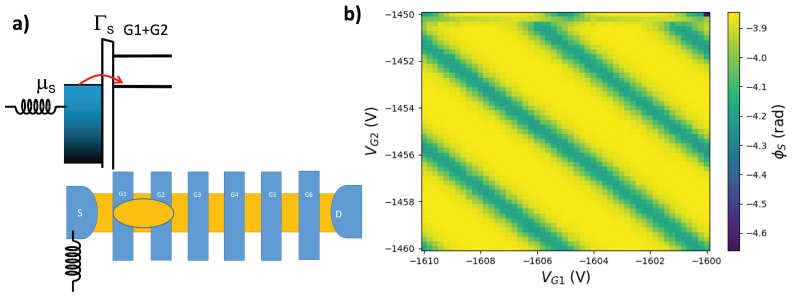

Figure 6.2: a) Bottom: Scheme of a six gate device with the position of the big dot coupled to the source. Top: energy level diagram indicating the condition of resonant tunneling between the dot and the reservoir. b) Measurement of a single dot controlled by gates G_1 and G_2. From the slope of the lines (-45 degree) we can conclude that both gates have the same degree of control (same lever-arm) over a single big dot lying underneath the two gates.

We then monitor the two charge detectors when we also charge the central dots QD_3 and QD_4. The sensor dots are capacitively coupled to the central dots and there is a jump in the detector electrochemical potential corresponding to each charge transition in the QDs.
In particular in the few holes regime each detector is mainly sensitive to the charge state of the dot nearby and we use the left detector (source) to probe the charge state of QD_3 (Fig. 6.3 a)) and the right one (drain) to probe the charge state of QD_4 (Fig. 6.3 b))

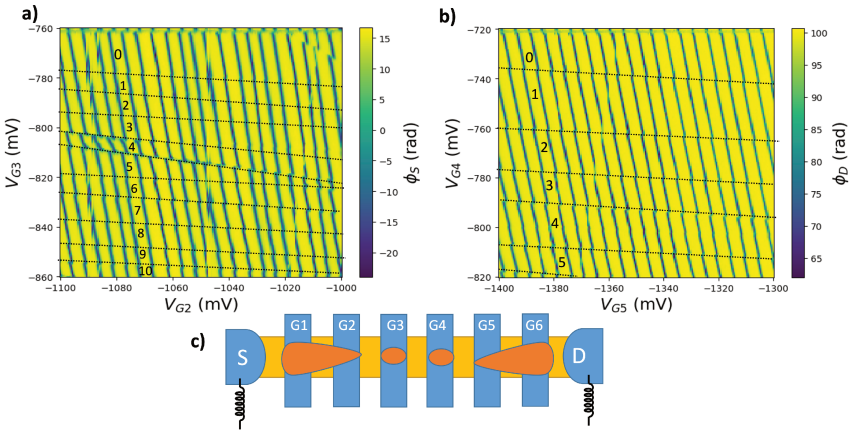

Figure 6.3: Stability diagrams: a) V_{G_2} vs V_{G_3} and b) V_{G_5} vs V_{G_4}. a) Shifts in the phase signal ϕ_S of the charge sensor on the source allows to count the charges of QD_3; b) Shifts in the phase signal ϕ_D of the sensor on the drain allows to count the charges of QD_4. Black dashed lines are a guide to the eyes to help following the charge transitions of each QD. The numbers indicate the number of holes in each dot c) Sketch of the QDs and detector configuration for the simultaneous charge detection.

It can be observed that, while we are quite sure about the number of charges in QD_4, we can see that not all the charge transition lines of QD_3 (highlighted by black dashed lines in Fig. 6.3 a)) are parallel. In particular the transition from the charge states $N_{G_3} = 3 \rightarrow 4 \rightarrow 5$ are steeper than the others, signature of a different capacitive coupling and hence different location or shape of the interacting object.
From this we can guess that we might have either a dopant nearby (closer to the sensor than QD_3) or that we are forming two corner dots on the opposite side of the gate.
We can also observe another transition on the top right of the plot 6.3 a), which is unrelated with the transition of the dot. Indeed, by changing the gate voltage of the sensor/barrier gates V_{G2}, V_{G5} we observed that these transitions are not moving accordingly with the dot transitions, signature that they are originated from another object that we don't want to investigate.

After probing individually the charge number in each dot we want to study the DQD formed by QD_3 and QD_4. To do so we first measured the coupling between the gates. We find $\alpha_{G3-G2} = 0.202$, $\alpha_{G4-G2} = 0.022$, $\alpha_{G4-G5} = 0.212$ and $\alpha_{G3-G5} = 0.014$. The knowledge of the coupling parameters allows to keep fixed the electrochemical potentials of the two sensors while scanning the voltage of G_3,G_4.
Differently from Chap. 5, the current setup allows to compensate the charge detectors also while pulsing on QD_3 and QD_4, by sending counter pulses, on gates G_2 and G_5, respectively. This also allows to increase the single-shot charge readout fidelity.

In Fig. 6.4 we show the DQD stability diagrams (in the same ranges as in Fig. 6.3), measured by each charge detector.
Such maps are collages of 25 consecutive measurement. The individual measurements are delimited by the black solid lines, that define a square. In each measurement the two detectors are recalibrated on their minimum in the center of each square. This is strictly necessary because, despite the gate compensation, the charge detector moves out of its sensitivity range after one or maximum two charge transitions in the nearby dot.
The detectors are initialized by setting $V_{G2} = -1085$ mV and $V_{G5} = -1390$ mV when the DQD is in the (0,0) charge state. Because of the detectors recalibration small shifts are visible between each measurement. These are clearly artifact and the charge transitions are identified by a switch of color within the same measurement.

We can observe that at low holes filling the first interdot charge transitions (ICT) are not visible on this scale. They can be resolved with a zoom at high resolution, and the lenghts of the interdot lines are $\simeq 0.1 - 0.3$ mV for (N,M)<(4,4).
We experienced an increased level of charge noise in the few-holes regime, where the quantum dots are more sensitive to Coulomb disorder. Consistently with other studies on similar devices[4] we have also observed a reduction of charge noise when the number of holes trapped in the DQD is increased.
The small size of the interdot lines, together with the increased level of charge noise, compromised reliable studies of the first spin blockaded transitions.

The mutual capacitance C_m determines the change in energy of one dot when an electron is added to the other dot and sets the distance between two triple points[5]. The mutual capacitance is a parameter which is experimentally tunable through modifications of the shape and distance of the two dots [6].
We have to consider that each dot feels simultaneously the attraction from the nearby gate (at negative voltages) and the Coulomb repulsion from the holes of the sensor dots

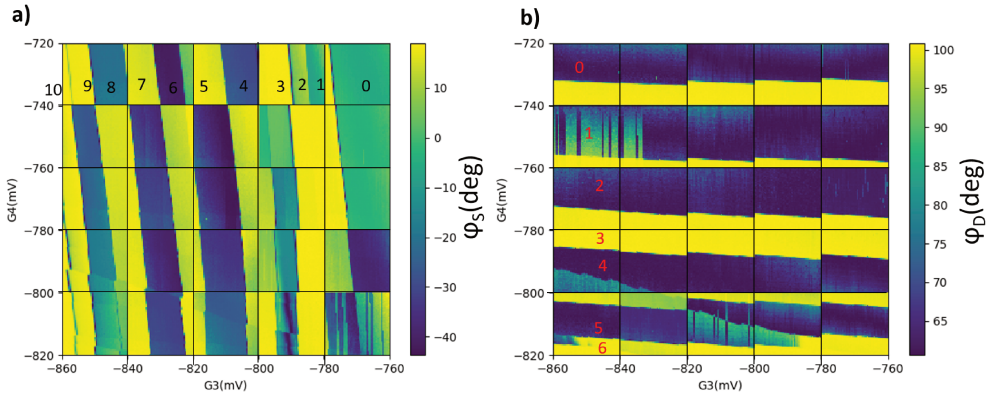

Figure 6.4: a,b) Stability diagrams G_3 vs G_4, recorded simultaneously from the two charge-detectors. The count of the charges is the same as in Fig. 6.3. The two plots are a collage of 25 simultaneous measurements (individual measurements are separated by solid black lines). Small shifts in the signal in correspondence of the black lines are an artifact due to the re-calibration of the detector.

and from the dot nearby.
While the attractive electrostatic field induced by the nearby gate is more or less kept constant, the effect of Coulomb repulsion is strongly dependent by the number of charges in the smaller dots.
Considering that the charges accumulated in the sensor dot $|Q| > 30e$ tend to repel the nearby dot (with charge $|q| < 10e$) with a Coulomb force $\propto Q \cdot q$, we can understand that the strength of the repulsion from the reservoir is dominated by the number of charges $|q|$ in the smaller dot. Empirically this effect is dominant compared to the mutual repulsion between the two central dots.
The interdot mutual capacitance can therefore be enhanced either by increasing the filling of the two dots (acting on the electrostatics) or by changing the tunnel barriers. We tried both the options.

In Fig. 6.5 we increase the filling of the central dots, and for $N_{G_3} > 10$ and $M_{G_4} > 5$ we can observe a clear honeycomb pattern.
We observed a very similar phenomenology also in a previous study on another device from the same batch (studied in Sec. 4.9).

The other way to increase the interdot mutual capacitance is to reduce the tunnel barriers by applying a negative top gate voltage.
The top gate is a nanowire located 300 nm above the channel and it affects the whole device.
By applying a negative top gate voltage, all the tunnel barriers are decreased, and consequently the interdot mutual capacitance is increased. In this way the interdot transitions can be resolved also at low holes filling.
Fig. 6.6 shows the stability diagram in the few holes regime, with a top gate voltage applied of $V_T = -30$ V. It demonstrates that by increasing the interdot coupling we can appreciate the first charge transitions in the DQD.
To better highlight all the charge transitions, we plot the derivative of the phase signal

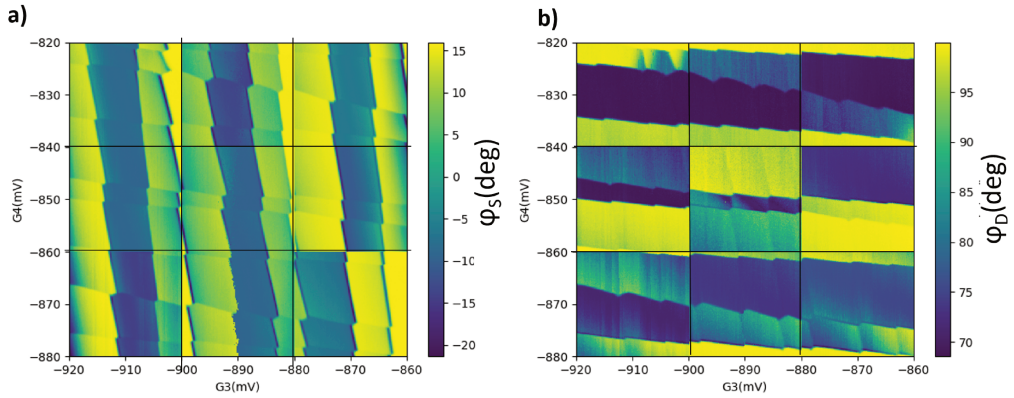

Figure 6.5: a,b) Stability diagrams G_3 vs G_4 recorded simultaneously from the two charge-detectors. By increasing the dot filling we start observing clear honeycomb pattern. The plots are a collage of 9 measurements (separated by solid black lines), recorded simultaneously by two separate detectors. Here $N_{G_3} > 10$ and $M_{G_4} > 5$.

of the source charge detector as a function of the voltage applied on G_3. The sign of the derivative is only dependent by the initial detector calibration in each measurements. Unfortunately this configuration was unstable, due to the slow recombination of charges in the oxide between the active channel and the top gate.

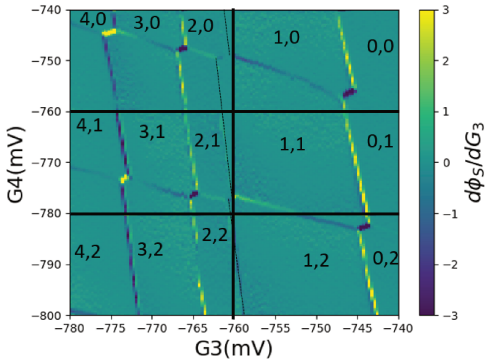

Figure 6.6: Stability diagrams G_3 vs G_4 while applyng a top gate voltage $V_T = -30$ V. Here we plot the derivative $\frac{d\phi_S}{dG_3}$ of the signal of the left detector, in order to better highlight all the charge transitions. The black lines separate each individual measurement.

The data shown, once again, highlights the need to have a fine control over the tunnel barriers.
Whereas in the present configuration it is not obvious how to control the interdot coupling, the tunnel coupling with the sensor dot can be tuned by varying the filling of the detector, as will be discussed in Sec. 6.4.

6.2. PROBING DOUBLE DOT DYNAMICS SIMULTANEOUSLY WITH DOUBLE CHARGE-SENSING

After having shown how to tune the six gate device to perform simultaneous double charge-sensing, we move to the analysis of an ICT between QD_3 and QD_4.
We demonstrate here that with the double charge sensor we can probe in real time (single-shot) the dynamics of each dot separately, and distinguish if the ICT is mediated by a reservoir or not.
We examine an ICT where the interdot tunnel rates are of the order of tens of kHz, such that the charge transitions can be resolved temporally with our detectors, which can resolve single-shot traces with an integration time down to 1-5 μs.

The direct interdot tunneling can be detected as a simultaneous jump by the two detectors. Conversely, when the tunneling is mediated by sequential particle exchange with the nearby Fermi reservoirs, the signals of the two charge detectors jump at different times, revealing the sequence of single-hole tunneling processes. As we will see, depending on the specific electrostatic configuration of the DQD one of the two processes can be dominant over the other.
We highlight that, for the way the charge detectors are conceived in our experiment, they are fundamentally sensitive only to the charge state of the closest dot, and only in some particular situation they can also be sensitive to the state of the dot further away. However, by combining the information of the two charge sensors we can resolve all of the charge states involved, as shown in Fig. 6.7.

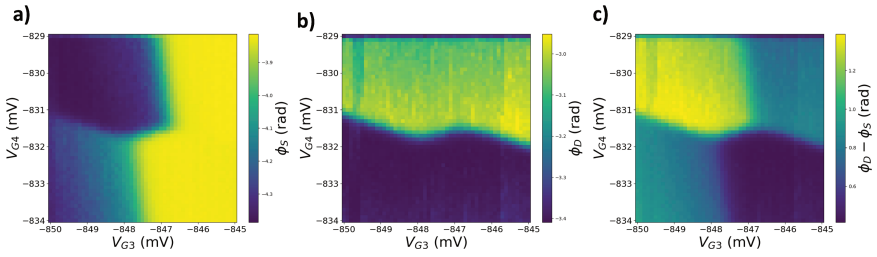

Figure 6.7: Stability diagram V_{G3} vs V_{G4} measured in a) from the charge sensor on the source side ϕ_S; in b) from the charge sensor on the drain side ϕ_D. In c) we plot the difference between the two signals, which discriminates all of the four charge states.

The following study shows that, by having only one charge sensor, we might lose precious information about the DQD dynamics, risking to misunderstand the experimental results. We'll see that the interdot tunneling process can be strongly affected by the coupling with the reservoirs and, depending on the relative energy detuning between dots and reservoirs, different types of dynamics are possible.

To discuss the stability diagram of the DQD we label the corresponding charge states as (N,M)=(QD_3,QD_4). We choose the charge transition $(10,5) \rightarrow (11,4)$. For simplicity from now on we'll refer to this ICT as ("0,1") → ("1,0"). As explained in the previous section, we expect a stronger dot-reservoir coupling for the dot with larger filling, i.e. QD_3 in this case.

We analyze the charge transition by initializing the system in ("0,1") and applying pulses "landing" in different regions of the ("1,0") ground state, as indicated by labels *a), b), c), d)* in Figs. 6.8, 6.9, 6.10, 6.11 a), respectively.
We can reasonably expect that, until the pulse lands in a region where the transition with the reservoirs are energetically forbidden, there is only one possible relaxation path, i.e. the direct interdot transition ("0,1") → ("1,0").
This configuration is shown in Fig. 6.8. Along the red and green dashed lines in the static stability diagram (Fig. 6.8 a)) the electrochemical potential of the DQD is aligned with the one of the reservoirs. In particular, along the red dashed lines the electrochemical potential of the DQD $\mu(1,0)$ and $\mu^*(1,1)$ are aligned with the Fermi level of the source. Along the green dashed lines the electrochemical potentials $\mu(0,1)$ and $\mu(1,1)$ are aligned with the Fermi level of the drain.

This can be better understood by looking at the energy diagrams of the DQD [5] (panels c) of the figures). In these diagrams the vertical axis represents the energy and the hole DQD energy levels are lowered by decreasing the gate voltages (i.e. by increasing the number of holes).
For analogy with panels a),b) we indicate the electrochemical potentials mainly controlled by gate G_3 in red, and the ones mainly controlled by gate G_4 in green.
The electrochemical potentials of the single-hole configurations $\mu(1,0)$ and $\mu(0,1)$ are localized in a single quantum dot (QD_3 and QD_4 respectively), and tunneling can be allowed only with the closest reservoir. The electrochemical potentials of the two-holes configurations $\mu^*(1,1)$ and $\mu(1,1)$ instead are extended over the DQD.
The electrochemical potential $\mu^*(1,1)$, as it will be clear later, represents an unstable configuration where a hole tunneling from the source can be allowed (as in Figs. 6.10, 6.11), bringing the DQD in a metastable ("1,1") state before reaching the ground state ("1,0").
In these energy diagrams, for simplicity, we move only the position of the electrochemical potentials of the dots relative to the sensors (fixed), but in principle, because of their capacitive coupling, also the potential of the sensors varies with gate voltages and the charge filling of the DQD.

In the case of Fig. 6.8 when we land at point *a)* we are still in a configuration ("0,1") and the electrochemical potential $\mu(0,1)$ falls below the drain level μ_D (upper green dashed line in the static measurement), preventing the hole to be unloaded through the drain. In this case only interdot tunneling is allowed.

In the b) panel of each figure we show the single-shot traces (red for QD_3 and green for QD_4) and the average phase signals (blue for QD_3 and orange for QD_4) recorded during the whole pulse sequence with each charge detector. In particular we pulse for 200 μs at the initialization point I, in ("0,1"), and 200 μs at points *a),b), c), d)*, in the ("1,0") ground state.
We note that the interdot tunneling event can be recorded as a simultaneous jump in the two charge sensors. In this configuration this is the only possible process and, by fitting the average phase signals with an exponential decay, we measure the typical interdot tunneling time $\tau_{3-4} = 45 \pm 5$ μs.

When going to the case of Fig. 6.9, the initial electrostatic configuration at point *b)* is such that in principle there are two distinct charge relaxation paths, i.e. the direct interdot tunneling and the indirect transition mediated by the reservoirs, i.e. ("0,1") →

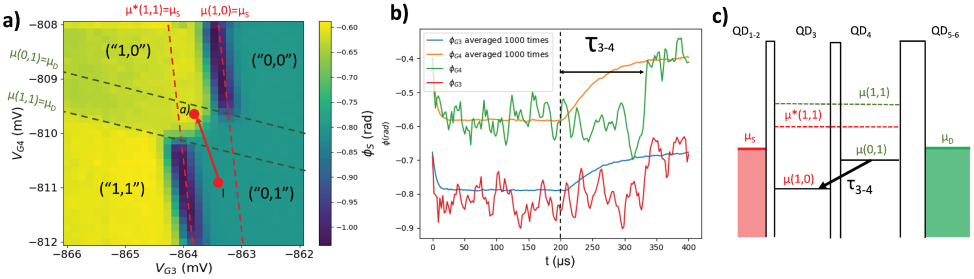

Figure 6.8: a) Static charge distribution of the DQD as a function of V_{G_3},V_{G_4}. b) Single-shot measurements of the charge distribution of QD_4 (green) and QD_3 (red), with 5 μs integration time per point. In orange (QD_4) and blue (QD_3) the time averaged traces. We acquire over the 2-step pulse sequence, i.e. 200 μs at point *I* and 200 μs at point *a)*. c) Energy diagram of the DQD at point *a)* of the stability diagram. In this case interdot tunneling is the only process allowed.

("0,0") → ("1,0").
We keep on observing simultaneous jumps of the two detectors and hence the interdot tunneling is still the dominant process.
We can also conclude that the tunnel rate of QD_4 with its reservoir is slower than the interdot tunneling. Moreover, due to the increased energy gap between the two QDs levels, the average interdot tunneling time τ_{3-4} is shorter than in the case of Fig. 6.8.

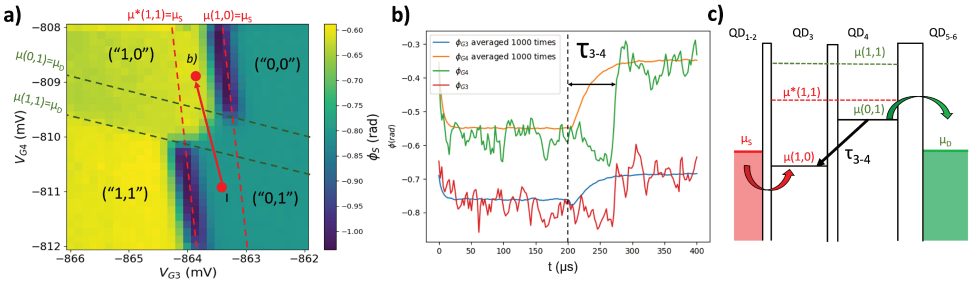

Figure 6.9: a) Static charge distribution of the DQD as a function of V_{G_3},V_{G_4}. b) Single-shot measurements of the charge distribution of QD_4 (green) and QD_3 (red), with 5 μs integration time per point. In orange (QD_4) and blue (QD_3) the time averaged traces. We acquire over the 2-step pulse sequence, i.e. 200 μs at point *I* and 200 μs at point *b)*. c) Energy diagram of the DQD at point *b)* of the stability diagram. In this case two tunneling processes are allowed, i.e. the direct interdot tunneling and the process mediated by the reservoirs ("0,1")→("0,0")→("0,1"). We observe that interdot tunneling is still the dominant process.

In the case of Fig. 6.10 the energetic configuration at point *c)* is such that the transition with both the reservoirs are energetically allowed, providing two possible relaxation paths plus the direct interdot tunneling.
We observe that the dominant relaxation process in this case involves a metastable ("1,1") charge state.
The transition ("0,1") → ("1,1") → ("1,0") can be understood by looking at the single-shot traces. We observed that the first detector to jump is the one measuring QD_3 (red trace), bringing the DQD in a metastable ("1,1") state. After a while also the QD_4 charge detector

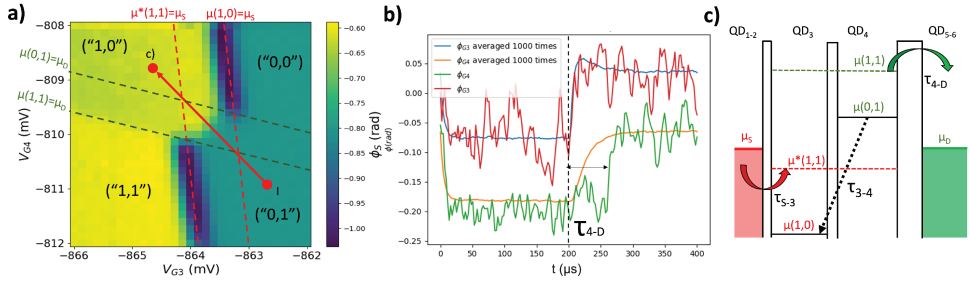

Figure 6.10: a) Static charge distribution of the DQD as a function of V_{G3},V_{G4}. b) single-shot measurements of the charge distribution of QD_4 (green) and QD_3 (red), with 5 μs integration time per point. In orange (QD_4) and blue (QD_3) the time averaged traces. We acquire over the 2-step pulse sequence, i.e. 200 μs at point *I* and 200 μs at point *c)*. c) Energy diagram of the DQD at point *c)* of the stability diagram. In this case three tunneling processes are allowed, i.e. the direct interdot tunneling and the processes mediated by the reservoirs ("0,1")→("0,0")→("1,0") and ("0,1")→("1,1")→("1,0"). We observe that the most probable relaxation process is ("0,1")→("1,1") →("1,0"), involving the loading of a hole from the source and the subsequent unloading through the drain.

jumps, bringing the DQD back to the ("1,0") ground state.
The characteristic time scales of this process are the QD_3 loading time through the source τ_{S-3}, which is faster than the integration time ($\tau_{S-3} < 5$ μs), and the unloading time of QD_4 through the drain, namely $\tau_{4-D} \simeq 15$ μs.
However, in this configuration the direct interdot tunneling process, denoted by simultaneous jumps of the two charge detectors, is not suppressed, still happening $\simeq 20\%$ of the times.

The fact that QD_3, as compared to QD_4, has a stronger tunnel coupling to its respective reservoir is consistent with its larger filling (approximately twice the one of QD_4), and hence the larger extension of its multi-hole wave function.
Indeed, we realized the same experiment in a similar even-odd charge configuration, but where QD_4 is at higher filling than QD_3, and we found that the dominant relaxation process was instead ("0,1") → ("0,0") → ("1,0"), involving a first charge transition with the drain.

For completeness we analyze one last scenario, where the energetic configuration is such that the unloading of QD_4 through its reservoir is forbidden, and the only two possible relaxation paths are interdot tunneling and the QD_3-reservoir mediated process ("0,1") → ("1,1") → ("1,0").
By pulsing to point *d)* (see Fig. 6.11), QD_3 begins to exchange charges back and forth with its reservoir, providing an additional dispersive signal (see red single-shot trace). This negative dispersive signal can be understood considering that, after a hole is loaded from the source, the system is in ("1,1") and a hole can be unloaded immediately, bringing again the system in ("0,1"), as it can be understood from the energy diagram of Fig. 6.11 c). This process repeats continuously until interdot tunneling.
However, the observation of an additional negative dispersive signal in the red single-shot trace was quite surprising. Indeed such a signal would be expected when $\mu^*(1,1) = \mu_S$, condition which is verified far away from point *d)*.
When the DQD is in the ("0,1") state instead interdot tunneling is allowed and then the

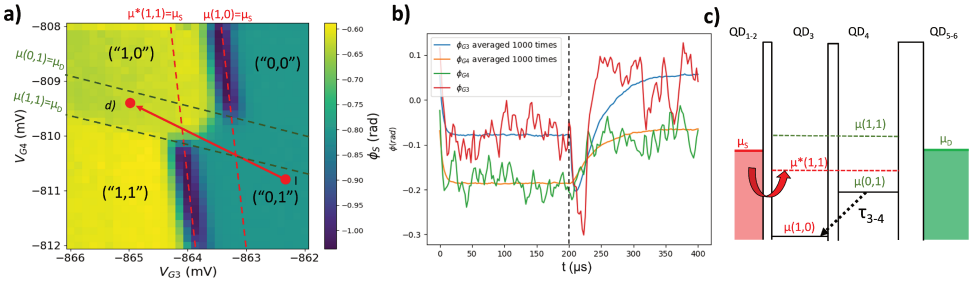

Figure 6.11: a) Static charge distribution of the DQD as a function of V_{G_3},V_{G_4}. b) Single-shot measurements of the charge distribution of QD_4 (green) and QD_3 (red), with 5 μs integration time per point. In orange (QD_4) and blue (QD_3) the time averaged traces. We acquire over the 2-step pulse sequence, i.e. 200 μs at point *I* and 200 μs at point *d)*. c) Energy diagram of the DQD at point *d)* of the stability diagram. In this case two tunneling processes are allowed, i.e. the direct interdot tunneling and the process mediated by the reservoir ("0,1")→("1,1")→("1,0"). We observe that the red single shot trace shows a signal corresponding to the resonant ("1,1")↔("0,1") transition, until the interdot tunneling event occurs.

system can reach a stable configuration. This is the dominant process, as can be understood considering that the characteristic tunneling time is still $\tau_{3-4} = 45 \pm 5$ μs, as the one extracted in the case a) of Fig. 6.8, where only interdot tunneling is allowed.

With this analysis we detected the presence of metastable charge states by observing the single-shot live traces during an interdot transition.
The characterization described above can be useful also to determine the dynamics of a (1,1)→(0,2)-like transition. In such a case a (1,1) state of a system strongly coupled with its reservoir might reach the ground state (0,2) passing through metastable states as (1,2) or (0,1). In these cases the sensitivity of a sensor coupled to only one QD does not always allow to discriminate if the tunneling process is direct or mediated by a reservoir. Ideally to realize PSB readout the optimal situation would be the one of Fig. 6.8, where only interdot tunneling is allowed and the spin information cannot be destroyed by tunneling into the reservoir.

However, the tunneling with a reservoir might also be exploited for the implementation of a latched PSB readout, especially in cases where the detector is placed symmetrically with respect to the DQD, and hence it is only sensitive to the total charge on the DQD [7], or when only one of the two dots is directly coupled to the reservoir [8] [9].
In particular, in the second case one can expect that, because of the different coupling of the two dots with the reservoirs, states as S(2,0) and T(1,1) would take different times to decay, for example, to the (2,1) charge state.
In this way, by realizing the readout in (2,1), the spin-relaxation process can be replaced with a charge-metastable one [8], thus providing a way to increase the contrast of the measurement and the duration of the charge signal, improving the readout fidelity. This improvement could be particularly pronounced when the spin-blockade lifetime is smaller or comparable to the temporal resolution of the charge detector, as for example in materials like GaAs, where the typical spin-blockade lifetime is about 10 μs [10]. A latched PSB readout can be beneficial at relatively high operation temperatures, where the spin lifetime can be significantly degraded.

6.3. MEASURING TUNNEL RATES

When a quantum dot is tuned such that its electrochemical potential is close to the Fermi level of a reservoir, holes (or electrons) can tunnel back and forth between the quantum dot and the nearby reservoir. The speed of this process is due to many physical factors such as the strength of tunnel barrier between the dot and the lead, the wavefunctions overlap, and the density of state of the leads[11].
The sensing dot can be seen as an effective extension of the reservoir, as in the measurement of the electronic temperature of section 3.4. Its energy spectrum, even though being quantized, is also broadened by tunneling to the thermally broadened Fermi sea of the reservoir. We therefore consider the sensor dot as a Fermi reservoir.

Similarly to the analysis of the single-shot counts of Sec. 5.6, we set a threshold to discriminate between the two states of the detector. Such a threshold is defined as the intercept between the distributions of the phases corresponding to each charge states, as in Fig. 5.14 .
If the tunneling events are slower than the integration time, usually between 2 and 10 μs with our setup, we can temporally resolve individual tunneling events from single-shot live traces.
The technique we are going to describe is widely used when the tunnel rates are below MHz[12][13], such that each charge state lasts more than the integration time.
The SNR of the detector is what determines how fast we can analyze the tunnel rates. Since with our setup the main noise source is the the RF amplifier at 3.6K, a higher contrast in the detector signal is what allows to further decrease the integration time.

The individual tunneling events follow a discrete probability distribution where individual events are not correlated. The outcomes of this probability distribution are 0 (dot empty) and 1 (dot charged).
The statistics of tunneling events between a QD and a single reservoir therefore follow a Poissonian distribution [14].
The waiting times τ_{in} and τ_{out} for a hole to tunnel into and out of a QD are exponentially distributed and characterised by the tunnelling-in and -out rates, Γ_{in} and Γ_{out}. The distribution of the waiting times can be derived considering, for example, to be initially in the 1 charge state and that the probability of waiting a certain time t before tunneling can be estimated from the probability $P_{in}(t)$ that the hole has not tunnelled out of the dot after t, multiplied with the likelihood $\Gamma_{out}dt$ that it does tunnel out within the infinitesimal time interval dt.
Therefore the probability of having a tunneling event after certain time t can be obtained from the following differential equation [15][16]:

$$\begin{cases} P_{in}(t=0) = 1 \\ \frac{dP_{in}(t)}{dt} = -P_{in}(t)\Gamma_{out} \end{cases} \tag{6.1}$$

In an analog manner we can write the same differential equation for the dot initially empty $P_{out}(t=0) = 1$ and a probability of tunneling in at a certain time dt given by $\Gamma_{in}dt$ obtaining:

$$P_{in}(t) = e^{-t\Gamma_{out}} \qquad P_{out}(t) = e^{-t\Gamma_{in}} \tag{6.2}$$

The tunnelling rates Γ_{in}, Γ_{out} define the time-scale of the exponentially decaying waiting times of a hole in or out of the QD. As a consequence also the population of a charge state

out of equilibrium, i.e. if $P_0(t=0)=0$ or $P_1(t=0)=0$, would decay to the ground state ($P_{0,1}(t\rightarrow\infty)=1$) as:

$$P_0(t)=1-e^{-t\Gamma_{out}} \qquad P_1(t)=1-e^{-t\Gamma_{in}} \tag{6.3}$$

and by fitting the averaged time trace of the charge distribution we can obtain $\Gamma_{in,out}$, as done in Sec. 5.12.
Conversely, when a quantum dot oscillates between two charge states the averaged charge sensor signal is just proportional to the average charge and, to get some information about the tunnel rates, we need to resolve individual tunneling events. The probability of tunneling in-out are still given by eq. 6.2.
Given the exponential distribution of waiting times and the independence of individual tunnelling events, the tunnel rates can be estimated from the inverse of the mean waiting time [16]:

$$\Gamma_{in,out}=<\tau_{in,out}>^{-1}=\frac{N}{\sum_{i=1}^{N}\tau^i_{in,out}} \tag{6.4}$$

In Fig. 6.12 it is shown a typical time trace when the QD_3 level is aligned with its reservoir. Here we use an integration time of 10 μs, an the two charge states 0 and 1 can be clearly distinguished. By averaging over all the $\tau^i_{out,in}$ we can extract the tunneling rates.

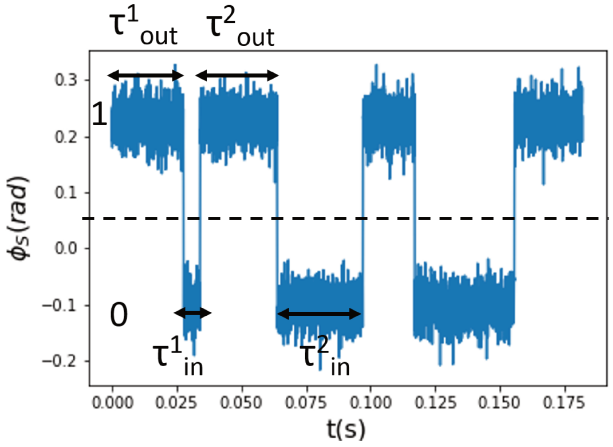

Figure 6.12: Example of a time-trace for a slow charge transition, with $\Gamma_{in},\Gamma_{out}\simeq 30$ Hz. The dashed line is the detection threshold. By averaging over all the $\tau^i_{out,in}$ measured we can extract the tunneling rates.

Here we also plot the distribution of the tunnneling times for another transition, faster than the one shown before. Fig. 6.13 demonstrates that, as expected, the tunneling events follow a Poissonian distribution.
In order to fit the probability of having k tunneling events (k=1) after a certain time t we have to adapt the Poisson distribution as following:

$$P(k,\lambda)=\frac{(\lambda)^k e^{-\lambda}}{k!}\Longrightarrow P(k=1,t)=(r\,t)e^{-r\,t} \tag{6.5}$$

The central value of the Poisson distribution (the mode) is the one such that $\lambda = k = 1$, i.e. at time t=1/r.
The mean value can be calculated again using formula 6.4 on the fitted probability distribution, after normalizing it. The good agreement between the two values demonstrates that the Poisson model is accurate in describing the statistics of the tunneling events.
In Fig. 6.13 we show the histograms of the experimental data and the fit over the normalized probability distributions.
An important remark is that the average value of the tunneling times is roughly two times the value of the mode of the probability distribution, and most of the individual tunneling events are faster than the average tunneling time extracted with eq. 6.4.

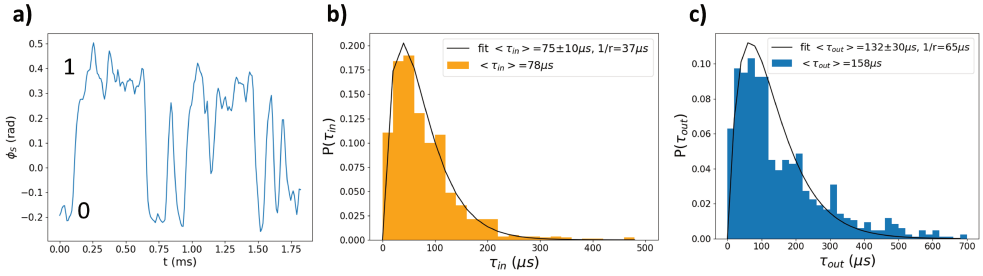

Figure 6.13: a) Portion of the time trace analyzed. b,c) Histogram of the measured τ_{in}, τ_{out} over 842 tunneling events in 200 ms, with an integration time of 10 μs per point. The solid black lines are the fit with the Poisson time distribution of eq. 6.5, after normalization. In the legend are reported the values of $\tau_{in,out}$ extracted from the Poissonian fit (black) and the mean value of the waiting times extracted from the histogram with formula 6.4. The value of 1/r is the mode of the probability distribution.

Moreover the measurement of the tunneling rates can be used to determine when the quantum dot is aligned with the Fermi energy of the reservoir and it can provide hints about the even-odd parity of the quantum dot charge state.
We find that the ratio $\frac{\tau_{out}}{\tau_{in}} = \frac{\Gamma_{in}}{\Gamma_{out}} \simeq 2$. This result is expected at the Fermi energy, where the ratio of the tunnel rates is proportional to the ratio of the degeneracies between the initial and final quantum state [16][17].
The impact of degeneracies onto the conductance through a QD has been studied theoretically in Ref. [18]. Experimental results demonstrate that the degeneracy influences the tunnelling dynamics of a QD[16][19], and that this effect can be modelled using a master equation approach [20].
Moreover, the detailed balance condition [21] [22], states that the ratio between the populations at equilibrium is equal to the ratio of the tunnel rates between the states. In this case:

$$P_0\Gamma_{in} = P_1\Gamma_{out} \tag{6.6}$$

Considering a QD containing N holes, each of the n degenerate states represents one possible microstate of the N-holes dot, all sharing the same energy E_N, with respect to the reservoir that we fix at $E_F = 0$. After a hole has tunnelled out, the dot contains $N-1$ electrons at energy E_{N-1}. If E_{N-1} is m-fold degenerate, this situation can be realized in m different ways. The partition sum of the QD–reservoir system at the transition $N \leftrightarrow N-1$

is therefore:

$$Z_{N,N-1} = \sum_{k=1}^{n} e^{-\frac{E_N}{k_B T}} + \sum_{j=1}^{m} e^{-\frac{E_{N-1}}{k_B T}} \tag{6.7}$$

and the probability of occupying each charge macrostate is given by the sum over each degenerate microstate into it:

$$\begin{cases} P_N = \frac{n}{Z_{N,N-1}} e^{-\frac{E_N}{k_B T}} \\ P_{N-1} = \frac{m}{Z_{N,N-1}} e^{-\frac{E_{N-1}}{k_B T}} \end{cases} \tag{6.8}$$

and the ratio between the two gives:

$$\frac{P_N}{P_{N-1}} = \frac{n}{m} e^{-\frac{(E_N - E_{N-1})}{k_B T}} = e^{\frac{-\mu_N + k_B T ln(n/m)}{k_B T}} \tag{6.9}$$

where $\mu_N = E_N - E_{N-1}$ is the addition energy.
By including the normalization condition $P_N + P_{N-1} = 1$, results that the occupation probability is given by a Fermi distribution centered at $\mu_N = +k_B T ln(n/m)$ above the Fermi energy $E_F = 0$.

$$P_N(\mu_N) = \frac{1}{1 + e^{\frac{-\mu_N + k_B T ln(n/m)}{k_B T}}} \tag{6.10}$$

By considering a state with $N = 1$ charges we expect it to have two-fold spin degeneracy and hence $n = 2$, whereas $m = 1$ for the non degenerate empty state $N - 1$=0. We expect that at the Fermi energy $\mu_N = 0$ and, using eq. 6.9, the ratio between the two populations is:

$$\frac{P_1}{P_0} = \frac{\Gamma_{in}}{\Gamma_{out}} = 2 \tag{6.11}$$

Conversely for a state with two charges we expect the degeneracy is n=1 for N=2 and m=2 for N=1:

$$\frac{P_2}{P_1} = \frac{\Gamma_{in}}{\Gamma_{out}} = \frac{1}{2} \tag{6.12}$$

This analysis is useful to determine the parity of our charge state and it holds not only for spin-degenerate, but also for orbitally degenerate states, allowing to determine if we are dealing with a good 2-level system or if further energy states are involved.

6.4. ENERGY-SELECTIVE READOUT OF A HOLE SPIN

We now want to study the spin properties of the holes in the QDs using energy dependent tunneling between the sensing dots and the two central quantum dots. In the community this readout technique is usually called energy-selective readout [23] or Elzerman readout [24].
The energy levels of the two spins are split ($\Delta E_Z = g\mu_B B$) through a static magnetic field, oriented along the Si nanowire.
Fundamentally the QD is loaded with a hole with unknown spin, which can be read by tuning its energy level with respect to the one of the reservoir. This technique requires a three stage pulse sequence, as shown in Fig. 6.15 and explained in Sec. 2.7.1, necessary to empty, load and finally read (E,L,R) the hole spin.

It is crucial to choose properly the tunneling rate between the QD and the reservoir, dependent on both QD and sensor filling.
The two main conditions to realize this energy-selective readout measurement are indeed the following:

- $\tau_{out} \ll T_1$, otherwise the excited spin would relax to its ground state before tunneling to the reservoir.
- $\tau_{in} > t_c$, where t_c is the integration time. Otherwise it wouldn't be possible to properly resolve the blip in the charge signal, cororresponding to a hole with spin $|\uparrow\rangle$ tunneling in/out of the reservoir.

We set an automatical routine to measure the tunnel rate of the same dot-reservoir transition ($N = 0 \rightarrow 1$), but varying the hole number in the sensor dot. In this way we can adjust the tunnel coupling between them. The routine is the following:

- Sit on the sensor signal and identify its direction, indicated by a red dashed line in Fig. 6.14 a). In the following we'll measure the tunnel rates and along this direction, which defines also the read level V_{read} of the spin measurement of Fig. 6.15.
  The direction of the sensor signal in the (G_3,G_2) or (G_4,G_5) planes provides also a measurement of the capacitive coupling between the gate accumulating the QD and its sensor, i.e. α_{G3-G2} or α_{G4-G5}.
  The pink cross indicates the half height of the charge signal and the position of $V_{read} = 0$. The value of the average phase at this point also defines the single-shot readout threshold.
  For clarity we remark that the position of $V_{read} = 0$ in Fig. 6.14 c) does not correspond to the Fermi energy E_F. This is just because of a time delay in the acquisition (going upwards in the plot a)) due to a slow time constant. The level of E_F for a QD with only one free charge can be identified when $\frac{\Gamma_{in}}{\Gamma_{out}} = 2$, as explained in the previous section.
- We measure the signal corresponding to the two charge states in the I/Q plane, to be sure to deal with a good two level system. Indeed, the appearance of a third bubble would represent the presence of an unwanted third charge state involved in the dot-lead charge transition.
  We show the bubbles with all the data points collected in the IQ plane in Fig. 6.14 b). The integration time for each data point is 10 μs, and the overall acquisition last 10 seconds, respectively 5 s at $V_{read} = \pm 1$ mV, along the direction of the sensor signal previously measured.
  The charge readout fidelity can be estimated from the overlap of the two Gaussian distributions and it is above 99% for the Y component, and hence for the phase signal ($\phi \propto \arctan(y/x)$).
- We measure the tunnel rates while varying the energy gap between the dot and the lead, along the V_{read} direction. In Fig. 6.14 c) we show the tunnel rates $\Gamma_{in,out}$ measured at each V_{read} point using formula 6.4.

By fitting the charge signal along the V_{read} axis as a Fermi distribution at $T = 440$ mK we measure the lever-arm $\alpha_{read} = 0.27$ eV/V.
Coherently from what expected from eq. 6.9, we observed that the two rates are equal for $\mu_{N=1} - E_F = k_B T ln(2) \simeq 27$ μeV (100 μV) above the Fermi energy E_F, where instead

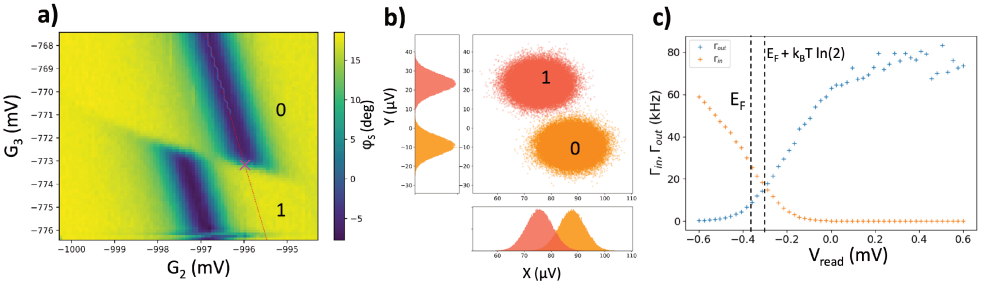

Figure 6.14: a) Charge sensor signal at the charge transition $N = 0 \rightarrow 1$. The red dashed line and the pink cross indicate, respectively, the dot-lead axis and the position of $V_{read} = 0$ in the plot c). b) I and Q values measured over 5 s in each charge region, with an integration time of 10 μs per point. c) Measured Γ_{in} (orange), Γ_{out} (blue) along the direction indicated by the dashed line in a). The position of the Fermi energy E_F and the expected crossing of the two rates $\Gamma_{out} = \Gamma_{in}$ at $\mu_{N=1} = E_F + k_B T ln(2)$ are indicated by black vertical dashed lines.

$\Gamma_{in} \simeq 30$ kHz $\simeq 2\Gamma_{out}$.
By realizing the same measurement for different filling of the sensor dot we observed that, as expected, the tunnel rates increase by increasing the sensor filling, but without following a clear trend.
To prepare the spin measurement, in Fig. 6.14 we tuned the filling of the sensor such that $\tau_{in} > t_c = 5$ μs. Then we can reasonably expect to resolve the blip in the charge signal when realizing energy-selective readout.

The averaged charge during the Elzerman pulse sequence is shown in Fig. 6.15 a). For this measurement it has been applied a magnetic field of $B = 1.3$ T along the nanowire direction.
We pulse for $t_{empty} = 20$ μs in the $N = 0$ charge state, then we spend $t_{load} = 10$ μs in the N=1 charge state, loading a spin $|\uparrow\rangle$ or a spin $|\downarrow\rangle$. While varying the read level V_R the loading and emptying pulse levels are at ± 1 mV from $V_{read} = 0$.
When loading a spin up we can observe the characteristic blip during the read stage, as shown by the green single-shot trace in Fig. 6.15 b). This is the signature of the loading of a hole with spin up, that goes back to the reservoir and only then another hole, with spin down, can enter in the QD.
Conversely when it is loaded a spin down nothing happens, as shown by the orange single-shot trace in Fig. 6.15 b).

As can be understood looking at the average signal between the loading and reading stage in Fig. 6.15 c), the loading of a spin up (dip in the signal) occurs only in a fraction of the loading events, while ideally we would like to load one of the two spin states with a 50 % probability.
In particular for the trace shown we can calculate, from the ratio between the charge signals for N=0,1 ($\Delta\phi \simeq 0.5$ rad) and the small dip observed ($\delta\phi \simeq 50$ mrad), that we can load a spin up in roughly 10% of the loading events.
Moreover we observed (not shown) that the spin up population is independent by the time spent in the load stage, for loading times between 5 μs and 150 μs. This observation suggests that the spin relaxation time T_1 at the load stage is shorter than 5 μs.
We believe that we realized the experiment with too high magnetic field, limiting drastically T_1, but at the same time, given the temperature of 440 mK we weren't able to properly

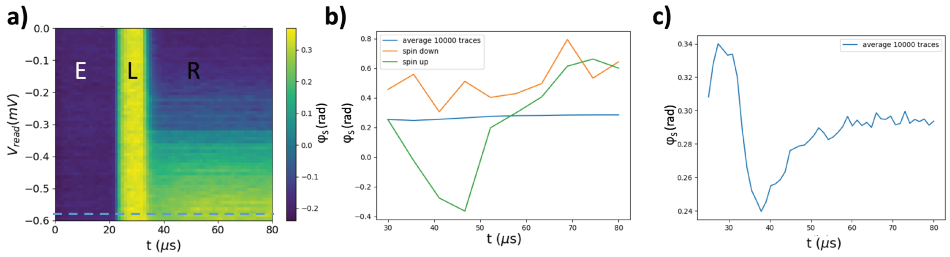

Figure 6.15: a) Energy-selective readout sequence. Empty and load level are kept fixed while varying the gate voltage position of the read level V_{read}. The signal is acquired continuously averaging over 10000 sequences. b) Comparison between two single-shot traces, for the loading of a spin up (green) and down (orange) for V_{read}=-0.58 mV, indicated by a blue dashed line in a). When loading a spin up the characteristic blip can be observed, signature of the tunneling out to the reservoir, that leaves the QD temporarily empty until another hole tunnels back. The blue line is the average of 10000 single-shot traces, zoomed in c). Here the static magnetic field B = 1.3 T is oriented along the Si nanowire.

resolve the signals of the two spins for lower fields.
Because of the difficulties imposed by a relatively high temperature, the few demonstrations of hot qubits ($T \simeq 1$ K) in silicon rely on PSB readout [25][26].

6.5. ENERGY-SELECTIVE READOUT OF A HOLE QUBIT

Adopting the strategy described previously, i.e. of using a big quantum dot to enable remote sensing from the reservoir, it has been possible to demonstrate coherent qubit oscillations of an isolated quantum dot. Most of the results described in this section served as a starting point for the characterization of the qubit described in Ref. [27], where it is discussed in detail the impact of charge noise on the qubit coherence times and it is revealed the existence of operation sweet spots where the impact of charge noise is minimized.
The experiment described here has been realized in a Blueforce dilution refrigerator with base temperature of 20 mK.
The temperature has a significative influence on the signal back reflected from the resonator placed on the reservoir. When we measured the electronic temperature in section 3.4, we also measured the magnitude of the phase signal as a function of the mixing chamber temperature, as shown in Fig. 6.16.
There is no remarkable difference between the setup used for this measurement and the one used in the experiment of the previous section. In between the two experiments there is a factor 3 in the magnitude of the phase signal and, since the noise is dominated by the amplifier noise at 3.6 K, this means also a factor 3 in the SNR.
The increased contrast in the phase signal can be understood considering that in this case a matching closer to 50 Ω is achieved when decreasing temperature. This means that, even if the shift in the resonance frequency due to the dot-reservoir resonant transition is roughly the same, the phase (and amplitude) response close to the resonance is way steeper in frequency at lower temperature, resulting in a higher contrast of the measured signal.

In Fig. 6.17 a) it is reported a cartoon of the energy levels of the system (lower panel) and a

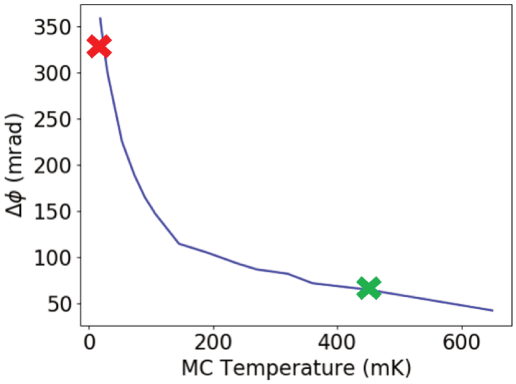

Figure 6.16: Contrast in the phase signal recorded for the dot transition $N = 0 \rightarrow 1$ (see Fig. 3.4) as a function of the mixing chamber temperature. The green cross indicates the temperature (440 mK) of the energy-selective readout experiment described in the previous section, while the red one indicates the temperature of the experiment described here (20 mK).

schematic representation of the device layout with the charge densities and readout setup. The detector has been tuned as explained in Sec. 6.1 on a similar p-type device with 4 gates in series, with channel width $W = 100$ nm, gate length $L_G = 40$ nm and spacing between each adjacent gate $S_H = 40$ nm.

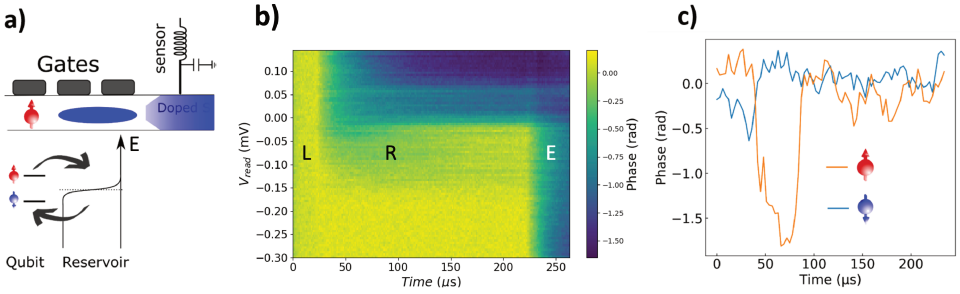

Figure 6.17: a) Scheme of quantum dots configuration and readout. b) Signal recorded by drain reflectometry while varying the read level V_{read}. Here B=0.913 T, oriented along the Si nanowire. c) Single-shot traces at $V_{read} = -0.1$ mV, for the loading of a spin $|\uparrow\rangle$ (orange trace) and $|\downarrow\rangle$ (blue trace).

The $N = 0 \rightarrow 1$ charge transition of the central dot is exploited to realize energy-selective readout with the drain reservoir, similarly to Sec. 6.4.

We can observe (Fig. 6.17 b)) that, compared to the previous case, the signal, due to the loading of a spin $|\uparrow\rangle$, lasts way longer. For this experiment indeed the typical loading time of the dot at the read stage is $\tau_{in} \simeq 80$ μs, much longer than the previous case, where $\tau_{in} \simeq 5 - 10$ μs.
The increased SNR and the longer τ_{in} at the read stage allow to distinguish the loading of a spin $|\uparrow\rangle$ or $|\downarrow\rangle$ with a readout fidelity above 99%, as can be understood from the two single-shot traces of Fig. 6.17 c).

Thanks to the strong spin-orbit coupling, typical of holes, it is possible to realize electrical manipulation of the hole spin.
A microwave burst of duration T_{burst} is applied on the gate controlling the qubit during the loading stage. At this manipulation point, both spin levels are far detuned below the electrometer electrochemical potential, preventing any tunneling.
In principle an empty dot can be loaded with a spin $|\uparrow\rangle$ or $|\downarrow\rangle$ with equal probability. Compared to the Elzerman sequence now we skip the emptying stage and the hole spin is initialized in the $|\downarrow\rangle$ state by waiting $t \gg \tau_{out}$ in the read stage.

In Fig. 6.18 a) we plot the probability of measuring a spin $|\uparrow\rangle$ as a function of the excitation frequency, centered at f_0, and the burst duration T_{burst}. The probability of loading a spin $|\uparrow\rangle$ is extracted by averaging over a 100 single-shot traces.
We observe the typical chevron pattern, demonstrating coherent qubit driving.
For $B = 0.913$ T the resonant frequency is at $f_0 = 19.116$ GHz, providing the value of the hole g-factor: $g = 1.496$.

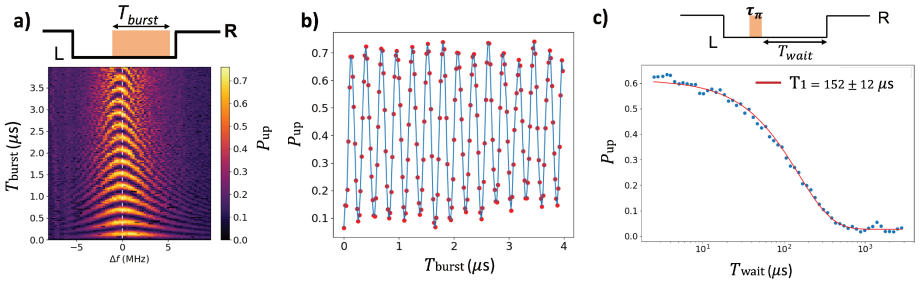

Figure 6.18: a) Top panel: scheme of the pulse sequence; a burst of microwave frequencies with duration T_{burst} is applied and then we pulse back for the spin readout and initialization (R stage). Bottom panel: the measurement of the probability of loading a spin up as a function of the burst duration and frequency provides the characteristic Chevron pattern. The magnetic field is set at B=0.913 T along the nanowire direction. The horizontal axis is centered around the Larmor frequency $f_0 = 19.116$ GHz. A cut at f_0 is shown in b), demonstrating Rabi oscillations with $f_{Rabi} \simeq 3.5$ MHz c) Measurement of T_1 for $B = 0.941$ T along the nanowire direction. T_{wait} is the time spent in the loading region after the π-pulse. Above a scheme of the corresponding pulse sequence. The T_{wait} axis is in log scale.

When driving in a close proximity to the Larmor frequency f_0 we can observe the Rabi oscillations (see Fig. 6.18 b)).
As in Fig. 6.26 d, the envelope of the Rabi oscillations is not well defined and we cannot estimate precisely the dephasing time T_2^{Rabi} from this measurement, but we can say that it is above 3-4 μs.

From the period of the Rabi oscillations we know the duration of the microwave burst necessary to realize a full rotation of the hole spin, that is $\tau_\pi \simeq 250$ ns and we can prepare the hole spin in the $|\uparrow\rangle$ state. By increasing the time spent in the loading stage T_{wait} after the π-pulse, the excited spin can relax to its ground state before the reading stage.
The probability of loading a spin $|\uparrow\rangle$ as a function of the waiting time T_{wait} provides a measurement of the spin relaxation time T_1, as reported in Fig. 6.5 c).
The spin up probability as a function of the loading time can be fitted with an exponential

decay. For this particular configuration we found $T_1 = 152 \pm 12$ μs.
We also observed a spin relaxation time up to $T_1 \simeq 1$ ms for $B = 0.4$ T and up to $T_1 \simeq 3$ ms for $B = 0.4$ T oriented perpendicularly to the channel [27].

We now turn to the estimation of the dephasing time T_2^*, measured through a Ramsey experiment.
We remark here that the two dephasing time, T_2^* and T_2^{Rabi} have a different physical meaning. Indeed whereas T_2^{Rabi} gives an estimation of the dephasing while precessing between the two poles of the Bloch sphere $|\uparrow\rangle$ or $|\downarrow\rangle$, T_2^* instead gives an estimation of the dephasing acquired starting from the equator of the Bloch sphere, where the qubit state is initially in a quantum superposition $(\alpha(t=0), \beta(t=0) = \frac{1}{\sqrt{(2)}})$ and evolves as $|\psi(t)\rangle = \frac{\alpha(\theta(t))|\uparrow\rangle - \beta(\theta(t))e^{i\phi(t)}|\downarrow\rangle}{\sqrt{\alpha^2(\theta(t))^2 + \beta^2(\theta(t))}}$, where ϕ is the angle in the equatorial plane of the Bloch sphere and θ is the out-of-plane angle.

By waiting $\simeq 600$ μs at the read stage we ensure that the spin is initialized in a $|\downarrow\rangle$ state. Then we pulse to the (former) load stage to avoid a spin $|\uparrow\rangle$ to tunnel out. A schematic of the pulse sequence is shown in Fig. 6.19 b). In order to go from a pure qubit state to a quantum superposition we need to apply a Hadamard gate. In terms of pulses this means to apply half rotation of the qubit state, with a pulse of duration $\tau_{\pi/2}$.

After realizing a rotation of the spin state of $\pi/2$, we wait a time T_{wait} during which the qubit state evolves freely. Finally we apply another $\pi/2$ rotation and read the spin state.
After the first rotation the spin, initialized in a superposition state, acquires a phase $\phi(t)$ in the equatorial plane of the Bloch sphere, due to the coupling with the surrounding environment, that determines the period of the Ramsey oscillations. The phase acquired out of the equatorial plane $\theta(t)$, destroys the quantum superposition, inducing a damping of the Ramsey oscillations, therefore providing the typical dephasing time T_2^*.
In Fig. 6.19 a) we show the Ramsey fringes as a function of T_{wait} and frequency applied.

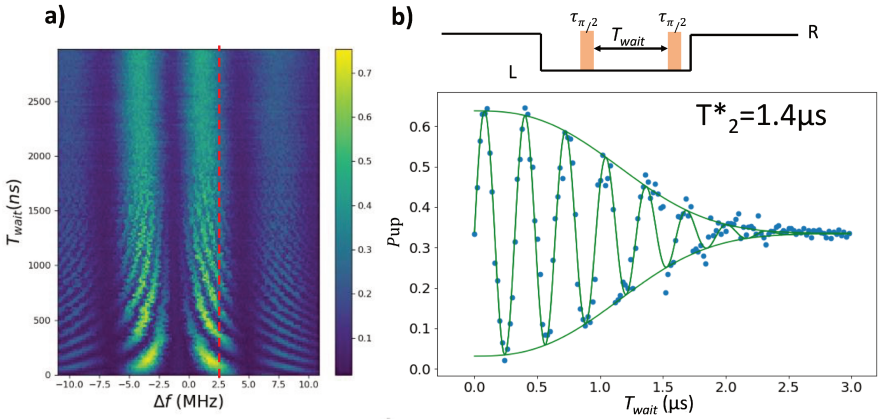

Figure 6.19: a) Measurement of Ramsey fringes for $B = 0.913$ T along the Si nanowire. b) Top panel: scheme of the pulse sequence for a Ramsey experiment. Bottom panel: line cut at Δf=+2.5 MHz, indicated by dashed red line in a). The fit of the fringes envelope with a Gaussian decay function provides $T_2^* = 1.4\mu$s.

The envelope of the Ramsey fringes, with the microwave excitation frequency detuned by $\Delta f = +2.5$ MHz from the Larmor frequency is shown in Fig. 6.19 b). It can be fitted with a Gaussian decay function [28] $P_\uparrow = Ae^{-(\frac{t}{T_2^*})^2} + B$, where A and B are fitting parameters to account for the measurement and initialization errors. We measure $T_2^* = 1.4$ μs.
This value of T_2^* is the highest reported so far for hole based spin qubit [29] [30] [31][32]. Moreover, by varying the magnetic field orientation an enhancement of T_2^* has been observed up to $T_2^* > 8$ μs, for a magnetic field orientation perpendicular to the plane of the Si nanowire [27].

6.5.1. TEMPERATURE DEPENDENCE OF T_1

In between the two energy-selective readout experiments shown in Secs. 6.4, 6.5, realized on very similar devices, we found a difference in T_1, for similar magnetic fields, of at least one order of magnitude, while the effective hole temperature in one case (T_1=150 μs for $B \simeq 1$ T and $T_{eff} \simeq 100$ mK) is roughly 4 times lower than in the other one (T_1<5 μs for $B \simeq 1$ T and $T_{eff} \simeq 450$ mK).
It is therefore worth to understand which is the effect of temperature on T_1.

When looking at the temperature dependence of T_1 we should consider that both photons and phonons contribute to the decay. Their density follows the Bose-Einstein distribution

$$n_B(E, k_B T) \propto \frac{1}{e^{\hbar\omega_L / k_B T} - 1} \tag{6.13}$$

where ω_L is the Larmor frequency, linearly proportional to the B-field applied. The spin relaxation rate $1/T_1$ is expected to be linearly proportional with the boson density, and therefore at first order the temperature dependence is the same for phonon and Johnson noise [33].

At sufficiently low temperatures ($\hbar\omega_L \gg k_B T$), from eq. 6.13 the spin lifetime is expected to depend exponentially on temperature. For $B = 1$ T we can expect T_1 to decrease rapidly by raising temperature up to 150-250 mK.
At higher temperature ($\hbar\omega_L \ll k_B T$) instead we recover the classical limit, where we expect the boson density to grow linearly with T, and hence we expect $T_1(T) \propto T^{-1}$.
However, by including the effects of two phonon processes we expect $T_1(T) \propto T^{-2}$ [34].
The exponential decrease of T_1 expected at low temperature, together with two-phonon processes might explain why, with an electronic temperature differing of a factor 4, the relaxation time T_1 is degraded by more than one order of magnitude.

We highlight that the processes governing holes spin relaxation are significantly different from the ones of electrons, where the dominant contribution can be due to spin-valley coupling. The expected relaxation time for valley relaxation is $T_1 \propto B^{-1}$ for photon induced decay and $T_1 \propto B^{-5}$ for phonon induced decay [33]. The valley relaxation mechanism goes to zero if the magnetic field is parallel to one of the three crystallographic axes [35], and we expect $T_1 \propto B^{-3}$ for photon induced decay and $T_1 \propto B^{-7}$ for phonon induced decay.
When looking at holes the spin relaxation is dominated by the band mixing between HH and LH bands, that couples the hole spin with phonons [36]. In this case a dependence $T_1 \propto B^{-9}$ is expected for Rashba SOI and a dependence $T_1 \propto B^{-5}$ is expected for Dresselhaus SOI [37].
However, with the device of Sec. 6.5 we observed B-field dependencies of T_1 between B^{-2}

and B^{-3}, depending on the field orientation. This may be understood considering that, with respect to bulk phonons ($T_1 \propto B^{-5}$), the relaxation rate is inversely proportional to the characteristic size of the system, and the dependence on the Larmor frequency, and hence on the magnetic field, is reduced by one power each time the phonons get confined in an additional direction [36]. However, further studies are required in order to clarify holes relaxation mechanism in silicon under different device geometries, confinement potentials and magnetic field directions.

When considering the temperature dependence of the relaxation time T_1 of electrons, we expect a behaviour similar to holes at low temperature, due to the boson density n_B, while instead when considering higher temperatures two-phonon processes give raise to a $T_1(T) \propto T^{-9}$[33] or $T_1(T) \propto T^{-5}$ [26] when involving intervalley piezophonons.

6.6. GATE REFLECTOMETRY DISPERSIVE READOUT AND COHERENT CONTROL OF A HOLE SPIN QUBIT IN SILICON

Most of the results reported in this section have been published in [38]. In this experiment coherent oscillations of a hole spin qubit are read through dispersive readout on the gate. This experiment was carried out in an Oxford Triton dilution refrigerator, with base temperature around 20 mK.

The device is a p-type double gate transistor. In Fig. 6.20 a), c) we show a cross section and a SEM top view of the device.
The transistor channel is a Si nanowire (light blue), 11-nm-thick and 35-nm-wide. It connects p-type, boron-doped source-drain contacts (dark blue). The Si channel lies on a 140-nm-thick SiO_2 buffer layer (pink). The two 35-nm-wide gates (gray) are separated by 35 nm. The Si_3N_4 spacers (cyan), prevent dopant implantation in the Si channel.
The right control gate (G_C) confines a hole quantum dot encoding the spin qubit, whereas the left one (G_R) confines a helper dot, enabling spin readout via gate reflectometry.
The phase and amplitude frequency response of the resonator is shown in Fig. 6.20 b). From the resonant frequency $f_0 = 339$ MHz, knowing the nominal value of the inductance $L = 220$ nF, it can be extracted a parasitic capacitance $C_p \simeq 1$ nF.
The demonstrated qubit readout scheme requires no coupling to a Fermi reservoir, thereby offering a compact and potentially scalable solution for the readout of many qubit arranged in arrays.
In the stability diagram in Fig. 6.21 it is possible to appreciate only the dispersive signal corresponding to interdot transitions and not the one corresponding to dot-lead transitions. This ensure us that the readout dot has a low tunnel coupling with the nearby reservoir (below MHz, probably kHz [39]).

Without a charge sensor it is not possible to precisely count the charges present in the system. However a rough estimation can be given by comparing the gate voltages of the transition with the threshold voltages (around +1.2 V) at room temperature and the addition voltage in the many hole regime.
In the bottom panel of the stability diagram of Fig. 6.21 the system is in the many hole regime, where the voltage spacing between the DQDs is approximately constant. The typical spacing in gate voltage between two charge states is about 25 mV, consistent with other experiments on similar samples [31, 40].
We estimate an order of magnitude of 5 holes in the readout QD (mainly controlled by V_R) and 10-20 holes in the control QD (mainly controlled by V_C).

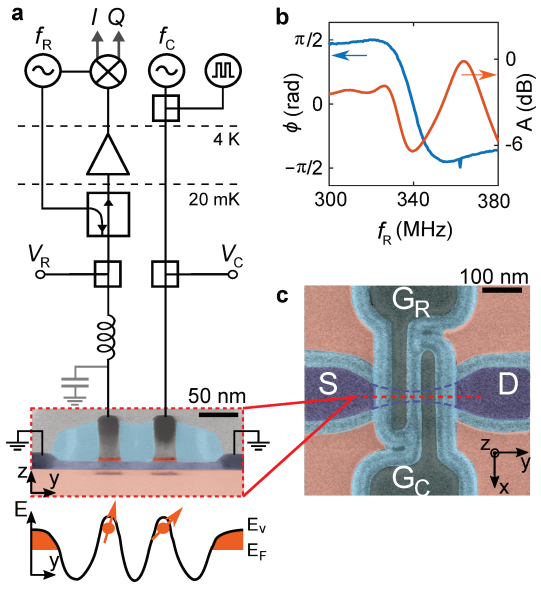

Figure 6.20: a) Scheme of the experimental setup and false-color transmission electron micrograph of a double-gate Si device. In the left circuit the DC voltage is added to the rf signal for dispersive homodyne detection with a lock-in. The incoming and outgoing reflectometry signal are separated by a directional coupler and the output signal is amplified with a cryogenic amplifier (Caltech). The circuitry of the right gate combines DC voltages for DQD electrostatic tuning, fast voltage pulses (MHz) and GHz excitations for EDSR. b) Phase response (ϕ) and attenuation (A) of the resonator at base temperature T=20mK. c) Scanning electron micrograph (SEM) top view of the device. The different colors in the cross-section and top-view identifies the Si nanowire (light blue), the source-drain contacts (dark blue), the buried oxide SiO_2 (pink), the gates (gray) and the spacers (cyan).

In the large stability diagram it can also be observed a series of nearly horizontal parallel lines. Such lines repeat quite regularly, even when the silicon channel is completely pinched off. Consequently, we speculate that these features are related to the charging of objects extrinsic to the channel.

Furthermore we notice that, for interdot tunnel couplings of few GHz and an effective temperature of 250 mK (both extracted by fitting the dispersive signal), the interdot transition lines are expected to be quite thin in gate voltage (see formula 2.24), and are very likely not resolved in large maps (obtained with large voltage steps).
Since a high resolution is required to observe these features it is beneficial to find some "tricks" to speed up the measurement. It is possible to act both on the hardware and on the measurement software.
The communication with the DACs takes $\simeq 2$ ms for each operation (ask and write), and getting rid of these dead times significantly speed up the measurements. This can be done by measuring continuously while applying a voltage ramp [41][42], in this way we can get rid of the dead times due to the continuous procedure of setting DAC values (write) and checking if the dac values is correct (ask).
For what concerns the software it is possible to save time by avoiding to measure the full stability diagram, and measuring only when a signal is expected. Deep learning techniques are a useful instrument for this purpose, as demonstrated recently by an increasing effort in applying it for measurement of DQDs stability diagrams[43][44][45]

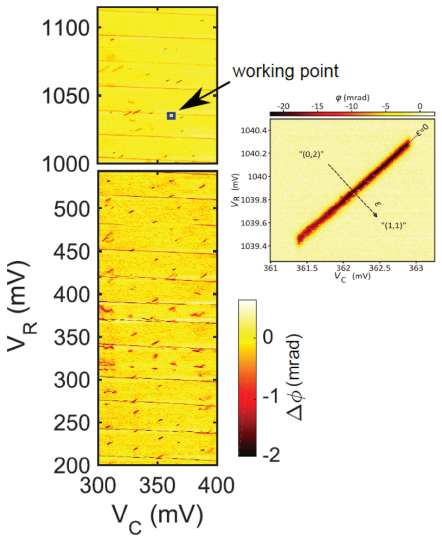

Figure 6.21: Dispersively detected charge stability diagram of the device as a function of the two top gate voltages, V_C (control gate) and V_R (readout gate). In the bottom panel, both gates are tuned in a strong accumulation mode, and the many hole regime, characterized by a regular spacing between the interdot transition lines, is reached. In the upper panel, V_R approaches the gate voltage threshold; as a result, interdot charge transitions are unequally spaced. The blue square denotes the area zoomed-in in the inset, where $B = 0$ T.

6

and Coulomb diamonds [46] .
These two approaches to speed up the measurement of stability diagrams regards separately software and hardware and are absolutely compatible, therefore a cointegration of the two would be the optimal solution.

6.6.1. MAGNETOSPECTROSCOPY OF THE HOLE DQD

Since we cannot rely on the interaction with a reservoir to realize spin-to-charge conversion, the option left is to realize it through PSB. The first step towards the realization of a spin qubit is therefore to find an ICT that shows signature of PSB, and hence whose parity is (even,even)-(odd,odd). As in Sec. 5.4, PSB can be detected through a displacement of the ground state with magnetic field and, consequently, from the vanishing of the dispersive signal, corresponding to inhibited interdot tunneling.
In this experiment the magnetic field is oriented along the Si nanowire.
Figure 6.22 b) shows the B-dependence of the phase signal at the detuning line indicated in Fig. 6.22 a).
We observe the signal displacing towards negative energy detuning, allowing to determine the parity of the two charge states.

Differently from the case of Fig. 5.7, in Fig. 6.22 b it can be noticed the appearance of a second peak (see linecut at $B = 0.46$ T in Fig. 5.7 c), that is due to the thermally populated $T_0(1,1)$ state, as it is explained in the following.
We recall that the magnitude of the quantum capacitance contribution to the dispersive signal is proportional to the curvature of each energy states $\phi_i \propto \frac{\partial^2 E_i}{\partial \epsilon^2}$.

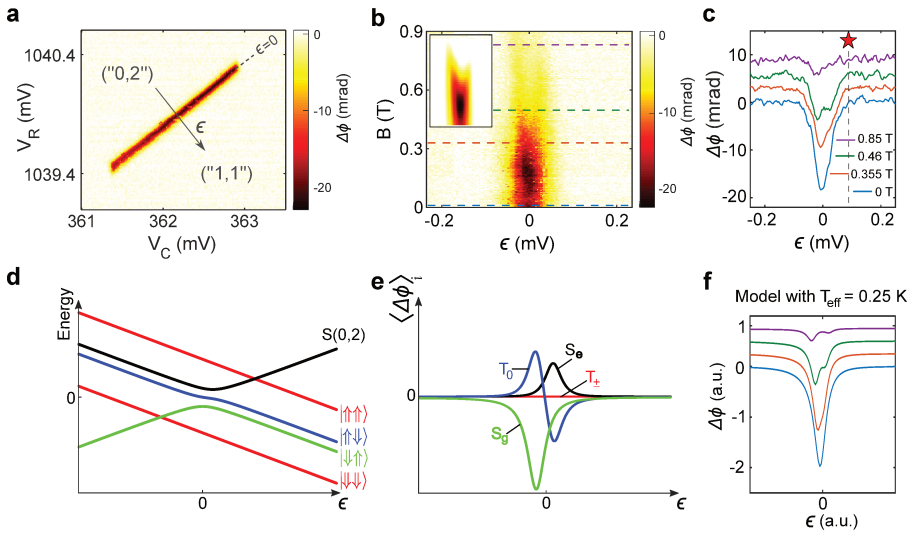

Figure 6.22: **Magnetospectroscopy of the DQD.** (a) Phase shift of the reflected signal as a function of V_C and V_R near the interdot transition line under study. The arrow indicates the detuning axis ϵ. (b) Interdot dispersive signal as a function of a magnetic field B, oriented along the nanowire axis. The phase response diminishes with B, denoting an interdot charge transition of $(0,2) \leftrightarrow (1,1)$ type. Inset: theoretical prediction of the dispersive response for a DQD model taking into account thermal spin populations. (c) Line cuts of the plot in panel b) at the position of the dashed lines. Data are offset for clarity. (d) Schematic of the DQD energy levels close to a $(0,2) \leftrightarrow (1,1)$ transition at finite $B = 0.65$ T and for $|g_L^* - g_R^*| = 0.5$ (e) Thermally-averaged phase response $\langle \Delta\phi \rangle_i$ with $T_{\text{eff}} = 0.25$ K. $\langle \Delta\phi \rangle_i$ is second derivative of the energy-level dispersion of each state i in panel d), weighted by its occupation probability. Here i labels the different DQD states, i.e. the singlets S_g (green) and S_e (black), and the triplets T_0 (blue), T_- (red), and T_+ (red). (f) Qualitative phase shift resulting from the sum of all $\langle \Delta\phi \rangle_i$ from panel e). A double-peak structure emerges at sufficiently high B in qualitative agreement with the experimental data in panel c). The one-dimensional cuts are taken at B= 0, 0.35, 0.5 and 0.85 T.

In the cases studied in Sec. 5.4.1 the only states with a curvature were the ground and excited singlets, and therefore no contribution was expected from $T_0(1,1)$. This is because we previously assumed that the two electrons were having the same g-factor and hence $S(1,1)$ and $T_0(1,1)$ were degenerate for high detuning in (1,1), even in presence of a magnetic field.
When dealing with holes instead this degeneracy is broken by different g-factors for the left (g_L^*) and the right dot (g_R^*). In the positive detuning regime, this results in four non-degenerate (1,1) levels corresponding to the following spin-orbit eigenstates: $|\Downarrow\Downarrow\rangle$, $|\Uparrow\Downarrow\rangle$, $|\Downarrow\Uparrow\rangle$, $|\Uparrow\Uparrow\rangle$ [47, 48, 49], where the first spin is in the dot below G_C and the second one below G_R. At large negative detuning, the ground state is a spin-singlet state $S(0,2)$ and the triplet states $T(0,2)$ lie high up in energy.

From the Hamiltonian 2.30[1] it can be derived the energy diagram of Fig. 6.22 d. The difference in g-factor ($|\Delta g = 0.5|$ is such that the excited singlet state S_e (in black) and $|\Uparrow,\Downarrow\rangle$, $|\Downarrow,\Uparrow\rangle$ are mutually coupled and hence anticross.
In other words, the origin of the anticrossing is the electric dipole moment that couples

[1]The Hamiltonian 2.30 can be written in both the singlet-triplet and single spins basis, as shown in the supp. info of Ref. [38]. The term t_{SO} is negligible in the present case.

$T_0(1,1)$ and $S(1,1)$ via $\frac{1}{2}(g_L^* - g_R^*)\mu_B B$. This might eventually imply also a second-order coupling with $S(0,2)$.
As a result in the $T_0(1,1)$ state it is induced a positive curvature for slightly negative detuning ϵ and a negative curvature for positive ϵ (see blue curve of Fig. 6.22 d). This negative curvature at $\epsilon > 0$ is responsible of the appearance of the second dip in phase for $B = 0.46$ T (green curve in Fig. 6.22 c).
To proper understand the contribution of this curvature we calculated the quantum capacitance contribution of each state, weighted by its Boltzmann occupation probability, as shown in Fig. 6.22 e.
Differently from the case of Sec. 5.4.1 also the triplet state $T_0(1,1)$ provides a non negligible quantum capacitance contribution and therefore the signal can be fitted by summing each contribution individually, weighted by its population:

$$\Delta\phi(\epsilon) = \sum_i \langle \Delta\phi(\epsilon) \rangle_i = \phi_i(\epsilon) P_i(\epsilon) \tag{6.14}$$

where $P_i(\epsilon) = \frac{e^{-\frac{E_i(\epsilon)}{k_B T_{eff}}}}{Z(\epsilon)}$ and ϕ_i is proportional to the energetic curvature .
The coupling term t can be extracted by fitting the trace along ϵ for $B = 0$ T (blue line in Fig. 6.22 c).
The lever-arm parameter α, relating ϵ to the energy difference between the electrochemical potentials of the two dots, is estimated by fitting the signal along the detuning line in Fig. 6.22, yielding $\alpha \simeq 0.58\ \frac{eV}{V}$.
The full width at half maximum (FWHM) of the dispersive signal as a function of temperature allows to estimate the tunnel coupling (supp. info of [38]). Depending on whether thermal populations of the excited states contribute or not to the FWHM, for B=0 T it is equal to $4t$ in the high temperature limit ($k_B T \gg t$), or to 3.2 t in the low temperature limit, ($k_B T \ll t$), as can be simulated using eq. 6.14, with energy given by the eigenstates of Hamiltonian 2.30.
We estimate t between 6.4 and 8.5 μeV.

The DQD spectrum as a function of ϵ (in Fig. 6.22 d) is calculated with $g_L^* = 1.62$, $g_R^* = 2.12$, $t = 8$ μeV and $B = 0.65$ T. This model, with the chosen hole temperature $T_{eff} = 250$ mK, qualitatively reproduces the emergence of the double-dip structure at $B \simeq 0.5$ T, as well as its gradual suppression for higher magnetic field, as shown in Fig. 6.22 f. Indeed the increasing of the Zeeman energy results in the losing of population of the singlet ground S_g and excited states S_e in favour of the new ground state $T_-(1,1)$, which has no curvature.

One last remark is that, with respect to the Hamiltonian (2.30), the term t_{SO}, responsible of anticrossing between the T_-, T_+ and singlet states is negligible ($t_{SO} \ll t$).
Significant spin-flip tunnelling terms like $t_{SO}^{|T_-\rangle} |T_-(1,1)\rangle \langle S(0,2)|$ and $t_{SO}^{|T_+\rangle} |T_+(1,1)\rangle \langle S(0,2)|$ would lead to an additional dispersive signal with a strong magnetic field dependence as it has been shown in Ref. [50].
Indeed, it is still possible that such spin-flip tunneling terms might be relevant for orientations of the external magnetic field different from the one investigated here.

6.6.2. EDSR AND READOUT OPTIMIZATION

After having clarified the nature of the dispersive signal and the energetic structure of the DQD it is possible to discuss the realization of a hole spin qubit.
Electric dipole spin resonance (EDSR) [31, 40, 51] is induced by a microwave voltage

modulation applied to gate G_C. A more general discussion about the microscopic origin the SOC enabling the EDSR can be found in Sec. 2.8.

To detect EDSR dispersively, the resonating states must have different quantum capacitances. The DQD is therefore initially tuned in a "shallow" (1,1) configuration, i.e. close to the boundary with the (0,2) charge state where the $T_0(1,1)$ state has a curvature. This detuning point, at $\epsilon \simeq +0.1$ mV, is indicated by a red star in Fig. 6.22 c.
Figure 6.23 shows the dispersive measurement of the EDSR. The microwave excitation with frequency f_C is applied continuously, while sweeping the magnetic field.

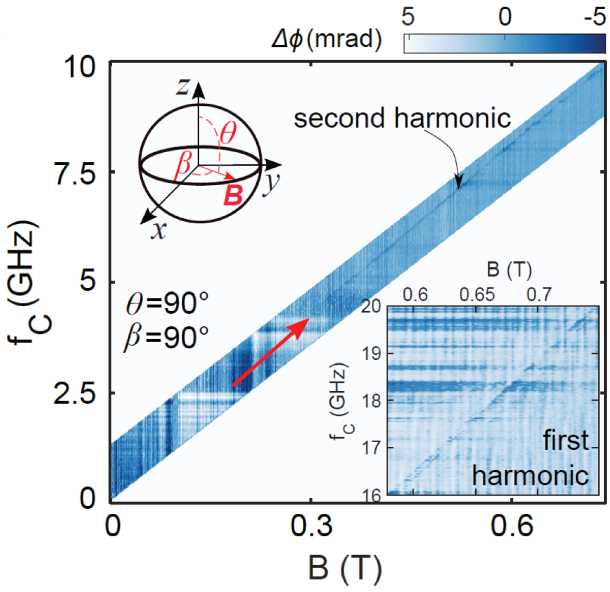

Figure 6.23: Phase response as a function of B and microwave frequency f_C. B is oriented along the nanowire direction y, corresponding to $\theta = 90°$ (out of plane angle), $\beta = 90°$ (in plane angle). The linear phase ridge, denoted by a red arrow, is a characteristic signature of EDSR. It corresponds to a second-harmonic signal, while the much weaker first harmonic is shown in the lower inset.

We attribute the resonance line to a second harmonic driving process where $2hf_C = g\mu_B B$. From this resonance condition we extract $g = 1.735 \pm 0.002$, in agreement with previous works [31, 40]. Even though both first and second harmonic excitations can be expected [52][53], the first harmonic EDSR line (inset of Fig. 6.23) is unexpectedly weak. A comparison of the intensity of the two signals requires the knowledge of many parameters (relaxation rate, microwave power, field amplitude) and it goes beyond the goal of the present work.
We attribute the observed EDSR line to a resonant transition between the ground state $|\Downarrow,\Downarrow\rangle$ and the excited spin state $|\Uparrow,\Downarrow\rangle$, indeed the microwave excitation drives the first spin, controlled by gate G_C. A further confirmation that we are not driving other spin transitions is given by the extrapolated intercept at 0 T of the EDSR transition line in Fig. 6.23, found much smaller (< 100 MHz) than the tunnel coupling energy t.

The visibility of the EDSR signal can be optimized by a fine tuning of the gate voltages and magnetic field orientation. In particular, the interdot signal is found to be heavily

impacted by the magnetic field orientation.
We observed that for magnetic field direction out of the Si channel plane (i.e $\theta \neq 90°$), and a static magnetic field of $B = 0.6$ T the pure ICT dispersive signal is enhanced, signature that the ground state would still be a spin singlet [42].

For this experiment we want to be in a regime where the contrast between the ground state dispersive signal, and the one of the excited state is maximized. It is therefore beneficial to initialize the system in the ground state $T_{-}(1,1)$ that shows no curvature at all, and excite in a regime where the curvature of the $T_0(1,1)$ is maximized.
We therefore measure the EDSR signal as a function of the in plane angle β, as shown in Fig. 6.24. The maximum intensity of the EDSR signal has been found for an in plane angle

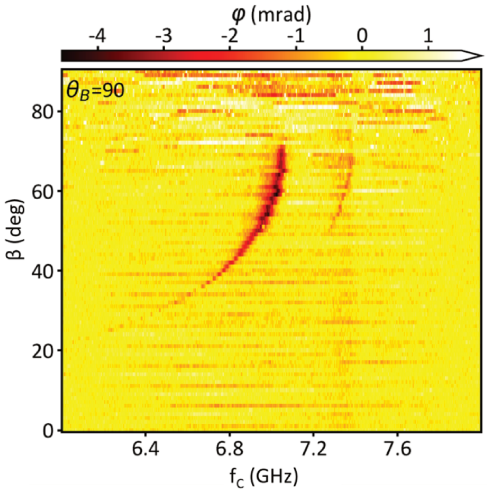

Figure 6.24: EDSR phase shift as a function of the in plane angle β of the applied magnetic field B and frequency f_C. The static field is set to $B = 0.5$ T. The highest signal is found for β=55°, which is the field such that the curvature of the $T_0(1,1)$ state is maximized.

$\beta = 55°$.
We also observed a thin replica of the EDSR signal due to the mixing with the reflectometry tone, as in Sec. 5.7.

The visibility of the EDSR can be further enhanced by a fine tuning of the gate voltage, such that the curvature of the $T_0(1,1)$ state is maximized. Fig. 6.25 shows the ICT while continuously applying the microwave tone at f_C=7.42 GHz. The static field is set at $B = 0.52$ T. Looking at the blue line cut in Fig. 6.25 b), it can be observed that the double peak structure of the interdot is maintained in this regime, also when the system is not excited, due to a residual thermal population of $T_0(1,1)$.
EDSR appears as an additional phase signal around $V_C \simeq 362.5$ mV and $V_R \simeq 1040$ mV, indicated by the black arrow as I/R. This point will be used for the qubit initialization and readout.
Such EDSR feature is extremely localized in the stability diagram. This can be understood considering that the hole g-factor exhibits a strong gate voltage dependence [40].
In the inset of Fig. 6.25 it is shown the comparison between the observed EDSR signal and

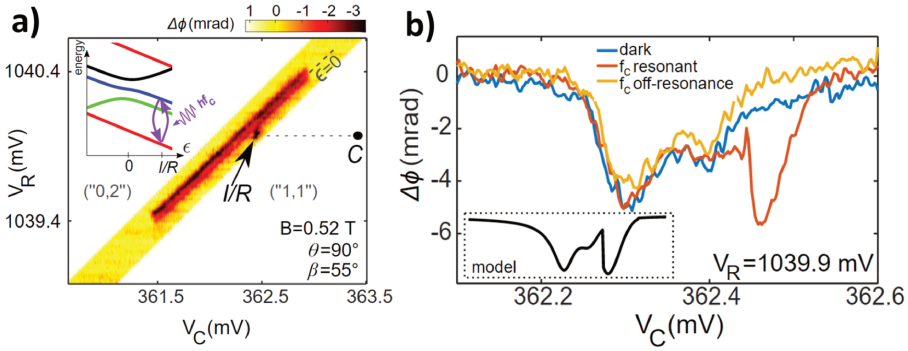

Figure 6.25: a) Stability diagram at $B = 0.52$ T (orientation $\beta = 55°$ and $\theta = 90°$ according to the diagram of Fig. 6.24) with microwaves applied continuously with frequency $f_C = 7.42$ GHz and power $P_C \approx -80$ dBm. In the stability diagram the increased population of the excited state $T_0(1,1)$, induced by resonant transitions with $T_-(1,1)$ (purple double arrows in inset), is visible as a localized phase signal at point I/R, indicated by the black arrow. Point C is the control point, where qubit manipulation is realized. b) Phase shift at $V_R = 1039.9$ mV as a function of V_C without microwave irradiation (blue line), and under on-resonance (red) and off-resonance (yellow) excitation at $f_C = 7.42$ and 7.60 GHz, respectively. EDSR-stimulated transitions appear as a pronounced peak whose position and line shape are compatible with our model (inset), using the following parameters $g_L^* = 1.575$, $g_R^* = 2.075$, $t = 6\,\mu$eV, $B = 0.52$ T and $T_{\text{eff}} = 0.25$ K.

the one calculated with the model described previously, using as parameters $g_L^* = 1.575$, $g_R^* = 2.075$, $t = 6\,\mu$eV, $B = 0.52$ T and $T_{\text{eff}} = 0.25$ K.
In the model we assume that for an excitation frequency $f_C = 7.42$ GHz at the point I/R the population of $T_0(1,1)$ and $T_-(1,1)$ is balanced equally by the coherent oscillations.

6.6.3. COHERENT MANIPULATION OF HOLE SPIN QUBIT

After having optimized the EDSR signal we are ready to drive coherent qubit oscillations. The two-step pulsing sequence used is schematized in Fig. 6.26 a. The spin oscillations are driven at the control point C ($\epsilon \simeq +1$ mV deep in the (1,1) region), where holes are strongly localized, with negligible interdot tunnel coupling.
A microwave burst of duration τ_{burst} and frequency f_C drives single spin rotations between $|\Downarrow\Downarrow\rangle$ and $|\Uparrow\Downarrow\rangle$; the system is then brought back to I/R in the "shallow" (1,1) regime for a time t_{wait} for readout and initialization.
The reflectometry tone f_R is applied during the whole sequence, with duration T_M and the reflected signal is acquired continuously. This means that it is acquired an average of the signal in deep (1,1), which gives no dispersive contribution and at I/R (1,1), where the $T_0(1,1)$ can be sensed dispersively.
Alternatively we could have triggered the acquisition only at the readout point. However the noise introduced during the manipulation stage at point C is washed out by averaging over many acquisition cycles.

The magnetic field direction is now set to $\theta = 60°$ and $\beta = 0°$. Indeed, after a refrigerator incident resulting in the warm-up of the sample, the device was cooled down again and it was found that the EDSR signal was maximized for this magnetic field direction.
We demonstrate coherent single spin control in Fig. 6.26 c. The phase signal is collected as a function of microwave burst time τ_{burst} and driving frequency f_C . The spin state is initialized at point I/R, waiting a time $t_{wait} = 1\ \mu$s$\simeq T_1$. From this plot we can extrapolate precisely the Larmor frequency, being $f_{Larmor} = 12.865$ GHz for $B = 0.512$ T. The g-factor

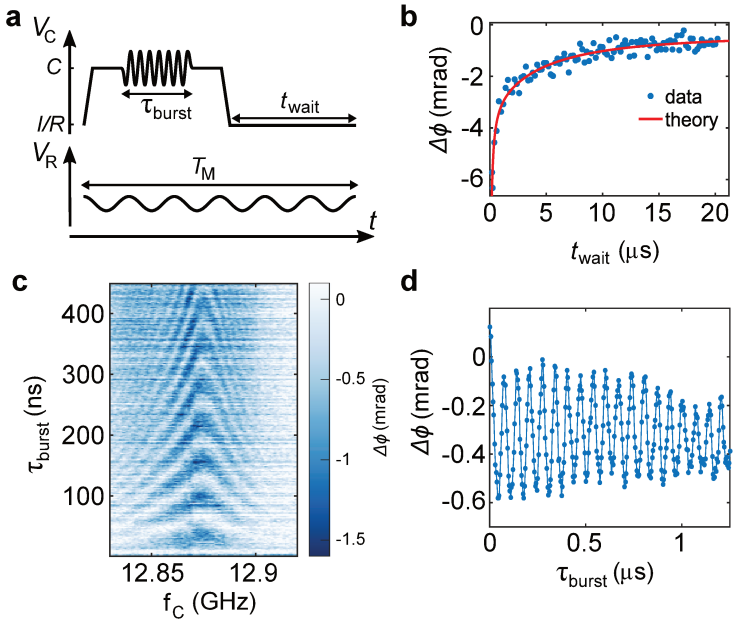

Figure 6.26: **Single spin control and dispersive sensing.** (a) The pulse sequence alternating between "deep" (1,1) regime (C) for spin manipulation and "shallow" (1,1) regime (I/R), close to the (0,2) ↔ (1,1) transition, for the readout and resetting of the spin system. A microwave burst rotates the hole spin during the manipulation stage. The readout tone is continuously applied throughout the sequence period T_M. (b) Phase shift as a function of t_{wait} for a ≃ 1 mV pulse on V_C with τ_{burst} = 100 ns and f_C = 14.294 GHz, with B = 0.62 T along $\beta = 0°$ and $\theta = 60°$. The phase signal approaches 0 when $t_{\text{wait}} \gg T_1$. A simple model yields $T_1 = 2.7 \pm 0.7$ μs. (c) Dispersive signal $\Delta\phi(f_C, \tau_{\text{burst}})$, measured with the detuning pulses of panel a) with t_{wait} = 1 μs. Four maps have been averaged. (d) Phase response as a function of EDSR burst time at f_C = 12.865 GHz. The plot shows Rabi oscillations with 15 MHz frequency due to coherent spin rotations. Each data point is integrated for 100 ms and then averaged over 30 traces.

extracted for this new field direction is then g=1.795.

In Fig. 6.26 d we plot the phase signal as a function of τ_{burst}, demonstrating Rabi oscillations with 15 MHz frequency. However, while we expect that the Rabi oscillations envelope should follow an exponential damping providing the characteristic spin dephasing time T_2^{Rabi}, the behaviour of the Rabi oscillations is quite irregular. This envelope can be attributed to random phase accumulation in the qubit state by off-resonant driving at $f_{\text{Larmor}} \pm f_R$ due to up-conversion of microwave and reflectometry tones during the manipulation time. Another possible explanation is the non perfect initialization, since $t_{wait} \simeq T_1$.

We increased slightly the magnetic field to B = 0.62 T (keeping it at $\theta = 60°$ and $\beta = 0°$), obtaining a new larmor frequency at f_C = 14.294 GHz, providing g = 1.64. We attribute the change in the g-factor to the new gate voltage readout point I/R found with a map analogue to the one of Fig. 6.25. In this regime the Rabi oscillations have been measured again, as shown in Fig. 6.27. The Rabi oscillations can now be fitted using as an

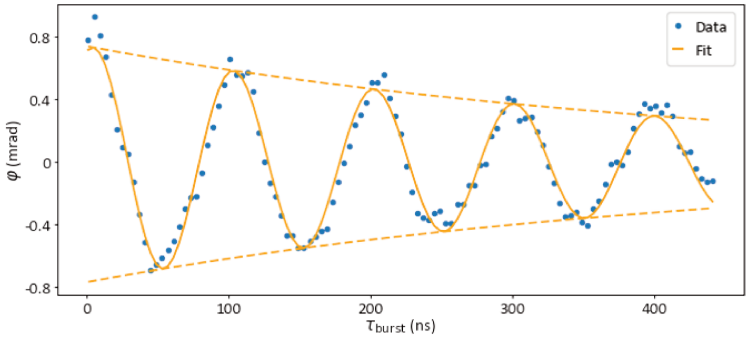

Figure 6.27: For this plot $B = 0.62$ T, The fit of the Rabi oscillations provides $T_2^{Rabi} = 0.45 \pm 0.03$ μs and $f_{Rabi} = 10.1$ MHz. Presented in [54].

exponentially damped sinusoid:

$$\Delta\phi = \phi_0 + \phi_1 e^{-\frac{\tau_{burst}}{T_2^{Rabi}}} (2\pi f_{Rabi} \tau_{burst} + C) \tag{6.15}$$

where ϕ_0, ϕ_1, C, f_{Rabi} and T_2^{Rabi} are the fitting parameters. From the exponential envelope of Fig. 6.27 it is obtained $T_2^{Rabi} = 0.45 \pm 0.03 \mu$s and $f_{Rabi} = 10.1$ MHz.

From the Rabi frequency we can extract $\tau_\pi \simeq 100$ ns, defined as the time necessary to execute a full rotation of the spin state, i.e. a π-rotation in the Bloch sphere.
Knowing τ_π we can initialize the DQD in a quasi-pure $|\Uparrow\Downarrow\rangle$ state and measure the characteristic spin decay time T_1 by varying the time spent in the readout point t_{wait}.
During this pulse sequence we spend 250 ns at the control point, applying a π rotation with a burst of duration $\tau_\pi = 100$ ns.
The amplitude of the phase shift is normalized by a factor $T_M / t_{wait} = 1 + \frac{250ns}{t_{wait}}$ since the signal is acquired during the whole period T_M.
The normalized phase signal can then be fitted with an exponential decay, as shown in Fig. 6.27 b, obtaining $T_1 = 2.7 \pm 0.7 \mu$s.
Moreover we observed that, by varying the position of the 100 ns microwave burst within a 12 μs pulse at the manipulation point C, no clear decay of the dispersive signal is detected, which suggests a spin lifetime longer than 10 μs at the manipulation point C, coherently with the fact that the two dots there are better isolated with respect to the point I/R.
Indeed, when working with isolated dots or a single qubit as in Sec. 6.5 the lower coupling with the environment can boost significantly the T_1.

The measured T_1 is compatible with the relaxation times obtained for hole singlet-triplet states in acceptor pairs in Si [55] and in Ge/Si nanowire DQDs [56]; in both cases T_1 has been measured at the charge degeneracy point with reflectometry setups similar to ours.

We highlight that T_1 could be boosted also by varying the magnetic field orientation [57]. Studies on magnetic field anisotropy can clarify whether T_1, together with the effective g-factors (and hence the dispersive shift for readout) and Rabi frenquency, could be maximized along a specific direction.

In a recent experiment [27], on the device of Sec. 6.5, we found a sweet spot for the spin relaxation where the gate voltage effect on the Larmor frequency is minimized, demonstrating a decoupling from background charge noise at this angle, leading to extended coherence reaching T_1 up to 1 ms and $T_2^{Echo} \simeq 88\,\mu$s, almost one order of magnitude larger than previous reports for spin-orbit qubits.

Moreover in the present setup no great effort has been done to optimize the resonator, which has a quality factor of $Q \simeq 18$, that could definitely be improved, thus enhancing the phase signal. Whereas a parametric amplifier could improve the SNR.
An enhancement in the phase sensitivity could push the implemented readout protocol to distinguish spin states with a micro-second integration time, enabling single-shot readout, as reported in a recent experiment with a gate-connected superconducting resonant circuit [58].

6.6.4. SCALING GATE REFLECTOMETRY DISPERSIVE READOUT

Using the approach described in the last section of this chapter, which does not require any coupling with a reservoir, we could think to use gate reflectometry combined with PSB readout in infinitely long bilinear arrays of split gates. The PSB readout should be implemented between two quantum dots facing each other, as in Refs. [50][59], instead than between adjacent qubits as described previously.
A representation of the proposed architecture is shown in Fig. 6.28. As in Sec. 5.8 one array encodes the information qubits, while the other one contains the helper dots (ancilla qubits), on which it can be realized gate-based dispersive readout. Nearby information qubits can be entangled through local exchange gates, that could be realized as local back-gates, as in Fig. 6.28 or with an upper layer of gates [60].

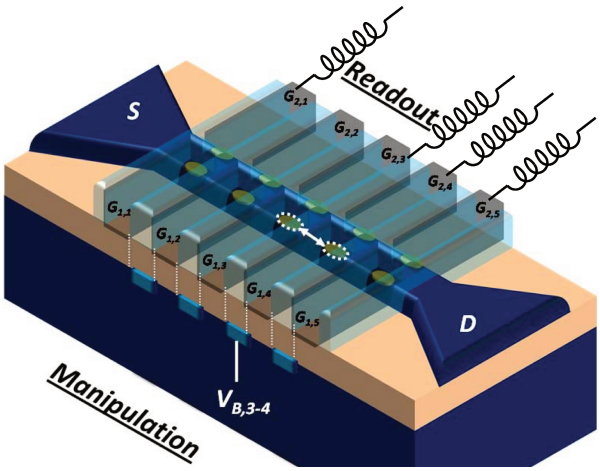

Figure 6.28: Bilinear array of qubits in a nanowire. Local back gates can provide tunability of the interdot coupling. The readout of each information qubit can be realized individually through PSB readout with the facing helper dot, or alternatively by realizing charge-sensing on an interdot transitions in the readout array. From Ref. [61].

However, using gate reflectometry dispersive readout would imply a fine tuning of both

the information and readout qubit gate voltages. This fine tuning, as explained in Sec. 6.6.2, is extremely sensitive to gate voltages variations, due to the strong gate voltage dependence of the holes g-factors and, consequently, of the Larmor frequencies.
A precise knowledge of the energy spectrum of each couple of manipulation and manipulation-readout dots is required to maximize the sensitivity of each detector. This makes the electrical tuning of the system not straighforward, especially when realizing two-qubit logic operations. To simplify this problem it would be helpful to completely isolate the readout dots from each other.
On the hardware side it would be beneficial to integrate the resonator in the back-end of the industrial chip, offering the possibility to engineer the resonant network at the wafer scale, guaranteeing controlled and reproducible qubit-resonator coupling.

Quantum error correction can be realized in linear arrays [62], and therefore the architecture of Fig. 6.28 could be used for the implementation of some proof of principle quantum algorithms.

BIBLIOGRAPHY

[1] Léo Bourdet and Yann-Michel Niquet. "All-electrical manipulation of silicon spin qubits with tunable spin-valley mixing". In: *Phys. Rev. B* 97 (15 Apr. 2018), p. 155433. DOI: 10.1103/PhysRevB.97.155433. URL: https://link.aps.org/doi/10.1103/PhysRevB.97.155433.

[2] Andrea Corna et al. "Electrically driven electron spin resonance mediated by spin–valley–orbit coupling in a silicon quantum dot". In: *npj Quant. Inform.* 4.1 (2018), p. 6.

[3] Will Gilbert et al. "On-demand electrical control of spin qubits". In: *Nature Nanotechnology* (Jan. 2023). ISSN: 1748-3395. DOI: 10.1038/s41565-022-01280-4. URL: https://doi.org/10.1038/s41565-022-01280-4.

[4] Cameron Spence et al. *Probing charge noise in few electron CMOS quantum dots*. 2022. DOI: 10.48550/ARXIV.2209.01853. URL: https://arxiv.org/abs/2209.01853.

[5] R. Hanson et al. "Spins in few-electron quantum dots". In: *Rev. Mod. Phys.* 79 (4 Oct. 2007), pp. 1217–1265. DOI: 10.1103/RevModPhys.79.1217. URL: https://link.aps.org/doi/10.1103/RevModPhys.79.1217.

[6] P. Scarlino et al. "In situ Tuning of the Electric-Dipole Strength of a Double-Dot Charge Qubit: Charge-Noise Protection and Ultrastrong Coupling". In: *Phys. Rev. X* 12 (3 July 2022), p. 031004. DOI: 10.1103/PhysRevX.12.031004. URL: https://link.aps.org/doi/10.1103/PhysRevX.12.031004.

[7] M. A. Fogarty et al. "Integrated silicon qubit platform with single-spin addressability, exchange control and single-shot singlet-triplet readout". In: *Nature Communications* 9.1 (Oct. 2018), p. 4370. ISSN: 2041-1723. DOI: 10.1038/s41467-018-06039-x. URL: https://doi.org/10.1038/s41467-018-06039-x.

[8] Patrick Harvey-Collard et al. "High-Fidelity Single-Shot Readout for a Spin Qubit via an Enhanced Latching Mechanism". In: *Phys. Rev. X* 8 (2 May 2018), p. 021046. DOI: 10.1103/PhysRevX.8.021046. URL: https://link.aps.org/doi/10.1103/PhysRevX.8.021046.

[9] Matias Urdampilleta et al. "Gate-based high fidelity spin readout in a CMOS device". In: *Nature Nanotechnology* 14.8 (Aug. 2019), pp. 737–741. ISSN: 1748-3395. DOI: 10.1038/s41565-019-0443-9. URL: https://doi.org/10.1038/s41565-019-0443-9.

[10] C. Barthel et al. "Relaxation and readout visibility of a singlet-triplet qubit in an Overhauser field gradient". In: *Phys. Rev. B* 85 (3 Jan. 2012), p. 035306. DOI: 10.1103/PhysRevB.85.035306. URL: https://link.aps.org/doi/10.1103/PhysRevB.85.035306.

[11] R. Schleser et al. "Time-resolved detection of individual electrons in a quantum dot". In: *Applied Physics Letters* 85.11 (2004), pp. 2005–2007. DOI: 10.1063/1.1784875. eprint: https://doi.org/10.1063/1.1784875. URL: https://doi.org/10.1063/1.1784875.

[12] K. MacLean et al. “Energy-Dependent Tunneling in a Quantum Dot”. In: *Phys. Rev. Lett.* 98 (3 Jan. 2007), p. 036802. DOI: 10.1103/PhysRevLett.98.036802. URL: https://link.aps.org/doi/10.1103/PhysRevLett.98.036802.

[13] Andrea Hofmann. “Thermodynamics and Spin-Orbit Interaction at the Level of Single Electrons”. en. PhD thesis. Zurich: ETH Zurich, 2017. DOI: 10.3929/ethz-b-000218647.

[14] S. Gustavsson et al. “Counting Statistics of Single Electron Transport in a Quantum Dot”. In: *Phys. Rev. Lett.* 96 (7 Feb. 2006), p. 076605. DOI: 10.1103/PhysRevLett.96.076605. URL: https://link.aps.org/doi/10.1103/PhysRevLett.96.076605.

[15] S. Gustavsson et al. “Electron counting in quantum dots”. In: *Surface Science Reports* 64.6 (2009), pp. 191–232. ISSN: 0167-5729. DOI: https://doi.org/10.1016/j.surfrep.2009.02.001. URL: https://www.sciencedirect.com/science/article/pii/S0167572909000193.

[16] A. Hofmann et al. “Measuring the Degeneracy of Discrete Energy Levels Using a GaAs/AlGaAs Quantum Dot”. In: *Phys. Rev. Lett.* 117 (20 Nov. 2016), p. 206803. DOI: 10.1103/PhysRevLett.117.206803. URL: https://link.aps.org/doi/10.1103/PhysRevLett.117.206803.

[17] Toshimasa Fujisawa et al. “Allowed and forbidden transitions in artificial hydrogen and helium atoms”. In: *Nature* 419.6904 (Sept. 2002), pp. 278–281. ISSN: 1476-4687. DOI: 10.1038/nature00976. URL: https://doi.org/10.1038/nature00976.

[18] C.W.J. Beenakker and H. van Houten. “Quantum Transport in Semiconductor Nanostructures”. In: *Semiconductor Heterostructures and Nanostructures*. Ed. by Henry Ehrenreich and David Turnbull. Vol. 44. Solid State Physics. Academic Press, 1991, pp. 1–228. DOI: https://doi.org/10.1016/S0081-1947(08)60091-0. URL: https://www.sciencedirect.com/science/article/pii/S0081194708600910.

[19] S. Gustavsson et al. “Counting statistics and super-Poissonian noise in a quantum dot: Time-resolved measurements of electron transport”. In: *Phys. Rev. B* 74 (19 Nov. 2006), p. 195305. DOI: 10.1103/PhysRevB.74.195305. URL: https://link.aps.org/doi/10.1103/PhysRevB.74.195305.

[20] A. Beckel et al. “Asymmetry of charge relaxation times in quantum dots: The influence of degeneracy”. In: 106.4 (May 2014), p. 47002. DOI: 10.1209/0295-5075/106/47002. URL: https://doi.org/10.1209/0295-5075/106/47002.

[21] James Clerk Maxwell. “IV. On the dynamical theory of gases”. In: *Philosophical Transactions of the Royal Society of London* 157 (1867), pp. 49–88. DOI: 10.1098/rstl.1867.0004. eprint: https://royalsocietypublishing.org/doi/pdf/10.1098/rstl.1867.0004. URL: https://royalsocietypublishing.org/doi/abs/10.1098/rstl.1867.0004.

[22] Ludwig Boltzmann, Stephen G. Brush, and Nandor L. Balazs. “Lectures on Gas Theory”. In: *Physics Today* 17.9 (1964), pp. 68–68. DOI: 10.1063/1.3051862. eprint: https://doi.org/10.1063/1.3051862. URL: https://doi.org/10.1063/1.3051862.

[23] Andrea Morello et al. “Single-shot readout of an electron spin in silicon”. In: *Nature* 467.7316 (Oct. 2010), pp. 687–691. ISSN: 1476-4687. DOI: 10.1038/nature09392. URL: https://doi.org/10.1038/nature09392.

[24] J. M. Elzerman et al. “Single-shot read-out of an individual electron spin in a quantum dot”. In: *Nature* 430.6998 (July 2004), pp. 431–435. ISSN: 1476-4687. DOI: 10.1038/nature02693. URL: https://doi.org/10.1038/nature02693.

[25] L. Petit et al. “Universal quantum logic in hot silicon qubits”. In: *Nature* 580.7803 (Apr. 2020), pp. 355–359. ISSN: 1476-4687. DOI: 10.1038/s41586-020-2170-7. URL: https://doi.org/10.1038/s41586-020-2170-7.

[26] C. H. Yang et al. “Operation of a silicon quantum processor unit cell above one kelvin”. In: *Nature* 580.7803 (Apr. 2020), pp. 350–354. ISSN: 1476-4687. DOI: 10.1038/s41586-020-2171-6. URL: https://doi.org/10.1038/s41586-020-2171-6.

[27] N. Piot et al. “A single hole spin with enhanced coherence in natural silicon”. In: *Nature Nanotechnology* 17.10 (Oct. 2022), pp. 1072–1077. ISSN: 1748-3395. DOI: 10.1038/s41565-022-01196-z. URL: https://doi.org/10.1038/s41565-022-01196-z.

[28] Kenta Takeda et al. “A fault-tolerant addressable spin qubit in a natural silicon quantum dot”. In: *Science Adv.* 2.8 (2016), e1600694.

[29] N. W. Hendrickx et al. “A single-hole spin qubit”. In: *Nature Communications* 11.1 (July 2020), p. 3478. ISSN: 2041-1723. DOI: 10.1038/s41467-020-17211-7. URL: https://doi.org/10.1038/s41467-020-17211-7.

[30] Leon C. Camenzind et al. *A spin qubit in a fin field-effect transistor*. 2021. arXiv: 2103.07369 [cond-mat.mes-hall].

[31] R Maurand et al. “A CMOS silicon spin qubit”. In: *Nature Comm.* 7 (2016), p. 13575.

[32] Jonathan H. Prechtel et al. “Decoupling a hole spin qubit from the nuclear spins”. In: *Nature Materials* 15.9 (Sept. 2016), pp. 981–986. ISSN: 1476-4660. DOI: 10.1038/nmat4704. URL: https://doi.org/10.1038/nmat4704.

[33] L. Petit et al. “Spin Lifetime and Charge Noise in Hot Silicon Quantum Dot Qubits”. In: *Phys. Rev. Lett.* 121 (7 Aug. 2018), p. 076801. DOI: 10.1103/PhysRevLett.121.076801. URL: https://link.aps.org/doi/10.1103/PhysRevLett.121.076801.

[34] Mircea Trif, Pascal Simon, and Daniel Loss. “Relaxation of Hole Spins in Quantum Dots via Two-Phonon Processes”. In: *Phys. Rev. Lett.* 103 (10 Sept. 2009), p. 106601. DOI: 10.1103/PhysRevLett.103.106601. URL: https://link.aps.org/doi/10.1103/PhysRevLett.103.106601.

[35] Charles Tahan and Robert Joynt. “Relaxation of excited spin, orbital, and valley qubit states in ideal silicon quantum dots”. In: *Phys. Rev. B* 89 (7 Feb. 2014), p. 075302. DOI: 10.1103/PhysRevB.89.075302. URL: https://link.aps.org/doi/10.1103/PhysRevB.89.075302.

[36] Jing Li, Benjamin Venitucci, and Yann-Michel Niquet. “Hole-phonon interactions in quantum dots: Effects of phonon confinement and encapsulation materials on spin-orbit qubits”. In: *Phys. Rev. B* 102 (7 Aug. 2020), p. 075415. DOI: 10.1103/PhysRevB.102.075415. URL: https://link.aps.org/doi/10.1103/PhysRevB.102.075415.

[37] Denis V. Bulaev and Daniel Loss. “Spin Relaxation and Decoherence of Holes in Quantum Dots”. In: *Phys. Rev. Lett.* 95 (7 Aug. 2005), p. 076805. DOI: 10.1103/PhysRevLett.95.076805. URL: https://link.aps.org/doi/10.1103/PhysRevLett.95.076805.

[38] A. Crippa et al. “Gate-reflectometry dispersive readout and coherent control of a spin qubit in silicon”. In: *Nature Communications* 10.1 (July 2019), p. 2776. ISSN: 2041-1723. DOI: 10.1038/s41467-019-10848-z. URL: https://doi.org/10.1038/s41467-019-10848-z.

[39] M. G. House et al. “Radio frequency measurements of tunnel couplings and singlet–triplet spin states in Si:P quantum dots”. In: *Nature Communications* 6.1 (Nov. 2015), p. 8848. ISSN: 2041-1723. DOI: 10.1038/ncomms9848. URL: https://doi.org/10.1038/ncomms9848.

[40] Alessandro Crippa et al. “Electrical spin driving by g-matrix modulation in spin-orbit qubits”. In: *Phys. Rev. Lett.* 120.13 (2018), p. 137702.

[41] J. Stehlik et al. “Fast Charge Sensing of a Cavity-Coupled Double Quantum Dot Using a Josephson Parametric Amplifier”. In: *Phys. Rev. Applied* 4 (1 July 2015), p. 014018. DOI: 10.1103/PhysRevApplied.4.014018. URL: https://link.aps.org/doi/10.1103/PhysRevApplied.4.014018.

[42] Rami Ezzouch. “Gate reflectometry as readout and spectroscopy tool for silicon spin qubits”. Theses. Université Grenoble Alpes [2020-....], June 2021. URL: https://tel.archives-ouvertes.fr/tel-03337854.

[43] V. Nguyen et al. “Deep reinforcement learning for efficient measurement of quantum devices”. In: *npj Quantum Information* 7.1 (June 2021), p. 100. ISSN: 2056-6387. DOI: 10.1038/s41534-021-00434-x. URL: https://doi.org/10.1038/s41534-021-00434-x.

[44] Natalia Ares. “Machine learning as an enabler of qubit scalability”. In: *Nature Reviews Materials* 6.10 (Oct. 2021), pp. 870–871. ISSN: 2058-8437. DOI: 10.1038/s41578-021-00321-z. URL: https://doi.org/10.1038/s41578-021-00321-z.

[45] H. Moon et al. “Machine learning enables completely automatic tuning of a quantum device faster than human experts”. In: *Nature Communications* 11.1 (Aug. 2020), p. 4161. ISSN: 2041-1723. DOI: 10.1038/s41467-020-17835-9. URL: https://doi.org/10.1038/s41467-020-17835-9.

[46] D. T. Lennon et al. “Efficiently measuring a quantum device using machine learning”. In: *npj Quantum Information* 5.1 (Sept. 2019), p. 79. ISSN: 2056-6387. DOI: 10.1038/s41534-019-0193-4. URL: https://doi.org/10.1038/s41534-019-0193-4.

[47] S Nadj-Perge et al. “Spin-orbit qubit in a semiconductor nanowire”. In: *Nature* 468.7327 (2010), pp. 1084–1087.

[48] S Nadj-Perge et al. “Spectroscopy of spin-orbit quantum bits in indium antimonide nanowires”. In: *Phys. Rev. Lett.* 108.16 (2012), p. 166801.

[49] KD Petersson et al. “Circuit quantum electrodynamics with a spin qubit”. In: *Nature* 490.7420 (2012), pp. 380–383.

[50] Rami Ezzouch et al. “Dispersively Probed Microwave Spectroscopy of a Silicon Hole Double Quantum Dot”. In: *Phys. Rev. Applied* 16 (3 Sept. 2021), p. 034031. DOI: 10.1103/PhysRevApplied.16.034031. URL: https://link.aps.org/doi/10.1103/PhysRevApplied.16.034031.

[51] Benjamin Venitucci et al. “Electrical manipulation of semiconductor spin qubits within the g-matrix formalism”. In: *Phys. Rev. B* 98.15 (2018), p. 155319.

[52] P Scarlino et al. “Second-harmonic coherent driving of a spin qubit in a Si/SiGe quantum dot”. In: *Phys. Rev. Lett.* 115.10 (2015), p. 106802.

[53] Erika Kawakami et al. “Electrical control of a long-lived spin qubit in a Si/SiGe quantum dot”. In: *Nature Nanotech.* 9.9 (2014), pp. 666–670.

[54] A. Aprà et al. “Physical and technological challenges towards silicon-based quantum computing”. In: *2021 Silicon Nanoelectronics Workshop (SNW)*. 2021, pp. 1–2. DOI: 10.1109/SNW51795.2021.00003.

[55] J van der Heijden et al. “Spin-orbit dynamics of single acceptor atoms in silicon”. In: *Science Adv.* 4.12 (2018), eaat9199.

[56] Andrew P Higginbotham et al. “Hole spin coherence in a Ge/Si heterostructure nanowire”. In: *Nano Lett.* 14.6 (2014), pp. 3582–3586.

[57] Bent Weber et al. “Spin–orbit coupling in silicon for electrons bound to donors”. In: *npj Quant. Inform.* 4.1 (2018), p. 61.

[58] Guoji Zheng et al. “Rapid gate-based spin read-out in silicon using an on-chip resonator”. In: *Nature Nanotechnology* 14.8 (Aug. 2019), pp. 742–746. ISSN: 1748-3395. DOI: 10.1038/s41565-019-0488-9. URL: https://doi.org/10.1038/s41565-019-0488-9.

[59] A. Aprà et al. “Dispersive vs charge-sensing readout for linear quantum registers”. In: *2020 IEEE International Electron Devices Meeting (IEDM)*. 2020, pp. 38.4.1–38.4.4. DOI: 10.1109/IEDM13553.2020.9372090.

[60] T. Bédécarrats et al. “A new FDSOI spin qubit platform with 40nm effective control pitch”. In: *2021 IEEE International Electron Devices Meeting (IEDM)*. 2021, pp. 1–4. DOI: 10.1109/IEDM19574.2021.9720497.

[61] S. De Franceschi et al. “SOI technology for quantum information processing”. In: Dec. 2016, pp. 13.4.1–13.4.4. DOI: 10.1109/IEDM.2016.7838409.

[62] Cody Jones et al. “Logical Qubit in a Linear Array of Semiconductor Quantum Dots”. In: *Phys. Rev. X* 8.2 (2018), p. 021058.

7

CONCLUSION

The future belongs to those who prepare for it today.

Malcolm X

Many different qubit platforms based mainly on superconductors, semiconductor, photons and ion traps have been demonstrated in the last 30 years, each of them offering unique advantages and drawbacks.
Among these, superconducting qubits seems to be the best candidates, as demonstrated by the latest 53 qubit Sycamore chip from Google[1].
However it must be said that when it was realized the first superconducting qubit [2], spin qubits in semiconductors had just been proposed theoretically by Loss-DiVincenzo[3], in 1997. The first spin qubit [4] (in GaAs) was realized only 8 years later.
Since then the engineering of materials, manipulation and readout tools have been considerably developed, leading to semiconductor spin qubit relaxation times (T_1) up to one minute [5], qubit operating at more than 1K [6] [7], single-[8][9][10] and two-qubit[11][12][13] gate fidelities above the threshold for fault-tolerant quantum computation [14], and architectures with up to six qubits[15].

Now that many of the basic requirements for quantum computation with spin qubits have been fulfilled, the focus is increasingly shifting towards the most relevant challenge: scaling to large-scale quantum systems.
The maturity of CMOS technology with silicon allows the realization of semiconductor spin qubit devices based on an industrial scale manufacturing process [16][17][18], offering a viable path towards the scalability.

Throughout this manuscript I studied qubit arrays based on both electrons and holes in silicon, trying to highlight the differences between them.
The main advantage of electrons, expecially in purified ^{28}Si, are the longer relaxation and coherence times [19], allowing gate operations with higher fidelities.
Electron spins can be manipulated either through an electric or magnetic AC field. The magnetic control requires an ESR line to generate the AC magnetic field. The electrical control instead relies on the spin-orbit coupling, that allows the electron magnetic moment to couple with external electric fields. The SOC of electrons in silicon is usually enabled by a micromagnet, but if the SOC is naturally strong, as it is the case for holes, the spin can be controlled simply with an AC electric field applied on the gate.

As discussed in Sec. 2.9, the ESR line and the micromagnet are quite invasive and hardly scalable. For this reason we focus solely on the direct electrical manipulation, for both electrons and holes.

In Sec. 4.9 we showed that the hole mobility is increased for gates far away from the reservoirs, mainly due to the diffusion of impurities during the doping process.
Even if the two readout schemes are completely different it is reasonable to suspect that the difference between the spin relaxation time $T_1 \simeq 150$ μs measured in Sec. 6.5 (at $B = 0.9$ T) and the $T_1 \simeq 3$ μs of Sec. 6.6 (at $B = 0.6$ T), might as well be related to the presence of defects near the reservoir, that could affect negatively T_1.
However further systematical studies are required to benchmark the qubit properties related to each step of the fabrication process, and in particular to the doping level and the physical distance between the qubit and the reservoir.

The observations of Sec. 4.9 motivated us to study qubits as isolated as possible from the reservoirs. This also means to get rid of current measurements and we focused on the dispersive readout, enabled just by an inductor connected to a gate, or to an ohmic contact.
An identical reflectometry setup can be used for both gate-based dispersive readout and RF charge-sensing. The two approaches are compared in Sec. 5.3. The gate-based dispersive readout minimizes the device overhead thereby facilitating scale-up to large qubit arrays. The charge-sensing readout, requires additional readout components but is less sensitive to the strength of the interdot coupling facilitating operation in the few-electron regime. Moreover, as shown in Sec. 5.6, it allows fast single shot readout.
The readout through an RF charge sensor is a simpler, faster and generally better approach in my opinion. One could argue that its limitation is the need for a nearby reservoir, as usually done in the literature, that would impose severe limitation for scalability. In Sec. 5.8 we instead propose that it could also rely on an interdot transition, rather than a dot-reservoir one.

In Sec. 5.7 we measured signatures of EDSR. However, because of the weak SOC, the electrical manipulation was too slow to observe coherent Rabi oscillations. The SOC could be enhanced by mechanisms such as orbital or valley-orbit mixing, but this would require an accurate tuning of the DQD energy spectrum [20].

Holes instead offers two main advantages compared to electrons: the stronger spin-orbit coupling, that enables coherent electrical spin manipulation; the strong g-factor variability, which can enable the dispersive readout of a spin qubit [21] away from the charge degeneracy point $\epsilon \simeq 0$, as well as guaranteeing individual spin addressability. In Chap. 6 we focus on the study of linear p-type qubit arrays.
In Secs. 6.1, 6.2 we studied a linear p-type six-gates array, demonstrating independent and simultaneous single-shot readout of the two quantum dots in the center of the array via remote charge-sensing on the two reservoirs. The remote sensing is enabled by a single quantum dot accumulated with two gates, that is used both as a charge sensor and as a reservoir.
In Sec. 6.3 I explain how to measure the tunnel rates with an RF charge sensor. An accurate knowledge of the dot-reservoir tunnel rates is crucial to set the energy-selective readout of the spin state of Sec. 6.4. Unfortunately, the high temperature ($T \simeq 450$ mK) and the high magnetic field required didn't allow a proper initialization of the spin state.
The same reservoir-based RF charge-sensing technique has been applied to study a single

quantum dot in another similar p-type four-gate array at lower electronic temperature ($T_e \simeq 100$ mK), demonstrating coherent control of the qubit via an electric field .
Further experiment on the same device, varying the magnetic field orientation, revealed the existence of sweet spots where the impact of charge noise is minimized[18]. This led to an extension of the Hahn-echo coherence time up to 88 μs, exceeding by an order of magnitude the best reported values for hole-spin qubits. These findings are encouraging for scalable quantum information processing with hole spin qubits in silicon.

In Sec. 6.6 it is reported the implementation of gate-based RF reflectometry for the dispersive readout a hole spin qubit, using a p-type double gate transistor. The demonstrated qubit readout scheme requires no coupling to a Fermi reservoir, thereby offering a compact and potentially scalable solution. This readout approach ultimately relies on the difference of g-factor Δg =0.5 between the two dots. With electrons the g-factor variability is way smaller and the dispersive readout of a fully functional electron spin qubit in silicon has not been demonstrated yet.

We demonstrated spin-to-charge conversion based on either PSB (in Chap. 5 and Sec. 6.6) or energy-selective readout (in Secs. 6.4 and 6.5).
Given a base temperature of T_e = 440 mK the PSB readout has proven to be generally better than energy-selective readout.
Indeed the T_1 is degraded with increasing magnetic field and temperature [22][23]. When doing energy-selective readout at T = 440 mK a relatively high magnetic field is required to resolve the spin states, such that the Zeeman splitting is bigger than the thermal broadening of the Fermi reservoir.
Conversely PSB readout allows to work at lower magnetic fields and then to increase T_1. Indeed it is just relying on spin dependent interdot tunneling that is not affected by the thermal broadening of a Fermi reservoir and it is still detectable at temperatures up to more than 1K [7][6] .

In our proposals for scaling the charge-sensing (in 5.8) and the gate-based dispersive readout (in 6.6.4) in qubit arrays it is required to turn on and off at will the interaction between information qubits and/or between qubits and sensors.
In the most recent LETI devices it has been added a second layer of gates [24], allowing local control over the tunnel coupling. This is a crucial step towards the scalability of the presented architectures.
The local control over the tunnel coupling is also fundamental towards the realization of two qubit logic gates. Indeed it allows to rapidly turn on and off the exchange coupling [25][26][27], that shifts the Larmor frequencies of each qubit depending on the state of the other one. By exciting at fixed Larmor frequency one qubit (the target qubit) is flipped only if the other qubit (the control qubit) is, for example, in a $|1\rangle$ state. This conditional spin operation defines a CNOT gate.

Linear quantum dot arrays, hosting up to 12 qubits [28] [29], have already been demonstrated experimentally. Logic quantum operations so far are limited between the first neighbours in the qubit chain. The number of first neighbours are two in linear chains and at most five in bilinear chains. The number of first neighbours can be increased by using 2-D[14] (8 first neighbours) or even 3-D architectures [30] (26 neighbours).
A qubit elementary cell can be defined as the minimum number of physical qubit that can define a logical qubit and it is estimated that should be composed by at least 13 qubits[31].
In linear (or bilinear) arrays logic operations between qubits that are not first neighbours

could be realized through SWAP gates, and hence these platform could be used for some proof of principle demonstrations of quantum algorithms. However, the realization of more complex algorithms in linear arrays would require a very high number of SWAP operations that might eventually degrade the qubit performances and therefore 2-D or 3-D architectures will probably be required.
Alternatively, logic qubits belonging to different elementary cells could be entangled by coupling them with photons in superconducting resonators [32][33][34].

What is sure is that there is still a lot to work on, but after 40 years from the proposal of Richard Feynman [35] (1982) quantum computing is becoming reality and the strong pace at which the field is growing leaves room for optimism.
The collaboration between researchers and industries will play a key role in the future development of this technology.

I hope that, by the end of the century, we will talk about an analogue of the Moore law for the scaling of quantum computation platforms. If not, as usual, all the scientific and technological effort on the physics and the fabrication of these complex devices will certainly find other useful applications.

BIBLIOGRAPHY

[1] Frank Arute et al. “Quantum supremacy using a programmable superconducting processor”. In: *Nature* 574.7779 (Oct. 2019), pp. 505–510. ISSN: 1476-4687. DOI: 10.1038/s41586-019-1666-5. URL: https://doi.org/10.1038/s41586-019-1666-5.

[2] Y. Nakamura, Yu. A. Pashkin, and J. S. Tsai. “Coherent control of macroscopic quantum states in a single-Cooper-pair box”. In: *Nature* 398.6730 (Apr. 1999), pp. 786–788. ISSN: 1476-4687. DOI: 10.1038/19718. URL: https://doi.org/10.1038/19718.

[3] Daniel Loss and David P. DiVincenzo. “Quantum computation with quantum dots”. In: *Phys. Rev. A* 57 (1 Jan. 1998), pp. 120–126. DOI: 10.1103/PhysRevA.57.120. URL: https://link.aps.org/doi/10.1103/PhysRevA.57.120.

[4] Jason R Petta et al. “Coherent manipulation of coupled electron spins in semiconductor quantum dots”. In: *Science* 309.5744 (2005), pp. 2180–2184.

[5] Leon C. Camenzind et al. “Hyperfine-phonon spin relaxation in a single-electron GaAs quantum dot”. In: *Nature Communications* 9.1 (Aug. 2018), p. 3454. ISSN: 2041-1723. DOI: 10.1038/s41467-018-05879-x. URL: https://doi.org/10.1038/s41467-018-05879-x.

[6] C. H. Yang et al. “Operation of a silicon quantum processor unit cell above one kelvin”. In: *Nature* 580.7803 (Apr. 2020), pp. 350–354. ISSN: 1476-4687. DOI: 10.1038/s41586-020-2171-6. URL: https://doi.org/10.1038/s41586-020-2171-6.

[7] L. Petit et al. “Universal quantum logic in hot silicon qubits”. In: *Nature* 580.7803 (Apr. 2020), pp. 355–359. ISSN: 1476-4687. DOI: 10.1038/s41586-020-2170-7. URL: https://doi.org/10.1038/s41586-020-2170-7.

[8] Kenta Takeda et al. “A fault-tolerant addressable spin qubit in a natural silicon quantum dot”. In: *Science Adv.* 2.8 (2016), e1600694.

[9] M Veldhorst et al. “An addressable quantum dot qubit with fault-tolerant control-fidelity”. In: *Nature Nanotech.* 9.12 (2014), pp. 981–985.

[10] Jun Yoneda et al. “A quantum-dot spin qubit with coherence limited by charge noise and fidelity higher than 99.9%”. In: *Nature Nanotech.* 13.2 (2018), pp. 102–106.

[11] Akito Noiri et al. “Fast universal quantum gate above the fault-tolerance threshold in silicon”. In: *Nature* 601.7893 (Jan. 2022), pp. 338–342. ISSN: 1476-4687. DOI: 10.1038/s41586-021-04182-y. URL: https://doi.org/10.1038/s41586-021-04182-y.

[12] Xiao Xue et al. “Quantum logic with spin qubits crossing the surface code threshold”. In: *Nature* 601.7893 (Jan. 2022), pp. 343–347. ISSN: 1476-4687. DOI: 10.1038/s41586-021-04273-w. URL: https://doi.org/10.1038/s41586-021-04273-w.

[13] Adam R. Mills et al. “Two-qubit silicon quantum processor with operation fidelity exceeding 99%”. In: *Science Advances* 8.14 (2022), eabn5130. DOI: 10.1126/sciadv.abn5130. eprint: https://www.science.org/doi/pdf/10.1126/sciadv.abn5130. URL: https://www.science.org/doi/abs/10.1126/sciadv.abn5130.

[14] Austin G. Fowler et al. “Surface codes: Towards practical large-scale quantum computation”. In: *Phys. Rev. A* 86 (3 Sept. 2012), p. 032324. DOI: 10.1103/PhysRevA.86.032324. URL: https://link.aps.org/doi/10.1103/PhysRevA.86.032324.

[15] Stephan G. J. Philips et al. “Universal control of a six-qubit quantum processor in silicon”. In: *Nature* 609.7929 (Sept. 2022), pp. 919–924. ISSN: 1476-4687. DOI: 10.1038/s41586-022-05117-x. URL: https://doi.org/10.1038/s41586-022-05117-x.

[16] A. M. J. Zwerver et al. “Qubits made by advanced semiconductor manufacturing”. In: *Nature Electronics* 5.3 (Mar. 2022), pp. 184–190. ISSN: 2520-1131. DOI: 10.1038/s41928-022-00727-9. URL: https://doi.org/10.1038/s41928-022-00727-9.

[17] R. Li et al. “A flexible 300 mm integrated Si MOS platform for electron- and hole-spin qubits exploration”. In: *2020 IEEE International Electron Devices Meeting (IEDM)*. 2020, pp. 38.3.1–38.3.4. DOI: 10.1109/IEDM13553.2020.9371956.

[18] N. Piot et al. “A single hole spin with enhanced coherence in natural silicon”. In: *Nature Nanotechnology* 17.10 (Oct. 2022), pp. 1072–1077. ISSN: 1748-3395. DOI: 10.1038/s41565-022-01196-z. URL: https://doi.org/10.1038/s41565-022-01196-z.

[19] Peter Stano and Daniel Loss. *Review of performance metrics of spin qubits in gated semiconducting nanostructures*. 2021. DOI: 10.48550/ARXIV.2107.06485. URL: https://arxiv.org/abs/2107.06485.

[20] Will Gilbert et al. “On-demand electrical control of spin qubits”. In: *Nature Nanotechnology* (Jan. 2023). ISSN: 1748-3395. DOI: 10.1038/s41565-022-01280-4. URL: https://doi.org/10.1038/s41565-022-01280-4.

[21] A. Crippa et al. “Gate-reflectometry dispersive readout and coherent control of a spin qubit in silicon”. In: *Nature Communications* 10.1 (July 2019), p. 2776. ISSN: 2041-1723. DOI: 10.1038/s41467-019-10848-z. URL: https://doi.org/10.1038/s41467-019-10848-z.

[22] L. Petit et al. “Spin Lifetime and Charge Noise in Hot Silicon Quantum Dot Qubits”. In: *Phys. Rev. Lett.* 121 (7 Aug. 2018), p. 076801. DOI: 10.1103/PhysRevLett.121.076801. URL: https://link.aps.org/doi/10.1103/PhysRevLett.121.076801.

[23] Jing Li, Benjamin Venitucci, and Yann-Michel Niquet. “Hole-phonon interactions in quantum dots: Effects of phonon confinement and encapsulation materials on spin-orbit qubits”. In: *Phys. Rev. B* 102 (7 Aug. 2020), p. 075415. DOI: 10.1103/PhysRevB.102.075415. URL: https://link.aps.org/doi/10.1103/PhysRevB.102.075415.

[24] T. Bédécarrats et al. “A new FDSOI spin qubit platform with 40nm effective control pitch”. In: *2021 IEEE International Electron Devices Meeting (IEDM)*. 2021, pp. 1–4. DOI: 10.1109/IEDM19574.2021.9720497.

[25] David M Zajac et al. “Resonantly driven CNOT gate for electron spins”. In: *Science* 359.6374 (2018), pp. 439–442.

[26] M. Veldhorst et al. “A two-qubit logic gate in silicon”. In: *Nature* 526.7573 (Oct. 2015), pp. 410–414. ISSN: 1476-4687. DOI: 10.1038/nature15263. URL: https://doi.org/10.1038/nature15263.

[27] TF Watson et al. “A programmable two-qubit quantum processor in silicon”. In: *Nature* 555.7698 (2018), pp. 633–637.

[28] D. M. Zajac et al. “Scalable Gate Architecture for a One-Dimensional Array of Semiconductor Spin Qubits”. In: *Phys. Rev. Applied* 6 (5 Nov. 2016), p. 054013. DOI: 10.1103/PhysRevApplied.6.054013. URL: https://link.aps.org/doi/10.1103/PhysRevApplied.6.054013.

[29] W. I. L. Lawrie et al. “Quantum dot arrays in silicon and germanium”. In: *Applied Physics Letters* 116.8 (2020), p. 080501. DOI: 10.1063/5.0002013. eprint: https://doi.org/10.1063/5.0002013. URL: https://doi.org/10.1063/5.0002013.

[30] Louis Houtin et al. *Quantum device with spin qubits*. URL: https://patents.google.com/patent/US10607993B2/en.

[31] Cody Jones et al. “Logical Qubit in a Linear Array of Semiconductor Quantum Dots”. In: *Phys. Rev. X* 8.2 (2018), p. 021058.

[32] LMK Vandersypen et al. “Interfacing spin qubits in quantum dots and donorshot, dense, and coherent”. In: *npj Quant. Inform.* 3.1 (2017), p. 34.

[33] F. Borjans et al. “Resonant microwave-mediated interactions between distant electron spins”. In: *Nature* 577.7789 (Jan. 2020), pp. 195–198. ISSN: 1476-4687. DOI: 10.1038/s41586-019-1867-y. URL: https://doi.org/10.1038/s41586-019-1867-y.

[34] Cécile X. Yu et al. *Strong coupling between a photon and a hole spin in silicon*. 2022. DOI: 10.48550/ARXIV.2206.14082. URL: https://arxiv.org/abs/2206.14082.

[35] Richard P Feynman. “Simulating physics with computers”. In: *International journal of theoretical physics* 21.6/7 (1982), pp. 467–488.

ACKNOWLEDGEMENTS

Finally it is worth to spend some words for all the people that made possible my Phd journey.
I admit we faced many difficulties during my Phd as the initial bad quality of the devices, problems with the cryostats, the transfer of the lab in a new building and also the pandemic, that kept us out of the lab for few months. Only thanks to all the people of the LATEQS team it has been possible to overcome all these difficulties. I will always be grateful to everybody!

First of all I want to say thank you to Iulian Matei. He built the cryostat I worked with in the past years. Moreover he was always there, ready to fix problems and to improve the cryostat depending on my needs. I will never forget when, during my first year (and not only), he guided me in the cooldown of Tritonito by phone while he was supposed to relax on the beach.

A very special thanks goes to Silvano De Franceschi, my thesis supervisor. He was the one convincing me to come to Grenoble. I enjoyed our discussions, debates, and sometimes arguments. When he is enthusiastic about something it is often contagious.
I learned from him how to think scientifically. Sometimes by playing the role of "the advocate of the devil", through his questions, he always managed to let me understand which other questions should have been addressed to demonstrate my thesis. It has been a pleasure benefiting from his experience and listening him sharing his physics knowledge.

Thank you Alessandro Crippa. Initially he was the post-doc supervising me, in the end we are good friends. He taught me probably more than everybody about the physics of quantum dots and the subtle details of dispersive readout. "OO il quantum".
Also Marco Tagliaferri, who joined our group for only one year was very keen in helping the "italian crew" of the lab, thank you Marco.

Thank you Romain Maurand. I liked a lot your very concrete approach to science. Thank you for spending time at my experiment discussing problems and results. I will never forget our discussions while smoking outside CEA, and also about the "big mama fridge".

Together with Iulian, also Xavier Jehl has been extremely helpful during my Phd. Besides helping me with the cryostat maintenance and cooldown he was my referent when I needed to discuss the electronics of the setup. I will never forget all the times when you were coming with an electronic device saying "this guy has almost my age, but it still works well".

During my last year I had the chance to work together with Boris Brun. It was fun working together and I am happy that, also thanks to our collaboration, you manage to realize the qubit of section 6.5 with Nicolas Piot. Good luck for your future.

I want to say thank you to Edoardo Catapano. He took time to deeply analyze my data,

bringing to the results of section 4.9. I enjoyed our fruitful conversations about the device physics, perhaps the other friends that were having dinner with us a bit less.

Thank you to Jing Li, who helped me in the understanding of the experimental results and in elaborating a theory to explain them. I enjoyed our lunches together.

Thank you to all the people responsible of the device fabrication at CEA-LETI, without you I would have had a hard time in the cleanroom. A special thanks goes in particular to Louis Hutin, Benoit Bertrand, Thomas Bedecarrats and Maud Vinet.

All the experimental activities in our group wouldn't have been possible without Marc Sanquer, the founder of the quantum silicon project in Grenoble. He was a very humble person and always available to calmly answer my questions. Rest in peace.

I would like to congratulate with Giorgio Parisi for his recent Nobel prize. It is an honour to say that I had the chance to discuss with him during my university.

Finally i would like to mention all the friends out of the lab, because a balanced life between work and distractions it is also important for a profitable research. I believe that it is hard to work well if the personal life doesn't go as well.
Therefore a special thanks goes to all the people I met in Grenoble: Marc, Pablo, Lorenzo, Francesco, Martina, Maria, Emma, Chris, Stefano, Salomé, Gonzalo, Paolo, Edo, Pippo, Nico, Tom, Robin, Seb, Valentina, Monica, Tessa, Koyomi, and many others I have forgotten.

It's also worth mentioning my friends from Roma, who helped me to become the person I am today. Grazie Daddi, Mich, Picculè, Giason, Darione, Nixon, Stief, Capata, Trotta, Frank, Gabriel, Mastro, Giulio, Mattia, Valeria, Eugenia.

Last, but not least, for obvious reasons: Thanks to my parents!

List of Publications

1. Crippa, A., Ezzouch, R., Aprà, A., Amisse, A., Laviéville, R., Hutin, L., Bertrand,B., Vinet, M., Urdampilleta, M., Meunier, T., Sanquer, M., Jehl, X., Maurand, R., and De Franceschi, S. Gate-reflectometry dispersive readout and coherent control of a spin qubit in silicon. *Nature Communications 10*, 2776 (2019)

2. Meunier, T., Urdampilleta, M., Niegemann, D., Jadot, B., Chanrion, E., Mortemousque, P.-A., Spence, C., Bertrand, B., Billiot, G., Casse, M., Hutin, L., Jacquinot, H., Pillonet, G., Rambal, N., Thonnart, Y., Amisse, A., Aprà, A., Bourdet, L., Crippa, A., Ezzouch, R., Jehl, X., Maurand, R., Niquet, Y.-M., Sanquer, M., Venitucci, B., De Franceschi, S., and Vinet, M. Qubit read-out in Semiconductor quantum processors: challenges and perspectives. In *2019 IEEE International Electron Devices Meeting (IEDM)* (dec 2019), vol. 2019-Decem, IEEE, pp. 31.6.1–31.6.4

3. Niquet, Y. M., Hutin, L., Diaz, B. M., Venitucci, B., Li, J., Michal, V., Fernandez-Bada, G. T., Jacquinot, H., Amisse, A., Aprà, A., Ezzouch, R., Piot, N., Vincent, E., Yu, C., Zihlmann, S., Brun-Barriere, B., Schmitt, V., Dumur, E., Maurand, R., Jehl, X., Sanquer, M., Bertrand, B., Rambal, N., Niebojewski, H., Bedecarrats, T., Casse, M., Catapano, E., Mortemousque, P. A., Thomas, C., Thonnart, Y., Billiot, G., Morel, A., Charbonnier, J., Pallegoix, L., Niegemann, D., Klemt, B., Urdampilleta, M., El Homsy, V., Nurizzo, M., Chanrion, E., Jadot, B., Spence, C., Thiney, V., Paz, B., de Franceschi, S., Vinet, M., and Meunier, T. Challenges and perspectives in the modeling of spin qubits. In *2020 IEEE International Electron Devices Meeting (IEDM)* (dec 2020), vol. 2019-Septe, IEEE, pp. 30.1.1–30.1.4

4. Aprà, A., Crippa, A., Tagliaferri, M. L. V., Li, J., Ezzouch, R., Bertrand, B., Hutin, L., Rambal, N., Catapano, E., Niebojewsky, H., Bedecarrats, T., Vinet, M., Urdampilleta, M., Meunier, T., Niquet, Y. M., Dumur, E., Sanquer, M., Jehl, X., Maurand, R., and De Franceschi, S. Dispersive vs charge-sensing readout for linear quantum registers. In *2020 IEEE International Electron Devices Meeting (IEDM)* (dec 2020), IEEE, pp. 38.4.1–38.4.4

5. Catapano, E., Ghibaudo, G., Cassé, M., Frutuoso, T.M., Paz, B., Bedecarrats, T., Aprà, A., and Gaillard, F., De Franceschi, S., Meunier, T., and Vinet, M., Statistical and Electrical Modeling of FDSOI Four-Gate Qubit MOS Devices at Room Temperature, in *IEEE Journal of the Electron Devices Society*, vol. 9, pp. 582-590, 2021

6. Aprà, A., Ezzouch, R., Bertrand, B., Rambal, N.,Catapano, E., Niebojewski, H., Bedecarrats, T., Hutin, L., Chanrion, E., Urdampilleta, M., Mizokuchi, R., Bassi, M., Piot, N., Vincent, E., Brun-Barriere, B., Zihlmann, S., Schmitt, V., Dumur, E., Jehl, X.,Maurand, R., Vinet, M., Meunier, T. and De Franceschi, S. Physical and technological challenges towards silicon-based quantum computing. In *2021 Silicon Nanoelectronics Workshop (SNW)*, 2021, pp. 1-2.

7. Ezzouch, R., Zihlmann, S. , Michal, V.P., Li, J., Aprà, A., Bertrand, B., Hutin, L., Vinet, M., Urdampilleta, M., Meunier, T., Jehl, X., Niquet, Y.M., Sanquer, M., De Franceschi,

S., and Maurand, R., "Dispersively Probed Microwave Spectroscopy of a Silicon Hole Double Quantum Dot". In *Physical Review Applied* 16 (3 Sept. 2021), p. 034031.

8. N. Piot, B. Brun, V. Schmitt, S. Zihlmann. V. P. Michal, A. Aprà,Abadillo-Uriel, X. Jehl, B. Bertrand,H. Niebojewski, L. Hutin , M. Vinet, M. Urdampilleta, T. Meunier, Y. -M. Niquet, R. Maurand and S. De Franceschi, A single hole spin with enhanced coherence in natural silicon. In *Nature Nanotechnology* 17.10 (Oct. 2022), pp. 1072–1077.

9. Catapano, E., Aprà, A., Cassé, M., Gaillard, F., De Franceschi, S., Meunier, T., Vinet, M.,"Characterization and Lambert – W Function based modeling of FDSOI five-gate qubit MOS devices down to cryogenic temperatures". In *2021 Joint International EUROSOI Workshop and International Conference on Ultimate Integration on Silicon* (EuroSOI-ULIS), 2021, pp. 1-4, 16 (3 Sept. 2021).

10. E. Catapano, A. Aprà, M. Cassé,F. Gaillard, S. de Franceschi, T. Meunier, M. Vinet, G. Ghibaudo, Modeling and simulations of FDSOI five-gate qubit MOS devices down to deep cryogenic temperatures. In *Solid-State Electronics* vol. 193, pp. 108291, 2022.